Development of a Multi-material Extruder System to

3D Print Hard Thermoplastics, Soft Elastomers and

Liquid Metals

by

Mohammad Abu Hasan Khondoker

A thesis submitted in partial fulfillment of the requirements for the degree of

Doctor of Philosophy

Department of Mechanical Engineering

University of Alberta

ABSTRACT

Functional sensors often consist of rigid parts, soft rubber-like parts and mechanically tunable electronic components. They are usually fabricated through numerous expensive processing steps and can require extensive assembly operations and manual labor. The fabrication techniques become even more complicated if complex geometry is involved. That necessitates the power of additive manufacturing or 3D printing, a technique that in theory is suitable for arbitrary any part geometry. As part of a larger project to 3D print flexible antennas, our group was tasked with developing a printer that could directly produce 3D stretchable electronics. Due to the unavailability of commercial 3D printers with such capabilities, in this research, development of a 3D printer system was aimed which can print hard plastic parts, soft rubber-like components, and stretchable conductive materials in a single process. In the beginning, it was expected that switching material composition & modulus and adding strong bonding between dissimilar materials would be vital for project success. First, an extensive literature review was performed in the field of stretchable electronics applications. Conductive fillers in elastomers and specialised folded geometries of metallic electrodes have been utilized in these applications; however they have limited conductivity compared to metals and an ultimate strain before failure because of inherent rigidity of metals, respectively. It was determined that gallium based liquid metal alloys are the most attractive candidates for stretchable antennas due to their deformability, non-toxicity and superior electrical conductivity. This review contains a comparative study of reported fabrication techniques of eutectic gallium-indium binary alloy (EGaIn) and gallium-indium-tin

ternary alloy (Galinstan) embedded in elastomers such as polydimethylsiloxane (PDMS) or other rubbers as well as the primary challenges associated with their use.

Initially, a bi-extruder system with two input channels was developed to print two different polymer materials using a single nozzle system that can change the composition of extrudate continuously. This extruder system is further distinguished because of its split design which gives users access to the internal channels. By inserting a static intermixer into the extruder, it was possible to co-extrude two chemically immiscible materials with enhanced mechanical bonding via mechanical interlocking. Several different intermixers were designed and printed with direct metal laser sintering (DMLS) with 20 μm resolution. This bi-extruder is targeted to print functionally gradient materials (FGM) with improved adhesion between dissimilar thermoplastics without the need for chemical compatibilization so that filaments from many different sources can be used effectively.

Fused filament fabrication style 3D printers have a limited material choice, depending on the commercial availability of the filaments of any thermoplastics. Additionally, filament-based feeding systems may not be suitable for elastomers having very low mechanical rigidity. Hence, an extruder system which can directly print from raw pellets was developed to widen input material choice as well as to lower the raw material cost. The new feeding system to be used - fused pellets printing (FPP) – permits almost any thermoplastic materials by converting screw extruders into a direct source for feed material of fused deposition modeling (FDM) style 3D printers. It was achieved by feeding thermoplastic pellets into a stand-alone single screw system

that melts and pushes the material through a flexible heated hose to the print head, through which the material is finally deposited onto the print bed to construct the 3D object. This connection element decouples the high quality or large mass extruder from an FDM hot end that can move with high speed and precision. Utility of the technique was demonstrated through direct printing of pneumatic driven soft robots which could in the future be used to control antenna shapes.

In the next phase of this research, a tri-extruder system with three input channels was manufactured. Two inputs were used to feed a hard-rigid thermoplastic and a soft, stretchable elastomer whereas the third input was intended for liquid metal printing. This system was successfully used to enhance adhesion between high impact polystyrene (HIPS) and SEBS which have nearly three orders of magnitude of difference in elastic moduli by introducing mechanical keying which does not require chemical compatibility. However, achieving a co-continuous binary polymer system from this intermixing requires the melt properties of the polymers to be within a specific range. To demonstrate, tendon-driven soft robotic actuators composed of HIPS and SEBS were printed and characterised. These FGM actuators did not show any noticeable interface failure after 10,000 cycles of operation whereas other samples printed with side-by-side co-extrusion experienced layer delamination. Using these FGM actuators, a fully compliant gripper with an agonist-antagonist balanced structure was used to grasp irregular objects with sizes larger than the gripper holder by actuating in both inward and outward directions.

With the inclusion of a syringe pump, needle-based dispensing of liquid metal was executed using the third input of the tri-extruder system. Therefore, the extruder system is capable to co-axially extrude liquid metal alloy within an encapsulating polymer shell, in this case, SEBS. Hence, an extremely stretchable and flexible conductive wire with a continuous stable core of liquid metal is produced which does not require any post-processing and an extra sealing step. To demonstrate the capacity of this tri-extruder system, a 2D spiral pressure sensor was printed on an SEBS substrate. A 3D inductor was also printed and characterized to measure circumferential strain by monitoring the change in inductance.

An immediate drawing process was also found to be useful to produce liquid metal based micro-wires (~50 μm) which are stretchable up to 400% without any noticeable mechanical and electrical loss. This opens up new possibilities to utilize this smart extruder system and fabricate microfluidic devices in a very simple method without needing a clean-room environment.

Keywords: additive manufacturing, fused deposition modeling, fused filament fabrication, fused pellets printing, 3D printing, multi-material printing, intermixing, mechanical bonding, co-extrusion, liquid metal, elastomer, and stretchable electronics.

PREFACE

The research work of this thesis was planned, designed, conducted, analyzed, interpreted and compiled by Mohammad Abu Hasan Khondoker, and was reviewed and supervised by Dr. Dan Sameoto, Associate Professor of Department of Mechanical Engineering at the University of Alberta. Other students of the research group have contributed by assisting in characterizing some parts of this thesis. The majority of this thesis has been published / submitted to multiple journal publishers and presented in multiple conferences.

Chapter 2: This is an open-access topical review article published as: M.A.H. Khondoker and D. Sameoto; Fabrication methods and applications of microstructured gallium based liquid metal alloys. *Smart Materials and Structures.* **25**: 093001.

Author Contributions: M.A.H. Khondoker conducted the literature review and both authors contributed to the writing of the manuscript.

Chapter 3: This is an original research work published as: M.A.H. Khondoker, A. Asad and D. Sameoto; Printing with mechanically interlocked extrudates using a custom bi-extruder for fused deposition modeling. *Rapid Prototyping Journal.* **24**: 921-934.

Author Contributions: D. Sameoto conceived the idea, M.A.H. Khondoker designed and executed the experiments and all authors contributed to the writing of the manuscript.

Chapter 4: This is an original research work accepted for publication as: M.A.H. Khondoker and D. Sameoto; Soft is no longer hard: a filament-free FDM technique compatible with soft and hard thermoplastics. *Progress in Additive Manufacturing.* ID: PIAM-D-18-00034R3.

Author Contributions: D. Sameoto conceived the original idea, M.A.H. Khondoker elaborated the plan and executed the experiments. Both authors contributed to the writing of the manuscript.

Chapter 5: This is an original research work provisionally accepted for publication as: M.A.H. Khondoker, N. Baheri and D. Sameoto; Tendon Driven Functionally Gradient Soft Robotic Gripper 3D Printed with Intermixed Extrudate of Hard and Soft Thermoplastics. *3D Printing and Additive Manufacturing.* ID: 3DP-2018-0102.R2.

Author Contributions: D. Sameoto conceived the original idea, M.A.H. Khondoker elaborated the plan, designed the setup and executed the experiments. N. Baheri assisted in characterization. M.A.H. Khondoker and D. Sameoto contributed to the writing of the manuscript.

Chapter 6: This is an original research work submitted for publication as: M.A.H. Khondoker, A. Ostashek and D. Sameoto; Direct 3D Printing of Stretchable Circuits via Liquid Metal Co-Extrusion within Thermoplastic Filaments. *Advanced Engineering Materials.* ID: adem.201900060.

Author Contributions: D. Sameoto conceived the original idea, M.A.H. Khondoker elaborated the plan, designed the setup and executed the experiments. All authors contributed to the writing of the manuscript.

Dedicated to those who helps and sacrifices for others

ACKNOWLEDGMENT

TABLE OF CONTENTS

LIST OF TABLES

LIST OF FIGURES

which causes rupturing leading to fluid leakage through the chamber walls. (d) Microscope images of the cross-sections of samples printed with 0.6 mm layer width and (i) 0.25 mm layer height, (ii) 0.35 mm layer height (before heat treatment), (iii) 0.35 mm layer height (after heat treatment), (iv) 0.45 mm layer height. [Scale bars are 1.5 mm] (e) The base of the SEBS actuator printed with 0.25 mm layer height and 0.5 mm layer width, resembling the bulk SEBS material with high optical transparency. 116

1. CHAPTER: INTRODUCTION

1.1 BACKGROUND

As new requirements in wireless communications are emerging, the use of large number of antennas with different bandwidths, radiation patterns and polarizations in modern aircraft, ships or land vehicles is increasing. Moreover, modern wireless applications also require flexible, stretchable and adaptable antennas which are sensitive to environmental conditions. Thus covering several frequency bands with a single radio frequency (RF) antenna with a small form factor and high efficiency is a major challenge [1]. Rather than using a multi-antenna system, several antennae functions integrated into one single system would reduce both the size and cost of communication systems [2]. One potential solution to this challenge is to use reconfigurable antennas which are tunable to different frequency bands [3]. This tuning can be achieved by using different electrical tuning elements [4-6] or by applying mechanical reconfigurations [7-9]. Using electrical tuning elements suffers from non-linearity, lossy characteristics at higher frequencies and complicated packaging processes [4-6]. On the other hand, soft polymer-based mechanical tuning of RF antennas are characterized by light-weight, low-cost and compatibility to complex surfaces [7-9].

Since mechanically tunable antennas correspond to a large strain, inkjet printing of conductive silver ink or other conductive inks may not be the best choice because of their limited inherent

stretchability without electrical loss [10,11]. In contrast, gallium-based liquid metals (LM) embedded in soft elastomers have recently gained significant popularity over conventional conducting elements [12-17], because of their non-toxicity and superior electrical conductivity while maintaining micro-patterns [18]. However, the fabrication methods of these LM based RF devices are either too complicated for complex geometries [15] or result in high roughness [12] and non-uniform widths [16,17]. Moreover, these conventional fabrication techniques are not suitable for 3D structures and require additional assembly steps to integrate the RF devices with other functional electronic rigid components, which may introduce defects and imperfections from the manual labor.

Hence, there is a need for a novel technique to fabricate LM based mechanical tunable RF antennas with complex 3D structures and built-in rigid components. These requirements could be fulfilled by additive manufacturing techniques where a material can be deposited to form almost any arbitrary geometry, hence have the potential to be used in fabricating integrated RF 3D antennas.

1.2   ADDITIVE MANUFACTURING

Additive manufacturing (AM) refers to a family of techniques where material is solidified to form successive layers, on top on previous layers, constructing a 3D object having almost any geometry. Among others, stereolithography (SLA), polymer jetting, selective laser sintering (SLS), selective laser melting (SLM), inkjet printing, fused deposition modeling (FDM) are the commonly used AM techniques available for fabrication of tunable RF devices. However, the polymer resins used

in SLA and polymer jetting techniques can be mechanically poor, have higher loss tangent and require difficult metal integration [19,20]. SLS mostly produces all-metal parts, suitable for only metallic components of RF devices [21]. In both SLS and SLM, multi-material printing capability is very challenging for polymers, they have limited material choice and often require plastic integration for RF applications [22]. Inkjet printing usually requires an additional sintering process and has a limited mechanical strain without electrical loss [23]. On the other hand, FDM has been found to be an effective technique for RF devices because of its low-cost system [24] and wider material choice [25]. This technique also offers users the ability to change fill volume to achieve different dielectric constant and loss tangent [26,27] or even to choose from a wide material choice suitable for RF applications [28,29]. For instance, PREPERM® [30] is a raw thermoplastic RF material which has dielectric constant and loss tangent as low as 2.6 and 0.0015, respectively at 22 GHz. Additionally, the FDM technique also has the potential to coextrude conductive materials to avoid the post-processing step of metal integration. Therefore, in this thesis, the FDM technique has been chosen to directly print mechanically tunable RF antennas.

1.3 FDM: CURRENT STATE-OF-THE-ART

Most of the commercially available FDM printers can print only a single thermoplastic material. Some commercial printers make use of a dual extruder system having two separate nozzles for two filaments [31]. These separate nozzle systems may be used for materials with two different colors but do not normally provide multi-material printing of different materials in a single part because of very limited fusion/bonding between dissimilar materials deposited from different

nozzles. There are a few commercial printers with a single nozzle system for multiple filaments [32], which introduce higher temperature fusion between materials before they are deposited on to the printer bed. Although these systems are useful for different materials which are chemically immiscible, but not capable of printing chemically immiscible polymers due to poor bonding/fusion at their interface. Therefore, there is a compelling need for a multi-material extruder which can print chemically immiscible polymers with engineered adhesion between them, because antenna devices may be composed of both soft and hard components to achieve both reconfigurability and integration with conventional electronics.

Due to the filament-based feeding systems used by almost all the commercial FDM printers, users have to rely on the availability of the filaments of any desired material. For instance, due to unavailability of filaments of shape memory polymers (SMP) in commercial scale, *Villacres, et al.* were not able to directly 3D print SMP without going through an additional filament making steps [33]. Filament-based FDM printers also involve higher material cost, as the high-quality filament making step adds an extra cost to the raw material. Therefore, to widen the material choice of thermoplastics and reduce the raw material cost, an extruder system is strongly desired which could take inputs of raw pellets similar to injection molding. This system would then allow printing using those thermoplastics which have low dielectric constant and loss tangent, even though their filaments are not commercially available.

The next challenge FDM is currently facing is its ability to print highly conductive materials like LM. Current FDM systems do not offer any engineering solution to print conductive pathways

4

integrated with other thermoplastic parts. There are some direct writing techniques reported in the literature [34]. However they are not suitable for thermoplastic integration. Another challenge with direct printing of LM structure is its surface tension, which restricts continuous dispensing of bare LM in the air [18]. Therefore, the extruder system of FDM printer needs to be re-designed allowing printing of LM structures already encapsulated in thermoplastic materials to avoid leakage.

1.4   OBJECTIVES OF THIS THESIS

This research was a part of a larger project aimed to directly print mechanically tunable RF antennas. It was discovered early on that no commercially available printer would have the capabilities discussed above. Hence, considering the background, the primary objective of this doctoral thesis was to develop a multi-material smart extruder system for an FDM printer with the following capabilities, which are essential for printing tunable antennas. The smart extruder system must be able to;

1. Print functionally gradient materials (FGM) devices using dissimilar thermoplastics having improved adhesion between chemically immiscible materials.

2. Directly print from raw pellets of any thermoplastics without needing to increase bulkiness or power requirements to move the print head.

3. Print circuities in 2D or 3D volume using coaxial extrusion of LM within a thermoplastic elastomeric shell.

1.5 ORGANIZATION OF THESIS

This paper-based doctoral dissertation contains seven chapters. Except chapter 1 and chapter 7, each intermediate chapter is written based on a journal article published/submitted for publication. Chapter 1 presents an overview of the background of this research, the motivation, and objective. It also provides a brief summary of the originality and challenges associated, followed by a brief description of the thesis structure.

Chapter 2 contains an extensive literature review on gallium-based LM alloys. It explores all the reported fabrication techniques to pattern LM microstructures and a comparative study on their pros and cons with minimum attainable pattern size. This literature review serves as the first foundation of this research to explore the characteristics of LM to understand its suitability for RF antenna fabrication.

Chapter 3 presents an earlier version of the bi-extruder developed to print two thermoplastic materials with a detail description of the static intermixer designed. The method to control the composition of the extrudate and the effect of the intermixer on the extrudate quality are discussed in this chapter.

Chapter 4 presents the development of a unique feeding mechanism to directly input raw pellets in the FDM extruders. The heated hose-based feeding system was shown, in this chapter, to work with any thermoplastic pellets regardless of their mechanical properties. That gives users a wide material choice at reduced material cost.

Chapter 5 presents the latest version of tri-extruder having three input channels. In this chapter, the printing of FGM devices composed of hard plastic, HIPS and soft elastomer, SEBS has been demonstrated. Use of an intermixer causes more than ten (10) times improvement of the adhesion between these chemically immiscible polymers. A tendon driven soft-robotic gripper printed with this tri-extruder has also been analyzed.

Chapter 6 presents the coaxial extrusion of LM with the SEBS shell. It discusses the mechanism of this complicated coflowing system and illustrates the conditions favorable to a stable continuous jet of LM core inside the SEBS shell. This chapter also shows the functionality of the developed system by printing the pressure sensor and strain sensor.

Although the detailed results are discussed at the end of each chapter. Chapter 7 summarises the overall results and makes concluding remarks. This chapter also discusses the possible future directions for this research work.

2. CHAPTER: FABRICATION METHODS AND APPLICATIONS OF MICROSTRUCTURED GALLIUM BASED LIQUID METAL ALLOYS†

2.1 INTRODUCTION

3D structures of electrically conductive materials embedded in elastomers have great potential in a number of smart material applications, such as soft-matter sensors, actuators, flexible electronics, reconfigurable antennas and others. These applications have three main requirements; high flexibility, extraordinary stretchability and high electrical conductivity. While the flexibility of elastomers is well known and easy to achieve with materials like polydimethylsiloxane (PDMS), polyurethane rubbers and others, achieving high electrical conductivity in materials that can achieve strains of more than 100% (as is typical for elastomers) is extremely difficult. There are many reports where researchers have used a combination of inorganic and organic materials for flexible and/or stretchable electronic applications not requiring superior electrical conductivity, such as a stretchable form of single-crystal silicon in microstructures [35], transparent ZnO film

---

† A version of this chapter has been published as: Khondoker, Mohammad Abu Hasan and Sameoto, Dan; Fabrication methods and applications of microstructured gallium based liquid metal alloys. *Smart Materials and Structures.* 25: 093001. Reproduced with permission from IOPscience.

8

and chalcogenides [36], polypyrrole conducting polymers [37], polypyrrole-poly (ethylene-co-vinyl acetate) composites [38], PDMS – CNT/graphene conducting polymers [39-43], silver-nanowire (AgNW) – polyacrylate composite [44], PDMS – Ag conducting composites [45,46], cellulose – indium tin oxide (ITO) electrodes [47], polyurethane/PEDOT:PSS conductive composite [48] etc. Inkjet printing technology [49-51] has also been utilized for flexible electronics applications, but still these applications have limited stretchability and relatively lower electrical conductivity compared to that of metals. In general, the introduction of electrically conducting fillers to elastomers is reasonably simple and can produce stretchable conductors, but they are multiple orders of magnitude less conductive than metals and frequently strain sensitive in their conductivity, which limits their use in applications requiring high currents, or very high frequencies. While flexibility is very important for thin-film electronics and their applications, bending flexibility doesn't necessarily mean that high elongations are possible, and stretchable electronic conductors may be more attractive in applications like artificial muscles [52], soft robotics [53] and tactile sensors [54,55].

Many examples exist where rigid, high conductivity components are integrated with flexible and stretchable materials for flexible or stretchable electronics. Because of its superior electrical conductivity, copper (Cu) might be a top choice electrically but its hardness makes it unable to withstand repeated bending, and it will experience plastic deformation with a strain of approximately 2% [56]. There are some reported methods and materials for stretchable electronics [57,58]. Among them, metallic wires with thin coil shapes encased in elastomer materials have become a very popular method to overcome this particular challenge in flexible and stretchable

electronics. They use specialized folded geometries of electrodes to permit stretching and compression without exceeding local elastic limits. Among them, micro-sized helical wires [59], horseshoe-like forms of gold [60] or copper [61], laser ablated copper foil in silicone [62], gold micro-wires with tortuosity [63], copper film by electroless deposition [64], meander-shaped nickel-gold layer in PDMS [65], and metal ion-implanted elastomers [66], showed some feasibility to be used in flexible and/or stretchable electronics applications due to their high conductivity. Furthermore, thin layers of copper, chrome or gold [67-69] and thermochromic liquid crystals (TLC) [70] have also been utilized with elastomers (e.g., PDMS) in epidermal electronics applications [71]. Rahimi et al. showed sewing enabled meander wire systems embedded in elastomer [72] and Wang et al. used pre-strained elastomers covered with metal that then buckles as an alternative to meander electrodes [73]. Unfortunately, these devices are still ultimately limited by inherent rigidity of the metal layers and require unnecessary design constraints by the increasing complexity of fabrication. At higher bending or stretching, they start beginning to crack at the micro level, and there is also the danger of possible delamination between the elastomers and the rigid materials contained within that may occur at extreme strains. While many of the thin-film electronics reported for flexible circuity make use of clever designs of electrodes and very thin materials to ensure they conform to a skin or other deformable surfaces, the applications only require very small currents, and the thin film strategies may not be scalable to smart materials where significant current may eventually be used.

Due to the challenges with traditional metallic micro-structures and organic/inorganic thin film structures, researchers began looking for materials with higher electrical conductivity as well as

better flexibility. Liquid metals at room temperature are the best suited conductive materials in this field because they enable conductive paths embedded in elastomers to be stretched or bent repeatedly without significant loss in their performance. As the best known liquid metal, Mercury (Hg) has been used in different flexible electronics applications [74-76]. Unfortunately, it has a serious disadvantage in that it is highly toxic [77,78]. Other elements which are liquid near room temperature also have their own drawbacks; cesium (Cs) may be radioactive and is violently reactive, and rubidium (Rb) has violent reactive nature. Pure Gallium is liquid at approximately 30°C, but this is too high to remain liquid in most room temperature applications (although it is perhaps compatible if in close contact with body heat). Therefore, these pure metallic elements are also limited in their use in flexible electronics and bio-applications.

Over the last decade, gallium based liquid alloys have gained increasing popularity as materials best suited for fulfilling both the requirements for high electrical conductivity and extreme flexibility. As a liquid metal at room temperature, the eutectic alloy of 75.5% gallium (Ga) and 24.5% indium (In), EGaIn has recently attracted considerable interest from many researchers. It can be attributed to the advantageous properties of this alloy in embedded elastomers. An alternative room temperature gallium alloy, galinstan is composed of gallium, indium and tin with varying compositions. Since the melting point of galinstan is dependent on the ratio of three components, there is no generic value of melting point. But the typical Galinstan (68.5% Ga, 21.5% In and 10% Sn) has a reported melting point of –19°C, whereas EGaIn has a melting point of 15.5°C [79]. Therefore, these non-toxic alloys [80,81] will remain liquid at most comfortable temperatures that may be found indoors and possess virtually no vapor pressure [76]. Also, they

have quite low viscosity in their liquid phase and a relatively high electrical conductivity (approximately 1/16th that of copper [82]). In their liquid state, these alloys are electrically more conductive than in their solid state [83]. If the oxygen level in the ambient atmosphere is above 1 ppm [76], liquid gallium alloys start oxidizing and form a thin passivation oxide layer (Ga_2O_3 and Ga_2O) on their surface [84]. The thickness of the electrically resistive [85] oxide skin was found to be approximately 0.7 nm in X-ray diffraction tests under vacuum conditions [86], but it is much thicker (~1 – 3 nm) in laboratory conditions [84,87-90]. This oxide layer acts as a skin and can decrease the effective surface tension of the liquid metal in electrochemical reactions [91], or if the oxide is breached. As a result, the liquid metal tends to wet other surfaces (unlike mercury), which helps to maintain non-spherical metal structure even in microchannels [89,92]. The wetting caused by this oxide skin can also lead to the tendency to stick to any solid surface [84] even if undesired, so this particular feature of gallium based alloys can be a benefit or drawback depending on the application. Doudrick et al. demonstrated that galinstan adhesion occurs in two steps [93]. First, the oxide skin doesn't rupture when galinstan contacts substrate surface. The nanoscale topology of the oxide skin allows only minimal adhesion between galinstan and substrate surface, regardless of its surface energy. In the second step, oxide skin ruptures and now old oxide skin – substrate surface, bare galinstan – substrate surface and new oxide skin – substrate surface adhesions occur. It also was found that the adhesion between the new oxide skin and the substrate surface dominates the total adhesion in this second step.

The ability of these alloys to flow through the channels on demand permits them to be designed as "reconfigurable" as the dimensions of the channels can be changed if they are made of

elastomers, and other fluid handling mechanisms, such as valves and pumps [94-98] may be used to control specific location and electrical connections of these liquid metals. Other than acting as the primary material, liquid metal can also be used just to exploit its fluidic nature. For example, Tang et al. demonstrated liquid metal enabled pump, where a droplet of liquid metal induces flow of a range of liquids without mechanical moving parts by means of electrowetting/de-electrowetting at the metal surface [99], and Boley and Gui proposed a liquid metal based electroosmotic flow pump [100]. Kim et al. reported real-time dynamically reconfigurable photomask, where on-demand injection and withdrawal of liquid metal in the microchannel was utilized to change the patterns of photomask [101]. Other benefits of using EGaIn /Galinstan for smart materials include their high thermal conductivity, and low vapor pressure (which ensures negligible evaporation and mass loss). Therefore, these gallium based liquid metals have been extensively utilized in flexible, stretchable electronics applications and can be an alternative to wavy and highly stretchable wearable electronics [57,102]. Because they are liquid at room temperature, the majority of applications using liquid gallium alloys have them contained inside some solid channel system (e.g., tunable frequency selective surfaces [103], micro-variable inductor [104], etc.), but the applications of these liquid metals are not limited to only embedded applications. For instance, in some reported work [105], liquid gallium alloy has been successfully used in the injection of femto-liter sized samples into cells. Ladd et al. successfully printed freestanding columns and spheres of EGaIn [106]. Other than electronics applications, liquid metals also have the potential to be used in thermal applications [107-109] as a heat sink or conductor to manage temperatures. Other than using as a main functional element, Kim et al.

used liquid metal as a secondary element [110] which was a liquid metal via connecting stretchable patterned gold layers. For comparison purposes, the properties of functional materials used in flexible electronics applications have been summarized in the following Table 2.1. From this point on, in this review, "liquid metal" will refer to the gallium-based alloys EGaIn and galinstan. This report is intended to present the comparative study on the fabrication processes of two- and three-dimensional microstructures of liquid metals using different techniques reported already.

Table 2. 1: Properties of selected liquid metals, low melting pure metals and other conductive materials.

Functional Materials / Composites	Melting Point T_m (°C)	Viscosity ν (cSt)	Surface Tension γ (mN/m)	Conductivity σ (10^7 S/m)	Major Drawbacks
EGaIn	15.5 [79]	0.32 [89]	624* [111]	0.34 [92,112]	–
Galinstan	-19 [113]	0.37 [113]	535* [76]	0.38 [113]	–
Ga	29.8	–	–	0.37	Solid
Hg	-39 [113]	0.11 [113]	428 [114]	0.10 [113]	Toxic
Cs	28.5	–	–	0.50	Violently reactive
Rb	39.3	–	–	0.83	Violently reactive
Cu	1085	–	–	5.97 [80]	Low flexibility
Ag	961.8	–	–	6.30 [80]	Low flexibility
Ni	1455	–	–	1.43 [80]	Low flexibility

ZnO film	1975 [115]	–	–	7.55×10^{-17} [116]	Low conductivity
polypyrrole-poly (ethylene-co-vinyl acetate)	–	–	–	$5\sim 7 \times 10^{-5}$ [38]	Low conductivity
polypyrrole conducting polymer	–	–	–	9.7×10^{-4} [117]	Low conductivity

*Oxidized value

2.2 FABRICATION PROCESSES OF LIQUID METAL MICRO-STRUCTURE

There are a number of reported fabrication processes of liquid metal to form embedded micro-structures. These techniques can be grouped under four major classes such as masked deposition, imprinting, direct patterning, and casting. Among these broad categories, masked deposition techniques result in relatively large feature sizes [17], whereas fabrication processes by casting are the most popular technique which produces smallest reported minimum feature size of approximately 150 nm [118]. Many of these techniques classified under these four main groups have been summarized in Table 2.2.

Table 2. 2: Reported fabrication techniques of liquid metal structures embedded in elastomers.

Fabrication Techniques		Minimum Reported Feature Size	Advantages	Disadvantages	Devices Fabricated
Masked Deposition	Using a stencil	Line width = 200 µm Spacing = 100 µm [17]	Relatively simple; Reliable; High throughput;	Large feature size; Limited class of geometries; Rough edge;	Shear and pressure sensor [119]; RFID antenna [17]; Galinstan heater [15];
	Selective wetting	Line width = 100 µm Spacing = 25 µm [120]	Relatively simple; Reliable; High throughput;	Rough edge; Limited class of geometries;	Patterned structures [120];
Imprinting	Printing in recesses	Line width = 2 µm Spacing = 1 µm [121]	Very small feature size;	Residue on outside of channels; Rough edge;	Coplanar capacitor [121];
	Printing using stamp	Line width = 0.75 mm Spacing = 1 mm [15]	Relatively simple; Can be performed manually;	Large feature size; Uneven wetting;	Planar circuit [15];

Fabrication Techniques		Minimum Reported Feature Size	Advantages	Disadvantages	Devices Fabricated
	Screen printing	Line width = 40 µm [122]	Micro-scale droplets	Requires pressure control;	[122];
	Micro-contact printing	Line width = 340 µm [15]	Any arbitrary planar geometry; Requires limited manual labor;	Requires motion control; Needs repeated contacts; Rough edge;	Comb capacitor [15];
Direct Patterning	Pressure driven 2D structure	Line width = 45 µm [123]	Any arbitrary 2D structure;	Relatively complex technique;	Interconnect [123]; Directly written traces [34]; Printed circuit and pattern [124];
	Pressure driven	Line width = 150 µm [106]	3D free-standing structures;	Need good control on injecting;	Free standing 3D structures [106];

Fabrication Techniques	Minimum Reported Feature Size	Advantages	Disadvantages	Devices Fabricated
3D structure				
Dielectro-phoresis based 3D structure	Width = 80 µm Spacing = 40 µm [125]	Finer 3D features with relatively smooth surface; Possible with wide range of designs.	Requires chromium/gold pads deposited previously; Requires power supply	Microelectrodes and micro fins [125];
Laser patterning	Line width = 100 µm [126]	Any arbitrary 2D structure;	Higher wastage of liquid metal;	Patterned LED circuit [126];

Fabrication Techniques		Minimum Reported Feature Size	Advantages	Disadvantages	Devices Fabricated
Casting	Needle injection	Line width = 150 nm [118]	Fast and reliable; Relatively simple; 3D embedded structures; Better resolution; Smoother sidewalls;	Limited class of geometries; Requires two terminals; Air trapping is common;	Stretchable interconnect [127]; Cube antenna [128]; Tunable antenna [129]; Microelectrodes [130]; Planar inverted cone antenna [131]; GaIn nanowires [118]; Capacitors and inductors [132,133]; Electrostatic actuator [134]; Radiofrequency antennas [135]; RF radiation sensor [136]; Diodes [137];

Fabrication Techniques	Minimum Reported Feature Size	Advantages	Disadvantages	Devices Fabricated
				Memristor [138]; Pressure sensor [139]; Soft artificial skin [140,141]; Force sensor skin [142]; Wearable tactile keypad [143]; Strain sensor [144]; Curvature sensor [145,146]; Ultrastretchable conductors [147,148]; Loop antenna [149];

Fabrication Techniques	Minimum Reported Feature Size	Advantages	Disadvantages	Devices Fabricated
Vacuum assisted infiltration	Line width = 250 µm [150]	No need of two terminals; Deep features; Structures with different height;	Needs repeated process;	Comb capacitor [128]; Planar circuit [150];

The broad category of techniques listed in the following section is organized roughly by the increasing quality and complexity of designs feasible with each technique, although there are large variations in those properties between individual reports.

2.2.1 Masked Deposition

There are a number of masked deposition techniques, which use different methods to selectively deposit liquid metal alloys. These techniques have been discussed below.

2.2.1.1 Using a Stencil

Embedded structures of liquid metal can be created using 3D printed masks [119] or stencils [15,17] to pattern the metal followed by encapsulation steps. In the case of work presented in [119], a mask was placed in contact with a silicone (Ecoflex 0050) which could conform to mask roughness and contain EGaIn which was dispensed manually. To remove the mask cleanly, the EGaIn was cooled below the freezing point to solidify it, and then another layer of silicone (Ecoflex 0010) was spin-coated on top while the EGaIn was still frozen, and then the silicone was cured at elevated temperatures. Repeating this process allowed multiple layers of independent liquid metal to be embedded within a flexible elastomer for the ultimate use as a capacitive sensor to detect shear and pressure. In another stencil-based process, as shown in Figure 2.1, a copper stencil is first placed on the partially cured PDMS substrate material. Then, the excess amount of liquid metal is poured on the stencil. To ensure the uniform thickness of liquid metal in the openings of the stencil, a liquid alloy wetted roller can be rolled repeatedly [17]. This roller also helps to remove excess alloy material. Finally, the stencil is removed, and the patterned structure of liquid

22

alloy remains on the substrate. After that, depending on the application, a sealing elastomer layer can be applied by successive spinning and curing process. Just as in [119], the stencil works well because the underlying PDMS can conform to make a good seal while having low inherent adhesion so that the stencil may be removed without difficulty. The smallest feature reported in this process was 200 µm and minimum spacing was 100 µm, although whether this was a limitation of the stencil or the deposition process was unclear.

The stencil technique is relatively simple, reliable and can have high throughput. But it's suitable for only relatively large features and a limited class of geometries. In particular, the surface of the liquid metal after deposition is frequently quite rough and not very uniform in thickness [17]. The stencils may also be more challenging to use multiple times without cleaning, as increased layers of oxidized gallium can build up and be transferred to unwanted locations. One primary attraction to the stencil process is that isolated areas of liquid metal can be readily patterned and in theory, quite large areas can be patterned in a single step.

Very recently, a new technique, atomization patterning, has been reported to produce liquid metal structures [151]. It sprays atomized liquid metal with nitrogen as a carrier gas onto a semi-cured PDMS surface with a tape transferred adhesive mask. This is also masked deposition, but unlike the previously described techniques, it uses a spray to apply liquid metal alloy. This method results in smooth line edges compared to other masked deposition techniques.
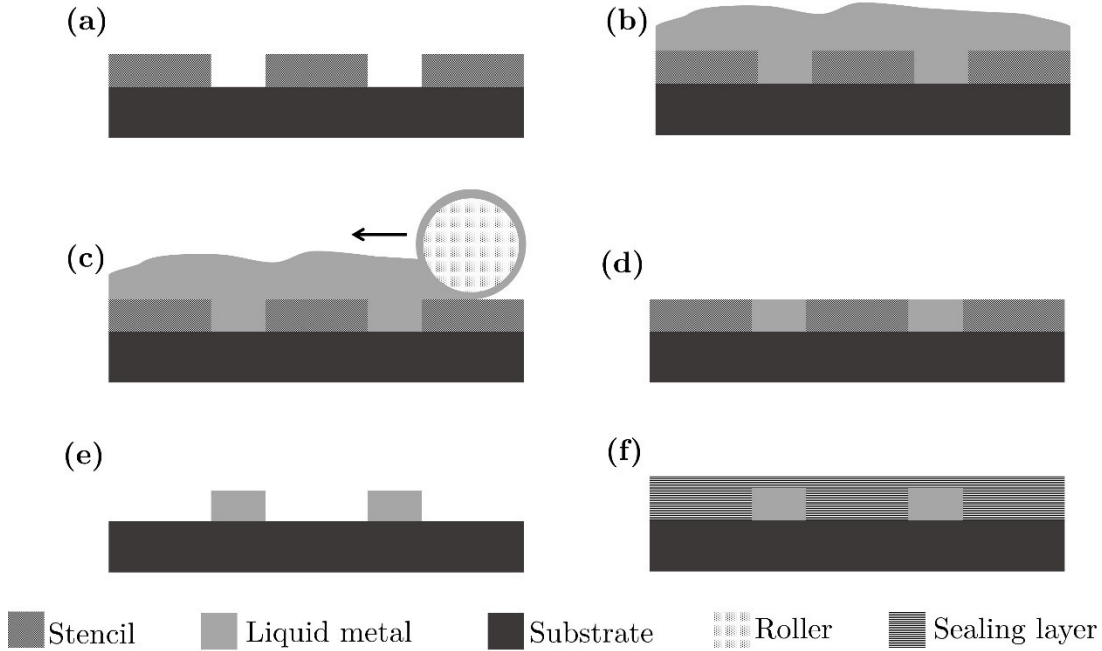
Figure 2. 1: Masked deposition using a stencil. (a) stencil placed on substrate, (b) excess amount of liquid metal is applied, (c) use of roller (d) uniform thickness of liquid metal in the openings of stencil, (e) patterned alloy after removal of stencil and (f) finally, application of sealing elastomer layer (inspired by [17] with permission of The Royal Society of Chemistry and with permission from [15] Copyright 2013 American Chemical Society.

2.2.1.2 Selective Wetting

This masked deposition technique uses a sacrificial layer instead of using a stencil to wet the substrate selectively by liquid metal (galinstan in this case). Kramer et al. [120] have described the whole process in detail as shown in Figure 2.2. First, a polytetrafluoroethylene (PTFE) particle-filled photoresist, tin foil, and PDMS are layered on a glass slide. Then, PTFE and tin foil are patterned using photolithography. A thin layer of PAA is applied by spin coating and it spontaneously dewets from the super-hydrophobic PTFE/photoresist. Now, the whole surface is sputtered with indium, and then flooded with acetone to lift-off indium on the photoresist. When the liquid metal is applied on the patterned tin foil, it reactively wets it while not adhering to the

photoresist. A thin-film applicator is used to wipe the excess amount of liquid metal off the surface.

Finally, the sputtered PAA layer is removed by rinsing in water and a sealing layer of elastomer

is applied. At this stage, the gallium is then frozen (below -19°C) and encapsulated with another

layer of curable silicone.
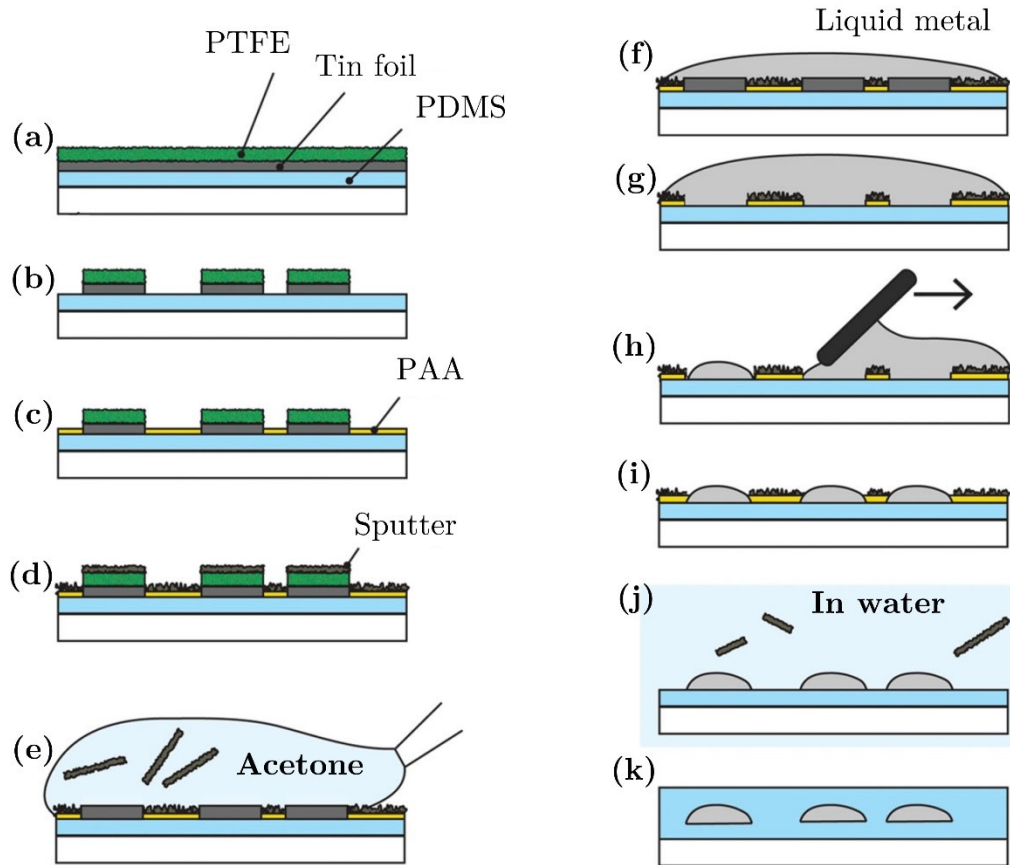
Figure 2. 2: The masked deposition through selective wetting (adapted from [120]. Copyright WILEY 2013 reprinted with permission).

This masked deposition technique usually produces rough edges and is appropriate only for a

limited class of geometries. The use of spontaneously wetting and de-wetting areas is a novel

approach but ultimately has similar capabilities and advantages in terms of patterning features

as the stencil systems described earlier. As implied in Figure 2.2, the features will still have a

rounded cross-section due to the surface tension effects on the liquid metal. The requirement of using photolithography and sputtering in this approach would be disadvantageous from a processing point of view, but the uses of microstructured surfaces to aid in repelling or enhancing bonding may still be valuable in future variations.

2.2.2 Imprinting

Imprint processing can be a conceptually very simple method to produce patterns using liquid metals. Variations on this technique include dipping a structured stamp into liquid metal and transferring it to another surface, embossing a liquid metal film and producing separate structures by squeezing out metal, or by transferring from a single liquid metal film into recesses on a structured surface.

2.2.2.1 Printing in recesses

This imprinting process using a mold is a very simple technique to pattern liquid metal and closely resembles a portion of the gravure or roll-to-roll (R2R) printing process [152,153]. As reported by Gozen et al. [121], a thin layer of liquid metal is applied on a flat surface. Separately, a PDMS mold with desired topographical features is produced. Then, the PDMS mold is pressed against the liquid metal layer which then fills in the recesses. Due to the stickiness property of gallium-oxide layer, a very small amount of liquid metal adheres to the elevated walls of the recesses of the mold, but the recesses can remain filled. In this way, even after the mold is removed, liquid metal alloy remains in the patterned structure. Finally, a sealing layer can be applied to embed the structure. This method is illustrated in Figure 2.3.

Using this technique, Gozen et al. fabricated a coplanar capacitor having only 2 µm thick lines with 1 µm spacing – several orders of magnitude smaller than the features reported with stencil processes. Unfortunately, the liquid metal is not completely non-wetting on the top PDMS surface and a reported problem with this method is that a residual layer of liquid metal is observed on the top of the walls outside of the channels. This technique could be potentially improved with the addition of super-hydrophobic structuring of the top surface to get more de-wetting, similar to the technique in [120], while not diminishing the subsequent bond-ability with silicone.

2.2.2.2 Printing using stamps

This technique is very similar to imprinting with mold but uses the raised surfaces of a stamp to transfer areas of liquid metal onto another surface. It starts with the preparation of a PDMS stamp with topographical features by casting. Tabatabai et al. [15] used a 3D printed mold to cast the PDMS stamp. Using a paintbrush, the raised surfaces of the stamp are inked with a liquid metal alloy. Then, the stamp is pressed on the substrate and the liquid metal is transferred. A frame is placed encompassing the patterned structure and using a successive spin coating and curing, a sealing layer of elastomer is applied on top of the patterned liquid structures. To reduce or eliminate displacement of the liquid patterned structure during spin coating, it might be helpful to freeze the liquid metal structure before spinning and therefore EGaIn is a better choice than Galinstan in this regard. The steps involving stamp lithography are shown in the Figure 2.4. Tape transfer printing [154] proposed by Jeong et al also uses the same principles to fabricate stretchable RF electronics.
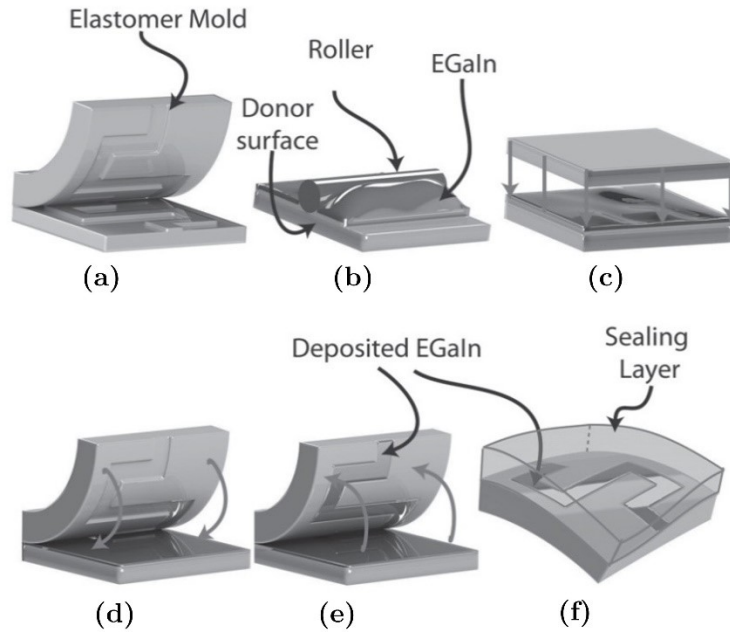
Figure 2. 3: Imprinting using a PDMS mold. (a) PDMS mold with desired topographical feature is prepared, (b) a thin layer of liquid metal alloy is applied on a flat surface, (c) flattening and removal of excess liquid metal, (d) the PDMS mold is pressed against liquid metal, (e) liquid metal adheres to the walls of recesses of the mold and (f) application of sealing elastomer layer (adapted from [121]. Copyright WILEY 2014 reprinted with permission).

Tabatabai et al. prepared a Sylgard 184 PDMS stamp with features protruding 2 mm from the stamp base and printed features with as small as 0.75 mm wide with 1 mm spacing using this process onto another silicone (Ecoflex 0030). This is a very simple process and can be done manually, but it is limited to relatively large features. Another problem arises because of uneven wetting of the stamp and target surface, which may result in non-uniform thickness or missing areas of the liquid metal features. Of the three distinct methods reported by Tabatabai et al. (inkjet printing, microcontact printing, and stamp lithography) this stamp lithography was determined to be the least reliable.

2.2.2.3 Screen printing

As described by Sen and Kim [155], the work by Truong et al. [122] applies a version of silk-screen printing with a screen prepared by KOH bulk etching of silicon to produce microscale openings. When a print-head containing a reservoir of liquid metal is pressurized, the liquid metal bulges out through the openings of the screen and is deposited on a surface that had been pre-patterned with gold to enhance the wetting of liquid metal. After that, as soon as the screen is withdrawn, the wetting pad forces liquid metal to form droplets and adhere to it. The schematic of this process is shown in Figure 2.5. The openings of the screen have a width distribution of 40 to 70 µm. This process requires a level of expertise to apply controlled pressure on the print head, which influences the amount of material transferred and the quality of the feature.
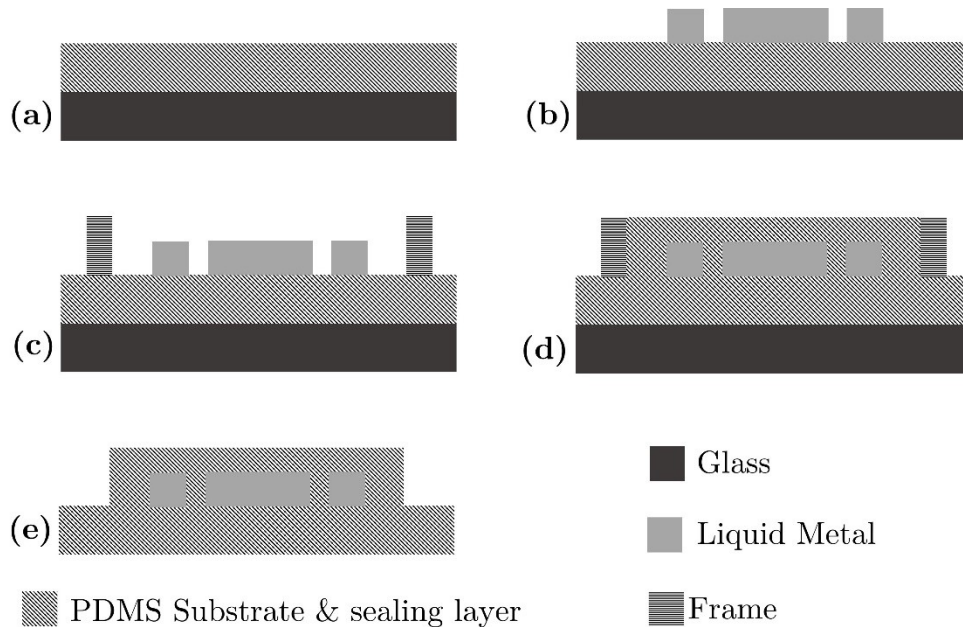
Figure 2. 4: The steps involved in stamp lithography. (a) Preparation of base PDMS layer on glass substrate, (b) patterned liquid metal after imprinting using wetted stamp, (c) placement of a frame encompassing the structure, (d) application of sealing layer of PDMS and (e) removal of glass plate and frame gives the embedded structure of liquid metal in PDMS (inspired by [15]).
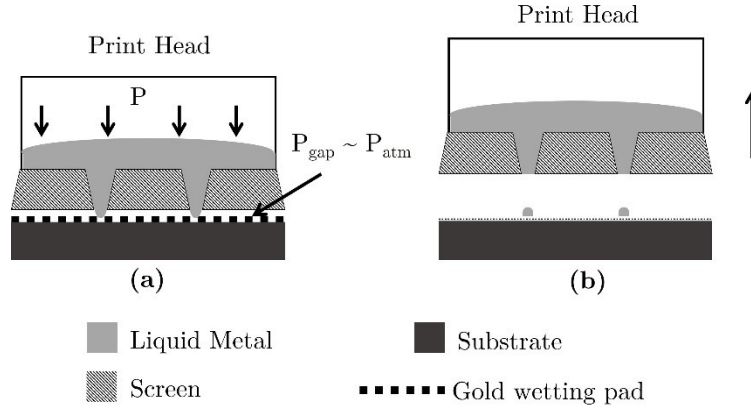
Figure 2. 5: The screen-printing technology. (a) The print head with a screen is pressed on the gold wetting pad and (b) the droplets of liquid metal are bulged out to pattern on the substrate (inspired by [122]).

2.2.2.4 Micro-contact printing

Micro-contact printing (µCP) of liquid metal alloy was first reported by Tabatabai et al [15]. In this imprinting technique, a hemispherical PDMS tip is used as the nozzle. This nozzle is mounted on the print head, which is controllable along x, y & z-directions by means of a user-defined Matlab program. When the tip is dipped into liquid metal, the nozzle collects a bead of liquid metal. Then, the nozzle is moved to contact the substrate to transfer a small droplet of liquid metal at the desired position. This imprinting technique mainly depends on the adhesion of liquid metal to the elastomer. Tabatabai et al measured the diameter of these droplets as 340 µm. If the successive droplets have a spacing less than their diameter (340 µm), these droplets coalesce to form a continuous line. In this manner, the desired pattern of liquid metal is printed on the PDMS substrate. Finally, when solidified, this pattern can be embedded by a sealing layer of PDMS. This technique is illustrated in the Figure 2.6.
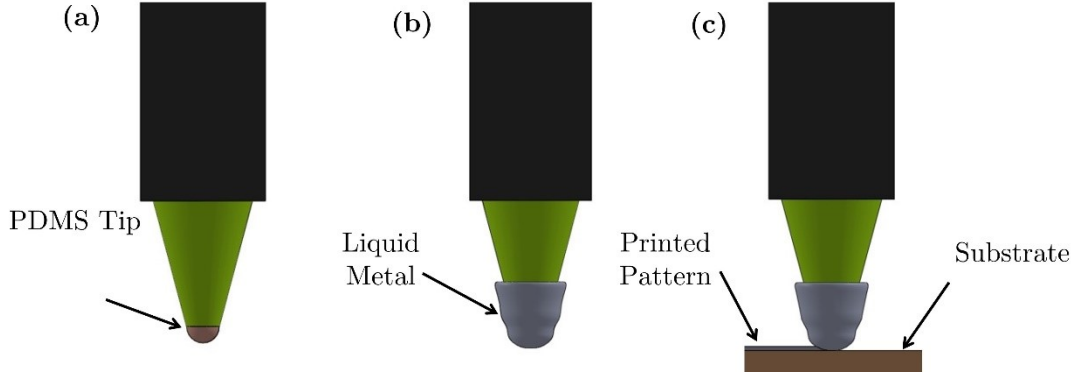
Figure 2. 6: The µCP of liquid metal inspired by [15]. (a) Printing head with hemispherical PDMS tip, (b) the nozzle is wetted in liquid metal and (c) The wetted nozzle makes lines comprising sequential droplets.

Since a separate motorized 3-axis Cartesian system controls the motion of the print head, any arbitrary planar geometry is possible in this method subject to the minimum dimension restrictions caused by the droplet size. It also requires minimal manual labor compared to many other deposition techniques reported in the literature. One major disadvantage of this technique is the need for repeated contacts rather than continuous printing.

2.2.3   Direct Patterning

In this section, the techniques to directly pattern 2D and 3D structures of liquid metal alloys have been summarized.

2.2.3.1 Pressure-driven 2D structure

In these pressure driven techniques, a simple roller-ball pen and brush pen were used to directly write conductive tracks of liquid metal ink on different substrates with relatively low resolution by Zheng et al. [156] and Gao et al. [157,158], respectively. Later on, high-resolution electronic circuits of liquid metal were successfully printed by Yang et al. [159] and Zheng et al. [124] using

a customized computer-controlled liquid metal printer. The printing head developed by Zheng et al. comprises a tiny rolling sphere inside the dispensing nozzle. Enforced pressure of liquid metal and the rolling sphere contribute to uniformly transfer liquid metal to the substrate, whereas the oxidation of liquid metal ensures the adhesion to the printing substrate. After printing the desired circuit on flexible PVC film, the circuit can be transferred to a PDMS film and subsequently sealed with another layer of PDMS to get the embedded structure described in [160]. In a separate work, Zheng et al. also developed a brush-like porous needle pen and customized commercial rubber dispenser to fabricate printed-circuits-on-paper flexible electronics [161]. In brief, the customized printer system was equipped with two syringes preloaded with liquid metal and room temperature vulcanization (RTV) silicone rubber. First, conductive patterns were printed on paper using one syringe, and then RTV silicone rubber was overprinted using another syringe to get three-dimensional hybrid electro-mechanical devices on paper.

In an alternative direct printing method, Kim et al. used a custom print head with an orifice to jet liquid metal onto the desired substrate [123]. This custom print head has HCl-impregnated flattened paper near the orifice to reduce oxidation and ease jetting. Another group of researchers, Boley et al. used a direct writing method to pattern a liquid metal structure on a substrate [34]. In this method, a stationary syringe needle was used to dispense liquid metal onto a movable substrate by using a syringe pump. Both Boley et al. and Kim et al have used a syringe pump to feed the liquid metal through the nozzle. The detailed procedure to fabricate the custom print head by Kim et al can be found in the literature [123]. The writing system reported by Boley et al is schematically illustrated in the Figure 2.7. Boley et al observed that for stable writing, the

ratio of standoff distance (h_0) above the substrate and the inner diameter (ID) of the writing nozzle must not exceed a critical value (h_0/ID $< \approx 0.21$ for stable writing) [34]. No failures were observed at very close distances, but there would be a possibility for the tip to contact and drag accidentally if h_0 was set too low.
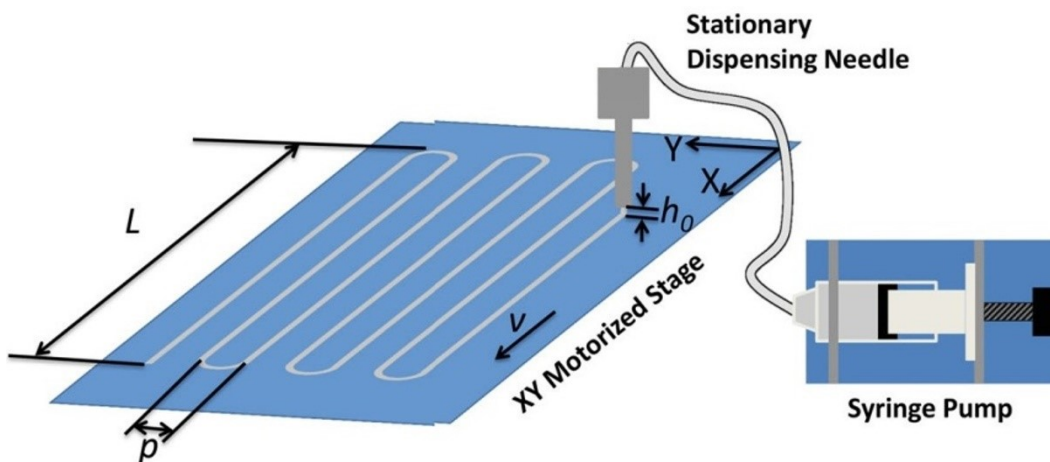
Figure 2. 7: The schematic of direct writing with dispensing needle adapted from [34]. Copyright WILEY 2014 reprinted with permission.

Inkjet printing of liquid metals is another fabrication technique, which results in the same pressure driven 2D structure but has different post-processing requirements to ensure proper coalescence of jetted droplets. Compared to the direct writing by Boley et al., inkjet printing has more size restrictions. For the inkjet printing system reported by Kim et al., the flow rate of liquid metal through the nozzle determines the size of the jetting droplets. For nozzles made of pure PDMS, flow rates below 0.5 mL/min could not overcome the surface tension caused by the native oxide to jet droplets and a large droplet at the outlet can continuously increase in volume. For the HCl-impregnated tip, the pinched off droplet diameters at this flow rate were approximately 500 µm. At higher flow rates, faster jetting produces smaller droplets (as small as 1 µm diameter) [123].

These techniques are comparable with traditional inkjet printing. The suitability of inkjet printing technique to any ink or fluid mainly depends on how the jet undergoes breakup to form droplets, which is governed by the fluid properties, i.e. viscous, inertial and surface tension forces. The fluidic properties of the liquid metal alloys do not favor its use in inkjet printing techniques without modifying those properties. On top of that, the oxide skin formed on to the liquid metal surfaces also impedes the droplet formation. For instance, Guangyong et al. used HCL vapor to consistently remove oxide skin from liquid metal and successfully utilized in the inkjet printing system without modifying the fluidic properties itself [162]. On the other hand, Boley et al have proved that if the dispersion of mechanically sinterable EGaIn nanoparticles is used, inkjet printing is a means for liquid metal devices like arrays of strain gauge with intricate wiring and contact pads [163]. Briefly, the dispersion of thiol-capped EGaIn nanoparticles (180 ~ 600 nm) was fabricated using multiple sonication stages of bulk liquid metal and ethanol/thiol solutions. The minimum reported feature size from 2D direct patterning is 45 µm [123]. Though the main advantage of this technique is the possibility of producing any arbitrary 2D structure, the major drawback is the requirement of a relatively complicated support system.

2.2.3.2 Pressure-driven 3D structure

Ladd et al. reported direct-write patterning methods to fabricate free-standing liquid metal structures, wires, fibers, arrays of droplets and array of in-plane free-standing lines [106]. A stationary syringe needle is used to extrude the liquid metal onto a movable, controlled stage and a syringe pump is used to apply appropriate pressure on the syringe.

To form the wires (Figure 2.8(a)), a modest gauge pressure ($<$ 5 kPa) is applied on the syringe. As a result, a bead of liquid metal is built-up at the tip of the needle. If the metal contacts the substrate and the syringe is taken away slowly with constant pressure, a wire forms and elongates because of the tensile force generated due to the oxide layer. Wire forming is terminated by applying a vacuum on the syringe. By this method, a wire 1 cm long and 30 µm wide has been fabricated successfully.

Secondly, fibers (Figure 2.8(b)) are produced by quickly expelling the liquid metal from the syringe using a burst pressure ($\sim$ 60 kPa). The stack of droplets shown in Figure 2.8(c) is fabricated by forming droplets using short burst pressure (20~60 kPa for 1~2 ms). The syringe needle carries the droplet until it touches the previous droplet. The droplets contact each other without coalescing into one bigger droplet.
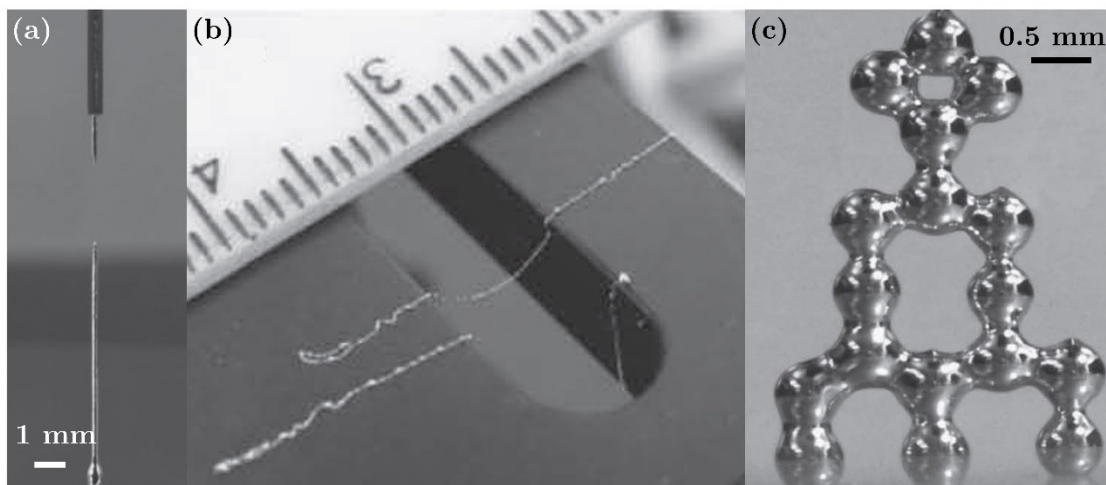
Figure 2. 8: (a) Formation of free-standing wire, (b) The suspended fibers using short burst pressure and (c) stacking the liquid metal droplets (adapted from [106]. Copyright WILEY 2013 reprinted with permission).

2.2.3.3 Dielectrophoresis based 3D structure

Tang et al. [125] introduced a novel technique to create 3D microstructures of liquid metal using dielectrophoresis (DEP). The process starts with producing microdroplets (0.1 µm ~ 0.35 µm) of galinstan in deionized (DI) water with the help of ultra-sonication. In the second step, the microdroplet suspension was applied to a DEP platform having pairs of planar chromium/gold microelectrode pads with a diameter of 80 µm and a similar microelectrode island between each pairs of pads. The gap between these microelectrodes was only 40 µm. The electrically conductive liquid metal droplets were immobilized between the microelectrode pads when a sinusoidal signal (15 V, 20 MHz) was applied. This immobilization was caused mainly by the DEP force. Finally, NaOH solution was used to partially remove the oxide skin formed on microdroplets letting them to amalgamate on gold microelectrode pads. Then, a high flow is used to wash out the unmerged droplets, which then results in the formation of 3D microelectrodes of liquid metal with a spherical cap as shown in the Figure 2.9.

2.2.3.4 Laser patterning

Direct patterning of liquid metal electrodes by using laser cutters was reported by Lu et al. [126]. In this method, a commercial CO_2 laser cutter (VLS 3.50, 30 W) was used to remove liquid metal in a subtractive manner. As shown in Figure 2.10, the process starts by encasing a thin layer of liquid metal between two layers of PDMS. The top layer of PDMS is cast and cured on top of the EGaIn to contain it, helps in initial removal of material by highly absorbing the laser light, and

protects the EGaIn layer from excessive oxidation and debris contamination during the laser

cutting process.
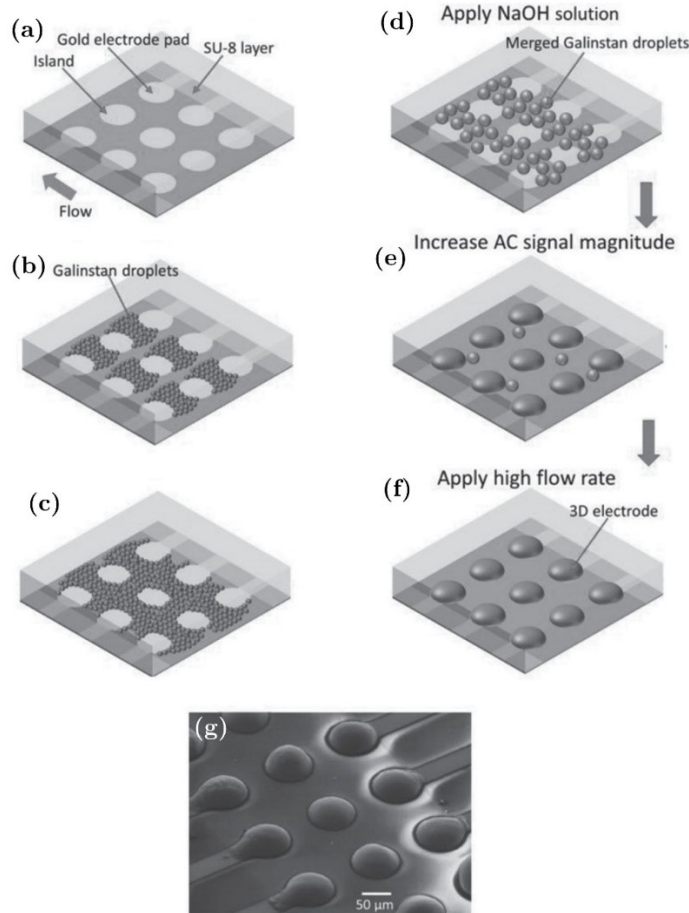
Figure 2. 9: (a) The DEP platform with pairs of microelectrode pads and islands. Immobilization of liquid metal microdroplets by electrophoresis after (b) 10 sec and (c) 20 sec. (d) Application of NaOH solution and (e) increasing AC signal magnitude to merge microdroplets. (f) High flow rate is used to wash out the unmerged droplets and finally (f) the SEM image of liquid metal 3D microelectrodes using dielectrophoresis (adapted from [125]. Copyright WILEY 2015 reprinted with permission).

When the CO_2 laser is applied at the desired location, the energy from the laser vaporizes the top

and bottom PDMS layers. The higher vapor pressure of vaporized PDMS punctures the liquid

film and escapes, which results in a patterned planar structure of liquid metal. The technique uses

the native Ga_2O_3 layer as an advantage, as the oxide can stabilize the EGaIn in its displaced

position and permit features approaching 100 µm to be produced rapidly. Once the metallic features are patterned, a new layer of PDMS is cast on the structure to produce the fully encased electrodes. Using this technique and electrically conductive silicone composite materials, soft matter sensors for pressure measurements and a flexible LED circuit were successfully demonstrated.
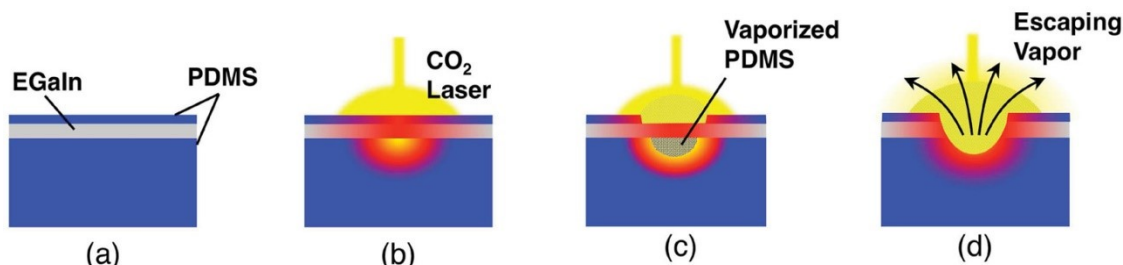
Figure 2. 10: Direct patterning using a laser. (a) Liquid metal encased between two PDMS layers, (b) application of CO_2 laser, (c) locally vaporized PDMS and (d) vapor is escaping results patterned planar structure (adapted from [126]. Copyright WILEY 2014 reprinted with permission).

2.2.4 Casting

In these processes, the liquid metal alloys are filled into a mold with a patterned cavity using different techniques and allowed to solidify by freezing, when required.

2.2.4.1 Needle injection

Injection casting is the most widely used method to pattern 2D and 3D structures of liquid metal. Unlike all the previous techniques listed for direct printing, imprinting and stenciling, the use of injection permits much higher degree of control over the electrode dimensions, and cross-section. This advantage is balanced by the more complex processes necessary to produce the sealed channels in the first place, and the requirement for all features to be connected for a given injection

step, which is a major drawback for more complex circuitry. Researchers have used the injection method in a great variety of applications ranging from flexible electronics to soft artificial skin [118,127-132,134-146,164]. In one particular implementation of the injection process, a flat glass plate is placed against a PDMS mold produced by casting or any other means. For example, White et al. [164] used a rod-coating technique first to prepare elastomer films and then laser ablation to fabricate micro-channels. Then, one syringe is inserted at one end to inject the liquid metal, and another syringe is inserted at other end to permit air to escape. Once the infiltration is done, the patterned liquid metal is frozen. Finally, if necessary, the solid structure can be embedded into elastomers. The steps involving needle injection casting are shown in Figure 2.11.
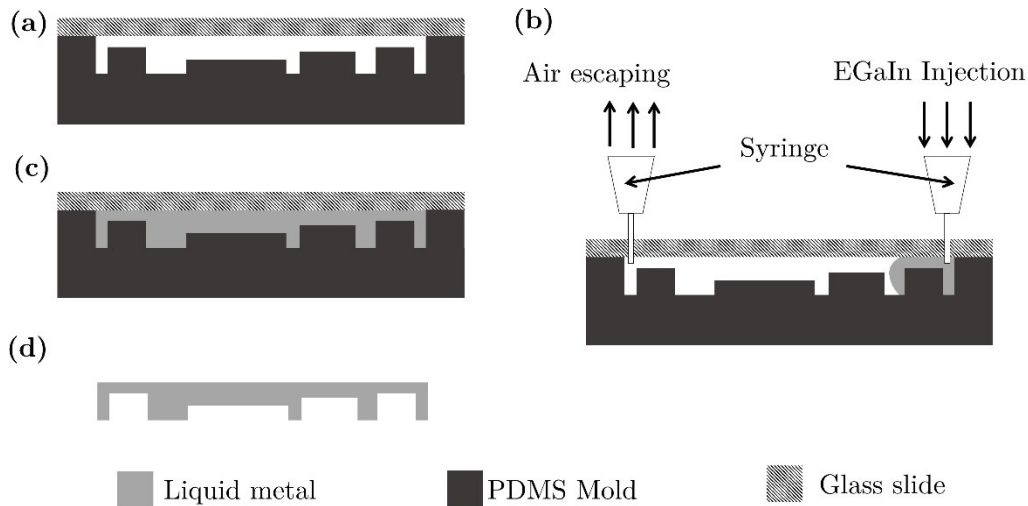
Figure 2. 11: Needle injection of liquid metal. (a) The PDMS mold, (b) injection of liquid metal, (c) liquid metal filled channels and (d) solid structure of EGaIn (inspired by [128]).

This freeze casting technique was developed to permit multiple independent electrodes, and 3D liquid metal structures to be produced, removed (as solids), and then arranged in new positions before casting a new encapsulating PDMS layer. While necessitating much more manual operation

to arrange electrodes in place, it can produce multi-thickness electrodes with high dimensional accuracy at independent locations within a solid elastomer block. The major disadvantage of this technique is the requirement to do all solid metal handling at significantly reduced temperatures, necessitating a cold plate within a humidity-controlled chamber to prevent condensation during the work. PDMS was cured at room temperature or higher as well, which meant that some complex features distorted as they were molten during the PDMS cure. A lower temperature curable PDMS or alternative mechanisms such as UV curing could permit encapsulation while the alloy was still solid [128].

It is also possible to use an elastomer mold with an enclosed 3D cavity instead of using a glass plate to seal the top of the mold [127,129-131]. Zhao et al. used the same method with high pressure (~10MPa) infiltration of liquid metal into hollow silica fiber and fabricated 150 nm diameter nanowires [118]. It is also possible to guide the liquid metal while filling with needle injection by using inherently aligned PDMS micro-pillars. So and Dickey fabricated devices by injecting liquid metal into 1000 µm wide channels between micro-pillars with only 50 µm spacing [130]. The oxide layer of liquid metal helps to flow along the electrode channel without leaking through the micro-pillars because of the very small gap between two neighboring micro-pillars compared to the width of the microfluidic channel. Needle injection method is a very fast, reliable and simple process. It can produce 3D structures with smoother sidewalls than most alternatives. One commonly faced problem is air trapping in a complex structure during infiltration.

2.2.4.2 Vacuum-assisted infiltration

Vacuum-assisted casting is best when fabricating 3D deep features. This method eliminates the problem of air trapping with needle injection, particularly if sharp changes in thickness are desired. One variation of vacuum-assisted casting was applied in conjunction with the freeze casting methods described earlier. As depicted in Figure 2.12, in this technique an initially excess amount of liquid metal is poured onto the PDMS mold. Then using a vacuum, any trapped air or air bubbles are removed, but their passage through the metal will leave small holes in the liquid alloy. Once degassing is done, the liquid metal layer is reformed without holes by perturbation of the mold while maintaining the vacuum. Release from vacuum helps to fill the mold completely, and excess materials can be removed by scraping the top surface. Finally, the liquid structure is frozen and the solid features removed for future embedding in a new PDMS casting.

An alternative vacuum assisted casting technique was described by Cumby et al. who used a polyimide film with 0.4 μm vertical pores to fill a mold quickly with liquid metal [150]. Liquid metal is filled between the porous film and the mold. The required pressure for liquid metal to enter the sub-micron sized pores is very high, so only air can enter the pores and become evacuated rapidly throughout the whole area while applying suction. To increase horizontal degassing, a textile can also be introduced between the vacuum table and vertically porous film as shown in Figure 2.13.

This vacuum-assisted infiltration has a higher filling rate compared to needle injection. But it also requires the repeated process to ensure no air is trapped inside the complex structure with different channel height. The reported minimum feature size using vacuum-assisted infiltration is 250 μm

41

[150]. This technique is suitable for structures with deep features. Unlike needle injection, it does not need two terminals to allow air escaping and infiltration. This technique is very similar to the technique used in microfluidics by Siegel et al. with low melting point metal (i.e. solder) [165]. Microsolidics basically uses techniques based on microfluidics, but ultimately develops solid metal structures. As an additional step, the inner surfaces of the microchannels were treated with plasma oxidation and silanization with (3-mercaptopropyl)trimethoxysilane to decrease surface free energy enhancing the wettability by the molten metal.
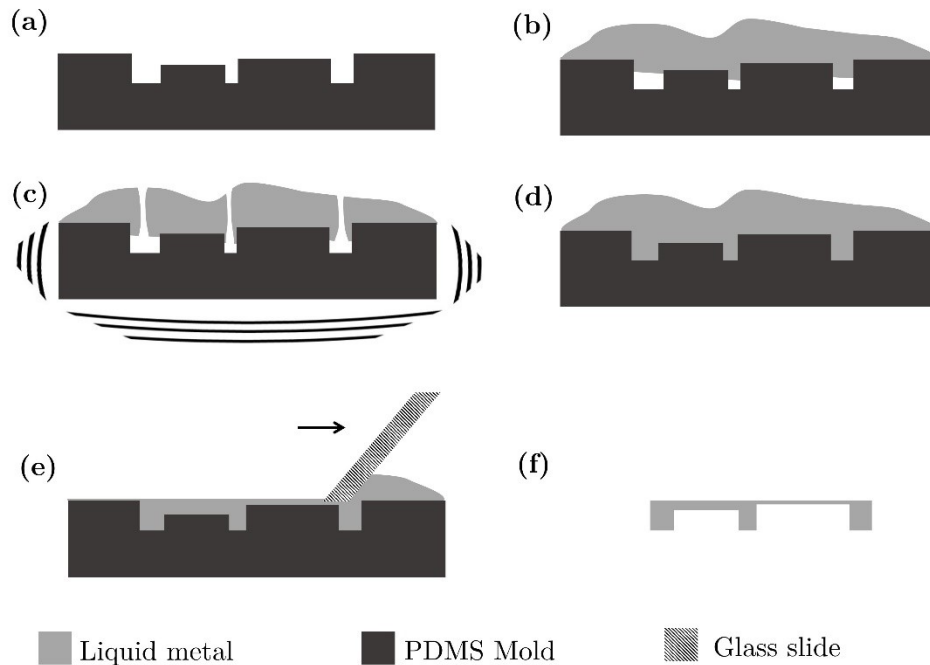
Figure 2. 12: Vacuum-assisted infiltration. (a) PDMS mold, (b) liquid metal is poured onto PDMS mold, (c) degassing in vacuum creates holes in the liquid metal layer to help air escaping, and perturbation helps to fill, (d) liquid metal is filled into channels, (e) excess amount of liquid metal is scraped and (f) after freezing the solid structure of EGaIn (inspired by [128]).
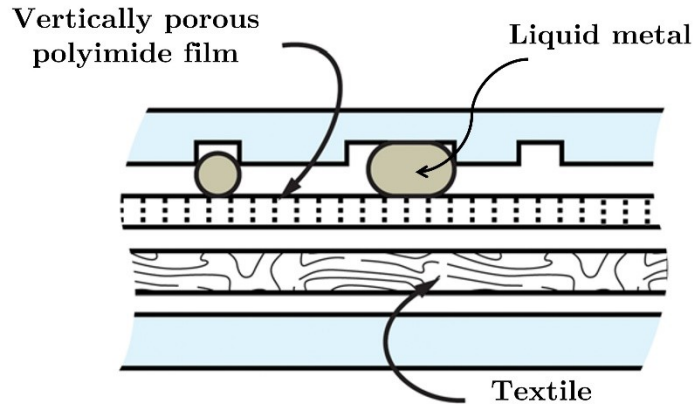
Figure 2. 13: Approach for faster vacuum infiltration of liquid metal into PDMS mold (adapted from [150]. Copyright WILEY 2012 reprinted with permission).

2.3 PARTICULARITIES AND OPPORTUNITIES OF LIQUID METAL MICROSTRUCTURES

While working with liquid metal, researchers have faced some challenges which limit its application. Some of these challenges have been overcome and reported by others. But still, there are some opportunities for further research. In this section, all the difficulties and their reported solutions are described. It also includes undone opportunities for future work.

2.3.1 Wetting Property Due to Oxide Layer

Gallium-based liquid metals form a thin passivation oxide layer on all exposed surfaces when in contact with atmospheric oxygen. This oxide layer has high surface energy, which causes the liquid metal to wet almost any surface and complicates its liquid behavior as it has both fluid and solid like behaviors. From Pourbaix diagram [166], this amphoteric oxide can be removed by acidic environment (pH < 3) or basic environment (pH > 10) [167]. There are some reports where researchers successfully controlled the wettability of liquid metal and removed the oxide layer

43

with techniques ranging from acid treatments, electrochemical reduction in electrolytes and even ultra-low oxygen environments [76].

2.3.1.1 Recovery of the non-wetting characteristic by acid treatment

Though the oxide layer formed on the liquid metal surface increases the stability of the structures in microchannels, it also causes viscoelasticity of the liquid metal resulting non-uniform shape and making the liquid metal behave as a non-Newtonian liquid. Firstly, Zrnic et al. [112] and Dickey et al. [89] successfully removed the oxide layer by treating with diluted hydrochloric acid (HCl) solution. The possible reactions of the acid with the metallic oxides in Galinstan or EGaIn are as follows [168]:

$$
\left.
\begin{array}{c}
HCl + Ga_2O + Ga_2O_3 \rightarrow GaCl_2 + GaCl_3 + H_2O \\
HCl + In_2O_3 \rightarrow InCl_3 + H_2O \\
HCl + SnO \rightarrow SnCl_2 + H_2O
\end{array}
\right\} \tag{2.1}
$$
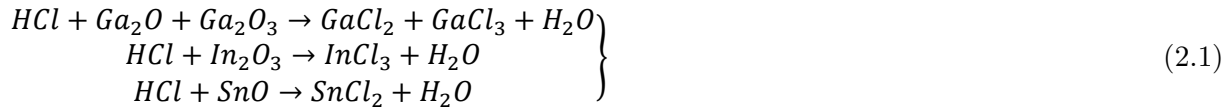
The primary reaction of importance is that of the gallium oxides to form gallium chlorides because gallium is the primary oxide formed on the liquid metals. Attractively, the chlorides that are formed do not have the same effects on liquid metal flow and wettability and permit the drop to behave more like a pure liquid. Later on, instead of using HCl solution, Kim et al. [169] used HCl vapor to recover the non-wetting property of the liquid metal by keeping a pendant drop of HCl (37 wt %, ~5 µL) just 2mm away from the liquid metal droplet for only 15 seconds. Before the HCl treatment, due to the oxide skin, the drops of liquid metal had non-uniform shape with 127.6° contact angle on a glass substrate, whereas after the treatment, the shape became uniform and contact angle increased to 139.5° on the same substrate. Kim et al. also performed a bouncing

test, which illustrates the non-wetting property of liquid metal after HCl treatment. An HCl treated Galinstan droplet of ~10µL was dropped from 3.5 cm height onto a Teflon-coated glass. The droplet bounced back rather than sticking to the surface. The time-lapse images of the droplet can be found in [169]. Researchers removed the oxide by the acid treatment and were successful in their applications. These include demonstration of movement of liquid metal in a microfluidic channel formed on HCl-impregnated paper [170] and a technique for selectively erasing and refilling unit cells of liquid metal based terahertz metamaterials [171].

Besides HCl, sulfuric acid (H_2SO_4) was also used to treat microfluidic channel inner walls to improve the non-wetting property of liquid metal [172]. Oxidized galinstan droplets were created, transported, separated and merged successfully in H_2SO_4 treated microfluidic channels, which demonstrates the possibility of reconfigurable applications.

2.3.1.2 Micro-texturing to control wettability

When a droplet of liquid metal is dropped on to any metallic surface, it may exhibit poor wetting with a very high contact angle or partial wetting with comparatively lower contact angle. Moreover, partial wetting has two cases, conventional partial wetting with no morphological change and partial wetting followed by reactive wetting with penetration into grain boundaries. In the case of reactive wetting, contact angle changes to a very small equilibrium value, making the liquid metal completely spread over the substrate [173]. Kramer et al. [174] have analyzed the wetting behaviors of liquid metal on bare and sputtered indium (In), and tin (Sn) foils. Analogous to controlling hydrophobicity of a surface by micro-texturing on it [175], the metallophobicity of

the foil substrates can be controlled by the surface roughness resulting from the sputtering operation. Due to the lower indium percentage in galinstan (21.5%) compared to EGaIn (24.5%), galinstan was found to partially wet indium foil, whereas EGaIn highly wets. On the contrary, galinstan reactively wets tin foils because of the presence of tin (10%) in galinstan. It has been confirmed using EDS, after reactive wetting, the percentage of tin in that interaction zone increased to $19.68\% \pm 0.2\%$ [174]. The results are summarized in table 2.3.

Table 2. 3: Wetting behavior of EGaIn/Galinstan on to Indium/Tin Substrates (inspired by [174]).

Liquid Metal	Substrate Material	Sputter Material	Type of Wetting
EGaIn	Silicon	Indium	No Wetting
	Indium Foil	Indium	Reactive Wetting
	Tin Foil	Indium	Partial Wetting
Galinstan	Silicon	Tin	No Wetting
	Indium Foil	Tin	Partial Wetting
	Tin Foil	Tin	Reactive Wetting

Li et al. demonstrated that a textured PDMS surface also enhances the non-wetting property of liquid metal [172]. First, the dual-scale micro-textures of normal A4 paper were transferred to the inner walls of PDMS microchannels. Then, for further improvement, titanium oxide (TiO_2) nanoparticles were coated on the micro-textured PDMS surfaces. It showed the highest advancing

angle of 167° and the lowest receding angle of 151°, a low hysteresis of only 16°. These results suggest the possibility of this surface modification for reconfigurable/tunable electronic applications.

2.3.1.3 Super-lyophobicity with multi-scale textured PDMS

There are some applications not requiring the elimination of the oxide skin. Rather than removing the oxide layer, the non-wetting behavior of liquid metal can also be maintained even with the oxide present. Kim et al developed a super-lyophobic three-dimensional PDMS channel to manipulate oxidized galinstan without wetting the surface [176]. Experiments to check the lyophobicity of modified PDMS surfaces in contact with already oxidized galinstan droplets were performed. These PDMS surfaces were textured with micropillars and microridges with or without a coating of fluoropolymers including Teflon and Cytop. It was found that the multi-scale textured PDMS micropillars with 75µm diameter and 100µm spacing coated with fluorocarbon polymer experience super-lyophobicity. It has a static contact angle of 156.9°, which is beyond the super-lyophobic regime of 150°. Also, it is believed that another reason for this super-lyophobicity is the low solid-fraction (f_s) due to the additional surface roughness of the multi-scale textured micropillars.

2.3.1.4 CNT based super-lyophobic surface

Kim et al. reported that a vertically aligned carbon nanotube (CNT) forest could contribute to maintaining lyophobicity of the PDMS surface in contact with galinstan [177]. Hierarchical micro/nanoscale combined structure of CNT is proved to have super-repellent property in contact

with oil or water [178-181]. First, the vertically aligned CNT was grown using chemical vapor deposition (780°C, 5 min) on an iron coating (6 nm thick) deposited by e-beam evaporation on a SiO_2/Si substrate. Then, a nano-imprinter was used to transfer the CNT forest from the Si substrate to the PDMS sheet. Finally, the static contact angle, dynamic contact angle, bouncing test and rolling test of galinstan droplet were measured and performed with (i) CNT on Si substrate, (ii) CNT on PDMS sheet with 0%, 50% and 100% stretching and (iii) CNT on PDMS with 0.1 mm^{-1} and 0.4 mm^{-1} curvature. Rolling tests of 7.8µL and 1.6µL droplets on curved PDMS sheets with CNT forest were performed by Kim et al., which proves the non-wetting behavior of galinstan as no residue was seen on the surfaces after rolling tests.

2.3.2 Critical Dimension and Line Edge Roughness

In microfabrication, the resolution and precision of patterning structures are characterized by two significant criteria, critical dimension [182] and line edge roughness [183]. The critical dimension is the size of the smallest possible feature fabricated, and line edge roughness measures the edge deviations of a critical dimension. Some techniques discussed in this review result in higher edge roughness. Except for needle injection and imprinting using molds, no other technique has been reported to fabricate features smaller than the micrometer range. Most of the techniques can develop patterns on the order of 100 µm in minimum dimension. Casting by needle injection and vacuum assisted filling produce relatively smooth walls and lines (which are primarily determined by the original molding process used to make the channels) when compared to all direct printing or patterning methods described to date. Pure liquid gallium was found inside carbon nanotube

(CNT) [184,185], which means it may be possible to produce finer features of liquid metal. Further research is required to enhance the resolution of the liquid metal structures by fabricating even smaller features in the submicron scale.

2.3.3 3D Freestanding Microstructures

Though the three-dimensional freestanding microstructures have been produced by Ladd et al. [106], they have not yet been utilized in any application. These structures also have issues with stability, repeatability, etc. To overcome these issues, the additive technique, 3D printing may be useful to fabricate liquid metal structures embedded in 3D printable elastomers or plastics. Wang and Liu utilized liquid phase 3D printing using the $Bi_{35}In_{48.6}Sn_{15.9}Zn_{0.4}$ alloy to quickly fabricate conductive metal objects with the help of cooling fluid to prevent oxidation [186,187]. The liquid phase 3D printing technique by Wang and Liu might be adopted to print liquid metal alloy. However, it remains to be proven how well the 3D patterns can be utilized in real-life applications.

2.3.4 Reconfigurability

Reconfigurable electronics refer to adaptive, multifunctional future devices for information and communications technology. Conventional reconfigurable devices use mechanical switches, transistors, diodes, or varactors to change the radiofrequency (RF) properties (e.g., resonant wavelength) by dynamically altering the static layout of electrical interconnects [188]. However, these conventional approaches have a limited variability and range of states. More versatile devices with the ability to dynamically reconfigure, tune, erase or write electrical circuits are possible if incorporating liquid metal components. Recently, the use of liquid metal in reconfigurable

microstrip RF filters [189,190], wideband RF switches [191], frequency selective surfaces (FSS) [192], antennas [16,129,193-196] and plasmonic devices [197] have been reported. In these applications, though the control of current paths is significantly enhanced by pneumatically actuating liquid metal using pumps or contact pressure, the use of an external control system increases overall complexity, reduces switching speed and is unable to reconfigure actual wires. These limitations can be overcome by enabling continuous electrowetting (CEW) [12] or Laplace pressure shaping [150] to actuate liquid metal in a capillary.

Researchers are still working on the shape reconfigurability. Due to the oxide skin, some residual amount of liquid metal remains in the channel even after evacuating that. Acid vapor treated surfaces [101,195,198], lyophobic surfaces [176,177,199], micro-textured surfaces [173,174] discussed in section 3.1 can be useful to control the wettability of liquid metal in reconfigurable devices and eliminate this residual material. However, the use of harsh chemicals (e.g., acid vapor) may not be desirable in many applications. Also, surface modification requires some additional steps and increases overall process complexity. Other successful research on enhancing reconfigurability of liquid metals is discussed below.

2.3.4.1 Use of carrier fluid

A simple method to prevent wetting of microchannels by liquid metal is to use an aqueous solution of 20 wt% poly (ethylene glycol) (PEG) and 5 wt% sodium dodecyl sulfate (SDS) [200]. The solution acts as a carrier fluid of liquid metal by assisting in forming microdroplets of liquid metal and maintains their spherical or non-spherical shape within microfluidic channels without adhering

to each other and channel wall. Though this water-based technique is useful in reconfigurable applications, water is not ideal for RF applications due to its high loss at high RF frequencies.

In addition to the use of carrier fluid, surface modification of the channel walls would also enhance the non-wetting property of the liquid metal. For instance, Koo et al. investigated the use of carrier fluid in microchannels coated with other materials to minimize EGaIn fragmentation and EGaIn residues on PDMS-based microfluidic channels during repeated actuation of an EGaIn plug for tunable RF applications [201]. It was found that a PDMS microchannel coated with 2 % of nonionic surfactant TWEEN 20 (Sigma, Saint Louis, MO) or 5 % of hydrophobic PTFE resulted in no residue of liquid metal even with the repeated flow when using high viscosity oil (Hydrocal 2400) as a carrier fluid. The stable result confirms the fulfillment of the requirement for repeated reconfiguration of RF devices. In another method, Khan et al. used water as an interfacial slip layer in a microchannel, which allows the liquid metal successfully to flow across the channel surfaces without sticking to it [202]. The microchannel was first prefilled with water, and then the liquid metal plug was injected. The water slip layer acts as a lubricant and allows continuous electrowetting (CEW) of the plug [203]. Unfortunately, the water evaporates relatively quickly, and after 10-12 minutes, there was insufficient water lubrication to prevent direct contact of the liquid metal with the channel sidewalls, and the slipping behavior was lost.

2.3.4.2 Recapillarity

Oxidation increases the surface tension of gallium based liquid metal alloys. For instance, the EGaIn droplet with oxide skin has an effective surface tension of around 624 mN/m [112] but will highly wet surfaces when the oxide is breached, whereas the oxide-free droplet has only 435 mN/m

51

surface tension [76,111] but can be non-wetting if the oxide formation is suppressed. Therefore, the oxide skin acts as an intrinsic "surfactant." The formation of oxide skin has been regulated by electrochemically depositing or removing with the help of very small voltage (<1V) [91]. Hence, the interfacial surface tension of liquid metal droplet was controlled using potential – that is, electrocapillarity. Tang et al. successfully steered liquid metal flow in microchannel using low voltages [204]. Khan et al. also successfully controlled the flow direction of liquid metal in a microchannel by application of a voltage in the presence of 1M NaOH [91]. It was found that the oxide skin can be removed by applying a modest reductive voltage (e.g., 1V) to induce capillary behavior. The introduction of capillary behavior of liquid metal by applying reductive voltage is termed as "recapillarity" [91,205]. Recapillarity enables liquid metal to flow in a microchannel without leaving any residue (Figure 2.14), which is the requirement of reconfigurable electronics applications. The biggest disadvantage of the electrochemistry is the need for a continuous power supply to maintain oxide-free metal.
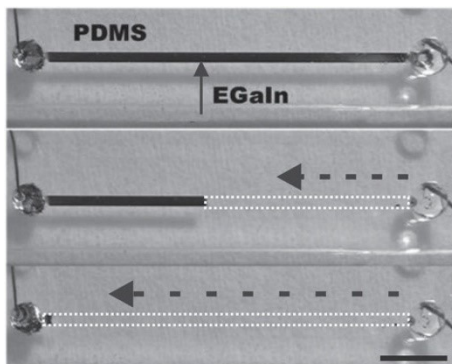
Figure 2. 14: Recapillarity in action. The liquid metal is withdrawn by applying small voltage without leaving any residue in a microchannel (adapted from [205]. Copyright WILEY 2014 reprinted with permission).

2.3.5 Corrosive Nature of Liquid Metal

Deng and Liu [206] observed the corrosive nature of liquid gallium, but this issue can be resolved using contactless geometry [206]. Not only the liquid gallium, galinstan and EGaIn alloys also have corrosive nature, which can be avoided using a multilayer graphene diffusion barrier [94]. However, the issue with corrosive nature of these liquid metals is something that has not been fully addressed in the literature and may have implications for long term use of these materials. It is believed that this is the amalgamation effect, for which the alloying process starts when liquid metal is in contact with other metals. It results in a new alloy with different composition accompanied by the corrosion of original solid metal.

Table 2. 4: Summary of the results of experiments to check the corrosive nature of liquid metal with common solid metals at room temperature (RT) and elevated temperatures

Materials	Samples	No noticeable corrosion until	Completely destroyed in
Aluminum	Tubes (OD: 1.6 mm, ID: 0.9 mm and length: 4 mm)	5 mins at RT;	30 mins at RT;
Brass (C36000)	Tubes (OD: 1.6 mm, ID: 0.9 mm and length: 4 mm)	24 hrs at RT; 5 mins at 100 ºC;	3 hrs at 230 ºC;
Copper	Rectangular sheet (3 mm × 3 mm × 0.12 mm)	24 hrs at RT;	1 hr at 230 ºC;
Stainless steel (316)	Washer (OD: 7 mm, ID: 3.2 mm, and thickness: 0.65 mm)	5 hrs at 230ºC	-

To demonstrate the damaging nature of galinstan, we tested several small pieces of different materials as summarized in Table 2.4 and shown in Figure 2.15. We kept the samples in contact with Galinstan for different lengths of time and at different temperatures. It was found that galinstan starts corroding the aluminum samples within 5 minutes and it destroys the aluminum samples in around 30 minutes even in room temperature. Compared to aluminum, brass showed less vulnerability with galinstan. At room temperature, no noticeable corrosion was seen in brass samples up to 24 hours. But it starts corroding the brass samples in about 5 minutes when heated at ~100°C, whereas at 230°C, the brass sample was completely corroded in galinstan within 3 hours. Copper samples also did not show any noticeable corrosion while keeping in contact with galinstan at room temperature up to 24 hours. But at higher temperature copper samples were corroded in galinstan over time, it took around one hour to corrode completely at 230°C. Among them, stainless steel showed superior resistance to the corrosive nature of galinstan. The washers made of stainless steel were not corroded even after 5 hours of heating at 230°C. Physically, it only changes the appearance to a reddish color. SEM images of the non-exposed washer and exposed washer (230°C for 5 hours) also confirm no significant change in surface topology. Therefore, for low-temperature applications, brass electrodes might serve the purpose of external wiring, but for higher temperature applications, stainless steel must be used. Aluminum is not recommended for this wiring purpose regardless of the working temperature. To overcome the challenge with direct-contact corrosion of liquid metal, co-axial extrusion of liquid metal wires already encapsulated in the thermoplastic shell might be a part of the future work. Still, it should

54

be considered that higher temperature exposures for these liquid metals may lead to damage to the extrusion die.

2.4 DISCUSSION AND CONCLUSION

Liquid metals can be processed with a variety of techniques to produce 2D or 3D microstructures embedded in elastomeric materials to perform as a highly stretchable, flexible, lightweight, self-healing devices with comparable conductivity with metals like Cu, Au, etc. This report highlights the recent research on liquid metals and their fabrication processes to aid those interested in manufacturing new stretchable, electronically functional smart materials. All the available fabrication techniques are grouped into four major categories such as masked deposition, imprinting, direct patterning, and casting. In each major category, there are some techniques involving different methods to develop liquid metal structures. In this report, a total of 12 different fabrication techniques with their unique advantages and disadvantages have been discussed. The minimum feature size reported using the corresponding techniques have also been summarized in Table 2.2. Needle injection and direct 3D patterning are the currently available processes for three-dimensional structures. On the other hand, imprinting and masked deposition processes are dedicated to planar structures. Imprinting using a mold and stamp are the simplest processes to fabricate 2D structures, but imprinting using a stamp is limited for relatively large features (~ 750 µm). The techniques reported up to now have relatively poor resolution compared to the conventional microfabrication techniques for polymers. The biggest challenge is, coercing the liquid metal into the micro / nano-sized feature because of the oxide skin and large surface tension.

But pure liquid gallium inside carbon nanotube (CNT) has been studied, which suggests a new horizon of possibility to create finer features of liquid metal.

After fabricating the functional structure, suitable wiring plays an important role in utilizing the designs in their applications. Most applications require connecting the liquid metal with other conductive components for electrical contacts. Gallium alloys with other materials, which may limit its use with a variety of possible electrode materials. For instance, if an aluminum thin film is used in direct contact with gallium-based alloys, aluminum readily is corroded even at room temperature. This phenomenon may be prevented using a multilayer graphene diffusion barrier or selection of chemically resistant metallic electrodes but needs to be considered for the expected lifetime and temperature range of the expected liquid metal application.
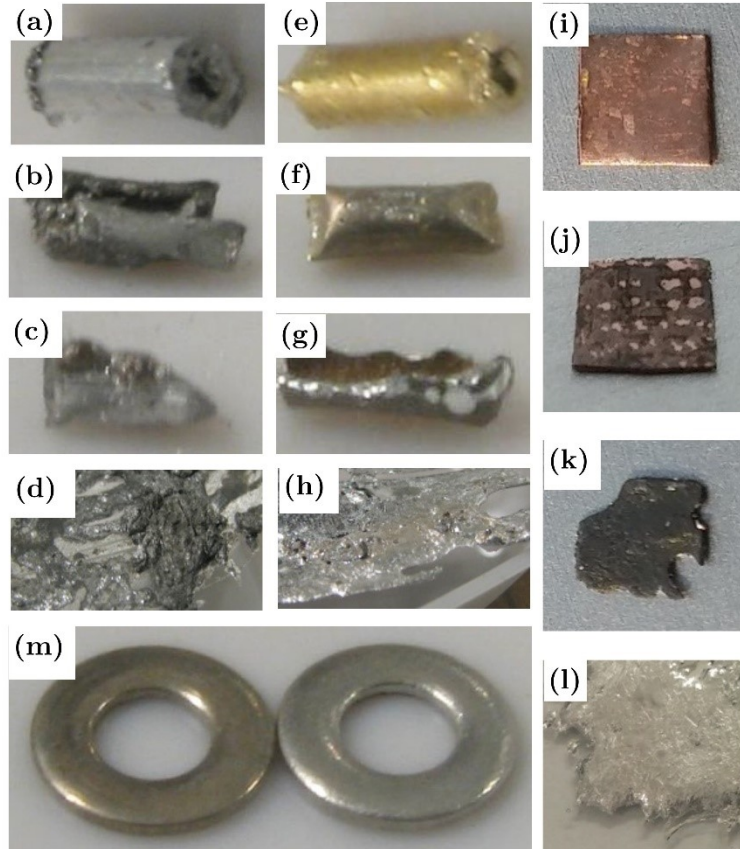
Figure 2. 15: (a) Non-exposed aluminum sample, exposed aluminum sample for (b) 15 minutes at room temperature, (c) 5 minutes at 100°C, (d) completely dissolved aluminum at room temperature for 30 minutes (e) Non-exposed brass sample, (f) exposed brass sample for 5 minutes at 100°C, (g) exposed brass sample for 2 hours at 230°C (h) completely dissolved brass for 3 hours at 230°C (i) Non-exposed Cu sample, (j) exposed Cu sample for 15 minutes at 100°C, (k) exposed Cu sample for 30 minutes at 230°C, (l) completely corroded Cu sample after 1 hour at 230°C and (m) non-exposed 316-stainless steel washer [right] & exposed washer [left] for 5 hours at 230°C.

3. CHAPTER: PRINTING WITH MECHANICALLY INTERLOCKED EXTRUDATES USING A CUSTOM BI-EXTRUDER FOR FUSED DEPOSITION MODELLING[†]

3.1 INTRODUCTION

Additive manufacturing (AM) is a group of techniques that use three-dimensional computer-aided-designs (CAD) to fabricate a three dimensional object by selectively adding materials, usually layer by layer, as opposed to the traditional subtractive manufacturing techniques like computer numerical control (CNC) machining where the desired object is fabricated by selectively removing the material [25]. The considerable benefits of AM technologies include, but are not limited to, higher fabrication speed, minimal material wastage, higher complexity of fabricated objects, and

reduced numbers of processing stages [207]. In 2009, the American Society for Testing and Materials (ASTM) approved a set of standard terminologies, where all the AM techniques were classified under seven major groups [208]. Table 3.1 shows a brief description of common AM techniques.

Table 3. 1: Brief description of the major classes of AM techniques [25,208].

Serial	Major Classifications	Brief Description	Other Processing Techniques under this Category
1.	Binder Jetting	A liquid bonding agent is selectively deposited on powdered build material by means of an inkjet head	
2.	Directed Energy Deposition	Powdered build material is selectively deposited into a heated zone by a focused thermal energy	Laser Metal Deposition (LMD), Laser Engineered Net Shaping (LENS)
3.	Material Extrusion	A molten material is selectively deposited from a heated nozzle	Fused Deposition Modelling (FDM) [209]

4.	Material Jetting	Droplets of build material (usually photopolymers and wax) are selectively deposited from an inkjet head	PolyJet Technology (PJT)
5.	Powder Bed Fusion	An energy beam selectively fuses powdered build materials	Direct Metal Laser Sintering (DMLS), Electron Beam Melting (EBM), Selective Heat Sintering (SHS), Selective Laser Melting (SLM) [210] and Selective Laser Sintering (SLS) [211]
6.	Sheet Lamination	Patterned metal sheets cut by a laser are bonded to each other	Laminated Object Manufacturing (LOM) [212], Paper Lamination Technology (PLT), Ultrasonic Additive Manufacturing (UAM)
7.	Vat Photopolymerization	A light curable resin in a vat is selectively cured by polymerization	Stereolithography (SLA) [213], Digital Light Processing (DLP),

Although ASTM International defines 3D printing as a group of technologies where the build material is selectively deposited using a print head or nozzle realizing the overall 3D object [208],

the term "3D Printing" is sometimes synonymously used with AM techniques. Among these AM techniques, FDM style 3D printing is an extrusion-based technique which involves low cost, efficient deposition of material and minimal wastage.

In FDM, a filament (mostly thermoplastic material) is fed from a material spool to the print head by a motor-gear feeder assembly. The print head consists of a melt-chamber, a heater block, a temperature sensor, and a nozzle. The heater block and temperature sensor are synchronized with a temperature controller to maintain the desired temperature of the melt-chamber. The fed filament is melted in the melt-chamber and then extruded through the nozzle orifice. Although in most FDM systems the print head moves along horizontal X and Y – axes, the mechanism of Z-movement may vary. Some systems have the print head movable along the Z-axis as well, while in other systems the Z-movement is achieved by moving the print bed itself. The molten material is deposited as successive 2D layers, where each new layer is added on top of the prior one, finally constructing the 3D object [214]. Figure 3.1 shows the schematic diagram of a typical FDM system.

There are some major limitations of FDM parts, such as inherent poor surface finish with ridges [215-217], low inter-layer bond strength [218], limited printing resolution, etc. In FDM parts, both intra-layer and inter-layer bonding are crucial in determining the overall mechanical strength of the printed object. However, generally the bonds between layers are not strong compared to that of other AM techniques [216]. It is worth noting that the mechanical strength is higher in the direction of deposited extrudates compared to that in the transverse direction [219]. Mechanical abrasion and solvent-vapor smoothing are the commonly used post-processing techniques to lower

61

the surface roughness [220,221]. Although using a smaller nozzle improves surface quality, it also increases overall printing time which is not typically desirable.

Most FDM systems use non-flexible, non-stretchable materials like ABS, PLA, HIPS, Nylon and many other hard thermoplastics. A few FDM systems can also print objects using specially modified semi-flexible but non-stretchable materials like NinjaFlex® commercialized by NinjaTek. There has been very limited reported work where soft elastomers are employed in FDM systems, however Elkins et al. modified the feeder system of a commercial printer to accommodate soft thermoplastics with hardness of 72 and 78 Shore A [222]. To the best of the author's knowledge, there are no available printers that use very soft thermoplastic elastomers like styrene ethylene butylene styrene (SEBS) based Kraton G1657 with hardness of only 47 Shore A [223]. The capability to print very soft stretchable materials like SEBS is highly desirable for fabricating tunable electronic devices [52,224] and is something that eventually this extruder is intended to achieve.
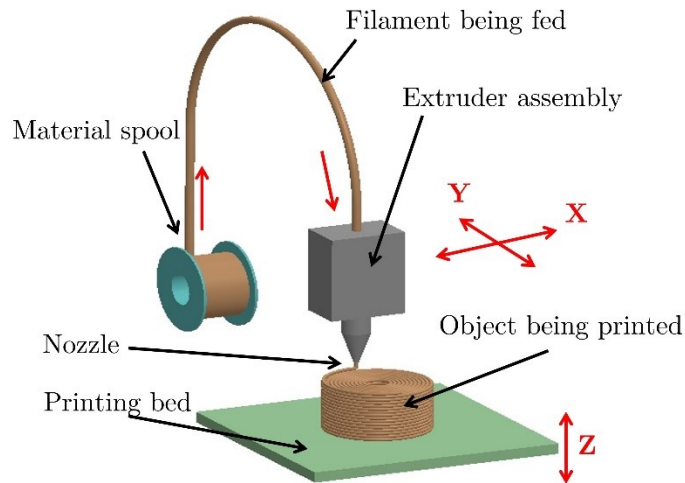
Figure 3. 1: Schematic of a typical FDM system (red arrows show the movement directions)

Most commercial FDM systems extrude only a single structural material. Currently, there are several commercially available FDM systems which can print multiple materials with separate nozzle systems. For instance, RoVa3D commercialized by ORD Solutions uses 5 separate nozzles for 5 different filaments. However, printing of functionally gradient material (FGM) requires use of a single nozzle for multiple materials which is an area still largely unexplored. The FGM defines a special class of engineering materials exhibiting spatially inhomogeneous content, tailoring the devices made of this material to specific functional and performance requirements [225-227]. In the last few years, a few studies were reported to print FGM devices using other AM techniques. For example, Bruyas et. al. successfully fabricated multi-material compliant joints using polyjet technology [228]. There are a few open source FDM systems from the hobbyist community, which use a single nozzle for two or three materials with limited reported flexibility in material choices as inputs. These have primarily been used for blending colors of the same material, for example PLA. Some of these FDM systems print only one material at a time and others print multi-material objects by simple side-by-side co-extrusion. It is hard to find quantitative data on the quality of mixing, miscibility, adhesion strength, or polymer compatibility for many commercial designs.

The miscibility of polymers can be determined from their solubility parameters, δ ($cal^{1/2}cm^{3/2}$). The closer the solubility parameters, the more miscible the polymers are [229]. For instance, Vadori found that, for best blending results with PLA, ABS must have solubility parameter, δ_{ABS} = ($\delta_{PLA} \pm 1$) $cal^{1/2}cm^{3/2}$, where δ_{PLA} = 9.58 $cal^{1/2}cm^{3/2}$ [230]. This parameter depends on the content of the polymer, and to achieve a solubility parameter of 9.58 $cal^{1/2}cm^{3/2}$ ABS needs approximately

38% of polybutadiene content [231]. If the polymers do not exhibit compatible solubility parameters, they become immiscible. As an alternative solution, there are a number of compatibilization methods to enhance interfacial adhesion between two immiscible polymers, such as incorporation of a third premade co-polymer [232], reactive polymer [233,234] or carbon nanotubes (CNTs) [235], etc. Without proper compatibilization, high interfacial tension between the immiscible polymers results in poor interfacial adhesion [236,237]. Hence, side-by-side co-extrudates of two immiscible polymers can experience delamination under a certain load. Most users of FDM systems use directly purchased filaments and thus do not have direct control over composition, molecular weight, and other material properties of the polymer to modify its solubility parameter. Moreover, compatibilization techniques may not be desirable as they give rise to additional processing steps in the original production of the filaments. Hence, as an adhesion mechanism, the direct mechanical interlocking of two polymer surfaces [238] would be desired in FDM-style multi-materials 3D printing. Therefore, intermixing of two polymers immediately next to the nozzle orifice can in theory greatly enhance bond strength of the polymer interface within and between filaments.

The primary requirement of the intermixing capability is to produce a blended polymer with a co-continuous structure, where the mechanical properties of the intermixed extrudate are defined by the maximum contribution from each component simultaneously [239]. In contrast to co-continuous structure, a matrix-dispersed phase structure may have an adverse effect on the mechanical strength of the intermixed extrudate. There have been some empirical models reported, to predict the conditions of co-continuous structure based on the volume fraction and viscosity

ratio of the binary polymer system [240-249]. To achieve a co-continuous structure, the composition of the binary system must be within a composition region about the phase inversion composition. This phase inversion composition can be estimated for different viscosity ratios using empirical models. Hence, the intermixed extrudates having only a range of intermediate composition will necessarily have the co-continuous structure, hence will result in enhanced mechanical adhesion and tensile strength.

In this work, we have designed an intermixer that results in mechanical keying of the extrudate as opposed to side-by-side co-extrusion. Mechanical interlocking or keying is one of the conceptually most straightforward approaches to overcome the bonding failures of polymers with FDM technology [238]. Mechanical keying refers to the process of joining two highly rough solid surfaces by physically engaging them to introduce adhesion between them. This report presents the design and characterization of a bi-extruder with the capability of printing two dissimilar thermoplastic materials with both side-by-side co-extrusion and mechanically interlocked extrusion. This intermixing feature can also enhance the inter-layer bond strength of the printed objects by ensuring at least some areas of the bonding interface are between the same material.

3.2   DESIGN OF THE BI-EXTRUDER

There are four major components of a typical FDM extruder, as shown in Figure 3.3, such as a motor-gear feeder assembly, guide-way, melt-chamber, and nozzle. The motor-gear assembly consists of a stepper motor, a drive gear, and an idler. The idler is grooved or toothed to enhance the friction between the idler and the filament [250]. The drive gear is coupled with the motor

shaft and the filament is placed between the idler and the drive gear. Hence, when the motor shaft

rotates the filament is fed towards the melt-chamber in a controlled manner. Above the idler-gear

contact, the filament is in tension because it's being pulled from the material spool to the feeder

assembly, and below the idler-gear contact, the filament is in compression because it is being

pushed from the feeder assembly to the melt-chamber [251]. Ideally, a no-slip boundary condition

is assumed between the filament surface and the idler / gear tooth. Slips may occur due to the

non-optimal design of idler / gear tooth, insufficient torque applied by the motor or higher pressure

in the melt-chamber due to an inadequate rate of polymer melting [250].

The fed filament travels towards the melt-chamber through the guide-way with the heat-sink.

The heat-sink is required to ensure that the solid filament experiences a temperature well below

the glass-transition temperature (T_g) before entering the melt-chamber. Acting as an effective

piston, the solid filament inside the guide-way pushes the polymer melt towards the nozzle [250].

With the help of one or more cooling fans, it is ensured that the temperature drop across the heat-

sink is large enough so that filament remains solid before entering the meal-chamber.
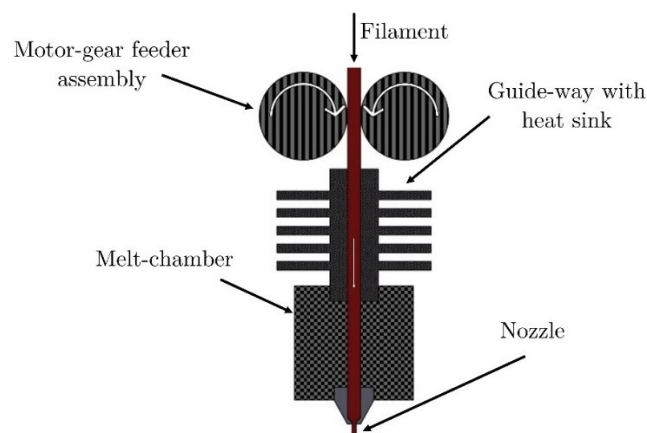
Figure 3. 2: Components of a typical FDM extruder. Copyright © 2016 by ASME, reprinted with permission [252].

The filament is melted in the melt-chamber, which houses a cartridge heater and a temperature sensor, usually a thermistor. The cartridge heater is the only element which supplies the heat required to melt the solid filament into a polymer melt. This heater and thermistor are coupled and programmed with a temperature controller, preferably a proportional–integral–derivative (PID) controller to maintain a constant desired temperature [25].

Finally, the molten polymer is extruded through the nozzle with a common range of orifice diameter ranging from 0.2 to 0.5 mm [253]. The extruded polymer experiences a sudden change in the surrounding temperature from the melt temperature ($> 200^{\circ}$C) to the ambient temperature ($\sim 20^{\circ}$C) and a significant change in shear stress. These abrupt changes cause the extrudates to have a slightly thicker radial dimension than the nozzle orifice when freely extruded. Additionally, due to the viscoelastic properties of the polymer melt, the extruded material tends to return to its original cross-section [254]. Therefore, the extrudates have a larger diameter than the nozzle opening. This phenomenon is known as die-swell and is very common in extrusion processes [255,256]. Moreover, while printing, heat is transferred from the newly deposited layer to the prior layers resulting in a vertical thermal gradient, which may lead to warping and distortion of the printed structure [257].

3.2.1   Components of the Bi-extruder

Figure 3.4 shows an exploded view of the 3D model of our bi-extruder designed to use 3-mm diameter filament. It has two guide-ways for two thermoplastic filaments, a melt-chamber split into two halves, and a nozzle. The design of the heat-sink of the guide-ways was optimized using

the concept of the design of experiments (DOE) to maximize the temperature drop. More details about the DOE analysis can be found in our previous work [252]. To ensure enough heat loss from the heat-sink, the guide-ways are made of 316-stainless steel with a thermal conductivity of only 12 ~ 45 W/m-K [258]. The split melt-chamber is made of Aluminum (221 ~ 247 W/m-K) [258] to ensure a uniform melting temperature throughout the melt-chamber. The uniqueness of this bi-extruder allows easy access to its interior channel so that insertion of a static mixer to manipulate the flow is possible and direct comparisons to co-extrusion can be made. To make the nozzle thermally conductive and ensure scratch-free, safe operation of the tiny tip, Brass - C36000 (~ 116 W/m-K) [258] was chosen as the nozzle material.

In the assembly, two guide-ways are threaded into the melt-chamber. Two partially threaded M3 screws with a shoulder are used to precisely align both halves of the melt-chamber and the nozzle is threaded from the bottom side of the melt-chamber. Figure 3.5 shows an image of the disassembled parts of the bi-extruder fabricated in our facilities. The inner diameters of the guide-ways and two upper sections of the Y- shaped interior channel are both 3.1 mm, which is slightly larger than the filament diameter (3mm) to reduce unnecessary mechanical friction between solid filaments and the metal walls. The diameter of the lower section of the Y-channel is 4 mm to allow for the insertion of a static intermixer with an outer diameter of 4 mm.

The extruder uses two 24V-40W cartridge heaters embedded into the melt-chamber and one 100 kΩ NTC thermistor. We have manufactured different brass nozzles with 1 mm, 0.5 mm and 0.35 mm tip diameters and 3-mm inner diameter at the other end.
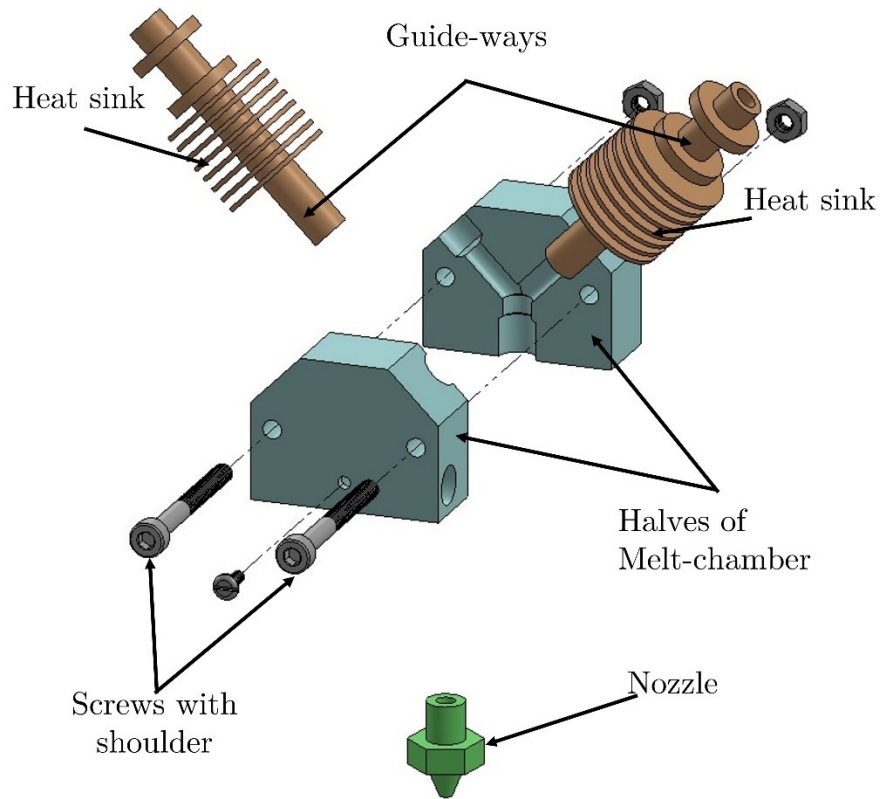
Figure 3. 3: An exploded view of the 3D model of the bi-extruder
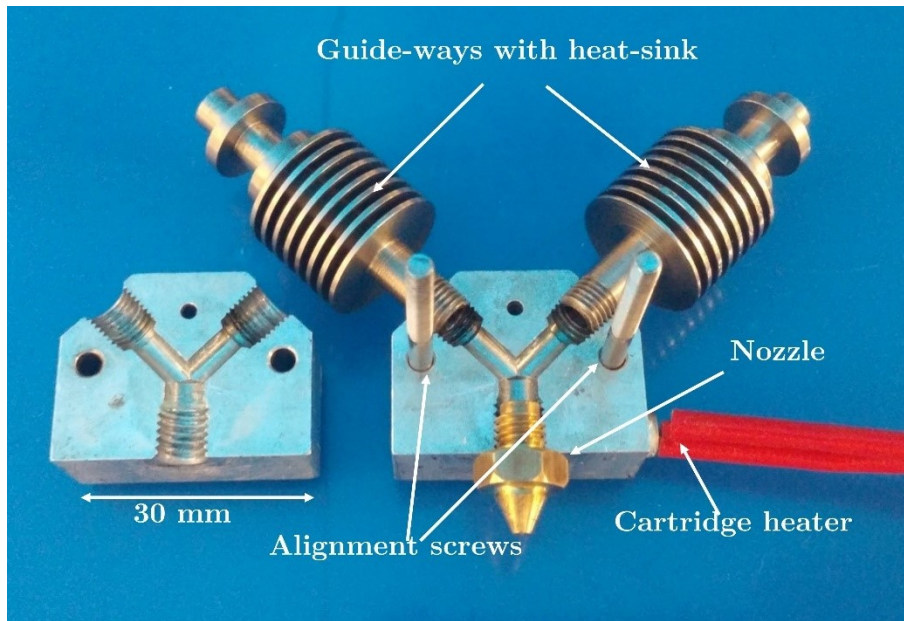
Figure 3. 4: Assembly of the bi-extruder manufactured

2.2 Analytical model of polymer flow in the bi-extruder

3.2.1.1 Geometry of the liquefier

The liquefier geometry has a significant impact on the polymer melt behavior in the melt-chamber. As shown in Figure 3.6, the internal liquefier of the bi-extruder can be divided into five major zones: two inlet sections in the melt-chamber, the intermediate section between where both flows meet and the nozzle, the internal channel in the nozzle, and the smallest section at nozzle tip having the exit diameter. Any gap between filament diameter and internal diameter of the channel would lead to thermal resistance to heat transfer through the channel walls. This effect is eliminated as the material melts and advances towards the nozzle. The lengths of these sections and corresponding diameters are also given in Figure 3.6 assuming that 0.5 mm nozzle is being used.

3.2.1.2 Melt properties

The viscosity (η) of the viscoelastic polymer melt is both temperature and shear rate dependent. Hence, it is usually expressed as the product of a temperature dependent and a shear-rate dependent term [259]. The shear-rate dependent term is commonly assumed to follow a power-law model with fluidity ϕ and flow exponent m, whereas the Arrhenius model is used for

temperature dependent term [251,260]. The power-law fit parameters are evaluated at some

reference temperature, T_0. Hence, viscosity is defined as:

$$\eta = e^{\left[\alpha\left(\frac{1}{T} - \frac{1}{T_0}\right)\right]} \cdot K(\dot{\gamma})^{n-1} \tag{3.1}$$

Where α is activation energy, $\dot{\gamma}$ is shear-rate, T is the absolute temperature of the polymer melt,

K is consistency index ($\phi^{-\frac{1}{m}}$) and n is the power-law index ($\frac{1}{m}$) [259].

$L_1 = 10.6\ mm$
$L_2 = 10.6\ mm$
$L_3 = 3.6\ mm$
$L_4 = 11.7\ mm$
$L_5 = 1.3\ mm$

$d_1 = 3.1\ mm$
$d_2 = 3.1\ mm$
$d_3 = 4\ mm$
$d_4 = 3\ mm$
$d_5 = 0.5\ mm$

$\dot{\gamma}_1 = 2.58\ s^{-1}$
$\dot{\gamma}_2 = 2.58\ s^{-1}$
$\dot{\gamma}_3 = 2.20\ s^{-1}$
$\dot{\gamma}_4 = 5.16\ s^{-1}$
$\dot{\gamma}_5 = 1152\ s^{-1}$

$\eta_1 = 12600\ pa \cdot s$
$\eta_2 = 12600\ pa \cdot s$
$\eta_3 = 13200\ pa \cdot s$
$\eta_4 = 7950\ pa \cdot s$
$\eta_5 = 300\ pa \cdot s\ (curve\ fitted)$
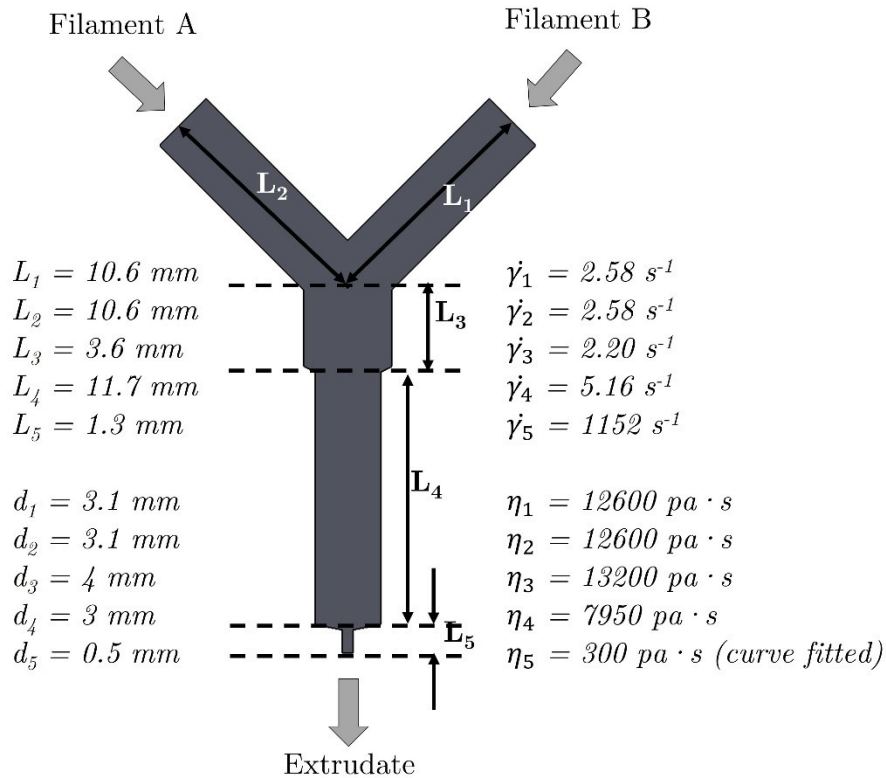
Figure 3. 5: Internal liquefier divided into five different zones. Approximate geometry and other melt parameters are calculated in the next section.

Due to the mathematical complexity, the temperature throughout the liquefier of the small scale

FDM extruders is often assumed to be uniform [260]. This assumption is supported by thermal

simulation in the next section. Hence, it is much simpler to directly use shear viscosity data (given

by the suppliers or measured by the users) over a range of shear rates in the analysis of melt

rheology of 3D printing materials. Due to the unavailability of the viscosity data from the supplier

of the filaments used in this work, shear viscosity data with Cross- Williams-Landel-Ferry (WLF)

model fitted curves for ABS has been adopted from literature [261] with the expectation that the

viscosity data for ABS used in this work would also be in a similar range. The apparent shear-

rate $\left(\dot{\gamma}_{app}\right)$ at the channel wall in each flow section of Figure 3.6 must be determined using the

following Equation (3.2):
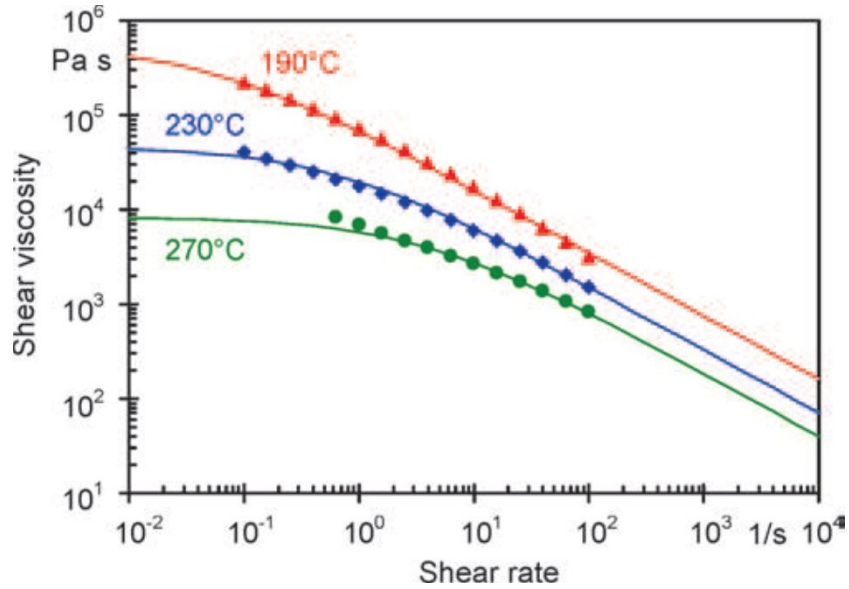
Figure 3. 6: Shear viscosity data with Cross-WLF fitted curve for ABS resin sourced from The Dow Chemical Company (adapted from [261] with permission, ©Carl Hanser Verlag GmbH & Co.KG, Muenchen).

$$\dot{\gamma}_{app} = \frac{4\,Q}{\pi\left(d/2\right)^3} \tag{3.2}$$

Where Q is the volumetric flow rate of the material in each section with diameter d. Once the

apparent shear rate is calculated, the apparent viscosity in each section is determined from Figure

3.7 at a certain temperature. In this case, viscosities of ABS melt at 230°C temperature in each section of the bi-extruder were estimated and given in Figure 3.6.

3.2.1.3 Estimation of heat flux

In extrusion, there are three consecutive rates involved: feed rate, melting rate, and extruding rate. If any or both of feed rate and melting rate is / are dominated by the extruding rate, the extrusion is said to be in a starved situation resulting in defects related to under-extrusion [262]. On the other hand, if feed rate dominates excessively then, it is overridden extrusion [262]. To avoid overridden extrusion, the maximum allowable feed speed of an extruder head should be determined which primarily depends on the wattage of the heater element and the available liquefier surface through which the heat is transferred to the materials. A simplified model was proposed by [251] which can be extended for a more accurate estimation of heat flux (q). This model would be useful to study the maximum allowable feed speed of the bi-extruder in future designs.

Heat flux, $q = \dot{m} \left[c_{p_1} \left(T_g - T_r \right) + c_{p_2} \left(T_m - T_g \right) + L_m + c_{p_3} \left(T_p - T_m \right) \right]$ (3.3)

And liquefier surface, $S = 2\pi(D)L$ (3.4)

Where $\dot{m}$ is the combined mass flow rate at both inlets ($2\rho vA$), ρ is the polymer density, v is the total feed speed of both inlets, A is the cross-sectional area of the filaments, T_r is room temperature, T_g is the glass transition temperature of the polymer, T_m is the melting temperature of the polymer, T_p is the print temperature, L_m is the latent heat of melting, the dimensions of the liquefier

channels are diameter, D and length, L, and c_{p_1}, c_{p_2}, and c_{p_3} are the heat capacities of the polymer under glass transition, above glass transition, and after melting temperature, respectively.

3.2.1.4   Pressure drop along the flow channels

The total pressure drop in the melt-chamber is the sum of the pressure drops in section 1 or 2 and in the other three sections of Figure 3.6. The pressure drops in each section $(\Delta P_1$ to $\Delta P_5)$ can be estimated using the model developed by [259] from a momentum balance on the liquefier. Key assumptions of this model include that the steady-state laminar flow of incompressible polymer melt is fully developed, and a no-slip boundary condition applies at the channel walls. Hence, the total pressure is, as follows:

$$\Delta P_{Total} =$$

$$2\left(\frac{v}{\phi}\right)^{\left(\frac{1}{m}\right)}\left[L_1\left\{\frac{m+3}{\left(\frac{d_1}{2}\right)^{m+1}}\right\}^{\left(\frac{1}{m}\right)} + L_3\left\{\frac{m+3}{\left(\frac{d_3}{2}\right)^{m+1}}\right\}^{\left(\frac{1}{m}\right)} + L_4\left\{\frac{m+3}{\left(\frac{d_4}{2}\right)^{m+1}}\right\}^{\left(\frac{1}{m}\right)} + L_5\left\{\frac{\left(\frac{d_4}{2}\right)^2(m+3)}{\left(\frac{d_5}{2}\right)^{m+3}}\right\}^{\left(\frac{1}{m}\right)}\right]e^{\left[\alpha\left(\frac{1}{T}-\frac{1}{T_\alpha}\right)\right]} \quad (3.5)$$

3.2.2   Thermal Analysis of the Bi-extruder

Two 24 V cooling fans with ratings of 7 cfm are used at the heat-sink of two guide-ways to induce forced convection. The convective film coefficient (h) of 24.92 W/m²-°C was estimated for this case using the following Hilpert correlation [263].

$$Nu = 0.683\, Re^{0.466}\, Pr^{1/3} \quad\quad\quad\quad\quad\quad\quad\quad\quad\quad\quad\quad\quad\quad\quad (3.6)$$

Where, Nu, Re, and Pr are the Nusselt number, Reynolds number, and Prandtl number, respectively, of the air flow through the heat-sink.

Figure 3.8 shows the temperature distribution throughout the bi-extruder from the thermal simulation performed in ANSYS Workbench. In this simulation, the heater block was set at 220°C and forced convection with an estimated convective coefficient (h) was assumed at the heat-sink. On the other surfaces of the extruder, free convection with 25°C room temperature was assumed. From the analysis, the temperatures of the upper ends of the guide-ways are found to be less than 40°C, which validates the design feasibility in accordance with the experimental use.
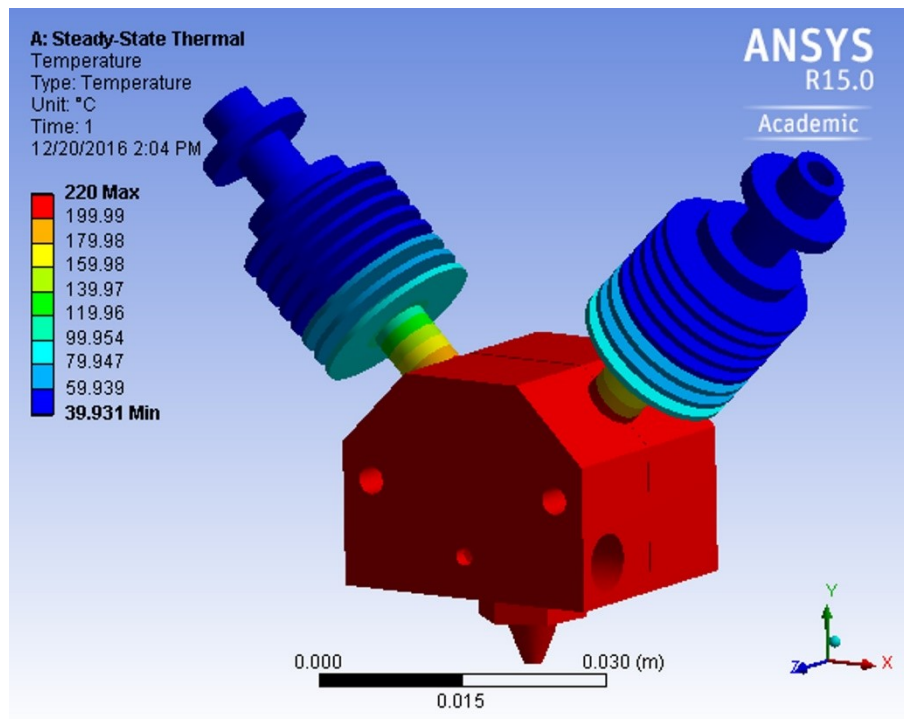
Figure 3. 7: The temperature distribution of the bi-extruder from the thermal analysis using ANSYS Workbench

3.2.3   Installation of the Bi-extruder in an FDM System

First, housing was built using ¼" thick clear acrylic (sourced from McMaster-Carr) cut by a CO_2 laser cutter. This acrylic housing firmly holds the bi-extruder, the direct-mount feeding motors,

the guideways, and the cooling fans. These components, along with the housing, comprise the extruder head. Then this extruder head was installed on an inexpensive FDM style 3D printer (Model: M201) purchased from Geeetech, China as a Do-It-Yourself (DIY) kit.
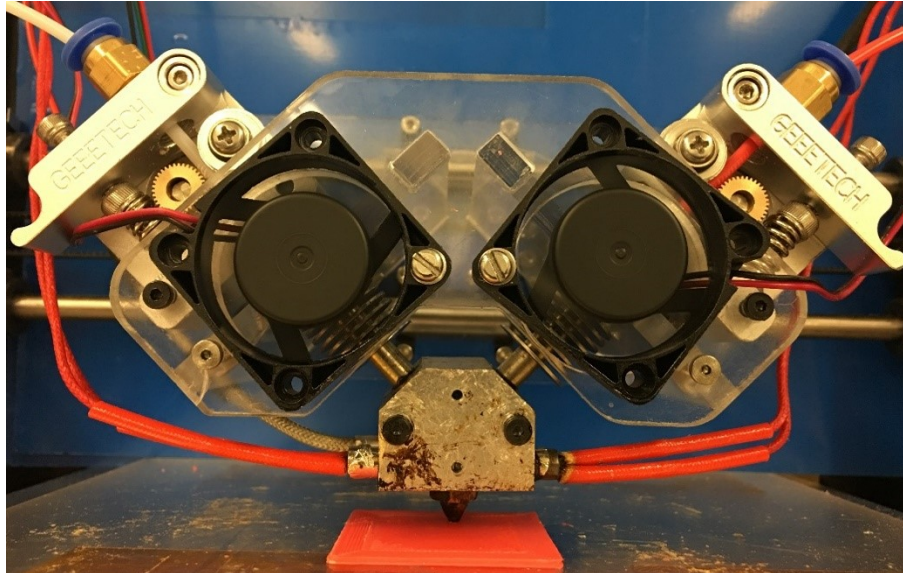
Figure 3. 8: The front view of the assembled bi-extruder print head

This 3D printer is driven by a GTM32 control system, which is based on the STM32 processor and paired with an ARM Cortex-M3. The driver comes with custom firmware uploaded, which can run two feeder motors at different speeds to achieve any desired composition of the fed filaments. Two bipolar stepper motors having 26 N-m holding torques with 1.8° step angles and two DC brushless cooling fans (24 V, 0.1 A) are used in this system. Figure 3.9 shows the assembled extruder head installed on the printer.

3.2.4 Fabrication of Intermixer

Without proper compatibilization, two immiscible polymers delaminate at the interfacial layer [236,264]. Since the reported compatibilization techniques [232-235,265] require some additional steps, they may not always be desired in FDM technology. Rather, printing using extrudates with sufficient mechanical keying of the composite polymers has the potential to reduce delamination problems. It is important to note here that complete blending is not necessary to overcome the delamination problem because if the materials are sufficiently mechanically interlocked bonding requirements will be fulfilled.
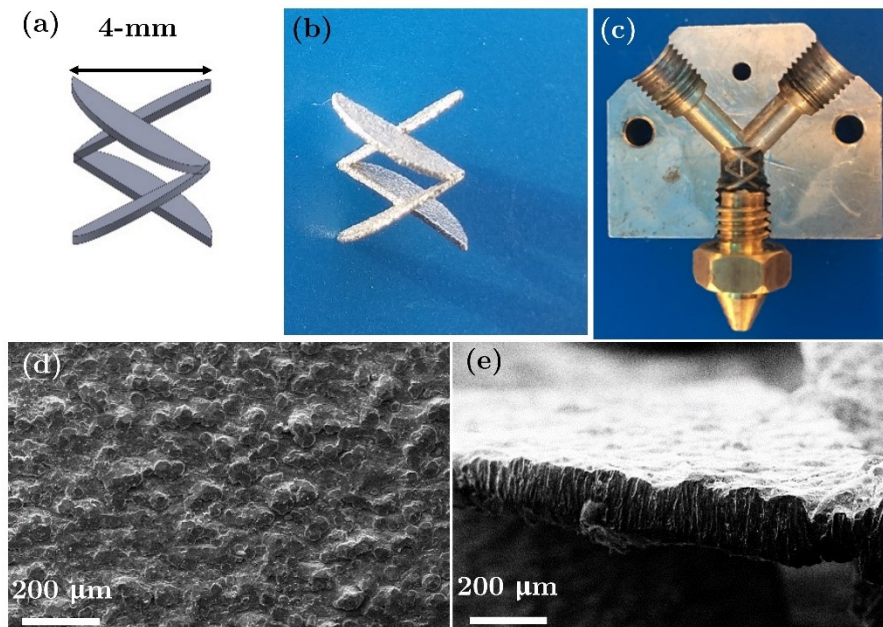
Figure 3. 9: (a) The 3D model of the passive intermixer, (b) an image of the same intermixer printed by DMLS, (c) an image showing the intermixer inserted into the bi-extruder channel, SEM images of (d) the surface and (e) the side-wall of the intermixer.

The mixing mechanisms can be divided into two groups: active mixing and passive mixing. In case of active mixing, an additional mixing element is usually energized from an external source

77

to perform the mixing [266]. In contrast, passive mixing is done by the chaotic advection of the flow itself [267]. To avoid the requirement of an additional energy source, a passive intermixer was preferred here to introduce mechanical keying of two polymers. Figure 3.10 shows the design of the passive intermixer inspired by the static mixer commercialized by Koflo Corporation, Illinois, USA. The intermixer used here has four 0.2 mm thick blades inclined at 30° to a horizontal. The individual blades have an elliptical shape to ensure that inclined blades fit in the circular channel. The intermixers were designed in SolidWorks and then printed using direct metal laser sintering (DMLS) by Proto Labs, Minnesota with 20 µm resolution. The print material was 316-stainless steel so that the intermixer can withstand a higher temperature (> 200ºC) inside the melt-chamber without noticeable changes in mechanical properties. Scanning electron microscope (SEM) images of the surface and the side-wall of the intermixer are also shown in Figure 3.10, to confirm its constituent structure. No porosity was observed over the surface.

3.3   RESULTS AND DISCUSSIONS

After installing the bi-extruder, several simple objects have been printed to examine the extruder's performance. In this work, filaments of ABS, PLA, HIPS sourced from filaments.ca with 3-mm diameter were used. While printing using the bi-extruder, two filaments come in contact in the Y-shaped channel when they are already in the molten state. Then, if no intermixer is present, both molten filaments advance and are extruded through the nozzle orifice in a side-by-side manner. Alternatively, if there is an intermixer inserted, both streams of molten polymer split, combine, re-split, and re-combine due to the orientation of intermixer's blade when passing

through it. Therefore, due to this chaotic advection-type passive mixing, extrudates with mechanical keying of both materials is achieved.

3.3.1   Maximum Feed Speed

In overridden extrusion, the filaments will not be fed to the melt-chamber causing a slip in the motor-gear feeding assembly. Usually, this leads to wear and tear of the filament at the location where the roller teeth touch the filament. Therefore, it is very important to know the maximum feed speed of an extruder for smooth extrusion without any kind of defects. It was found that the maximum allowable combined feed speed of the filaments for our system is 120 mm/min, which corresponds to feeding a 60-mm length of 3-mm diameter filament in one minute at each of the guide-ways. This feed rate is equivalent to a print speed of approximately 72 mm/s and 146 mm/s when using 0.5 mm and 0.35 mm nozzles respectively.
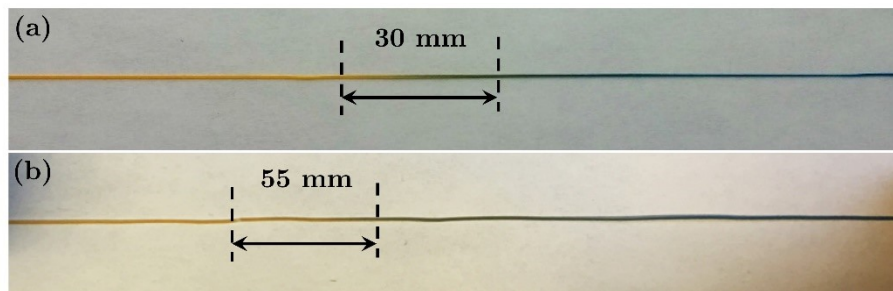
Figure 3. 10: The step response test of the bi-extruder (a) with intermixer inserted and (b) without an intermixer.

3.3.2   Response Test of the Bi-extruder

The Y-shaped internal channel has a volume of 10.8 mm^3, as estimated from the 3D model. When the extruder is instructed to change the composition of the extrudates, the material from this

volume must be extruded first, then the material with the new composition can be realized. Therefore, this volume acts as a lag-volume. The smaller the lag-volume, the quicker the response of the extruder to a change in the feed composition. Inserting an intermixer not only results in interlocked extrudates, it also reduces the lag-volume, speeding the response of the extruder. Figure 3.11 shows that when using a 0.5 mm nozzle, the bi-extruder requires around 30 mm long extrudates to change the composition with an intermixer inserted. Without the intermixer, this length is nearly doubled (~ 55 mm). In this test, the bi-extruder was instructed to change the composition as a step input from 100% orange to 100% blue PLA.
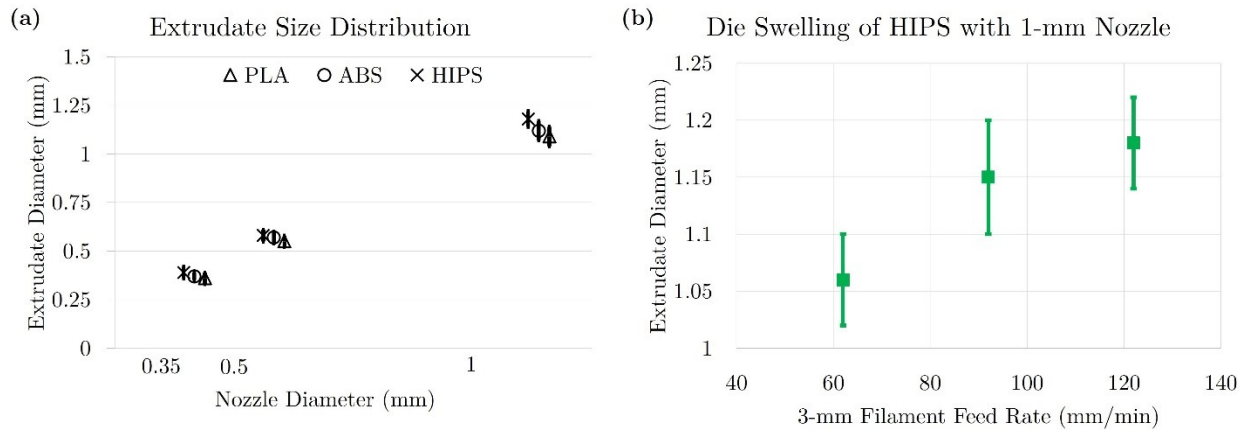
Figure 3. 11: (a) A graphical representation of the extrudate diameter from different nozzles and (b) die-swelling of HIPS when extruded with a 1-mm nozzle.

3.3.3   Die-swell

Die-swell is a common phenomenon in polymer extrusion processes which should be considered while adjusting the layer width set by the slicing program used for 3D printing. While programming the trajectory of the print head to print an object by FDM technique, considering the effect of die-swell will result in an optimal amount of overlap between adjacent deposited

materials. To examine the die-swell of ABS, PLA, and HIPS with this bi-extruder, the same filament was fed from both guide-ways, and it was allowed to deposit a molten stream of polymer to get long extrudates of a single material. Then the diameter of each extrudate was measured at different locations and the statistics of the extrudate diameter vs. nozzle diameter were calculated as given in Figure 3.12(a). It was found that regardless of nozzle diameter, HIPS extrudates show a slightly higher swelling ratio compared to ABS and PLA. The effect of extrusion speed or feed speed on die-swell has also been examined for different nozzle diameters. Die-swell with 0.5 mm and 0.35 mm nozzles do not appear to be affected by feed speed to a statistically significant extent however with 1 mm nozzle the die-swelling ratio is slightly higher at higher feed speed. This phenomenon is shown in Figure 3.12(b) for HIPS.

(a)	(b)	(c)	(d)	(e)
100% Red PLA	77% Red PLA & 23% Green PLA	49% Red PLA & 51% Green PLA	27% Red PLA & 73% Green PLA	100% Green PLA
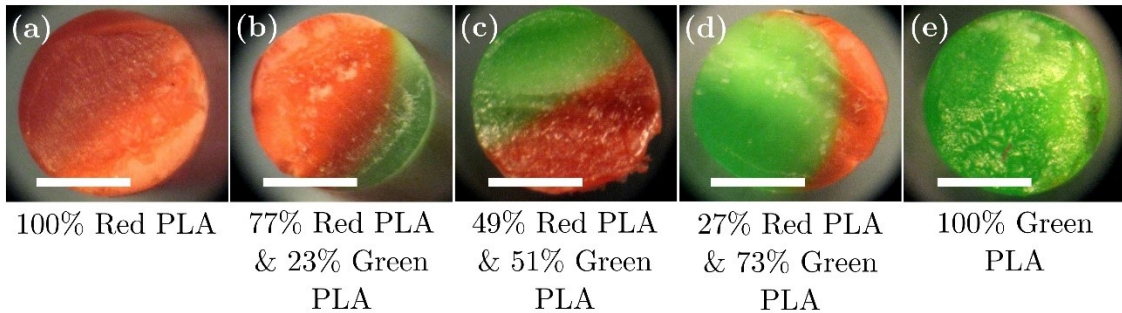
Figure 3. 12: Microscope images of cross-sections of extrudates with different desired compositions with the ratios of Red: Green = (a) 1:0, (b) 3:1, (c) 1:1, (d) 1:3 and (e) 0:1; The estimated compositions are also given for each image. The scale bars are 0.25 mm long.

3.3.4 Regulating Extrudate Composition

The composition of the extrudates was controlled by regulating the relative feed speeds of the filaments within the limit of maximum allowable feed speed (120 mm/min). For instance, to

achieve a composition of 25 % filament 1 and 75 % filament 2, a feed speed of 30 mm/min was applied on filament 1 side while filament 2 was fed at 90 mm/min. If only one material is desired, then that particular filament would be fed at 120 mm/min speed and other filament will not be fed at all. Figure 3.13 shows microscope images of cross-sections of the extrudates with different compositions controlled by the relative feed speeds of the filaments while using a 0.5 mm nozzle. These extrudates were extruded without an intermixer inserted, so they are just side-by-side co-extrudates of red and green PLA. Instead of printing onto the bed, these extrudates were extruded in air approximately 15 cm above the print bed to allow cooling before reaching the print bed. Once the long extrudates were solidified, they were cut gently in the transverse direction such that the cross-section had little or no scratches from cutting. A 6-mm thick acrylic holder with through holes of different sizes cut by a CO_2 laser cutter was used to position the cross-sections of the extrudates facing up, to examine under a microscope. After post-processing of those images using National Instruments Vision Builder for Automated Inspection, the compositions were estimated as shown in Figure 3.13.

3.3.5   Use of an Intermixer for Mechanical Interlocking

With the help of an intermixer inserted into the bi-extruder, mechanically interlocked extrudates of two dissimilar immiscible polymers have been achieved. This circumvents the delamination problems common in multi-material FDM. Figure 3.14 shows some microscope images of cross-sections spaced approximately 5-mm along the length of a single extrudate. It is obvious from the

82

images that the mixing does not have any specific pattern, confirming the randomness of the mixing. The analysis was performed using all 1 mm, 0.5 mm, and 0.35 mm nozzles.
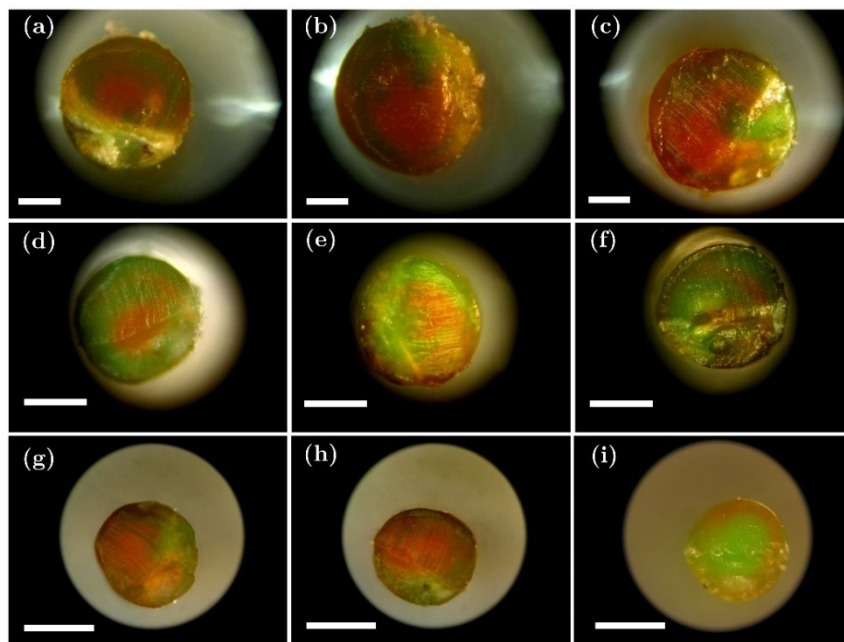
Figure 3. 13: Microscope images of cross-sections of mechanically interlocked extrudates of green and red PLA. Extruded from (a), (b), (c) a 1 mm nozzle, (d), (e), (f) a 0.5 mm nozzle, and (g), (h), (i) a 0.35 mm nozzle. Scale bars are 0.25 mm long.
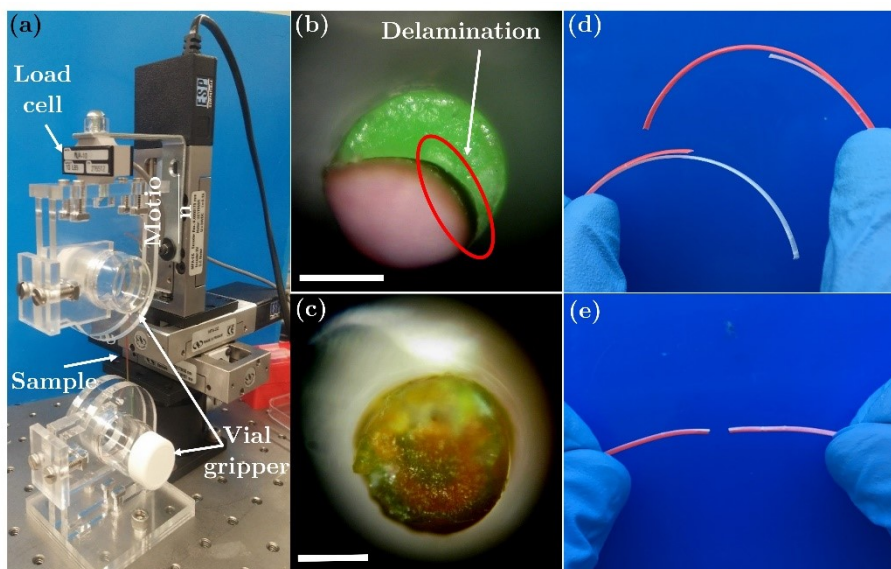
Figure 3. 14: (a) Tensile test setup for extrudates; microscope images of the cross-sections of fractured extrudates of green PLA and red HIPS (50%-50%) by (b) delamination and (c) full

filament fracture. Qualitative test images of (d) side-by-side co-extrudate and (e) mechanically interlocked extrudate of red HIPS and white ABS (1:1) deposited from a 1-mm nozzle. Scale bars are 0.25 mm long.

3.3.6   Nature of Failure in the Tensile Test

A tensile test setup was designed as shown in Figure 3.15(a). This setup consists of a load cell (Transducer Techniques, MLP-10), a National Instrument Motion Controller (Model No. ESP301), a data acquisition (DAQ) hub (NI USB-6289) and two custom acrylic grippers using vials. The extrudate sample was wrapped around the smooth vial, and the acrylic gripper was used to securely hold the extrudate in position without affecting the extrudate surface. Then the load cell with the upper gripper was moved up slowly (50 µm/s) using a Windows Presentation Foundation (WPF) application written in C# by Samuel Lehmann, which is available as an open source solution. This tensile test was performed for both side-by-side co-extrudates and mechanically interlocked extrudates to observe the nature of the failure. Figures 3.15(b) and (c) show microscope images of fractured cross-sections of the side-by-side co-extrudate with a diameter of 0.56 ± 0.03 mm and mechanically interlocked extrudate with a diameter of 0.54 ± 0.04 mm, respectively. Both samples had a 50% - 50% composition of green PLA and red HIPS. Due to the uneven cross-section of the fractured extrudates, the entire cross-section could not be focused, which can be seen in Figure 3.15(b) where the red part is out of focus however the green part is focused. Figures 3.15(d) and (e) show similar qualitative experiments using extrudates of red HIPS and white ABS with 1:1 composition deposited using a 1-mm nozzle. To better demonstrate the delamination, thicker extrudates were used in this test. Delamination of the side-

84

by-side co-extrudate is clearly shown in Figure 3.15(d) whereas extrudate with mechanical keying shows full filament fracture (Figure 3.15(e)).

After appropriate calibration of the load cell, the failure strengths of four extrudate samples were measured as shown in Figure 3.16. Each tensile test was repeated using five different samples. The failure strength of 1:1 HIPS-ABS extrudate lies between the failure strengths of pure HIPS and ABS extrudates. ABS extrudate exhibited the highest tensile strength of 27.1 MPa before failure, which is also in good agreement with the literature [268]. It was also found that the blended 1:1 HIPS-ABS extrudate failed at a tensile stress of 25.4 ± 0.5 MPa, whereas side-by-side co-extrudate of the same material with the same composition showed failure strength of 24.2 ± 1.2 MPa. The overlap of the error values of intermixed and side-by-side extrudates indicates that the intermixing does not have any adverse effect on the extrudate tensile strength.
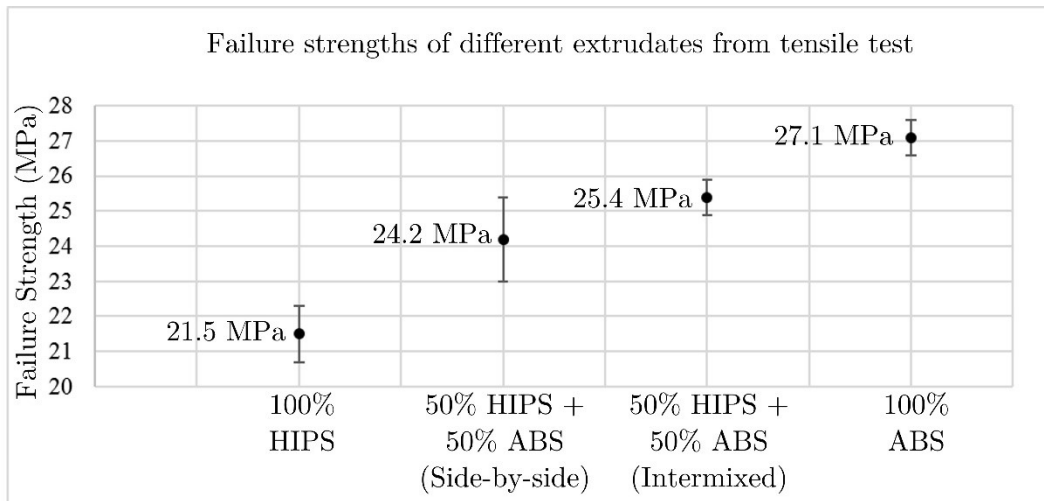
Figure 3. 15: The failure strengths of 100% HIPS extrudate with a diameter of 1.02 ± 0.02 mm, 1:1 HIPS-ABS extrudate (side-by-side) with a diameter of $1.03 \pm .04$ mm, 1:1 HIPS-ABS extrudate (intermixed) with a diameter of $1.04 \pm .03$ mm and 100% ABS extrudates from the tensile tests.

3.3.7 Relative Inter-layer Bond Strength

The tensile test set-up used in Figure 3.15 was used to estimate relative inter-layer bond strength of sheets printed by side-by-side and intermixed co-extrusion. The acrylic-based gripper system was designed to firmly hold the samples without affecting their inter-layer bonding. The acrylic grippers have a patterned surface to increase friction between the sample and the gripper for better clamping. First, planar samples employing ASTM D1708 test standard were printed using a 1:1 composition of red ABS and green HIPS. The average thickness of the samples of only one layer thickness is approximately 0.32 mm when using 0.35 mm nozzle. While printing the samples, perimeter features were intentionally avoided, and a linear fill pattern was chosen to reduce the effect of longitudinal borderlines. The test set-up and sample details are shown in Figure 3.17. The test aimed to compare the relative inter-layer bond strengths of beads printed by side-by-side and intermixed co-extrusion. Once the failure force was measured, using the cross-sectional area of the samples (~ 0.32 mm $\times$ 5 mm), it was converted to the bond strength in MPa. By this metric, the bond strength of three side-by-side co-extruded samples was measured as 15.7 MPa, 16.8 MPa, and 15.4 MPa. The bond strengths of intermixed co-extruded samples were found to be 21.3 MPa, 21.9 MPa, and 22.2 MPa. Figure 3.17(d) shows the comparison between the bond strengths of both types of samples. Figure 3.17(e) and 16(f) show microscope images of both cross-sections of an intermixed sample where it failed during the tensile test, and Figure 3.17(g) and 3.17(h) show the same for side-by-side samples. In the case of the intermixed samples, particularly from Figure 3.17(f), the red ABS material was interlocked within green HIPS material which resisted delamination from the material-based phase separated region. In contrast, side-by-side

co-extruded samples failed by complete delamination at lower tensile force at the interface of the two materials. Figure 3.17(i) and 3.17(j) illustrate the microscope images of surfaces printed by side-by-side and intermixed co-extrusion, respectively. The bimorph structure is clearly visible in side-by-side co-extruded surfaces in Figure 3.17(i), whereas in Figure 3.17(j) there is no distinct edge of red Abs and green HIPS.
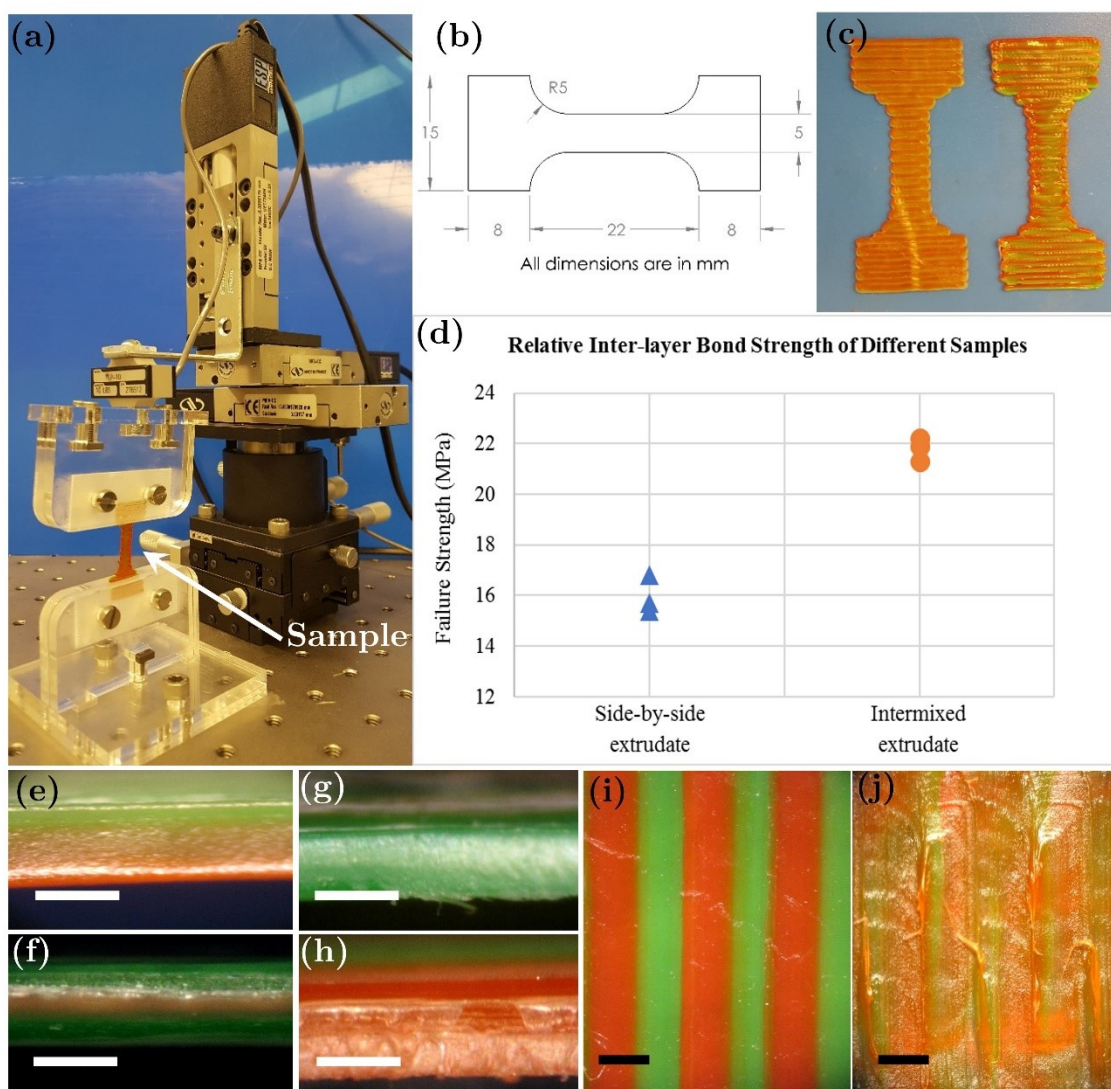
Figure 3. 16: (a) Test set-up with the modified gripping system to measure relative inter-layer bond strength of different samples. (b) dimensions of the samples according to ASTM D1708 test standard, (c) intermixed (left) and side-by-side (right) co-extruded samples with only one layer.

(d) comparison between the failure bond strengths of side-by-side and intermixed samples. The cross-sections of (e) & (f) intermixed and (g) & (h) side-by-side samples where they failed. The printed surfaces from (i) side-by-side and (j) intermixed co-extrusion. The scale bars are 0.3 mm long.

3.3.8   Objects Printed using Bi-extruder

This section displays a number of simple objects printed with the bi-extruder. Some of these parts were printed using two different polymers, with or without the intermixer. Figure 3.18 shows six cylinders made of either a single polymer or a pair of PLA, ABS, or HIPS with a 1:1 composition, printed without an intermixer. During printing, as the print head moves from left to right on the print bed, the extruded material from the left filament stays on top of the material from the right filament and vice versa. Therefore, although the entire object has the same composition; the front side of the printed object seems to have one material dominant while the back side seems to have other material dominant. This phenomenon can be easily observed in Figure 3.18(f), where, due to the orientation of the printed object, some parts look mostly red while others look mostly green. However the entire object has the same 1:1 composition of both red and green materials.
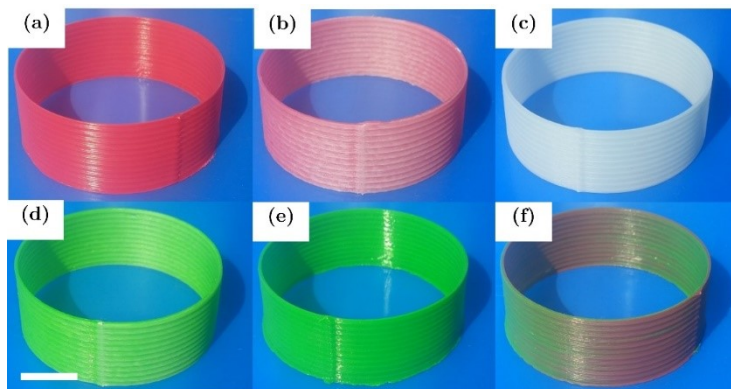
Figure 3. 17: Hollow cylinders (OD: 40mm, height: 15 mm) with wall thicknesses of only one layer printed using the bi-extruder made of (a) 100% red HIPS, (b) 50%-50% of red HIPS and

white ABS, (c) 100% white ABS, (d) 50%-50% of white ABS and green PLA, (e) 100% green PLA and (f) 50%-50% of green PLA and red HIPS. Scale bar is 10 mm long. Copyright © 2016 by ASME, reprinted with permission [252].

Figure 3.19 shows some square objects printed with an intermixer inserted except Figure 3.19(d), which was printed with side-by-side co-extrudates. Although both boxes in Figure 3.19(c) and 3.19(d) have the same 1:1 composition, the box printed with intermixed extrudate has a uniform color distribution on all four sides whereas the box printed with side-by-side extrusion has walls with one color more prominent on a certain side. The object in Figure 3.19 (g) was printed to show the transition from one material to another within a specified height.
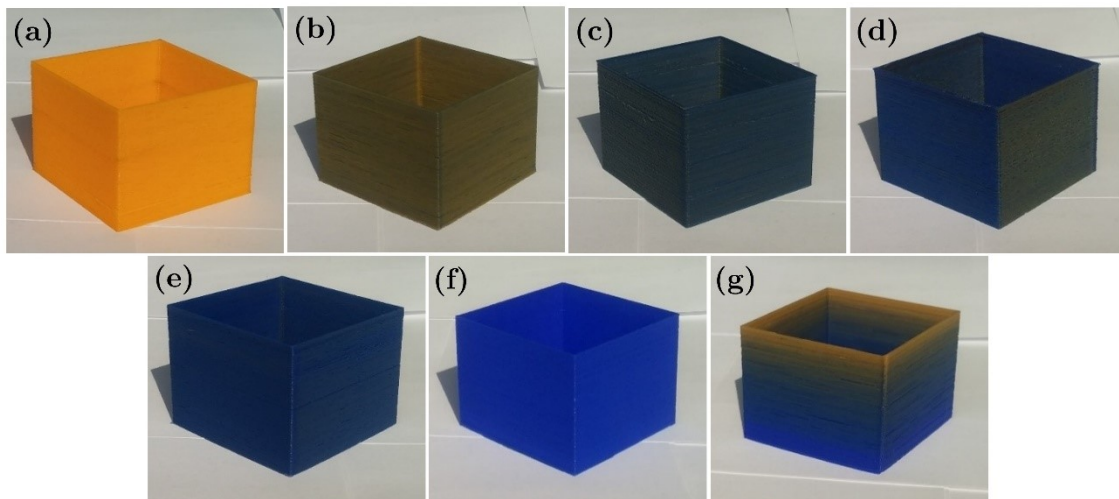
Figure 3. 18: Square hollow boxes (60 mm × 60 mm × 45 mm, wall thickness, one layer) printed using the bi-extruder with different compositions of orange and blue PLA. The compositions are (a) 100 % orange PLA, (b) 75 % orange and 25 % blue PLA, (c) 50 % orange and 50 % blue (intermixed), (d) 50 % orange and 50 % blue (side-by-side), (e) 25 % orange and 75 % blue PLA, (f) 100 % blue and (g) object with transition from 100% blue at the bottom layer to 100% orange at top layer. All the objects were printed with an intermixer inserted, except (d) which was printed with side-by-side co-extrudates.

3.4 CONCLUSIONS

In summary, we have created the first-ever 3D printed objects to use blended extrudates of two immiscible polymers by using our custom bi-extruder. The unique advantage of this bi-extruder is its split structure which permits easy access to the internal channels and its modular design with the separate mixing chamber, inlet feed-guides, and nozzle, providing great flexibility for future modifications and optimization. With the insertion of an intermixer into the channel, side-by-side co-extrusion becomes intermixed co-extrusion resulting in a mechanically interlocked extrudate. Intermixed extrudates are found to have reduced delamination issues compared to side-by-side extrudates. Moreover, the bond strength of two adjacent filaments of intermixed polymers was higher than that of side-by-side polymers. Hence, it is expected that objects printed with mechanical keying of two polymers will have reduced delamination issues and improved mechanical bonding in the transition from one material to another in printing FGM devices. The reduced internal lag-volume also improves the overall response time of the bi-extruder when changing the extrudate composition. The bi-extruder was successfully used to print some simple structures to examine its initial performance. It can successfully extrude two polymers from a single nozzle with varying compositions, and these printed objects showed satisfactory intra- and inter-layer bonding. The composite sheets with mechanical keying showed a higher breaking force compared to that of the side-by-side co-extruded sheets of the same materials.

There are some important findings pertaining to the performance of our bi-extruder. Firstly, it was designed for 3 mm filament, which is not suitable for smaller nozzles. Using 3 mm filament

with nozzles smaller than 0.5 mm diameter increases pressure drop in the internal channel significantly, which may result in feeding issues like slip between the filament and the drive gear coupled with the motor. To allow smaller nozzles, our next version of the melt-chamber will be designed to use commercially available 1.75mm filaments. Future works will also include analyses of complex structures with inclined surfaces printed with the bi-extruder system and more quantitative tests on the effect of process parameters on inter-layer and intra-layer adhesion parameters.

It suggests that this bi-extruder system requires the viscosity ratio of both polymers to be within a range. It is important to note that, the co-continuous structure may not be achieved if the volume fraction of the binary system is outside of the favorable range specified for that particular viscosity ratio. Hence, when printing two dissimilar polymers, the extrudates with only certain compositions would have a co-continuous structure. Therefore, when transitioning from one material to another material some of the initial and final compositions will not have co-continuous structure, rather the intermediate compositions would be favorable to the co-continuous structure.

4. CHAPTER: SOFT IS NO LONGER HARD: A FILAMENT-FREE FDM TECHNIQUE COMPATIBLE WITH SOFT AND HARD THERMOPLASTICS‡

4.1   INTRODUCTION

Fused deposition modeling (FDM) is an additive manufacturing (AM) technique where a molten material is extruded through a nozzle to develop two-dimensional (2D) layers. Each layer is deposited onto the previously deposited layer, thus constructing the whole three-dimensional (3D) object [269]. Generally, in FDM, the feed material is provided as a previously formed filament from a roll, with full control over the feed rate by virtue of a motor-roller feeder assembly. Then, the filament is liquefied inside a melt-chamber and then extruded through a nozzle. The melt-chamber and the nozzle assembly are commonly known as the hot-end. The filament between the spool and roller assembly is in tension, whereas between the roller and melt-chamber the filament is in compression [217]. Three major factors control the operation of a motor-roller feeder assembly

---

‡ A version of this chapter is under review for publication as: Khondoker, Mohammad Abu Hasan and Sameoto, Dan; Soft is no longer hard: a filament-free FDM technique compatible with soft and hard thermoplastics. *Progress in Additive Manufacturing.* ID: PIAM-D-18-00034R3. Reproduced with permission from Springer.

— the maximum torque supplied by the feeder motor, the amount of force transferred from the motor shaft to the solid filament, and the column strength of the filament before entering the melt-chamber [222].

The main driving force is the torque (τ) supplied by the feeder stepper motor. Here, the solid filament acts as a piston to push the highly viscous polymer melt through the print nozzle. The required motor power (P_{motor}) can be estimated from Equation 4.1 [251,259,260]:

$$P_{motor} = \frac{1}{2} \Delta P \, A \, \omega_r \, R_r \tag{4.1}$$

Where ΔP is the pressure drop in the melt-chamber, A is the cross-sectional area of the filament, ω_r and R_r are the angular speed and radius of the toothed gear of the driving motor. The coefficient of friction (f) between counter-rotating wheels and the filament determines how much force can be transferred to the filament from the motor shaft. *Elkins et al.* showed that due to the larger coefficient of friction, use of a soft rubbery wheel resulted in higher force transferred to the filament when compared to a hard epoxy wheel [222]. While serving as a piston under compression, the filament must also have enough column strength (also known as axial rigidity) to avoid buckling between the motor-roller assembly and the melt-chamber. A higher viscosity of the polymer melt increases the force on the solid filament that is required to push the molten polymer through the nozzle. This force cannot be supplied by the solid filament if the column strength is insufficient. The column strength can be estimated from the critical buckling pressure ($P_{critical\ load}$) using Euler's buckling theory as follows [270,271]:

$$P_{critical\ load} = \frac{\pi^2 E d^2}{16\ L^2} \tag{4.2}$$

Where, E, d and L are the elastic modulus, diameter and length of the solid filament between the rollers and the melt-chamber. Hence, the solid filament must have high E or small L to overcome resistance within the hot end while not buckling or otherwise failing to feed. All of these requirements by the motor-roller feeder assembly limit how soft an input filament can be, and the majority of FDM printers are optimized for rigid filament materials like acrylonitrile butadiene styrene (ABS), polylactic acid (PLA), and high impact polystyrene (HIPS).

Specific applications such as soft robotics require 3D printing of soft elastomeric materials, which is challenging because the column strength of their filament is often lower than the limit imposed by the rollers. Researchers have printed thermoplastic elastomers with a hardness of approximately 70 Shore A by using a modified version of the feeder-roller assembly [222]. Commercially available semi-flexible FDM filaments, such as NINJAFLEX® [272], PolyFlex™ [273], and FlexSolid® [274] can be used in feeder-roller assembly, but are relatively stiff and may not be appropriate for certain low pressure or high deformation applications. If softer materials are to be used in FDM processing, alternatives to the filament feed system are required. There is at least one patented technique, some commercial solutions and published reports where a mini-extruder mounted on the print head was exploited to 3D print directly from pellets [275-282]. However, having a pellet extruder directly attached to a print head increases its size and weight, requiring stronger components, and limiting the use of this feeding system in multi-material FDM printing. The direct mount pellet extruder also has issues with clogging the print material in the screw [278] and difficulty in immediate ON/OFF control of the melt flow [279]. Hence, it is of great interest to design a custom feeder system for FDM printers which can function for any

thermoplastic materials, regardless of their hardness, and minimizes the extra loads placed on the linear stages and motors. Using such a feeder system, a multi-material FDM system would be able to directly print soft robots with different components made of materials with varying hardness, all in a single step.

By using a custom flexible heated hose, we demonstrate the newest 3D printing technology, fused pellets printing (FPP), a novel feeder system to print almost any thermoplastic material if it melts at a temperature below the maximum temperature rating of the thermistor/heater used in the system, i.e., 400 °C in this case. The following sections focus on the design and development of the heated hose feeder system and fine-tuning the process parameters to achieve quality prints.

4.2   EXPERIMENTAL SETUPS

An inexpensive FDM style 3D printer (Model: M201) was purchased from Geeetech, China. The original print head of this printer was a 2-in-1-out type hot end, which inputs two filaments to co-extrude them in a side-by-side manner or change the composition of the print in each new layer to be deposited. The original printer head was replaced by a custom tri-extruder system described in the following section. The pre-installed firmware of this printer also allows users to change the composition of the print at any time by regulating the relative feed rate of both polymers.

4.2.1   Materials

Soft thermoplastic elastomer pellets of Kraton G1657 (styrene ethylene butylene styrene (SEBS)) purchased from Kraton Corporation, USA were used as received. SEBS is a triblock copolymer composed of styrene end blocks and ethylene/butylene interior blocks. Kraton G1657 is optically

transparent, has a hardness of approximately 47 Shore A, and in its bulk form, it can stretch up to approximately 600% [223,283]. In addition to elastomeric pellets, rigid pellets of MM3520 shape memory polymer (SMP) purchased from SMP Technologies Inc., Japan were also successfully used in our system. This SMP has a hardness of 77 Shore D in its glassy state; however, by heating well above its glass transition temperature (35 °C), its hardness can be lowered to approximately 80 Shore A in its rubbery state.

4.2.2   Design of the Print Head

Direct printing from pellets comprises three major components: a pellet extruder, a flexible heated hose, and print head. The schematic diagram in Figure 4.1(a) shows all the major components of FPP technology. The actual system is presented in Figure 4.1(b), and the exploded 3D model of the print head is shown in Figure 4.1(c).

4.2.2.1   Pellet extruder

The original pellet extruder [284] was bought from Filastruder, USA as a Do-It-Yourself (DIY) kit. This extruder uses a single screw (15.5 mm in diameter and 18 cm in length) with hex shank coupled with a GF45 series 12 VDC gearmotor (max 8 rpm and 15.6 N-m torque). The voltage and current supplied to the gearmotor can be regulated using a closed loop PWM controller to control the speed and torque of the gear motor, respectively. It enables the user to adjust the extrusion speed which mainly depends on extrusion temperature. The extrusion temperature was controlled using a collar heater on the barrel, a K-type surface mount thermocouple, and a PID controller.
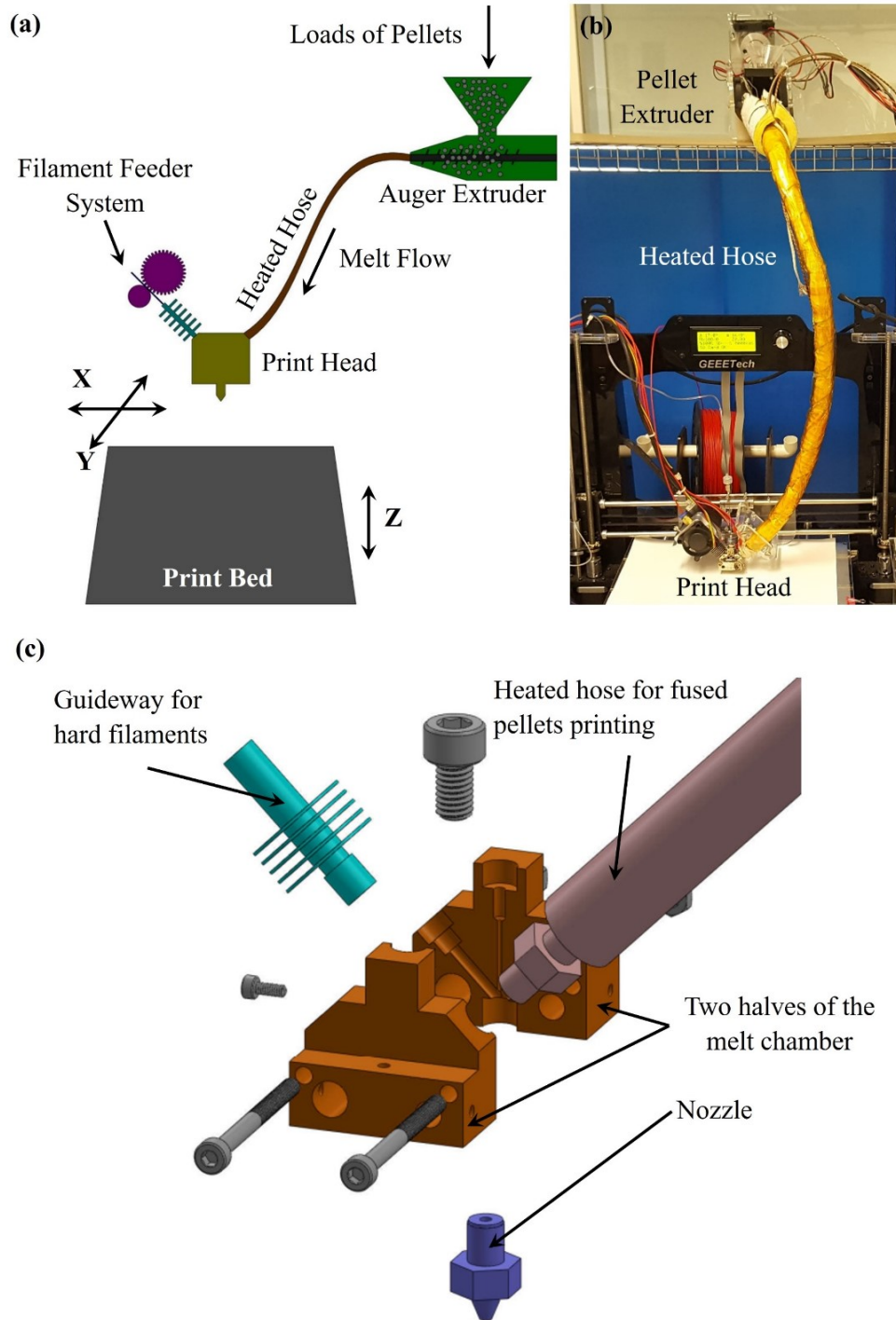
Figure 4. 1: The schematic diagram of the fused pellets printing technology showing all three major components (i.e.) pellet extruder, flexible heated hose, and the print head, (b) the actual fused pellets printing system and (c) the exploded 3D model of the tri-extruder print head.

4.2.2.2   Flexible heated hose

The 2-foot (0.61 m) long flexible, heated hose is the major component which connects the pellet extruder with the print head. A B-series 2-foot long PTFE hose with 1/8 in (3.18 mm) nominal internal diameter (part number: SS-BT 2 TA2 TA2-24) was purchased from Swagelok, Canada. This hose has a PTFE core with 304 stainless steel braided cover. The hose has a maximum limit of working pressure of 206 bar (2.06×10^7 Nm^{-2}) rated at 20°C and a maximum temperature of 230°C, according to the manufacturer's specification. This maximum temperature puts a limit on input material choice for this system but is sufficient for demonstrating the concepts. The hose has a 1/8 in (3.18 mm) Swagelok tube adapter on both ends whereas both the pellet extruder and print head have M6×1 mm female thread opening. To fulfill the assembly requirement, ¼ in NPT (6.35 mm) male tube fittings were purchased and swaged to M6×1 mm male fitting. To ensure the polymer melt remains in the molten state while being transported from the pellet extruder to the printing head, the hose must be kept above the melting temperature of the polymer at all time. For this purpose, the hose was first wrapped with a 4-foot (1.22 m) long, 120 VAC, 78 W flexible heat cable (part number: 4550T162) purchased from McMaster-Carr. Then a K-type surface mount Ni probe thermocouple (part number: 9251T93) from McMaster-Carr was attached so that it never touches the heat cable directly - rather it maintains contact with the braided metal surface of the hose. Finally, a 3 mm thick fiberglass insulation was wrapped around the tube and secured with an extra layer of Kapton tape. Using a separate PID controller, the temperature of this flexible, hot tube was controlled independently.
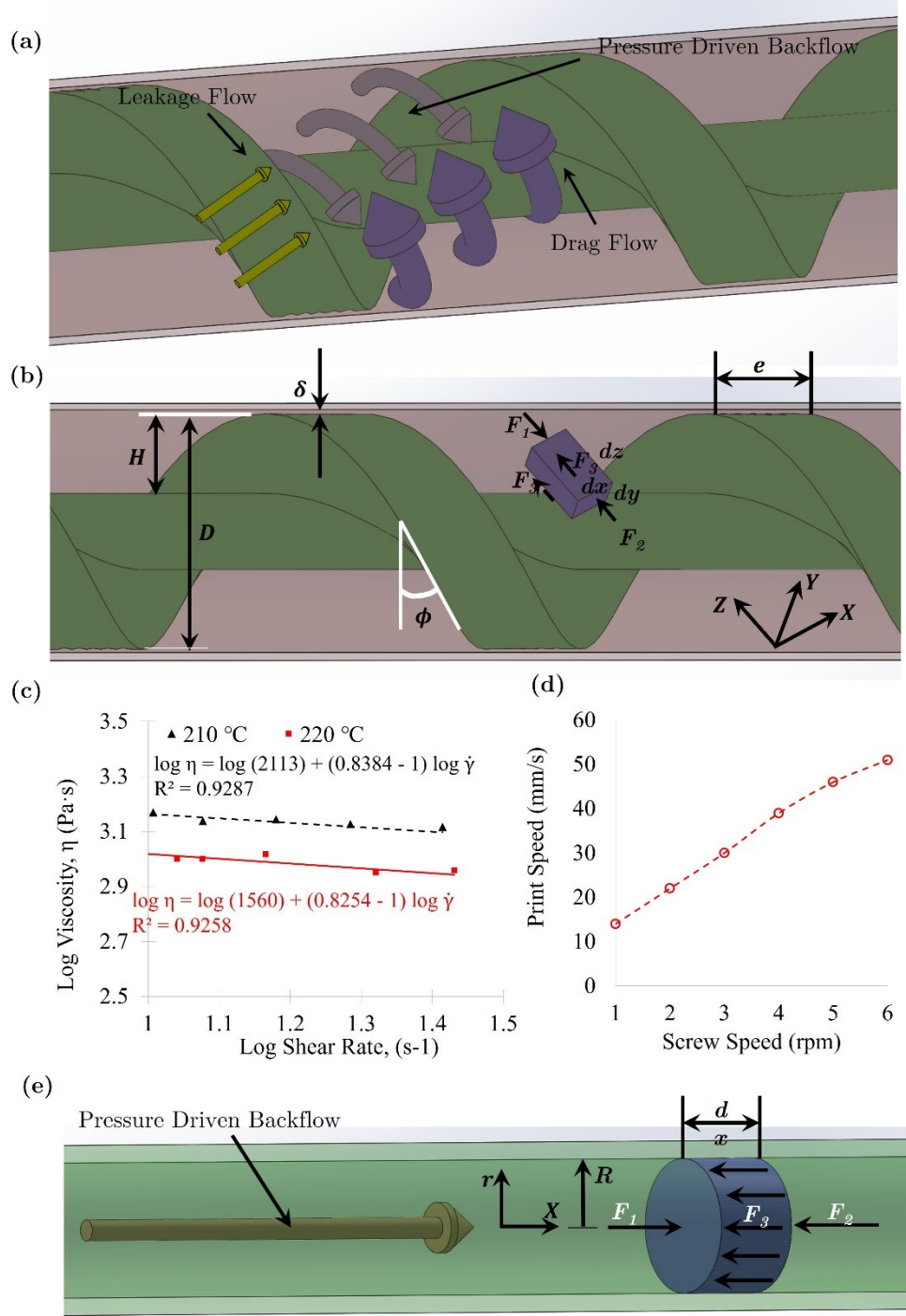
Figure 4. 2: (a) Three melt-flows inside the screw system, (b) flow inside the auger screw system, (c) the flow curves of SEBS at 210 ℃ and 220 ℃ temperatures in log-log scale, (d) the variation in theoretical (only drag flow) and actual print speed using 0.5 mm nozzle at different screw speeds and (e) flow inside the heated hose.

4.2.2.3   Print head

A custom tri-extruder, reported elsewhere [252,285], was employed here which has three inputs. One input channel was attached with a regular motor-roller feeder assembly to feed filaments of rigid polymers. Another input channel was connected to the flexible heated hose to feed soft thermoplastic pellets using the FPP technology. The third input of this tri-extruder was kept inactive and is intended for future use.

4.2.3   Flow Analysis

This system involves two major melt flows, single screw extrusion flow inside the barrel and laminar pipe flow through the heated hose. The physics of the single screw extrusion is well developed in the literature which consists of three types of flows [286], as shown in Figure 4.2 (a). They are a drag flow, caused from the interaction of the rotating screw and stationary barrel, an opposing pressure flow due to the pressure gradient developed along the screw length, and a leakage flow through the clearance between screw and barrel, which reduces the overall output of the extruder. This leakage flow may be negligible if the screw is not significantly worn [287]. Apart from these flow components inside the extruder, there is another opposing pressure flow resulting from the pressure gradient developed within the heated hose. From literature [288], the drag flow, Q_d can be estimated using the following equation.

$$Q_d = \frac{1}{2} \times (\pi D \tan\phi - e) \times \left(\pi D \frac{N}{60} \cos^2\phi\right) \times H \qquad (4.3)$$

Where the diameter of the screw $D = 15.5$ mm, helix angle $\phi = 35°$, flight width $e = 11$ mm, channel depth of the auger $H = 5.25$ mm and $N =$ screw speed in rpm. Hence, for our system, drag flow (Q_d) reduces to –

$$Q_d = (3.3 \times 10^{-8} N) \quad \text{m}^3/\text{s} \tag{4.4}$$

The mathematical model for pressure flow inside the extruder has also been developed in literature as follows [286,288].

$$Q_p = \frac{w\,H^3\,\sin\phi}{12\,\eta} \times \left(\frac{dp}{dL}\right)_{Extruder} \tag{4.5}$$

Where the channel width of the screw, $w = (\pi\,D\,\tan\phi - e)\cos\phi = 18.92$ mm, $\eta =$ viscosity of the polymer melt and $\left(\frac{dp}{dL}\right)_{Extruder} =$ the pressure gradient along the screw length inside the pellet extruder. This equation was derived for a Newtonian fluid which follows the simple linear viscosity relation i.e. $\tau = \eta\,\dot{\gamma}$. However, polymer melts are highly non-linear viscoelastic fluids. Thus, it is reasonable to consider the power-law fit equation for the melt viscosity, assuming the temperature is uniform throughout the extruder. Hence, we get the viscosity relation as [251]:

$$\eta = K\,\dot{\gamma}^{n-1} \tag{4.6}$$

Here, $K =$ consistency index and $n =$ power-law index. These power-law fit parameters can be estimated from the viscosity curve (viscosity vs. shear) of the polymer melt. So, using equation (4.6) in conjunction with the model developed by *Crawford* [287], the pressure flow equation has been re-formulated as follows.

Let's consider an infinitesimal element of the polymer melt inside the auger system, as shown in Figure 4.2(b). There are two normal forces F_1 and F_2 acting on two ends of the element and two

shear forces (both are F_3) acting on top and bottom surfaces of the element. If the pressure gradient along the screw length is assumed to be constant, then by balancing all the forces, one may obtain the following equation:

$$\left(P + \frac{\delta P}{\delta z}\, dz\right) dy\, dx = P\, dy\, dx + 2\, \tau_y\, dz\, dx \tag{4.7}$$

$$\text{Or, } y\, \frac{dP}{dz} = \tau_y \tag{4.8}$$

For a non-Newtonian power-law fluid:

$$\tau_y = \eta\, \dot{\gamma} \tag{4.9}$$

$$\text{Where, } \eta = K\, \dot{\gamma}^{n-1} \quad \text{and,} \quad \dot{\gamma} = \frac{dV}{dy} \tag{4.10}$$

Hence, by combining the Equations (4.8), (4.9) and (4.10):

$$y\left(\frac{dP}{dz}\right) = K\left(\frac{dV}{dy}\right)^n$$

Which can be re-arranged as:

$$\sqrt[n]{\frac{y}{K}\left(\frac{dP}{dz}\right)} = \frac{dV}{dy}$$

By integrating:

$$\int_0^V dV = \sqrt[n]{\frac{1}{K}\left(\frac{dP}{dz}\right)} \int_{\frac{H}{2}}^{y} y^{\frac{1}{n}}\, dy$$

So, the melt velocity, $V = \left(\frac{n}{n+1}\right) \sqrt[n]{\frac{\sin\phi}{K}\left(\frac{dp}{dL}\right)_{Extruder}} \left[y^{\frac{n+1}{n}} - \left(\frac{H}{2}\right)^{\frac{n+1}{n}}\right]$ \tag{4.11}

Here, $\frac{dP}{dz} = \sin \phi \left(\frac{dp}{dL}\right)_{Extruder}$

Thus, the pressure driven backflow rate, Q_p becomes:

$$Q_p = \int_0^{\frac{H}{2}} 2\, V\, w\, dy \tag{4.12}$$

Hence,

$$\left(Q_p\right)_{Extruder} = \frac{2n\,w}{(2n+1)} \times \sqrt[n]{\frac{\sin \phi}{K}\left(\frac{dp}{dL}\right)_{Extruder}} \times \left(\frac{H}{2}\right)^{\left(\frac{2n+1}{n}\right)} \tag{4.13}$$

Using a HAAKE™ Minilab twin screw micro-compounder, the viscosity curves for SEBS and SMP were obtained, from which power-law fit parameters (K, n) can easily be estimated. In this work, for demonstration purpose, only the SEBS data has been presented. Figure 4.2(b) shows the flow curves of SEBS at 220°C temperature with the power-law fit parameters estimated as K = 1560 and n = 0.8254. By using these power-law fit parameters and the geometric parameters of the screw system into Equation (4.13) the pressure flow equation of SEBS can be reduced to Equation (4.14), assuming the pressure gradient is linear over the screw length (L_A = 0.18 m):

$$\left(Q_p\right)_{Extruder\,(SEBS)} = 3.33 \times 10^{-14} \times \sqrt[0.8254]{(\Delta P)_{Extruder}} \qquad \text{m}^3/\text{s} \tag{4.14}$$

Since the screw system does not have any wear and has a very small clearance (δ = 0.0005 m) between the flight surfaces and the barrel surface, the leakage flow will be very small and be neglected in this study.

In addition to the flow components inside the screw-barrel system, there is another melt flow that arises from the pressure gradient developed inside the heated hose. This pressure gradient also

reduces the overall melt flow and can be mathematically modeled using the fundamentals of pipe flow [289] applying to power-law polymer melt as derived below for a flexible tube with internal radius of R.

Let's consider an element of the polymer melt with infinitesimal thickness (dx) inside the flexible hot-tube, as shown in Figure 4.2(e). There are two normal forces F_1 and F_2 acting on two sides of the element and one shear force F_3 acting on the peripheral surface of the element. If the pressure gradient along the tube length is assumed to be constant, then by balancing all the forces, one may obtain the following equation:

$$\pi\, r^2 \left(P + \frac{\delta P}{\delta x}\, dx\right) = \pi\, r^2\, P + 2\pi r\, \tau_r\, dx \tag{4.15}$$

$$\text{Or,}\ \frac{r}{2} \frac{dP}{dx} = \tau_r \tag{4.16}$$

For a non-Newtonian power-law fluid:

$$\tau_y = \eta\, \dot{\gamma} \tag{4.17}$$

$$\text{Where,}\ \eta = K\, \dot{\gamma}^{n-1}\ \text{and,}\quad \dot{\gamma} = \frac{dV}{dy} \tag{4.18}$$

Hence, by combining the Equations (4.16), (4.17) and (4.18):

$$\frac{r}{2}\left(\frac{dP}{dx}\right) = K\left(\frac{dV}{dr}\right)^n$$

Which can be re-arranged as:

$$\sqrt[n]{\frac{r}{2K}\left(\frac{dP}{dx}\right)} = \frac{dV}{dr}$$

By integrating:

$$\int_0^V dV = \sqrt[n]{\frac{1}{2K}\left(\frac{dP}{dx}\right)} \int_R^y r^{\frac{1}{n}}\, dr$$

So, the melt velocity, $V = \left(\frac{n}{n+1}\right)\sqrt[n]{\frac{1}{K2}\left(\frac{dp}{dL}\right)_{\text{Flexible tube}}} \left[r^{\frac{n+1}{n}} - (R)^{\frac{n+1}{n}}\right]$ (4.19)

Thus, the pressure driven backflow rate, Q_p becomes:

$$Q_p = \int_0^R 2\pi r\, V\, dr$$ (4.20)

Hence,

$$\left(Q_p\right)_{\text{Heated Hose}} = \frac{n\,\pi}{(3n+1)} \times \sqrt[n]{\frac{1}{2K}\left(\frac{dp}{dL}\right)_{\text{Heated Hose}}} \times (R)^{\left(\frac{3n+1}{n}\right)}$$ (4.21)

Again, the Equation (4.21) can be re-written for SEBS flowing through the heated hose. However, the temperature of the flexible tube is 210 °C for SEBS which is different than that of the pellet extruder. Therefore, a new set of power-law fit parameters ($K = 2113$ and $n = 0.8384$) for 210 °C estimated from Figure 4.2(b) must be used in the Equation (4.21) for 2-foot long ($L_T = 0.61$ m) hose with internal radius, $R = 1.5875$ mm. That reduces the Equation (4.21) as follows.

$$\left(Q_p\right)_{\text{Heated Hose}} = 1.17 \times 10^{-16} \times \sqrt[0.8384]{(\Delta P)_{\text{Heated Hose}}} \qquad \text{m}^3/\text{s}$$ (4.22)

Finally, the total melt flow can be expressed by the following single equation:

$$Q_{Total} = Q_d - \left(Q_p\right)_{Extruder} - \left(Q_p\right)_{Heated\ Hose}$$ (4.23)

Which can again be written for SEBS as follows:

$$Q_{Total} =$$

$$Q_{Total} = (3.3 \times 10^{-8}N) - 3.33 \times 10^{-14} \times \sqrt[0.8254]{(\Delta P)_{Extruder}} - 1.17 \times 10^{-16} \times \sqrt[0.8384]{(\Delta P)_{Heated\ Hose}}$$ (4.24)

This equation can be used to determine the screw speed in rpm for a desired flow rate or print speed. However, it requires an experimental measure of the pressure drop across both the extruder and the heated hose, for accurate estimation. However, due to a relatively small pressure drop at lower screw speeds, by considering only the drag flow, the first term of the Equation (4.24), one may get an approximate relation between desired print speed and required screw speed using the following equation:

Print speed, $S = \dfrac{Q_d}{\pi\,(r_{nozzle})^2}$ (4.25)

Table 4. 1: Printing parameters for SEBS and SMP extrusion

	SEBS	SMP
Temperature of the pellet extruder (°C)	220	200
Temperature of flexible Heated hose (°C)	210	190
Temperature of printing head (°C)	220	200
Nozzle sizes (mm)	0.35, 0.5 and 1.0	

4.2.4   Pellet Extrusion

The process of pellet extrusion requires setting and maintaining temperatures of three major components of this system. This set of temperatures may vary for different materials, i.e. SEBS and SMP, in this work. Some initial tests were conducted to fine-tune the process and identify this set of temperatures for both materials to obtain continuous defect-free extrudates. Table 4.1

lists the sets of temperature for both SEBS and SMP which resulted in high-quality extrusion. The temperature of the heated hose was kept at a lower temperature than the pellet extruder and print head, that is 20 °C below the maximum temperature limit (230 °C) of the PTFE core of the heated hose. Figure 4.2(c) shows the actual print speed or extrusion rate of the FPP system at different screw speed using a 0.5 mm nozzle diameter. This plot clearly shows that the extrusion rate tends to reach a plateau at higher screw speed due to the pressure-driven backflows developed which were not experimentally measured in this work. The maximum screw speed attainable with the pellet extruder set-up was approximately 6 rpm where the supplier's specification of maximum screw speed was 8 rpm. This analysis was performed to identify the suitable screw speed for desired print speed. Hence, for accurate measurements, two pressure transducers installed across the pellet extruder and flexible tube would be highly recommended for future work. Based on these trials, a print speed of 30 mm/s was chosen for printing when using a 0.5 mm nozzle and setting the screw speed to 3 rpm.

4.2.5   Dynamics of the Flexible Heated Hose

As the heated hose is the main element of this system for transporting the polymer melt from the pellet extruder to the print head, we also consider the flow of polymer melt inside this heated hose because it may put an additional limit on the print speed and power requirements.

4.2.5.1   Melt properties

Polymer melts have highly non-linear, shear rate dependent viscosity properties. The shear rate is determined by the flow rate and the geometry of the tube and the apparent shear rate ($\dot{\gamma}_{app}$) for a power-law polymer melt can be estimated using the following equation [286]:

$$\dot{\gamma}_{app} = \frac{4\,Q_{Total}}{\pi\,(R)^3}\left(\frac{3n+1}{4n}\right) \tag{4.26}$$

For a print speed of 30 mm/s with SEBS and using a 0.5 mm nozzle, the apparent shear rate at the channel wall of the heated hose was calculated as 1.875 s^{-1}. This shear rate, at the temperature of 210°C, corresponds to the viscosity of 1909 Pa·s, estimated using the power-law fit equation from the viscosity curve given in Figure 4.2(b).

4.2.5.2   Heat flux requirements

Since the polymer is in its molten state before entering the heated hose, ideally it would be an adiabatic process to transport the melt to the print head, if there is no heat loss. However, in practice, though 3-mm thick fiberglass insulation was applied on the outer surface of the hose, there is still some heat loss to the environment. This heat loss is compensated for by using an external band heater which supplies a variable heat flux to maintain the desired temperature of the heated hose.

4.2.5.3   Pressure drop estimation

From a momentum balance on the heated hose, the pressure drop across it can be predicted as performed for an extrusion die [259]. By solving both momentum and energy balances, the pressure drop within the liquefier of a 3D printer was modeled by *Ramanath et al.* [260], which can be used

for determining the pressure drop across the heated hose. Hence, the equation has been re-written as follows:

$$\Delta P_{\text{Heated Hose}} = \frac{2\,L_T\,K}{R^{3n+1}} \times \left[\frac{(3n+1)\,Q_{\text{Total}}}{\pi\,n}\right]^n \times e^{\left[\alpha\left(\frac{1}{T}-\frac{1}{T_\alpha}\right)\right]} \tag{4.27}$$

All the parameters are already discussed in previous sections except T for the temperature of heated hose, α for activation energy and T_α for a reference temperature where the temperature dependency of the melt viscosity disappears. This model was developed with some assumptions [253]: (a) the melt is incompressible, (b) the flow is laminar, fully developed and steady state, (c) shear-rate dependency of the viscosity can be expressed using the power-law model and (d) melt viscosity also depends on temperature and follows the Arrhenius model. We also do not consider any axial or radial expansion of the hose in this analysis.

4.2.6   Printing of SEBS Soft Robotic Actuator

FPP system has the potential to revolutionize the field of soft actuators through its capacity to directly print very soft, stretchable thermoplastic materials. Figure 4.3(a) shows a soft, flexible octopus printed with SEBS that has stretchable arms extensible over 300% without failure. The 3D model of the octopus was downloaded from thingiverse.com and designed by *Laurens Kempjes.* Commercially available flexible filaments can be directly used to print objects with limited flexibility but are not as reversibly stretchable as the SEBS used here. This ability to print very stretchable devices opens up new possibilities in 3D printing applications such as soft robots where extreme deformations over many cycles are needed.

Inspired by the ability of soft-bodied biological systems to interact with the uncertain environment and achieve compliant motion without multiple mechanical joints, many recent works focus on soft robotic actuators [290,291]. Therefore, to demonstrate the performance of the FPP system we choose to print soft robotic actuators made of SEBS. In this work, the pneumatic networks (PneuNets) based soft robots were designed inspired by work done by the Whitesides group at Harvard University [292]. This actuator has channels and reservoirs embedded into the elastomeric materials which can be inflated using pressurized air to achieve mechanical actuation. The 3D model of the soft robotic actuator is shown in Figure 4.3(b), and 3(c), whereas its actual printed version is shown in Figure 4.3(d).

Inherently, FDM parts have poor surface quality due to the staircase effect and chordal error while slicing the object [215]. FDM parts are not usually air-tight in their 3D volume, and air gaps between deposited fibers and layers contribute to fluid leakage throughout the printed body. This limits the feasibility of FDM technology in printing PneuNets based soft robotic actuators. However, this issue may be overcome by selecting proper layer height, layer width and printing temperature to enhance the fusion between deposited fibers and layers. An additional annealing process may also contribute in relieving the residual thermal stress if heated sufficiently higher than glass the transition temperature (T_g) to allow the material to re-flow, filling the voids between fibers or layers. As a result, an air-tight 3D printed part may be realized with substantially reduced voids in its 3D volume. Hence, after printing the soft robotic actuators of SEBS, if required, they were also heat treated at 135 °C for 30 min.
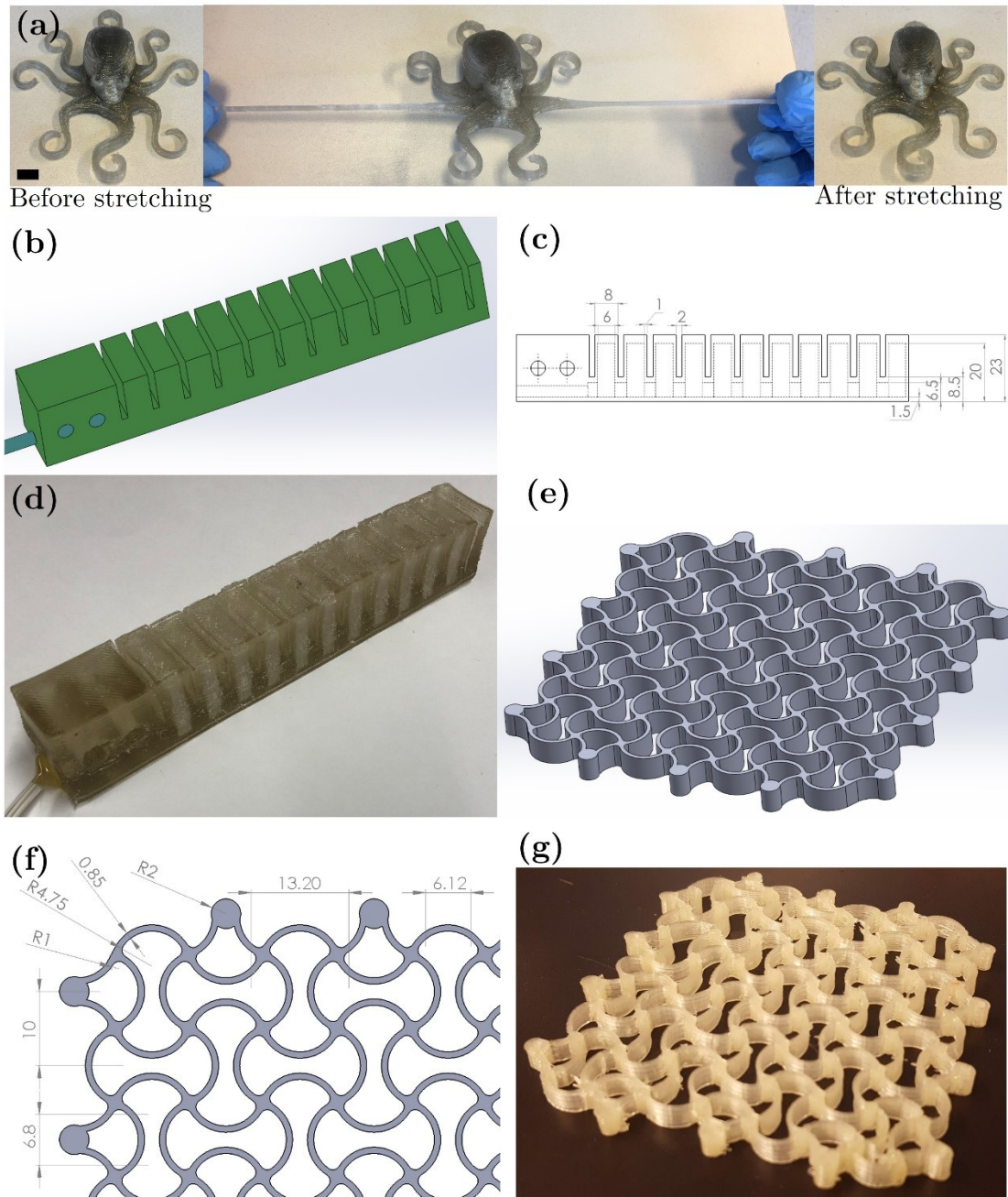
Figure 4. 3: (a) A stretchable octopus with 300% stretchable arms without any mechanical failure. The 3D model (b) of the soft actuator with dimensions presented in (c). The photograph of the actual actuator shown in (d). (e) The 3D model of the auxetic structure with dimensions presented in (f). The printed structure is depicted in (g). All dimensions in 3D models are in mm.

4.2.7 Printing of SMP Auxetic Structure

In addition to the pellets of soft materials, the FPP system is also capable of printing pellets of rigid polymers if the pellets are less than 5 mm in size in any of the dimensions [284]. To demonstrate this capability, rigid pellets of SMP were used to print functional devices like re-entrant structures. Such structures are getting increasing attention for their ability to unlock "4D" printing capabilities and morphable metamaterials but have mainly been prototyped via proprietary resins or more expensive additive manufacturing processes [293]. Re-entrant structures have auxetic behavior due to their negative Poisson's ratio, which is of great interest due to their counter-intuitive behavior under deformation [294]. By using SMP materials, their thermo-mechanical coupling is utilized in re-entrant auxetic structures for controllable one-way actuation [295]. The degree of auxeticity is determined by the particular geometry of the material system and its deformation mechanism when loaded. Higher auxetic performance often requires complex geometry [296]. Complex auxetic structures generally involve time-consuming and complicated fabrication techniques; hence rapid prototyping technologies may be useful to fabricate such material systems [294]. A re-entrant auxetic structure with sinusoidal connectors inspired by the design used by *Dolla et al.* for drug diffusion [297], has been printed with SMP to demonstrate proof-of-principle for our system to be used for this purpose. Figure 4.3(e) shows the 3D model of the sinusoidal auxetic structure with dimensions of its unit cell in Figure 4.3(f), and the actually printed structure shown in Figure 4.3(g).

4.3   RESULTS AND DISCUSSION

4.3.1   Thermal Simulation of the Heated Hose

The insulated, heated hose was assumed to be a hot vertical tube having a uniform diameter of

20 mm. The tube was further considered to be in a free convection situation where the temperature

of the heating element is kept fixed at 210 °C. The connectors on both ends of the hose were

assumed to have a uniform fixed temperature of 220 °C. Since a 4-foot (1.22 m) long heater band

(15 mm wide) was wrapped on to the 2-foot long hose, it is reasonable to assume the heater as a

continuous annular tube fitted on the hose. With these assumptions, first, the constants of the

Hilpert correlation (C, m) were estimated for laminar free convection over a slender circular

cylinder as developed by *Cebeci* [298]. Finally, the convective film coefficient (h) of 22.0 W/m²-

°C was estimated using the Equation (4.28).

$$Nu = \frac{h\,L}{k} = C\ (Gr_L\ Pr)^m \tag{4.28}$$

Where, Nu, Gr_L, and Pr are the Nusselt number, Grashof number and Prandtl number,

respectively, of the air flow around the heated hose. L and k are the characteristics length and

thermal conductivity of the flexible tube. Then, the thermal analysis was performed in ANSYS

as shown in Figure 4.4(a) and 4.4(b). In this steady state thermal simulation, the temperature of

the surrounding environment was assumed to be 25 °C. Figure 4.4(a) shows temperature

distribution along the radial direction (cross-sectional) of the heated hose. It indicates that the

core Teflon tubing is nearly 220 °C and the temperature of its outer surface is just more than 120

°C which was experimentally measured as ~110 °C. From the thermal simulation, the temperature

distribution along the axis of the heated hose was found to be approximately uniform except a slight temperature variation near the ends of the tube. Figure 4.4(b) illustrates the temperature distribution in the tri-extruder, which required the estimation of convective film coefficient (h) of the forced convection around the heat-sink of one input of the tri-extruder, as performed in previous work [285].

4.3.2   Ultimate Strength of Extrudates

When the materials were successfully extruded using the FPP system, the extrudates were characterized to analyze their mechanical properties. The printer was allowed to extrude the material from a height of approximately 10 cm above the print bed so that when the free extrudate touches the bed, it is already solidified. These extrudates were then tested in a custom test-setup reported elsewhere [285] to measure ultimate tensile strength (UTS) and elongation at break. Since elongation at break of the SEBS extrudates was significantly higher than the elongation range of the reported test-setup, they were tested in a different approach. First, a specified length of the SEBS extrudate was hung from an analog mass balance and the other end of the extrudate was pulled down until the extrudate failed. The whole process was video recorded, which was later used to estimate the elongation at break and the length of extrudate when the failure occurred. Table 4.2 summarizes the extrudate diameter, UTS, elongation at break for both SEBS and SMP extrudates. Each measurement was repeated five times. The SEBS extrudates could stretch to more than 800% which is higher than the reported stretchability (~600%) of bulk SEBS [223].

This phenomenon may be explained by the increased linearity of the polymeric chains from an extrusion process [286]

Table 4. 2: Experimental results from tensile testing of the extrudates

Materials	Nozzle Diameter (mm)	Extrudate Diameter (mm)	Tensile Strength (MPa)	Elongation at break (%)
SEBS	0.35	0.33 ± 0.01	12.5 ± 2.2	850 ± 70
	0.50	0.52 ± 0.02	11.1 ± 1.8	875 ± 78
SMP	0.35	0.36 ± 0.01	33.2 ± 2.3	32 ± 1.4
	0.50	0.54 ± 0.03	35.0 ± 3.6	34 ± 2.1
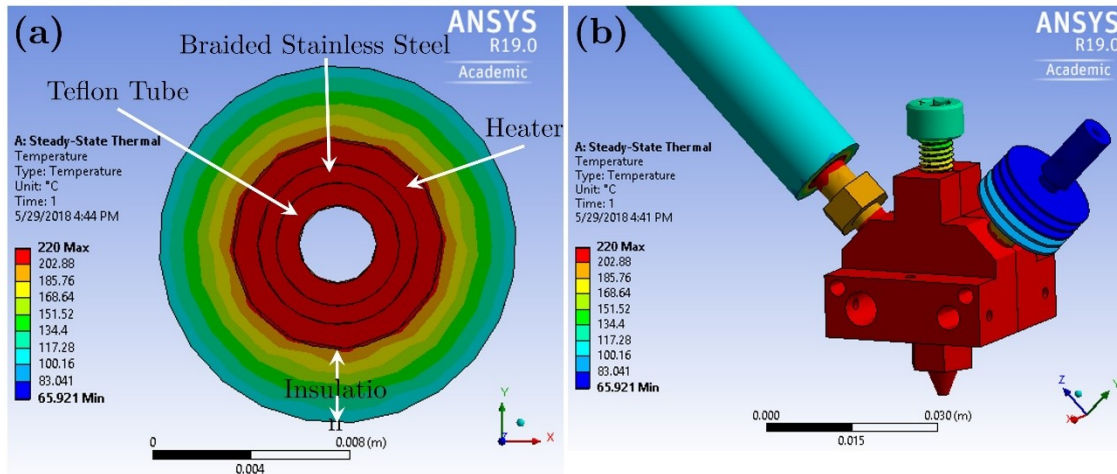
Figure 4. 4: The temperature distribution across the (a) cross-section of the heated hose and (b) at the end connector with the tri-extruder, from the thermal simulation using ANSYS.
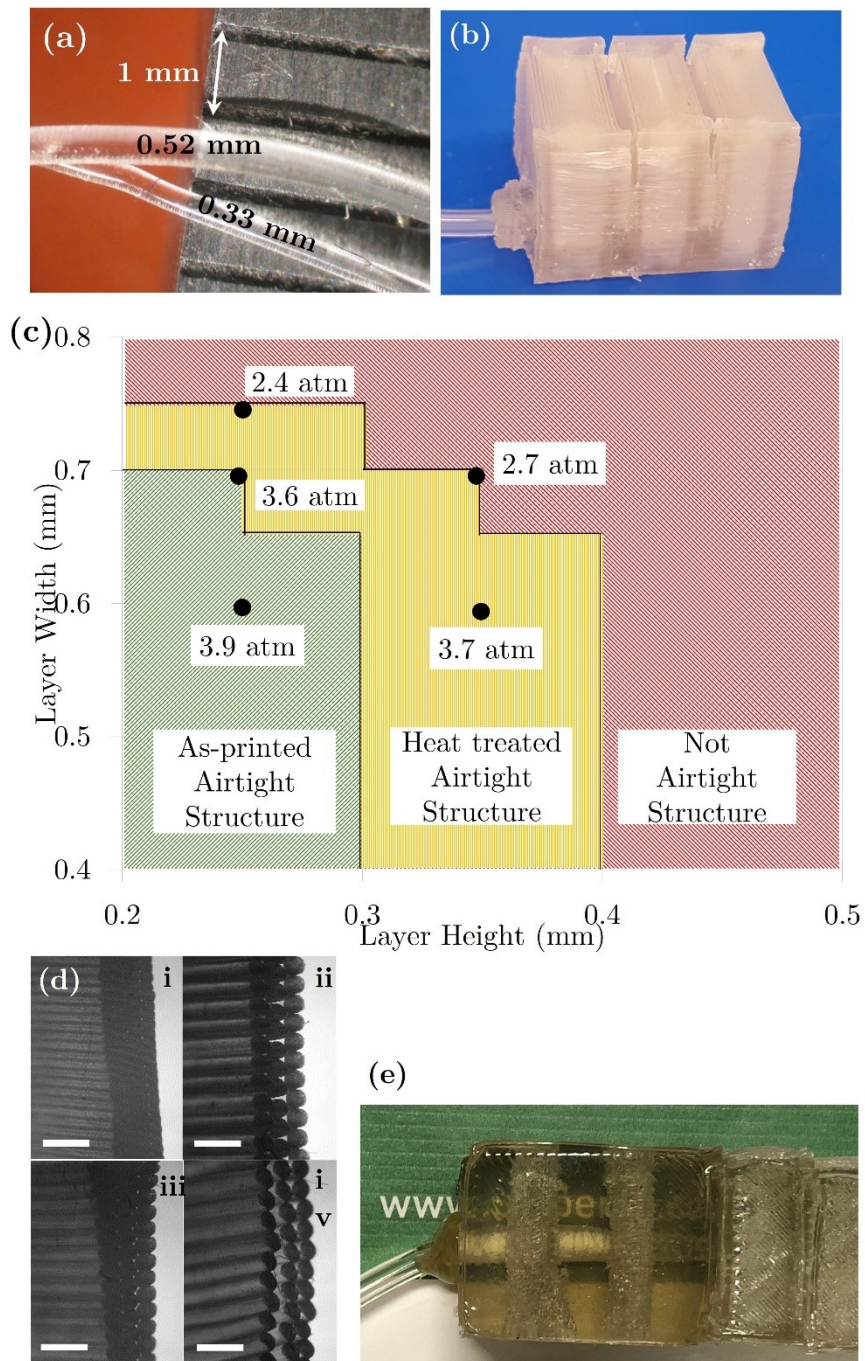
Figure 4. 5: (a) Microscope images of two representative SEBS extrudates from 0.5 mm and 0.35 mm nozzles, a metric scale is in the background. (b) A small actuator with only three chambers printed with SEBS was used to determine the effect of printing parameters on airtightness of soft robots, (c) a graphical representation of the effect of printing parameters on airtightness of printed walls. Three distinct regions printing parameters which result in as-printed air-tight structure, heat-treated air-tight structure and not air-tight structure. Data points represent the air pressure which causes rupturing leading to fluid leakage through the chamber walls. (d) Microscope images

of the cross-sections of samples printed with 0.6 mm layer width and (i) 0.25 mm layer height, (ii) 0.35 mm layer height (before heat treatment), (iii) 0.35 mm layer height (after heat treatment), (iv) 0.45 mm layer height. [Scale bars are 1.5 mm] (e) The base of the SEBS actuator printed with 0.25 mm layer height and 0.5 mm layer width, resembling the bulk SEBS material with high optical transparency.

4.3.3 Effect of Printing Parameters on Airtight SEBS Structure

The major printing parameters affecting the size and number of inter- and intra-layer voids were found to be layer height and layer width. These settings are defined in the slicing step when the 3D model is converted to a number of 2D layers. In this work, an open source slicing program, Slic3r [299] was used for the slicing step. A number of small actuators with only three hollow chambers, as shown in Figure 4.5(b), were printed with different layer widths and heights. Then, pressurized air was applied to inflate them until they ruptured to measure the air pressure (gage) which causes pneumatic failure. The microscope images of chamber-walls of the samples were also examined to study the voids present in those samples. Figure 4.5(c) shows the printing parameters needed to achieve airtight SEBS walls when using a 0.5 mm nozzle. There are three distinct regions in the plot, printing of SEBS structures in the first region deposits the material with a "squashed" cross-section rather than a more typical circular cross-section. It also causes a degree of over-extrusion to help to fill the possible voids between the deposited fibers. These phenomena contribute to air-tight FDM parts with minimal voids in their 3D volume. Because the SEBS is a clear material, the boundary effect of the internal layers also disappears, leading to a more transparent printed part. Figure 4.5(e) shows a part with 20 mm depth, still transparent enough to read text through this thickness.

117

The second region in Figure 4.5(c) represents the print settings that result in an object which is mostly airtight except for some random air-leaking locations. These printed parts require an additional heat treatment process to allow the materials to re-flow - filling-up the unwanted voids or sealing-up the cracks. It was experimentally determined that if an SEBS part printed with parameters defined by the region B undergoes a heat treatment at 135 °C for 30 minutes, it becomes air-tight, suitable for pneumatic applications. The third region has too many voids for the part to become air-tight even with the heat treatment step.

Five small actuator samples printed with SEBS were tested to determine the maximum air pressure before rupturing. Once a sample was ruptured it went through an additional heat treatment process (135 °C for 30 min) to seal the crack and tests were repeated five times. Figure 4.5(c) also shows the average air pressure which caused the actuator chamber to rupture. It shows that the samples printed with parameters corresponding to the first region (without heat treatment) and the second region (with heat treatment) have statistically indistinguishable rupturing pressure.

4.3.4   Performance of SEBS Soft Actuator

Once the SEBS soft robotic actuator has been directly printed, it was characterized to measure the actuator force and the tip deflection induced for a range of air pressure (gage) applied to its PneuNet. The custom setups in Figure 4.6(a) and 4.6(b) with acrylic holders were used to characterize the actuator. A National Instrument data acquisition (DAQ) hub (NI USB-6289)

along with a Windows Presentation Foundation (WPF) application written in C# and a load cell

(Transducer Techniques, MLP-10) were used to measure the actuation force.
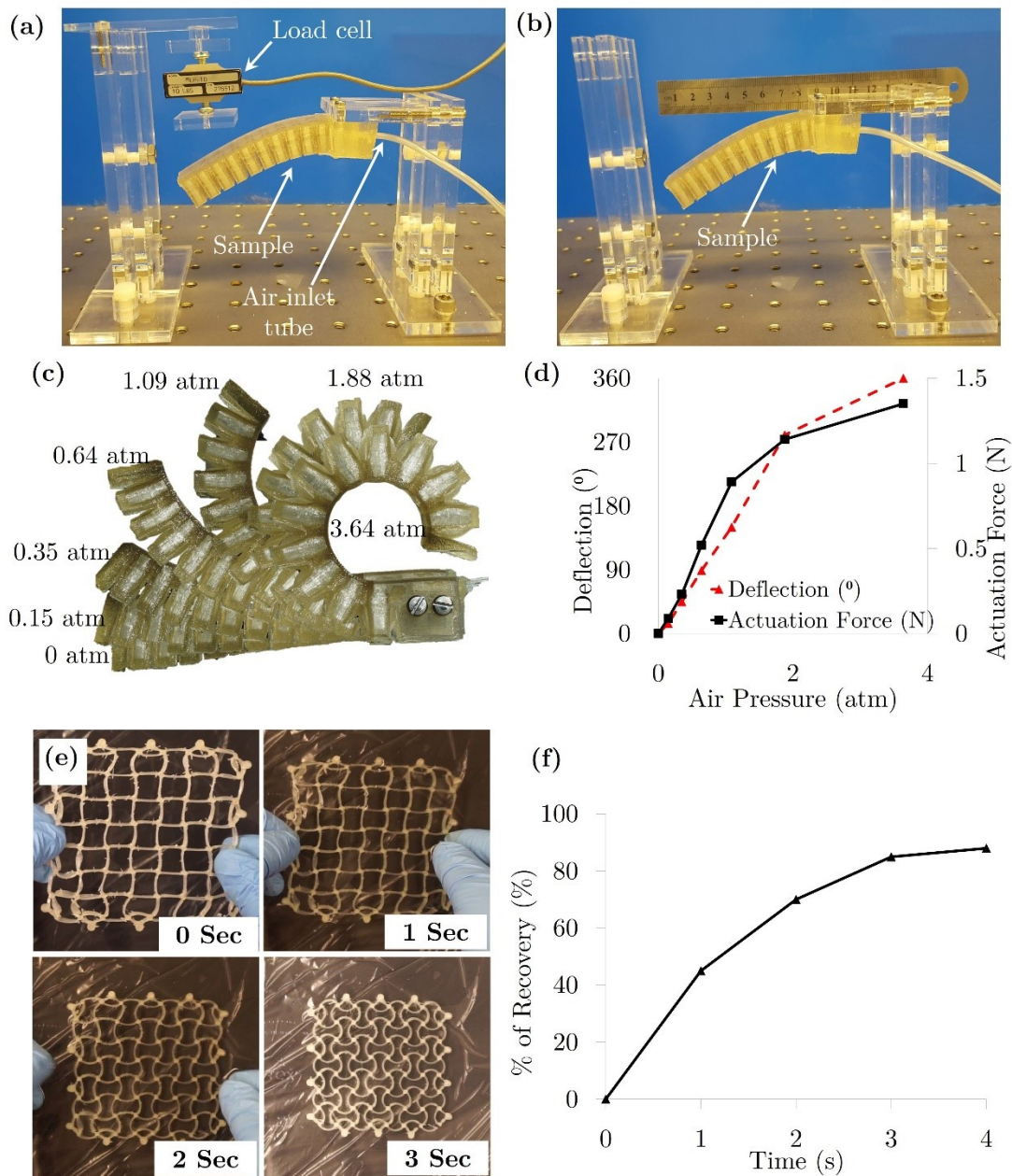
Figure 4. 6: The custom set-ups for measuring the (a) actuation force and (b) tip deflection of the SEBS soft robotic actuator. (c) Different states of actuation of a representative SEBS soft robot. (d) The dependences of the actuation force and deflection angle plotted against the air pressure applied. (e) Time lapsed photos of sinusoidal re-entrant structure showing its shape recovery and (f) the % recovery of the as-printed re-entrant structure over the period of recovery.

To measure the tip deflection of the actuator, a camera was used to take photos of the deflected actuator. These photos along with image processing software were used to measure the angle of deflection of the actuator tip. Figure 4.6(c) shows the different states of actuation of the soft robotic actuator displaying corresponding air pressure (gage). A graph showing the dependence of actuation force and tip deflection of the actuator on the air pressure applied is presented in Figure 4.6(d).

4.3.5   Recovery of SMP Auxetic Structure

Previous 3D printing of SMP was recently reported where researchers first used a pellet extruder to fabricate SMP filament, which was then used in FDM systems to print SMP devices following with an annealing process before utilizing the shape memory property [300]. However, in this work, the SMP auxetic structures were printed directly from its pellets using the FPP system and did not require a post-processing heat treatment step. Figure 4.6(e) shows time-lapsed photos of the sinusoidal re-entrant auxetic structure (size: 8 cm $\times$ 8 cm $\times$ 5 mm) depicting its shape memory property. First, the as-printed structure (T_g = 35 °C) was heated to 40 °C under hot water and stretched 2 cm along both length and width direction (deformed size: 10 cm $\times$ 10 cm $\times$ 5 mm). Then it was cooled down to room temperature and kept for 2 minutes while maintaining the deformed shape. To observe the recovery, the object was then put again under hot water of ~ 50 °C, (T_g + 15 °C) recommended by *Raasch et al.* [300]. The *% recovery* was calculated based on the overall length of the auxetic structure as shown in Figure 4.6(e) and using the following equation.

$$\% \text{ Recovery} = \frac{\left(L_{\text{deformed}} - L_{\text{current length}}\right)}{\left(L_{\text{deformed}} - L_{\text{original}}\right)} \times 100 \% \tag{4.29}$$

Where, $L_{deformed}$ = the length of the deformed and cooled down structure, $L_{original}$ = the original as-printed length of the structure and $L_{current\ length}$ = the current length of the structure. Figure 4.6(f) shows the *% Recovery* of the auxetic structure over a period of time, where it is clearly shown that the structure returns to around 8.1 cm on both length and width directions which is equivalent to *95% Recovery*. In addition to the auxetic structure, a number of prototypes were also printed using this system. The movie file in the supplementary information shows recovery of a "UofA" object under 50 °C hot water.

4.4   CONCLUSIONS

To the authors' best knowledge, this is the first time that material-extrusion based 3D printing has been demonstrated directly from pellets by using a flexible heated hose as the feed mechanism. Since the pellet extruder is fixed while the print head moves, it decouples the power/heating limitations from the speed/resolution needs of the printer hot end. Using this FPP technology, industrial-scale extruders coupled to FDM printers could deposit materials, in future, with properties and deposition rates previously impractical. While the motivating drive for the development of this technology was to solve the issue of working with extremely soft elastomers partially, the effective feed speeds achievable and economic savings of direct pellet extrusion can make the heated hose-based extrusion a very valuable improvement to all FDM type printers.

5. CHAPTER: TENDON DRIVEN FUNCTIONALLY GRADIENT SOFT ROBOTIC GRIPPER 3D PRINTED WITH INTERMIXED EXTRUDATE OF HARD AND SOFT THERMOPLASTICS§

5.1   INTRODUCTION

In nature, most animals are composed of soft, stretchable and flexible components enabling them to interact with uncertain environments. On the other hand, typical engineered systems or robots are primarily composed of rigid, hard materials allowing precise control of position in 3D space.[301] However, this rigidity limits the applicability of traditional robots to only particular environments. For instance, hyper-redundant robotic systems are composed of serially connected rigid links with a high degree of freedom resembling biological systems.[302] These systems have a high degree of articulation making them superior in highly constrained environments.[303]

---

§ A version of this chapter is under review for publication as: Khondoker, Mohammad Abu Hasan, Baheri, Nadia and Sameoto, Dan; Tendon Driven Functionally Gradient Soft Robotic Gripper 3D Printed with Intermixed Extrudate of Hard and Soft Thermoplastics. *3D Printing and Additive Manufacturing.* ID: 3DP-2018-0102.R2. Reproduced with permission from Mary Ann Liebert, Inc.

However, due to their dexterity and compliance, finger systems with a continuous soft body have also gained popularity.[304] A tendon system can also be used to actuate both hyper-redundant and continuum bodied robotic systems.[305]

Inspired by soft-bodied biological systems, much of the recent work in soft robotics has been implemented by developing tendon driven artificial fingers such as prosthetic fingers,[304] or shape memory alloy driven caterpillars.[306] A fully soft-bodied system experiences actuation lag due to its deformation at the tendon/soft matter interface. Integrating soft and rigid materials in a single actuation system would facilitate actuation response. However, this integration is not simple for the commonly used molding-casting fabrication processes which require user expertise.[292,307] These techniques also place a limit on the structural complexity achievable in the soft robots because of the processing requirements of molding and demolding steps. The limited structural complexity is one of the reasons the natural biological systems out-perform engineered systems. Emerging 3D printing technologies have a role to play to enable printing of geometrically complex soft-robotic structures such as a combustion-powered robot,[308] a hydraulic hexapod robot,[309] a legged soft robot,[310] a prestressed soft gripper[311] and a tentacle-like artificial muscle.[312]

For untethered applications, soft robots can benefit from the inclusion of some rigid components with their soft body.[313] The rigid and soft materials may not be readily bonded, and this can result in recurring adhesion failures at the interface between different parts. Therefore, a novel 3D printing technique engineered to print both rigid and soft materials resisting separation of chemically immiscible polymers once printed is of high value to the field of soft robotics

123

manufacturing as it can help bypass many of the challenges of assembling and bonding parts in the final manufacturing process.

In additive manufacturing (AM) processes, a part is produced by adding material into successive two-dimensional cross-sections.[269] In a multi-material fused deposition modeling (FDM) technique, multiple polymers are used in the same system to print objects with specialized materials at strategic locations within the volume to increase functionality and performance.[314] In 2000, fused deposition of multiple ceramic (FDMC) was developed which is an extended version of the FDM technique to print objects with up to four ceramic materials.[315] *Pilleux et al.* used a multi-material FDM system to print structures consisting of an alumina base material and a support material made of wax.[316] In a recently published work, functionally gradient materials (FGM) devices were successfully printed using an off-the-shelf FDM style 3D printer.[317] The composition was controlled by regulating the feed rates of two filaments. However, there was no intermixing function in this system and blending of nylon & PLA was said to be uneven and could often result in globs rather than smooth extrusion. The limitation of multi-material FDM systems using separate nozzles for each material is they are unable to print FGM devices with a gradual transition from one material to another. This gradient may be crucial for functional devices for reducing internal stress gradients and delamination. *Kumar et al.* successfully printed graded conical end effectors having enough anchoring stability compared to other purely soft or rigid objects[318] but had to make use of a different AM technology to achieve this result (Connex500 printer based on PolyJet Matrix™ Technology). *Bruyas et al.* also printed statically balanced compliant joints using a multi-material polyjet technique.[228] This type of printing is useful but

can only produce parts from specialized resins which may not have the same attractive properties as true engineering polymers. For instance, *Lee et al.* reported that the 3D printed connectors printed from resins were easily torn.[319] Multi-material FDM systems with a single nozzle for all materials can, in theory, be used to print true FGM objects by continuously varying the composition of the extrudate in 3D space. There are very few FDM systems which can print two or three thermoplastic materials using the same nozzle system,[320-322] and most of these multi-material FDM systems have been used with multiple filaments of the same material but with different colors so that materials bond well, but also have no mechanically different performance.

When polymers are printed with simple side-by-side co-extrusion, the adhesion between the materials at their interface is crucial to prevent potential delamination and other bonding issues. If the Hildebrand solubility parameters, δ ($cal^{1/2}cm^{3/2}$) of two polymers are comparable, the materials are miscible.[229] In this case, due to mutual diffusion, the polymer pair has a symmetric concentration profile of both polymers without a sharp transition,[323] which makes the polymer pair less prone to bonding failure. If the difference between the solubility parameters of the polymers increases, they become immiscible.[229] In the case of an immiscible polymer pair, they are likely to have bonding failures at their interface. There are some reported compatibilization methods to enhance bonding at the interface of two immiscible polymers.[232,234,235,237] However, these techniques are designed for flat sheets of polymers and are not suitable for FDM systems without additional processing steps. As an alternate solution to this issue, mechanical approaches to resist separation of the polymers at their interface can be applied [238]. Mechanical interlocking is one of the conceptually most straightforward approaches to overcome the bonding

failures of polymers with FDM technology. Compared to other blending structures of immiscible polymer melts, a co-continuous structure facilitates a synergistic effect on the mechanical modulus from each constituent polymer[239]. However, to ensure the co-continuous structure of a pair of polymer melts, the volume fraction of any material should be in the range of 0.3 to 0.7 if the viscosity ratio is near unity[239]. Therefore, when switching from one material to another during 3D printing, at a 3D volume where the composition does not satisfy the requirements of the co-continuous structure, it will have one material continuous with a dispersed phase of the other material. However, in the majority of the print volume, the co-continuous structure should be realized and thus have enhanced adhesion between layers compared to the case of side-by-side co-extrusion. Hence, an extruder head with the capacity to partially intermix immiscible polymers to introduce mechanical keying and ensuring the co-continuous structure of constituent polymers is highly useful for multi-material FDM. This capability can be used to directly print FGM soft robotic fingers with hard and soft components.

In this paper, a multi-material extruder system with the capacity to insert a static intermixer enabling extrusion of a mechanically interlocked extrudate of two chemically immiscible polymers is reported. It was developed first to demonstrate that two rigid thermoplastics that bond poorly, acrylonitrile butadiene styrene (ABS) and high impact polystyrene (HIPS), could have strongly enhanced bonding. The degree of intermixing or mechanical interlocking is a key to analyze the performance of the static intermixer. Samples printed with intermixed co-extrusion were compared to samples printed with side-by-side co-extrusion without the intermixer. It was the first step to confirm the capability of printing FGM devices using this custom extruder system. A custom

system for printing styrene-ethylene-butylene-styrene (SEBS) elastomers was used to examine bonding between SEBS and HIPS with approximately three orders of magnitude difference in moduli. Once the bonding between layers was found to improve due to the intermixing, a variety of tendon-driven fingers with both rigid and soft components were directly printed. Afterward, the actuation force and bending angles of the fingers with different geometries were measured to identify optimized design. Finally, a fully compliant, tendon-driven soft robotic gripper was fabricated, and its performance was measured.

5.2   MATERIALS AND METHODS

5.2.1   Materials

Filaments of rigid plastics, acrylonitrile butadiene styrene (ABS) and high-impact polystyrene (HIPS) sourced from filaments.ca were used as received. Pellets of styrene-ethylene-butylene-styrene (SEBS) with the commercial name Kraton G1657 was used as a soft elastomer for rubbery printed parts.

5.2.2   Printing using Intermixed Co-extrusion

Using a custom bracket cut by a CO_2 laser from 6-mm thick acrylic sheet, a tri-extruder head was assembled and attached to an inexpensive 3D printer purchased from Geeetech, China. An early version of this extruder, the bi-extruder was reported in our previous work[285]. This tri-extruder has three input channels, two of them were intended for feeding thermoplastic materials whereas the third input was kept unused by sealing with an M6 screw. The complete printer setup is shown in Figure 5.1(a), and a close view of the assembled tri-extruder is presented in Figure

127

5.1(b). An exploded 3D model of the dissembled tri-extruder can be found in Figure 5.1(c). The detailed drawings of the extruder head are given in the appendix of the supporting document.

A helical intermixer as shown in Figure 5.1(e) was designed and fabricated using Direct Metal Laser Sintering (DMLS) of 316-stainless steel powder by Proto Labs, Minnesota with 20 µm resolution. The intermixer has an overall diameter of 3.5 mm which can be inserted into a nozzle having an internal diameter of 4 mm. The 3D model of the intermixer is given in Figure 5.1(d). The intermixer is kept static, and polymer melt flows around the intermixer with mixing achieved by chaotic advection of the melt flows[267]. Mixing comes at the expense of extra resistance to flow, with longer static intermixers providing better blending but more losses from friction. Inserting the intermixer into the nozzle enables intermixed co-extrusion whereas, without the intermixer, simple side-by-side co-extrudates are achieved. To ensure that intermixing has no adverse impact on the quality of the extruded filaments, intermixed extrudate samples and side-by-side extrudate samples of ABS and HIPS were produced and compared for their fracture strength. Figure 5.1(f) and 5.1(g) show microscopic images of side-by-side and intermixed co-extrudates of red HIPS and blue ABS with the same (1:1) volume fraction. The co-continuous structure of HIPS and ABS was observed from their cross-sectional microscopic images. It was also found that the ultimate strengths of intermixed co-extrudates with different composition were comparable with those of side-by-side co-extrudates with the same polymer compositions, which indicates that the intermixing does not result in any voids or axial discontinuities in the material composition that could result in early failure of the extrudates
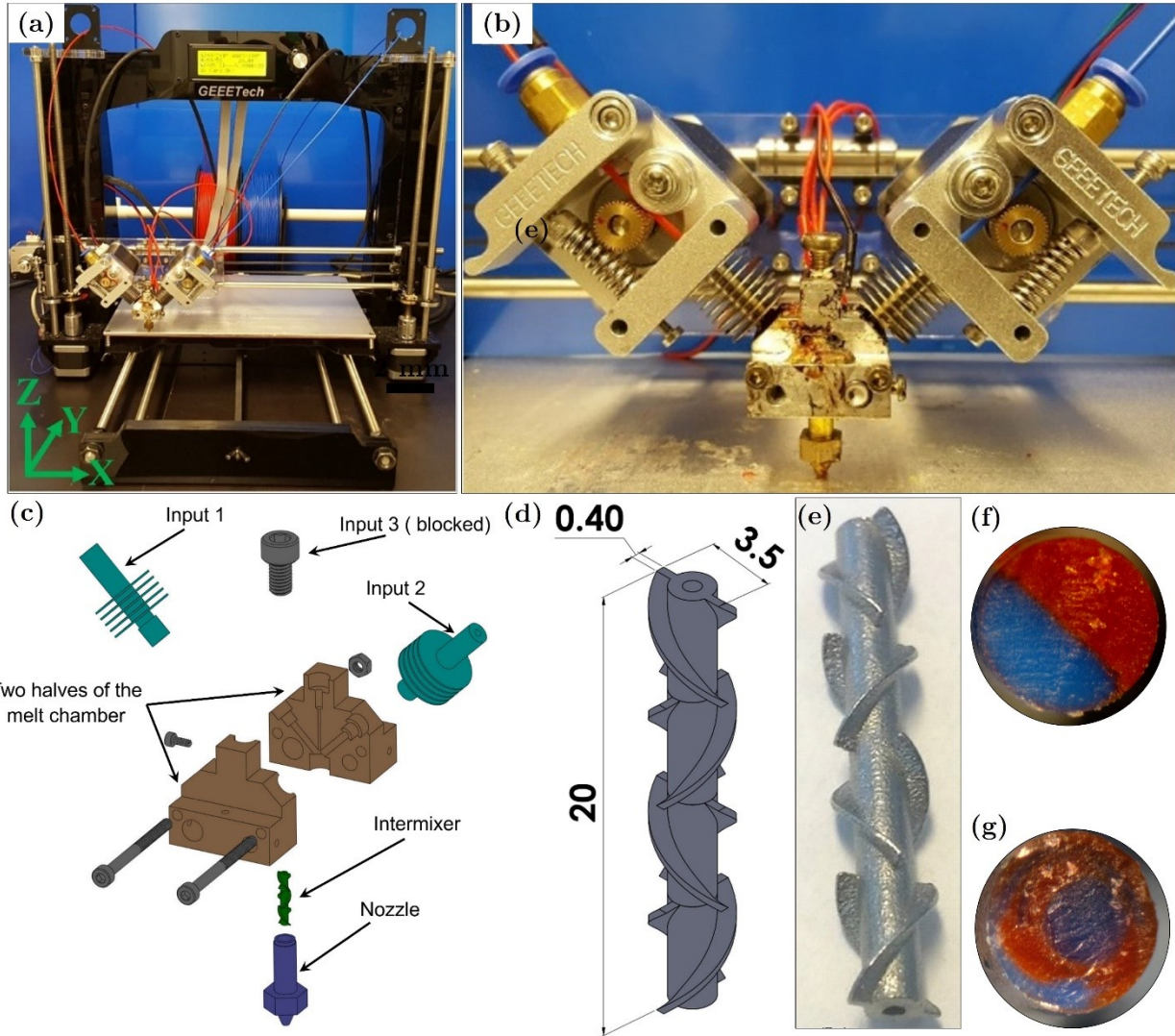
Figure 5. 1: (a) the complete 3D printer with the custom extruder installed, (b) a close view of the tri-extruder system, (c) The exploded 3D model of the tri-extruder hot end with helical intermixer, (d) the 3D model of the helical intermixer with dimensions in mm, (e) the helical static intermixer printed with direct metal laser sintering, (f) side-by-side co-extrudate and (g) intermixed co-extrudate of red HIPS + blue ABS with a ratio of 1:1.

5.2.3   Preparation of 2D Planar Samples

Planar samples with a single layer thickness are used to test the average adhesion strength of

adjacent deposited fibers. First, rectangular sheets with different compositions of ABS and HIPS

having only a single layer were printed with linear infill lines aligned along either the X or Y axes of the print bed. The test specimens were then cut from the rectangles by a CO_2 laser cutter. The dumbbell-shaped samples, as per ASTM D1708 guidelines[324], were cut to align the deposited fibers perpendicular to the loading direction. The ultimate strength of these samples represents the inter-fiber adhesion strength. Microscope images of the cross-sections where the samples failed were carefully examined to determine the mode of failure. Sections cut by a scalpel were used for image analyses of the original cross-section of the samples.

In the case of side-by-side co-extrusion (without intermixer), there are two types of samples, X-samples and Y-samples, with a distinctly different appearance. The X-samples are cut from the rectangle sheet which was printed by depositing infill fibers aligned with the X-axis, whereas, the Y-samples are from the sheets printed with infill fibers aligned with Y-axis. Figure 5.2(a) shows the orientation of the print head and the directions of the print axes while printing X-samples. It also shows microscopic images of the sections across the deposited fibers. Figure 5.2(b) shows details of Y-samples and confirms that the cross-sections of Y-samples have more of a true alternating arrangement which further reduces the degree of same-species diffusion of polymers. Figure 5.2(c) presents the dimensions of these 2D planar samples. The samples printed with intermixed co-extrusion do not have such an effect of print orientation; instead, the nature of intermixing is random without any pattern, as shown in the microscopic image in Figure 5.2(d).
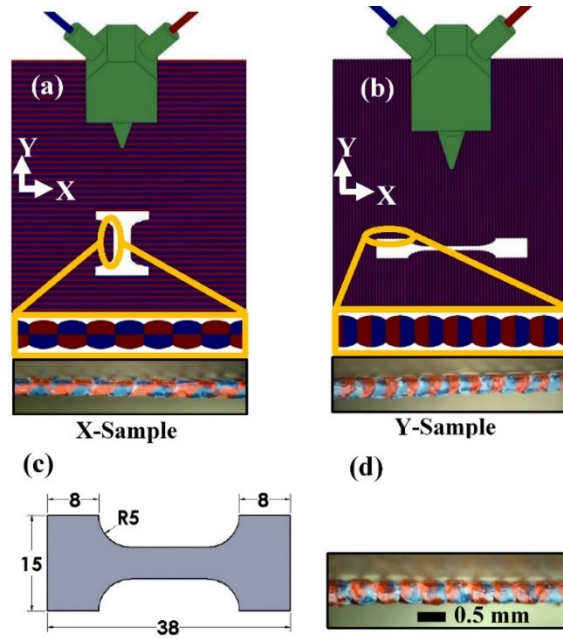
Figure 5. 2: The print orientation and microscopic images of flat sheets printed for (a) X-samples and (b) Y-samples in side-by-side co-extrusion. (c) The dimensions (in mm) of the 2D planar samples and (d) the microscopic images of the intermixed samples across the deposited fibers.
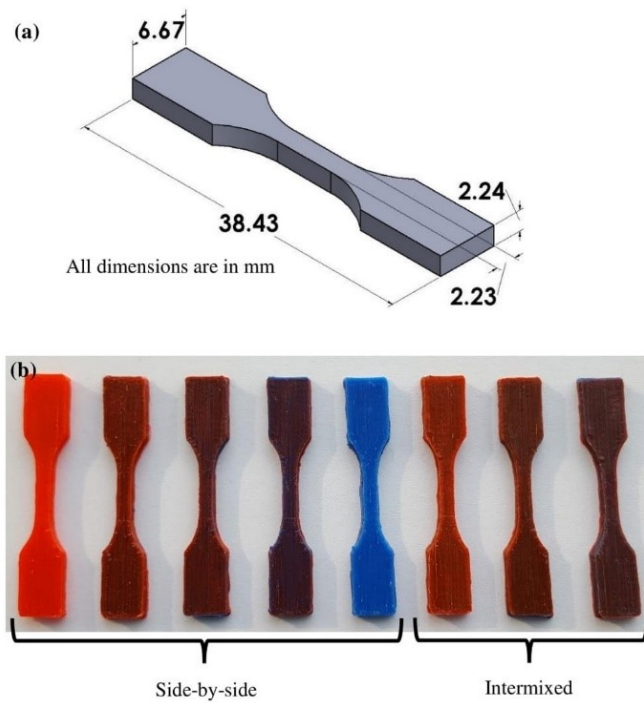
Figure 5. 3: (a) Dimensions of the 3D models modified from test coupon Type V of ASTM D638 standard and (b) photographs of the printed 3D samples of red HIPS and blue ABS.

131

5.2.4 Preparation of 3D Samples

3D dog-bone style test coupons were printed for ultimate strength testing based on a version of ASTM D638-10 standard. The ASTM guideline has five different test coupons, type I through type V. A modified test coupon of type V was used for this study following the similar method reported in liturature[325] to balance print size and load cell limits for our MTS system. Photos of 3D samples of different composition of red HIPS and blue ABS printed with both types of co-extrusions are depicted in Figure 5.3. These samples were printed using 0°/90° raster angles with each alternating layer having a 0.5 mm layer width and a 0.4 mm layer height. The print-bed temperature was set at 90°C during printing.

5.2.5 Design of Tendon-Driven Finger

The finger designed in this work has four main components: a flexible main structural body, two rigid channels for the tendon systems, two soft rubbery layers on both gripping surfaces and two inextensible tendon systems. Figure 5.4(a) shows these components where the capability of the bidirectional actuation system of a finger can be seen. The flexible main body serves as the backbone of the finger. The overall stiffness of the finger is determined mainly by the composition and thickness of this flexible backbone. In this work, eight different finger samples (A through H) were designed and characterized to compare their actuation forces and bending angles with respect to the tendon displacement. These fingers differ in thickness or composition of their backbone unit as illustrated in Figure 5.4(b). Except for sample F, all other samples were printed with an intermixer inserted. Samples A and B have identical dimensions with a 2 mm thick backbone unit. The only difference is that sample B is printed entirely from SEBS. Unless explicitly

mentioned, when switching between red HIPS and transparent SEBS during printing, the composition was changed gradually within four layers. This gradual transition of HIPS and SEBS can be seen in Figure 5.4(c). When these fingers are actuated, one side of the finger will be under compression while another side will be under tensile loading. As they are symmetric, the neutral axis lies on the geometric center line of the finger. Both samples C and D have a 4 mm thick backbone unit; however, sample D has one 100% HIPS layer at the neutral axis of the finger to enhance overall axial stiffness. This stiffness enhancing HIPS layer with abrupt transition can be seen in Figure 5.4(d). Sample E, F and G have an 8 mm thick backbone unit with different composition and extrusion type. The backbone units of Sample E and F are entirely composed of SEBS but printed with intermixed and side-by-side extrusion, respectively. On the other hand, the backbone unit of sample G is composed of 33% HIPS and 67% SEBS. Lastly, sample H has a thicker SEBS backbone unit with 12 mm thickness. All these samples have a 1 mm thick SEBS layer on the upper surfaces of the rigid channels on both sides to increase the coefficient of friction of the gripping surface. The dimensional comparison of these samples can be found in Figure 5.5.

Nylon string was used as an inextensible tendon for the fingers. A rectangular channel within the rigid pillars was used for the tendon system. The purpose of having extended upper surfaces of these pillars is to increase the grasping contact area. It is necessary to have a rigid channel for the tendon to avoid deformation of these individual sections when actuated. Each of the fingers has two tendon systems on both sides to enable bidirectional actuation. Another advantage of this bidirectional actuation is its agonist-antagonist balanced structure which ensures the finger can

hold an actuated position even when being loaded. The free end of the finger has a slope to avoid

edge contact with the object when actuated.
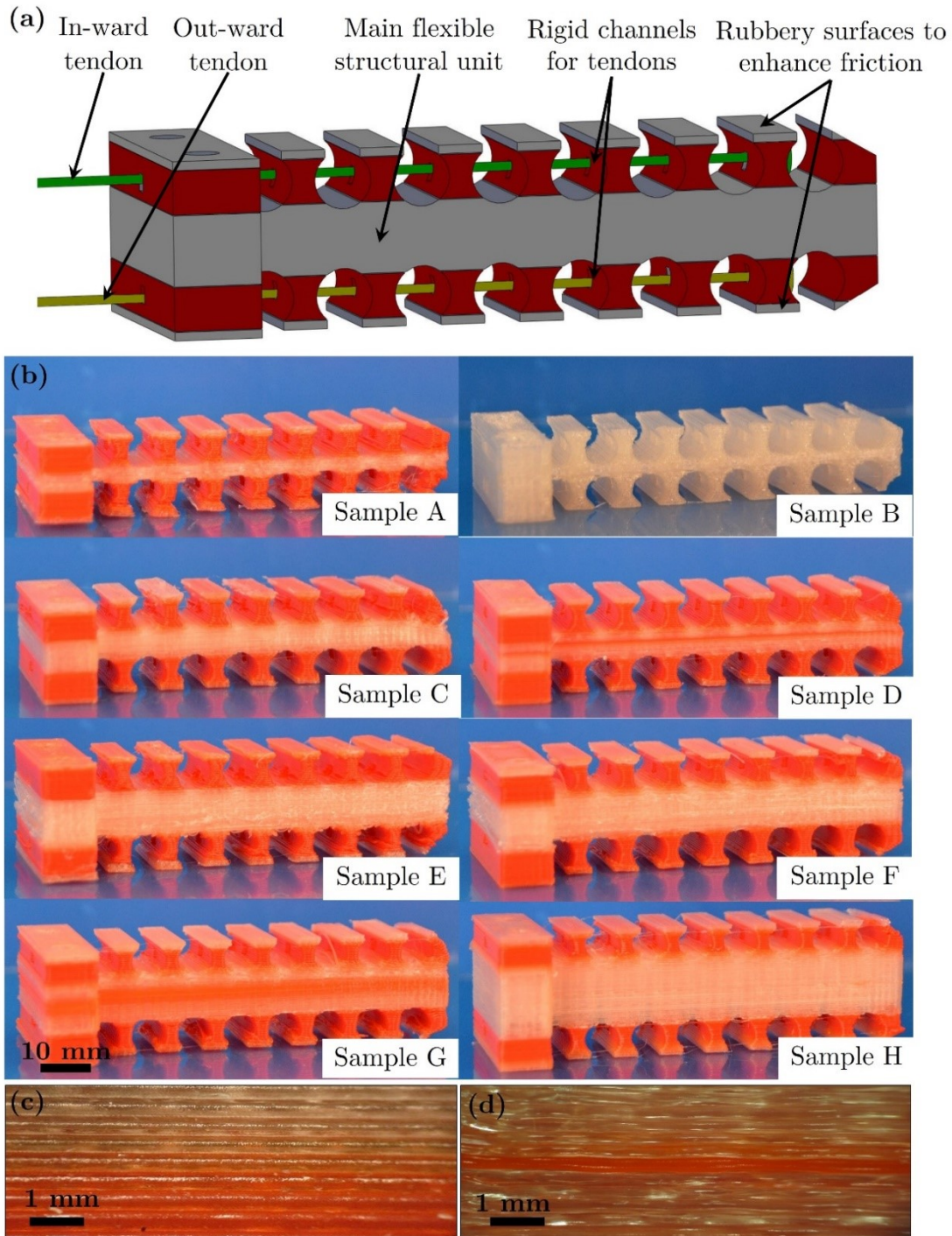
Figure 5. 4: (a) The 3D model of a tendon driven soft actuator showing all functional structural components, (b) photographs of all eight different samples printed, microscopic image showing

134

vertical transition from red HIPS to transparent SEBS (c) and sharp transition with single layer of red HIPS at the neutral axis of sample D.
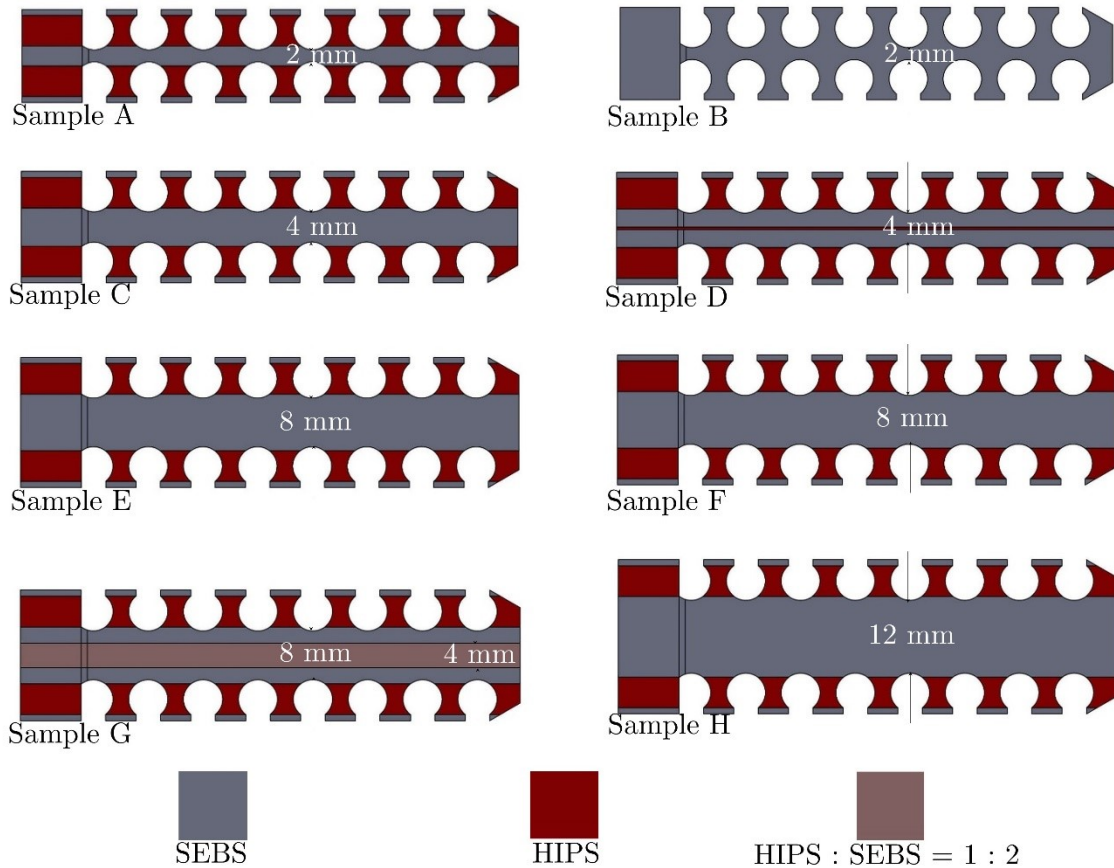
Figure 5. 5: The structures of different samples of the tendon driven actuator.

5.3   RESULTS AND DISCUSSION

5.3.1   Tensile Tests of 2D Planar Samples

Once the 2D planar samples are prepared, they were tested with an ElectroForce® 3200 Series III Test Instrument to compare the inter-fiber adhesion of samples printed from side-by-side and intermixed co-extrusions. The side-by-side Y-samples have the closest to true alternating materials across the infill lines which provide the most favorable condition for delamination. In contrast,

135

the X-samples demonstrate some degree of same-species polymer diffusion near the center of the interface of two adjacent deposited fibers as shown in Figure 5.2(a). Intermixed samples show much more mechanical keying in the individual deposited fibers by possessing the co-continuous structure of both HIPS and ABS. After tensile testing, the cross-sections of all the samples at their failure locations were photographed under a microscope to determine the mode of failure. It was determined that all the side-by-side samples failed by separation of two fibers having weakest adhesion at their interface, suggesting adhesive failure mode. The following sections describe the effect of significant printing parameters on the adhesion strength of these samples. Table 1 lists ranges of all the parameters tested while printing the 2D samples examined in this section. When printing the samples to test the effect of a particular factor, other factors were kept fixed at the mid-level in Table 5.1

Table 5. 1: Factors with their high, low and mid-levels

Factors	*Levels*		
Nozzle temperature	235 ºC	250 ºC	265 ºC
Layer width	0.35 mm	0.5 mm	0.65 mm
Print speed	30 mm/s	60 mm/s	90 mm/s
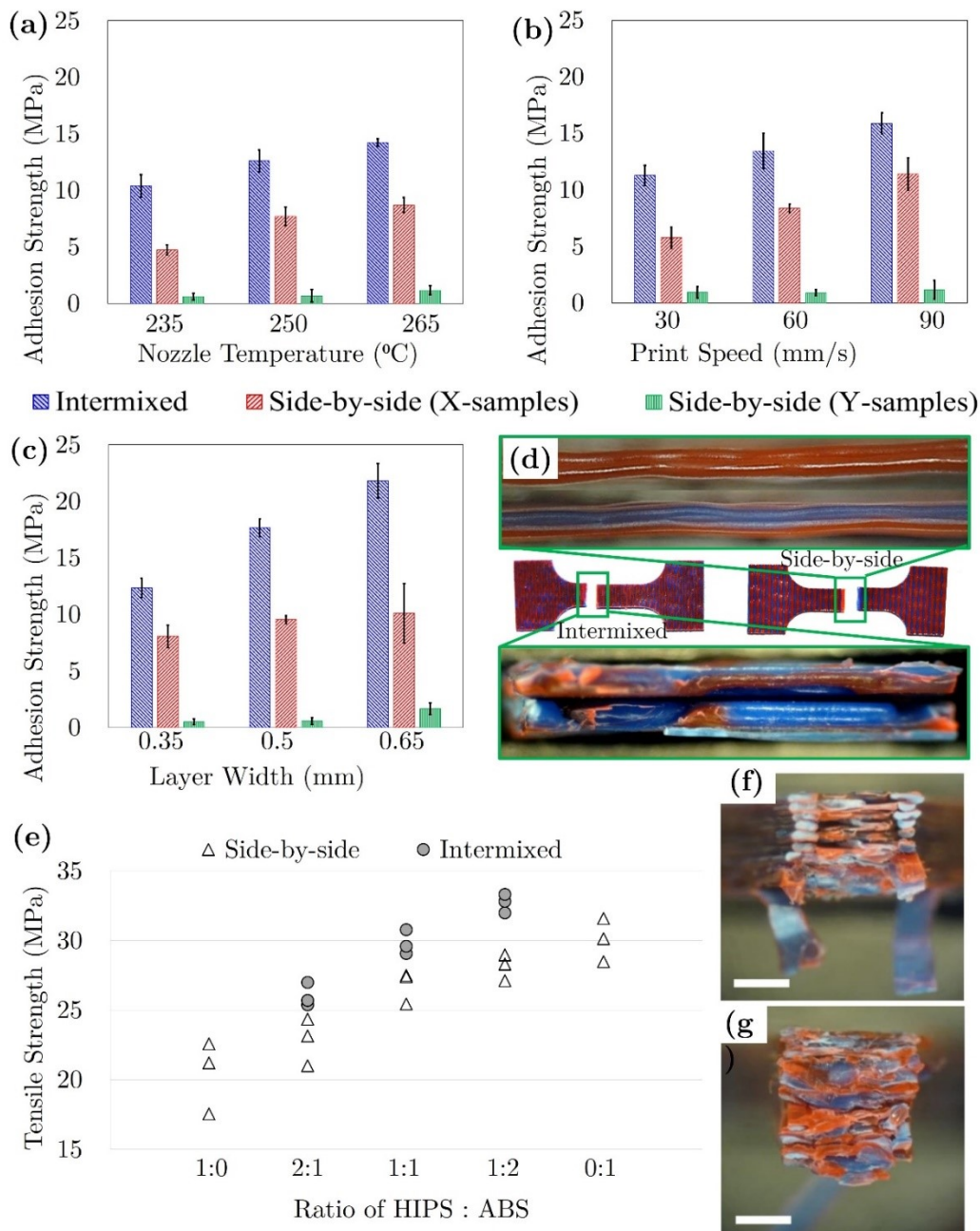
Figure 5. 6: The effect of (a) nozzle temperature, (b) layer width and (c) print speed on the adhesion strength of adjacent fibers in 2D planar samples. (d) photos of an intermixed 2D sample (left) and a side-by-side 2D sample (right). The microscope images of the failed cross-sections of these planar samples: side-by-side X sample (inset-top) and intermixed sample (inset bottom). (e) Ultimate tensile strength (UTS) of 3D samples (both intermixed and side-by-side) with different composition of HIPS and ABS. The microscopic images of two representative side-by-side (f) and intermixed (g) samples having the same 50%-50% composition of red HIPS and blue ABS (scale bars are 2 mm).

137

5.3.1.1   Effect of Nozzle Temperature

Nozzle temperature is a very important factor to be considered in FDM printing. In FDM, the nozzle temperature governs the temperature of the deposited fibers being adhered to the previous fiber[326]. This initial temperature of just deposited fiber controls the degree of thermal motion such as reptation and diffusion of polymer chains across the interfaces of deposited fibers. Therefore, a higher nozzle temperature results in higher adhesion strength of adjacent layers. However, excessively high nozzle temperature may also induce degradation of the polymer materials, so it cannot be increased indefinitely without cost. From Figure 5.6(a), higher extrusion temperatures increase adhesion strength for all types of printing, but in all cases, the intermixed adhesion strengths were the highest. Y-samples showed very weak bonding compared to X-samples, which is true for all the tests performed in this section. This phenomenon indicates a major weakness of side-by-side co-extrusion in manufacturing robust gradient parts as these interfaces will result in substantial bond weaknesses within larger components.

5.3.1.2   Effect of Layer Width

The layer width is defined by the user while slicing the object. A higher layer width increases the polymer extrusion rate. Therefore, if the air gap between each deposited fiber is kept the same that results in a larger overlap between adjacent deposited fibers, it reduces voids within the fill volume and favors the thermal movement of polymer chains because of more contact area; overall resulting in higher adhesion strength. A larger layer width also slows down the cooling due to more thermal mass;[327] thus it increases the degree of diffusion of polymeric chains through the

fiber interface. Increasing layer width increases the apparent adhesion strength between fibers as shown in Figure 5.6(c), but it primarily improves bonding between filaments due to increased bonded area. In this analysis, the adhesion strength was estimated based on the thickness of the sample, assuming the cross-sectional area to be the same for all samples with different layer width. An increase in layer width from 0.35 mm to 0.65 mm resulted in over 70% increase in adhesion strengths in intermixed samples. For side-by-side X-samples, this increase in average adhesion strength was only ~25%. In Figure 5.7, the adhesion strength corrected for the measured thickness is presented where the layer width effect disappears; confirming that the increased contact area due to higher overlapping caused the apparent increase in adhesion strength.
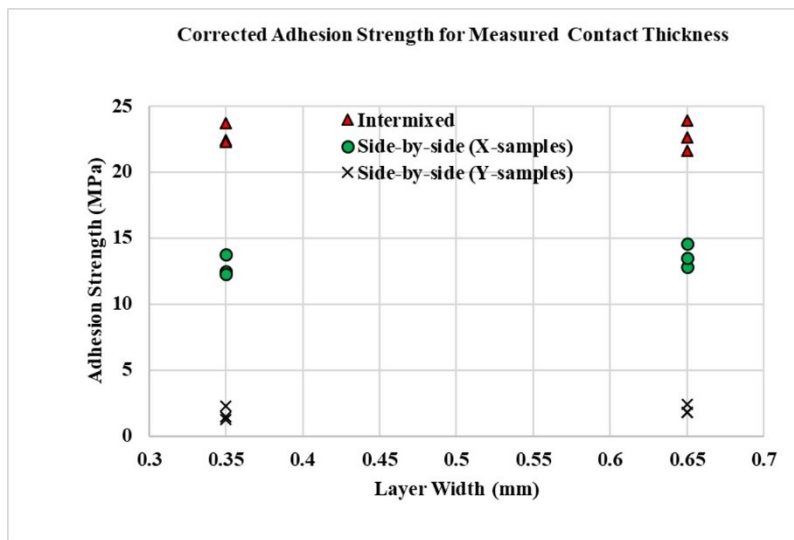
Figure 5. 7: The adhesion strength of the samples corrected with measured thickness of the samples printed with two different layer widths.

5.3.1.3   Effect of Print Speed

The effect of print speed is not as significant as layer width, but it also plays a role in governing

the adhesion between adjacent fibers. Faster print speed enhances adhesion strength as shown in

Figure 5.6(b). In the case of higher print speed, each fiber has less time to cool before the next

fiber is deposited, resulting in more diffusion with newly deposited fiber. Hence, samples printed

with 90 mm/s have on average 40% higher adhesion strength compared to samples printed with

30 mm/s. In literature,[328] a similar effect was also observed by Pan *at el.* However, as the print

object size increases this effect seems to diminish because the deposited fibers take only on the

order of a few seconds to cool down, hence imposing a time limit for improved adhesion.

Figure 5.6(d) explains the mode of failure in the case of side-by-side (X-samples) and intermixed

samples with a 1:1 ratio of red HIPS: blue ABS. In the inset images, the microscopic images of

the failed cross-sections of 2D samples are shown. The side-by-side (X-samples) have an obvious

bimorph structure of the polymers resulting in delamination dominated adhesive failure. On the

other hand, the intermixed samples show a combination of adhesive and cohesive failures as

depicted in the inset image which contributes to the higher layer adhesion of deposited adjacent

fibers.

5.3.2   Tensile Tests of 3D Object Samples

3D samples were also tested on the same ElectroForce® 3200 Series III Test Instrument to measure

the ultimate tensile strength (UTS) of side-by-side and intermixed samples. Each data point of

this analysis represents the average strength of three repetitions, and the overall consistency of

measured strength demonstrates that intermixing enhances the mechanical strength of 3D objects of ABS and HIPS. From Figure 5.6(e), pure HIPS and ABS samples showed an average tensile strength of 20.44 MPa and 30.06 MPa, respectively. As the composition of ABS increases, the UTS of the sample also increases for both intermixed and side-by-side extruded parts roughly suggesting the rule of mixture holds for these parts despite potential bonding challenges. In all cases, the intermixed 3D samples showed more than 10% higher UTS than their side-by-side extruded counterparts, which is not as significant as the 2D samples. This can be attributed to the fact that in 3D structures the materials are already partially interlocked in all three directions due to different fill angles and the subset of filaments already aligned in the direction of the loading. After the tensile tests, the fractured samples were imaged and examined to understand the mode of failure better. As expected, the side-by-side samples (Figure 5.6(f)) showed significant inter-layer delamination, which was not seen in the case of intermixed samples (Figure 5.6(g)).

5.3.3 Characterization of Tendon Driven Actuators

To compare the performance of different finger samples, the actuation force and deflection angle generated by the fingers were measured for different tendon displacements. These properties are mainly determined by the overall stiffness of the finger. The ideal finger should have a higher actuation force and a higher deflection angle for a specific tendon displacement. Once the tests are performed, the best sample finger was used to develop a compliant gripper.

5.3.3.1   Actuation Force Measurement

An acrylic support was designed to hold the fingers horizontally to ensure that the tip of the finger barely touches another flat acrylic sheet which is fixed to a load cell (Transducer Techniques, MLP-10) held by acrylic support. A National Instrument motion controller (Model No. ESP301) along with a data acquisition (DAQ) hub (NI USB-6289) and a Windows Presentation Foundation (WPF) application written in C# was used to apply tendon displacements and measure the corresponding actuation forces. The test setup is presented in Figure 5.8(a), and the variation of measured actuation forces for different tendon displacements of all samples are shown in Figure 5.9. Samples A and B showed relatively higher bending angles, and lower actuation forces compared to the other samples. Sample G was found to generate the largest actuation force up to 10 mm of tendon displacement. The actuation force of this sample was even larger than that of sample H with the thickest (12 mm) flexible backbone unit because it was stiffest in bending. Sample D experienced major interface failure when actuated by a 15 mm tendon displacement. A close observation, as in Figure 5.10(a), indicates that this failure was mainly because of the sharp transition between HIPS and SEBS – further evidence of the importance of gradient and intermixed parts. Hence, from the perspective of actuation force, samples E, F and H showed the best potential to be used in compliant grippers.

5.3.3.2   Displacement Angle and Tensile Force Measurement

Another acrylic support was designed to hold the fingers horizontally and keep one end of the finger fixed as a cantilever beam. Then the tendon cable was attached to one side of a load cell and another tendon was attached from the other side of the load cell to a three-axis stage. The same DAQ system was used to measure the linear displacement of the tendon cable and corresponding tensile force applied through the tendon cable. A high-speed camera was positioned horizontally to capture the images of the deflected finger. A ruler placed beside the finger was useful when measuring the deflection angles via image processing. Figure 5.8(b) shows the experimental setup to measure the angles of deflection and applied tensile force of the fingers. Figure 5.8(c) and 5.8(d) show successive actuation of two samples with different stiffnesses. The sample with only a 2 mm thick backbone unit has low stiffness which is confirmed from its higher tip deflection whereas another sample with an 8 mm thick backbone unit results in much less actuation for the same amount of tendon displacement. From Figure 5.9, sample A shows the highest bending with a lower tensile force requirement, indicating its stiffness is the lowest. Sample B also shows a similar trend; however, its deflection angle is slightly less than that of sample A. This is believed to be caused by the fact that under tendon displacement the soft tendon channel is also deformed nullifying some degree of actuation by the tendon. By increasing the thickness of the backbone unit to 4 mm, samples C and D require higher tensile force to actuate to a certain angle. This force requirement was highest in the case of sample G which had an 8 mm thick flexible backbone unit with a 4 mm thick semi-rigid backbone unit. It was necessary to apply more than 15 N tensile loads to continue actuation after a 5 mm tendon displacement with very

143

limited deflection angle. Sample H showed reasonable deflection with actuation force; however, its tensile force requirement was also noticeably higher than that of samples E and F. Therefore, based on the actuation force, angle and tensile force requirements, samples E and F were found to have potential to be used in developing the compliant gripper. These two samples have the same dimensions and construction with the only difference being their constituent extrudate type, intermixed vs. side-by-side. To further examine the effect of extrudate type on the actuation performance of the finger, a cycle-test was conducted where the fingers were actuated 10,000 times in both directions. In this study, a complete cycle includes actuating the finger in one direction, de-actuating back to neutral position with the same tendon, actuating again in the other direction with the other tendon and finally de-actuating back to the neutral position. The deflection angles of both fingers before and after the cycle test were plotted as shown in Figure 5.10(b). It was found that, though the intermixed sample E does not show any major discrepancy in deflection angle after 10,000 runs, however, sample F printed with side-by-side co-extrusion results in a noticeable decrease in deflection angle after the cycle test. To understand the reason behind this phenomenon, both the samples were carefully observed under a microscope. At no actuation condition, no changes were visible. However, when they were actuated and observed under the microscope, it was found that the side-by-side sample F showed localized, small-scale layer-wise delamination (as depicted in Figure 5.10(c)) at selected HIPS and SEBS interfaces where hard HIPS and soft SEBS were in poor contact. Sample E did not show any such failure even after 10,000 cycles. This study confirms the necessity of intermixed co-extrusion of two mechanically

144

distinct polymers in gradient printing to eliminate anisotropy in mechanical properties resulting from printing orientation.
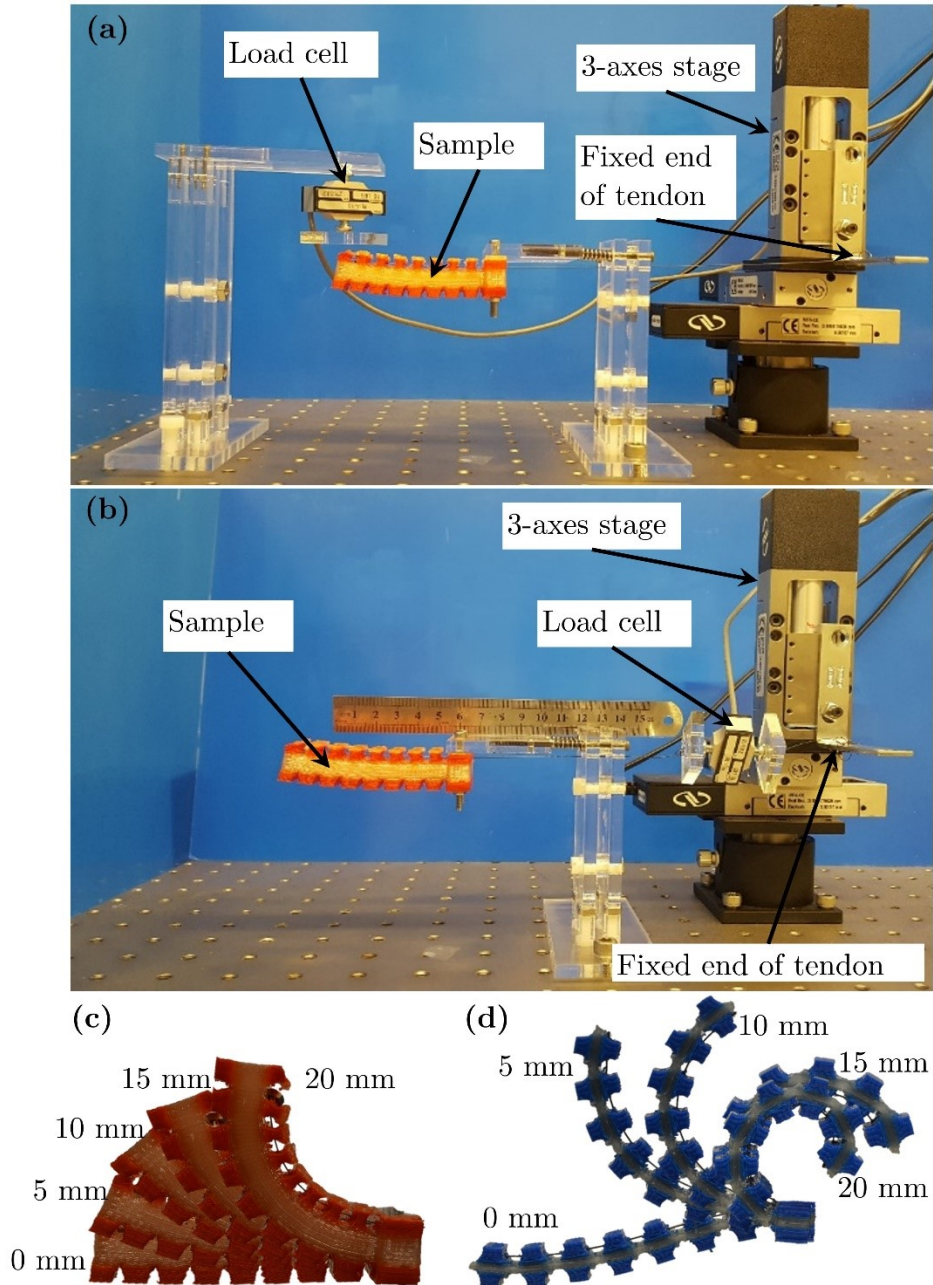
Figure 5. 8: Test set-up to measure actuation force vs. tendon displacement applied (a), and tip deflection & applied tensile force vs. tendon displacement. Time lapsed superimposed images showing the actuation of (c) sample E and (d) sample A for 0 mm, 5 mm, 10 mm, 15 mm, 20 mm tendon displacement. It shows that actuator with low stiffness results in higher tip deflection.
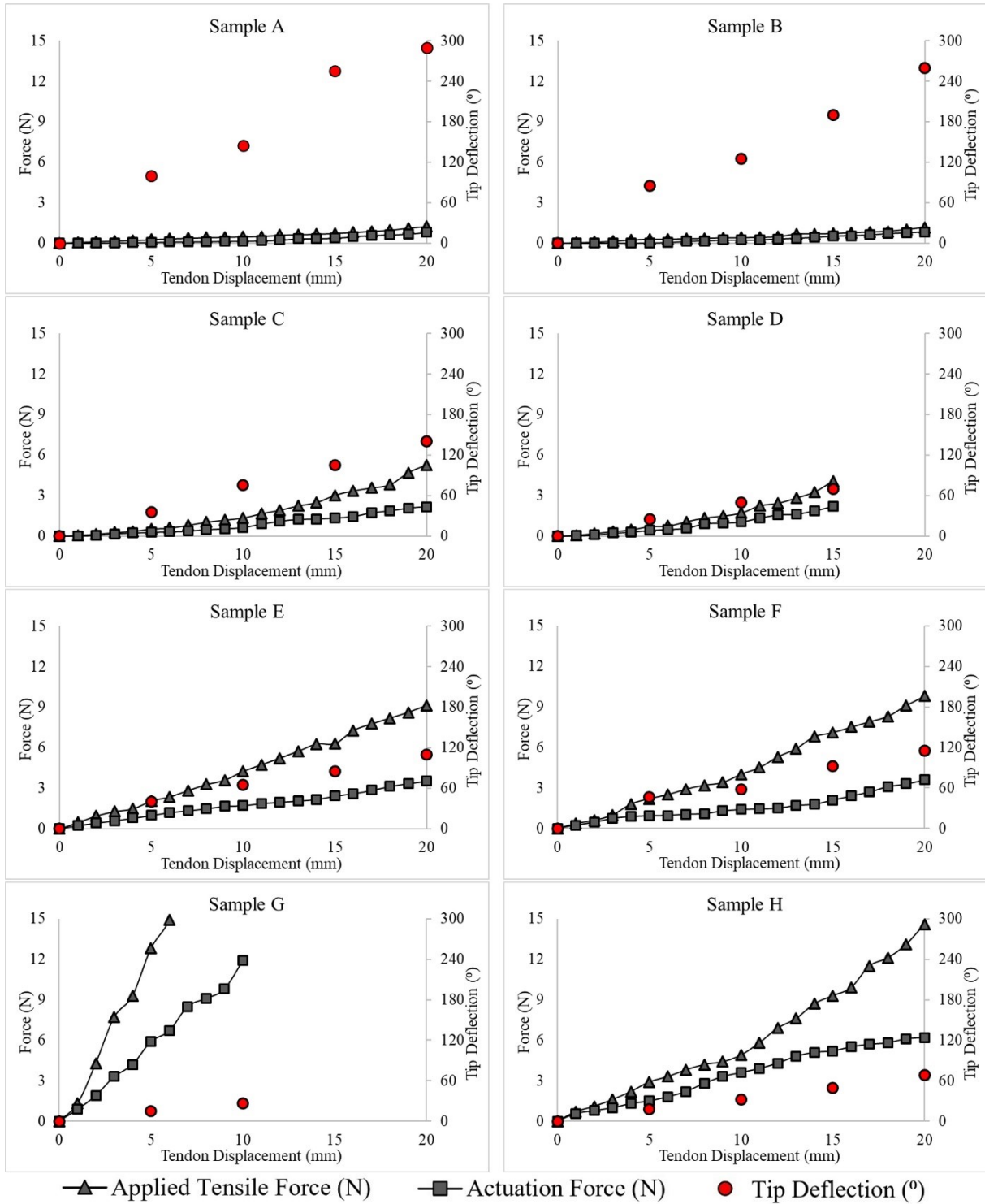
Figure 5. 9: The measured tip deflection, actuation force and applied tensile force vs. tendon displacement of sample A through sample H.

146
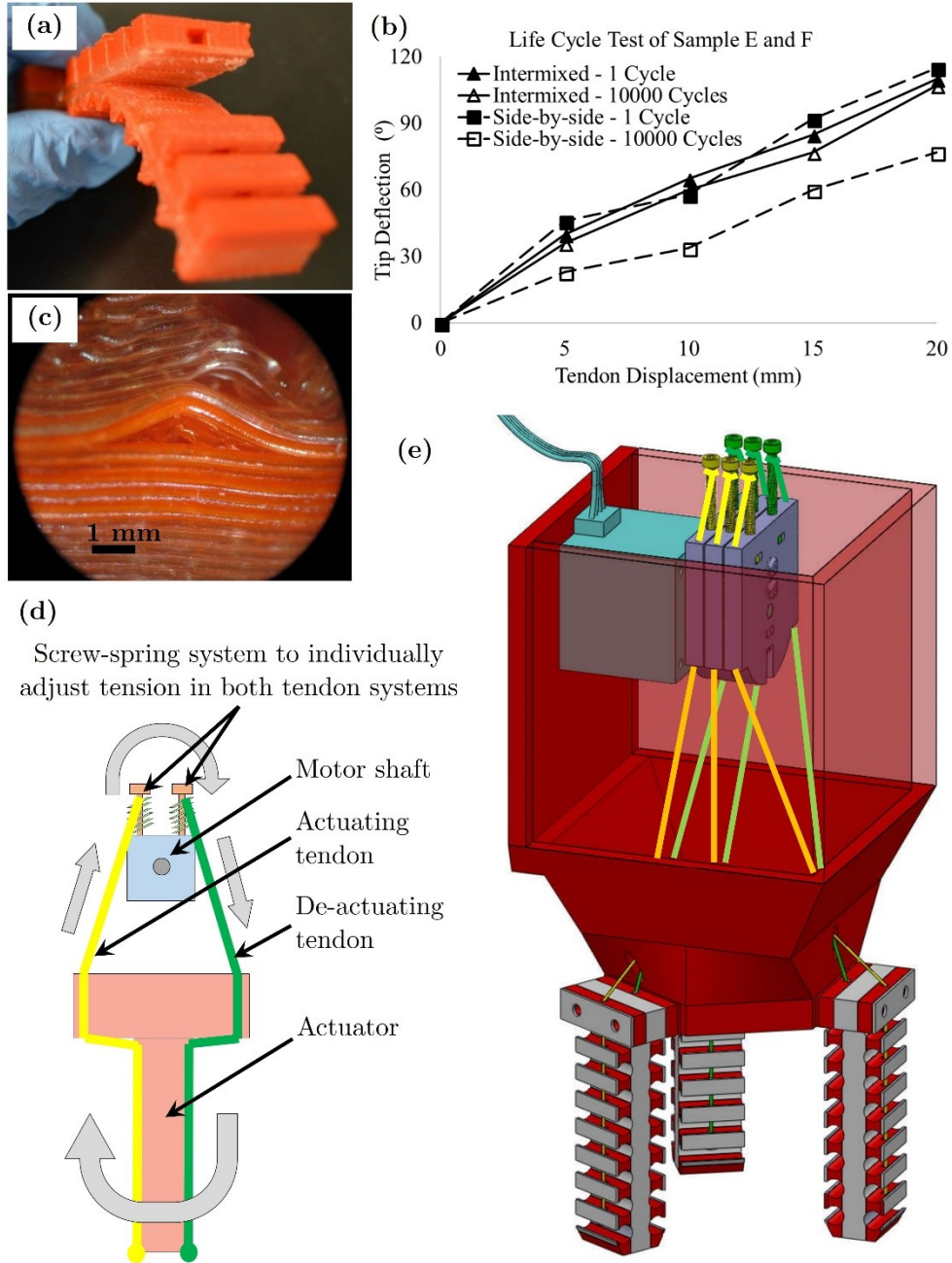
Figure 5. 10: (a) A photograph showing the interface failure of sample D due to sharp transition between red HIPS and transparent SEBS, (b) actuation angle vs. tendon displacement for sample E and sample F before and after 10000 actuation cycle tests, (c) a microscopic image of one of the layer adhesion failure of side-by-side printed sample F after 10000 cycle test, these types of adhesion failures were not seen in intermixed sample E. (d) a schematic of two-way actuation mechanism of the printed actuators showing its agonist-antagonist balanced system. With clock-wise rotation of motor shaft, green tendon displaces exactly same amount as yellow tendon displaces, resulting in clock-wise actuation of the actuator. And (e) a 3D model of the tendon

147

driven soft robotic gripper based on sample E. The screw-spring mechanism ensures each tendon can be individually adjusted to maintain same degree of tension resulting no actuation of all three fingers. Yellow tendon system is used for out-ward actuation whereas green tendon system induces in-ward actuation.

5.3.3.3   Stiffness Measurement

The tensile force required to actuate the finger was measured over a range of tendon displacements as discussed above. This tensile force showed a nearly linear relationship with the tendon displacement. Hence, the overall stiffness of the finger can be calculated, as done by Mutlu *et al.,*[304] as the linear fit slope of the tensile force vs. tendon displacement plot as shown in Figure 5.9. The deviation of these plots from a linear fit is believed to be caused by the gap between tendon cable and its channel, possible slack in tendon cable, slight initial stretching of the cable itself and the deformation of the finger. The measured actuation force generated by the finger was substantially smaller than the tensile force applied through the tendon cable. This mechanical loss may be due to different forms of losses such as friction between tendon and finger, the energy dissipated to deflect the finger, and loss due to deformation in soft components.

5.3.4   Development of a Fully Compliant Gripper

Finger E was found to have the best performance based on all the analyses, so two more fingers were printed with the same dimensions. A fully compliant gripper with three fingers was constructed to demonstrate the conformity of the proposed fingers with both hard and soft components. Three tendon cables from each finger form a set of tendons. Hence, there are two

sets of tendon systems; one set is for actuating all fingers toward the inward direction of the gripper while the other set actuates them outward. The inward tendon system is actuated when a grasping action is desired whereas the outward tendon system is actuated when a releasing action is required. Due to the ability of these fingers to actuate in both directions, the gripper can grasp objects which are larger than its size. It was necessary to make sure that all the tendon cables actuate at the same time which was ensured by keeping both sets of tendon systems always in tension. Figure 5.10(d) shows a schematic diagram of a finger depicting its agonist-antagonist balanced structure. With the help of a screw-spring mechanism, each tendon can be adjusted individually to control the tension. The tendons were attached to an acrylic rotor which was coupled with the shaft of a stepper motor. As shown in Figure 5.10(d), if the motor rotates in a clock-wise direction, it induces tension in the yellow tendon and reduces tension in the green tendon. That results in an outward actuation of the fingers as shown in the figure. This agonist-antagonist balanced system ensures that the displacements in both tendons remain the same with the opposite direction. The 3D model in Figure 5.10(e) was based on red HIPS and transparent SEBS with green inward and yellow outward tendon systems. The actual gripper was successfully used to handle different sized objects with non-geometric irregular shapes softly. Figure 5.11 shows time-lapse images of the gripper where it was used to grasp a ceramic table-clock. This action starts with outward actuation to open the gripper, followed by a no-actuation step when it surrounds the object being handled. Then, by actuating in the inward direction, the fingers touch the object and exert force over the contact area. Finally, grasping is complete, and the object can be lifted and handled accordingly. Apart from being able to grasp larger objects, the benefit of

bidirectional actuation also includes the capability of this gripper to grasp objects from inside a

hole, for example, a beaker.

(a) No actuation   **(b)** Opening: out-ward actuation

(d) Lifting: gripping complete   **(c)** Grasping: in-ward actuation

Lifting
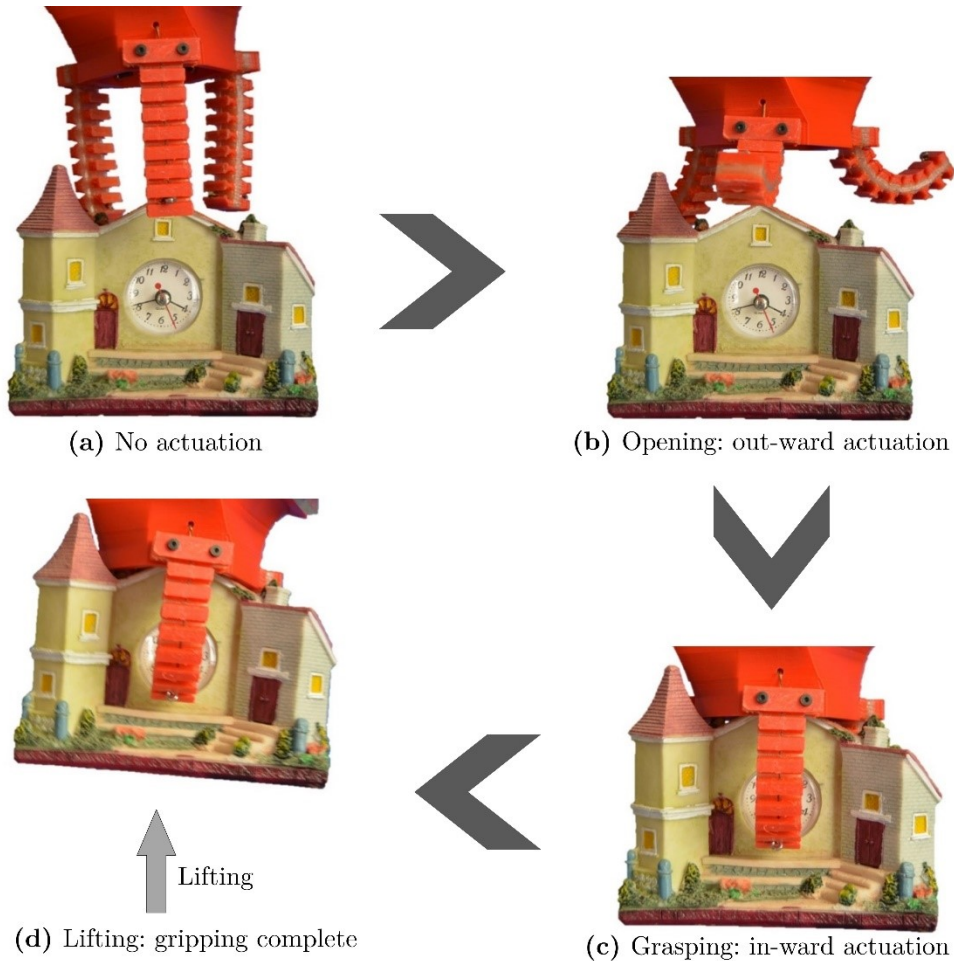
Figure 5. 11: A series of photographs (background removed for clarity of the illustration) of grasping action of the developed gripper. The gripper was used to handle a table clock which is larger than the size of the gripper.

5.4   CONCLUSIONS

The custom extruder system developed in this work has the intermixing capability to co-extrude

multiple dissimilar thermoplastic polymers with mechanical interlocking structure within the

extrudate. The intermixing was found to have the same composition percentage along the length of the extrudate and has no adverse effects on the mechanical strength of the extrudates. Without the intermixer, the extruder is also able to co-extrude materials in a simple side-by-side manner but doing so resulted in high bonding strength anisotropy depending on the direction of deposition. Compared to samples printed with side-by-side co-extrusion, the samples from intermixed co-extrusion showed significantly higher adhesion strength of two adjacent fibers deposited in the same layer with at least 12 times higher adhesion strength compared to side-by-side Y-samples. Moreover, the 3D objects printed with intermixed extrudate also have higher ultimate tensile strength compared to their counterpart from side-by-side co-extrusion. To demonstrate its performance, tendon-driven fingers with both hard and soft body parts were 3D printed in a single process using the custom extruder. To resist interface failure of hard and soft materials, the parts made of mechanically interlocked co-extrudates were printed with a gradual transition from one material to another. As a result, flexible fingers with rigid stiffer tendon systems without any bonding failure were 3D printed in a single step. Finally, these fingers were successfully integrated into a compliant, soft robotic gripper which can handle irregularly shaped objects.

6. CHAPTER: DIRECT 3D PRINTING OF STRETCHABLE CIRCUITS VIA LIQUID METAL CO-EXTRUSION WITHIN THERMOPLASTIC FILAMENTS[**]

6.1 INTRODUCTION

Three-dimensional conductive microstructures embedded in elastomers have a great potential for uses in flexible and stretchable electronics applications [18]. Liquid metals (LM) with superior conductivity have gained popularity among the research community because their conductive structures embedded in elastomers can withstand repeated stretching and bending without any noticeable electrical or mechanical loss [89]. Although Mercury (Hg) was initially used in this field [74,75], recently its use has been avoided due to its toxicity [77,78]. In the last decade, gallium-based, non-toxic [81], LM alloys have been applied in numerous applications where uninterrupted electrical conductivity at high mechanical strain is necessary [18,89,155]. There are two widely used gallium based LM alloys: eutectic gallium indium (EGaIn) and Galinstan. EGaIn is a eutectic

---

[**]A version of this chapter is submitted for publication as: Khondoker, Mohammad Abu Hasan, Ostashek, Adam and Sameoto, Dan; Direct 3D Printing of Stretchable Circuits via Liquid Metal Co-Extrusion within Thermoplastic Filaments. *Advanced Engineering Materials.* ID: adem.201900060. Reproduced with permission from John Wiley & Sons.

alloy of gallium (Ga) and indium (In) with a typical composition of 75.5% Ga and 24.5% In, having a melting point of 15.5 ℃ [79]. Galinstan represents a family of eutectic alloys of different compositions of Ga, In and tin (Sn) without a generic melting point. However, the most common form of Galinstan has a composition of 68.5% Ga, 21.5% In and 10% Sn and a melting point of − 19 ℃ [79]. Both classes of LM alloys show similar physical properties. Currently, they are considered to be superior electrical conductors for extremely stretchable electronics such as wearables and mechanically tunable antennas because these functional devices can be integrated onto non-rigid substrates like textiles, clothing, and sensors [102,329,330]. These LM alloys have a very high electrical conductivity (approximately 1/16th that of copper [82]) compared with most electrically conductive inks or composites, and their ability to strain while remaining conductive is limited primarily by the mechanical properties of the surface or material to which they are bonded. When exposed to air, gallium alloys form a "skin" of gallium oxide [84], which helps pin the metal to different surfaces. Unlike electrically conductive composites, these LM alloys are not as susceptible to large resistance changes at high elongations due to the separation of conductive fillers. Rather, the LM alloy deforms to fill the volume in which it is contained. The most common fabrication techniques of LM-based microstructures include stencil printing, injection into microchannels, direct writing, and droplet deposition [18,82]. The low inherent viscosity of gallium based LM alloys, combined with non-Newtonian behavior caused by the native gallium oxide layer, makes a direct extrusion of the unmodified material exceptionally difficult to achieve, although one recent solution that holds some promise involves the combination of micro-particles with LM alloys to form thixotropic pastes [331]. Regardless of the patterning method, for all

actual end applications, an encapsulation step or an additional injection step is necessary to prevent liquid metal circuits from being destroyed by mechanical abrasion or contact with other surfaces [140,147,332]. Because of this, direct printing of liquid metal in additive manufacturing processes is still an unsolved issue. Only one paper to date has demonstrated a method for direct encapsulated printing of EGaIn, and it was difficult to achieve consistent streams of liquid metal because the viscosity of the surrounding silicone rubber was relatively low [333]. To address this encapsulation challenge, we demonstrate for the first time the use of a thermoplastic FDM extruder combined with a coaxially extruded LM core to produce directly printed stretchable wires that can be deposited in 2D or 3D shapes. This printing method is compatible with other thermoplastic or thermosetting process steps and can also produce very thin wire cross-sections through a combination of extrusion and drawing processes – eliminating most of the challenge of injecting liquid metal into small diameter channels [7]. Although in this work, only LM alloy was used as the conductive material, however, the technique can also be utilized to print with other low-melting-point metals and alloys such as gallium, bismuth, tin, and indium-based alloys which melt up to around 250 ℃ [334]. Using low melting point metals or alloys has potential in the applications where stretchability is not a desired property, but rather the mechanical strength, conductivity or density are of primary concern.

As an insulating material, thermoplastic material with high stretchability, flexibility, and mechanical stability was desired. Based on these properties, a thermoplastic elastomer, styrene ethylene butylene styrene (SEBS), was chosen because of its superior mechanical properties suitable for stretchable electronics applications [223,283]. In this work, a commercially available

154

type of SEBS, Kraton G1657 was used, which has a very high elongation at break (~750%), relatively high tensile strength (23.4 MPa), low hardness (47 Shore A), low 300% modulus (2.4 MPa) and high melt index (22 g/10 min at 230 ℃, 5 kg) [335].
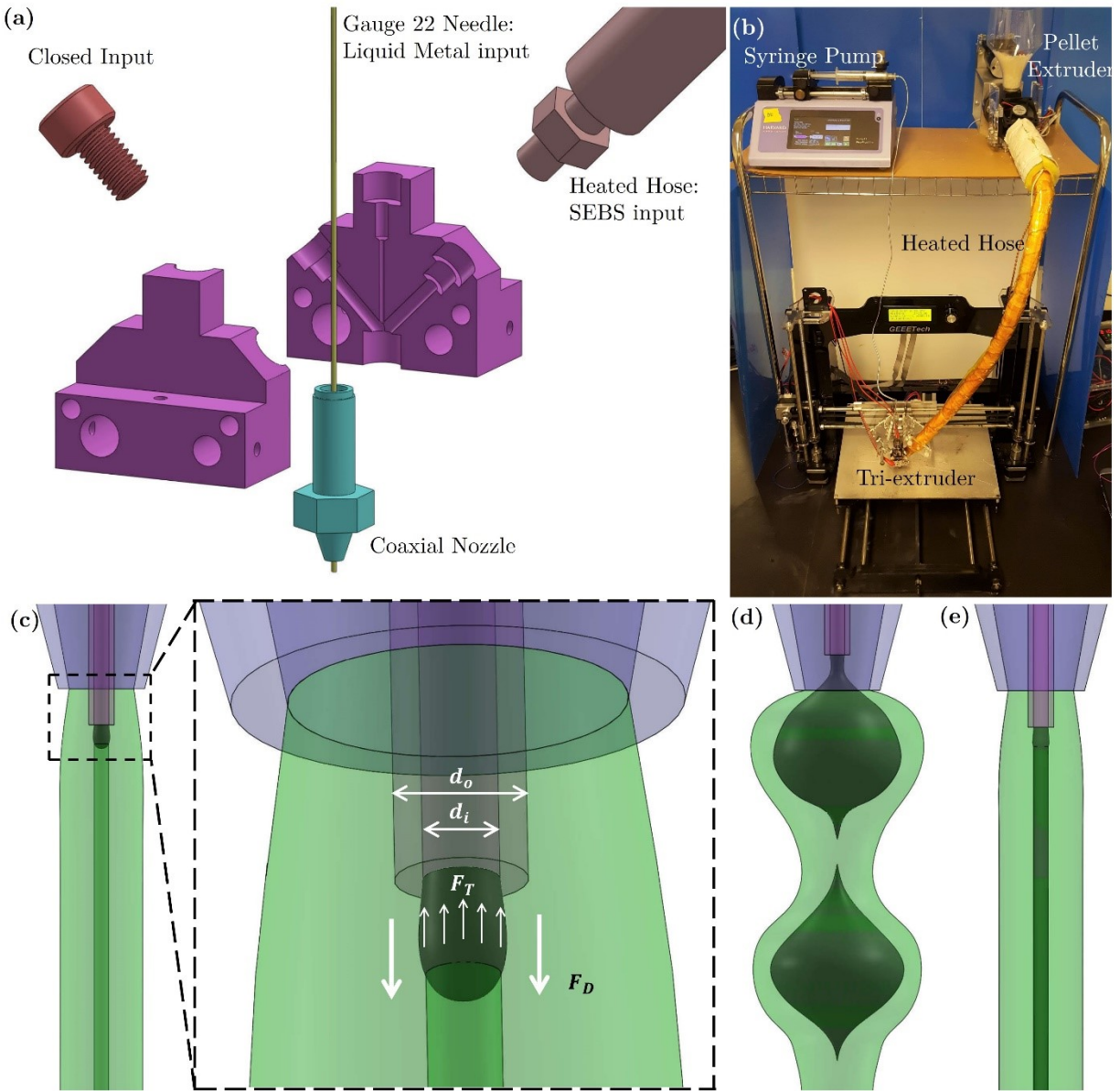
Figure 6. 1: (a) The exploded 3D model of the tri-extruder used for coaxial extrusion of LM with an SEBS elastomeric shell. (b) The entire FDM setup, showing a heated hose conveying the SEBS melt from the pellet extruder to the tri-extruder print head and a syringe pump injecting

the LM via a silicone tubing. (c) Device geometry of the coaxial system showing the coflowing mechanism of LM with an SEBS shell. (Inset) Illustration of surface tension force (F_T) and viscous drag (F_D) which determine the nature of coaxial extrusion. (d) If the LM leaves the needle while inside the nozzle when the SEBS melt has significantly low viscosity due to high temperature, the surface tension dominates the viscous drag and results in droplets of the LM. (e) Higher viscous drag is favorable for a continuous smooth core of LM which requires the needle tip to be outside of the nozzle (~ 1 mm).

6.2   COAXIAL EXTRUSION OF LM WIRE

We have built a thermoplastic tri-extruder system compatible with FDM printers that is capable of both intermixed and co-axial extrusion of multiple materials in a single process, as presented in our previous works [252,285,336,337]. The printing head has three input channels where two angled inputs are designated for feeding thermoplastic materials with the third input reserved for co-axial extrusion of a central core fluid. A 3D model of the tri-extruder is presented in Figure 6.1(a). In order to directly 3D print thermoplastic elastomers from pellets, we have also developed an extruder-based feeding system, as described elsewhere [336]. The feeding system consists of a screw extruder coupled with a heated hose to convey the polymer melt to the print head. The screw extruder system is a modified version of a filament extruder system purchased from Filastruder, USA [284]. In this work, one thermoplastic input channel was kept inactive using an M6 screw but can normally take other thermoplastic filament inputs for blending functions [337]. The central LM core was fed using a central needle (reusable stainless-steel dispensing needle: gauge 22, ID 0.016" (~ 400 μm), OD 0.028" (~ 700 μm), McMaster Carr) which was carefully kept concentric to the nozzle having an opening of 1.8 mm. The needle was connected to a syringe pump (Harvard Apparatus, Pump 11, Pico Plus Elite) through a flexible silicone tubing and luer-

156

lock connectors. The tri-extruder system was installed on an inexpensive FDM 3D printer (Model: M201) purchased from Geeetech, China [32]. The whole setup is shown in Figure 6.1(b), where all major components are illustrated. Once the stretchable wire was extruded, an immediate drawing step while the temperature of the extrudate was still above the glass transition temperature (T_g) of SEBS resulted in an ultrafine stretchable wire. By varying the drawing speed, it was possible to fabricate different diameters of wires from the same extrusion settings. Using this method, ultrafine conductive wires can be produced which may be used in future applications such as micro-electrode interconnects for nerve systems [338]. Lin *et al.* reported a manual drawing process of liquid metal wires at room temperature using curable polymers [339]. However, that process is not suitable for producing continuous wire because the length of the drawn wire is limited by the initial size of the LM droplet, and it is solely a manual method whereas the technique developed in our work requires less manual effort with better control over the diameter of wire through the use of a motorized winder.

6.3 MECHANISM OF LM COAXIAL EXTRUSION

While the FDM extruder system is much larger than typical microfluidics devices, the higher viscosities of thermoplastic melts provide similar Reynolds numbers and design principles applied to very laminar flows despite being a non-Newtonian fluid. Hence, the coaxial extrusion of LM and SEBS can be explained by the dripping and jetting mechanism in coflowing microfluidic systems of two immiscible fluids [340]. Dripping occurs when the inner fluid forms periodic droplets that pinch-off from the injecting tip. However, in the jetting regime, the inner fluid first forms a

jet which may be broken up into droplets downstream away from the tip. The dynamics of this coflowing system are determined by the viscosities of both fluids and their average velocities, densities, surface tension, surface chemistry and device geometry [341]. As shown in Figure 6.1(c), once the LM is injected through a needle surrounded by the viscous polymer melt, there are two major forces which define the continuity of the core fluid – the surface tension force and viscous drag [342]. In comparison with these forces, the effects of gravity, buoyancy and momentum transfer terms can be assumed to be negligible [342]. Initially, the force due to interfacial surface tension (F_T) dominates the viscous drag applied by the outer fluid and minimizes the surface area by forming a spherical droplet and tends to adhere the droplet to the needle. This surface force, F_T is approximately $1.3\,\pi d_i \gamma$, where, d_i is the internal diameter of the LM needle and γ is the surface tension of the LM and molten SEBS interface [342]. On the other hand, the viscous drag forces the LM downstream away from the needle tip, which can be approximated from a modified version of the Stokes formula as: $3\pi \eta_{SEBS}(d_{LM} - d_i)(u_{SEBS} - u_{LM})$ [342], where η_{SEBS} is the dynamic viscosity of the SEBS melt, u_{SEBS} is the average velocity of SEBS melt, u_{LM} is the average velocity of the LM and d_{LM} is the diameter of LM core. The viscous drag takes into account the shielding of the LM droplet due to the needle and reduction in drag due to the relative velocity between both fluids. Continuous feeding of LM causes the droplet to grow, which eventually contributes to an increase in the viscous drag. Once the viscous drag overcomes the surface tension force, and the droplet is forced to move away from the needle which creates a slight undulation on the droplet tail. Due to Plateau-Rayleigh instabilities, the droplet is then pinched-off and encapsulated. In our case, the LM droplets are oblong because the temperature of the polymer

158

melt quickly drops below T_g and restricts droplets from becoming fully spherical. A 3D model of a discontinuous series of LM droplets encapsulated in SEBS is shown in Figure 6.1(d). To achieve a continuous jet of LM encapsulated in SEBS, the viscous drag should be high enough to force LM away from the needle before droplets can grow. We achieved a continuous jet by lowering the LM needle tip outside (~1 mm) of the extruding nozzle. The viscosity of the polymer melt increases non-linearly by decreasing the temperature and shear rates outside of the nozzle. Hence, when the LM is injected, it is surrounded by the highly viscous polymer melt which restricts droplet growth, and the combined flow of both fluids favors the condition of a continuous jet as shown in Figure 6.1(e). There are a number of assumptions made to circumvent the limitations of the current experimental setup. They are listed here first:

- The shear rate of SEBS immediately after it is extruded is assumed to be 10s^{-1}.

- Although the viscosity decreases at a higher shear rate resulting from a higher flow rate of the polymer melt, we assumed the same viscosity for all the flow rates estimated from the viscosity curve at a shear rate of 10s^{-1}.

- The viscosity of the SEBS at 180 ℃ is estimated as approximately $2600\ \text{Pa} \cdot \text{s}$, at a shear rate of 10s^{-1}. They are extrapolated from our previous study reported elsewhere.

There are also some limitations of the existing experimental setup. They are as follows:

- Due to the eccentricity of the needle, the shear rate around the needle is not uniform.

- The actual temperature of the SEBS melt 1 mm below the nozzle is assumed to be same as the temperature of the melt-chamber because the current setup is not capable of measuring the temperature of the polymer melt around the LM.

With all the assumptions and limitations in consideration, it is expected to develop a theoretical model to predict the required flow rates of SEBS and LM when an LM core of a specific diameter is desired. Once the LM is extruded, as the droplet grows, when its diameter becomes as large as the needle ID (d_i), the droplet starts to experience the viscous drag applied by the polymer melt. However, it is negligible compared to the surface tension force. Let's assume when droplet diameter reaches a critical value (d_{cr}) which is larger than the needle ID (d_i), the viscous drag is large enough to nullify the surface tension force and favors the condition of a continuous jet formation. This condition requires:

$$1.3\pi d_i\, \gamma \;\leq\; 3\pi\eta_{Shell}\,(d_{cr}-d_i)\,(u_{Shell}-u_{Core}) \tag{6.1}$$

$$\text{Or, } d_{cr} \geq d_i\left[1+\frac{1.3\,\gamma}{3\pi\eta_{Shell}\,(u_{Shell}-u_{Core})}\right] \tag{6.2}$$

As suggested by Utada *et al.*, the conditions favorable to a continuous jet of LM encapsulated in SEBS can be expressed by the capillary number of the SEBS and the Weber number of the LM [340].

$$Ca_{SEBS} = \frac{\eta_{SEBS}\,u_{SEBS}}{\gamma} \tag{6.3}$$

$$We_{LM} = \frac{\rho_{LM}\,d_{cr}\,u_{LM}^2}{\gamma} \tag{6.4}$$

u_{SEBS} is the feed rate of SEBS and u_{LM} is the relative (with respect to SEBS) feed rate of LM. Substituting u_{SEBS} and u_{Core} from the Equations (6.3) and (6.4) into Equation (6.2) gives the following condition:

$$\sqrt{We_{LM}} \leq \left(\frac{\sqrt{\rho_{LM} d_{cr} \gamma}}{\eta_{SEBS}}\right) Ca_{SEBS} - \left(\frac{1.3 d_i \sqrt{\rho_{LM} d_{cr} \gamma}}{3\eta_{SEBS}(d_{cr}-d_i)}\right) \tag{6.5}$$

This equation is useful to predict the required We_{LM} and Ca_{SEBS} to achieve a desired diameter of the core fluid (d_{cr}), for a specific system with specified η_{SEBS}, ρ_{LM}, γ and d_i.
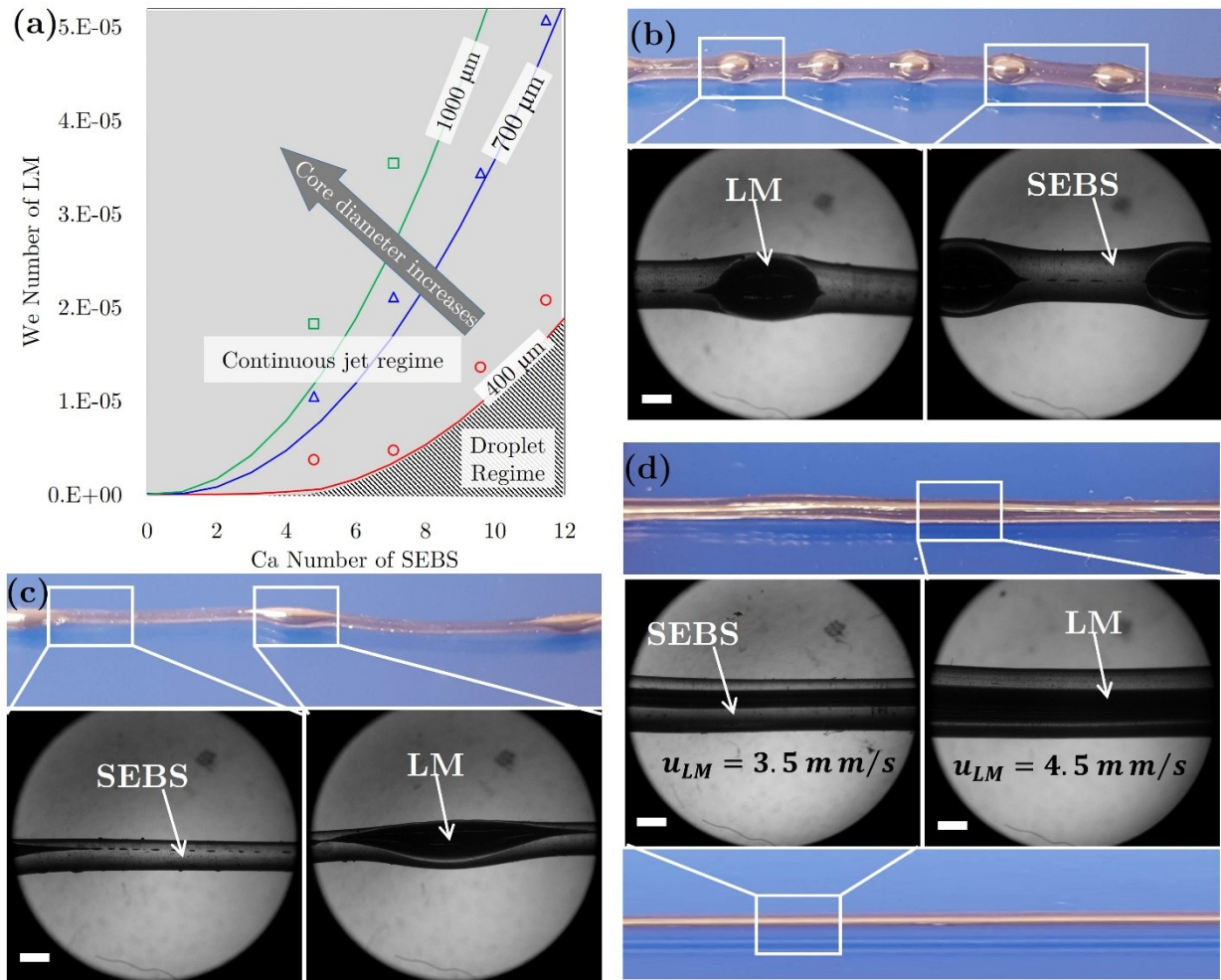
Figure 6. 2: (a) The state diagram for LM wire extrusion showing two distinct regions - droplet regime and continuous jet regime. The hatched area represents the conditions where a continuous

161

LM core may not be produced. The lines represent different theoretical combinations of Ca_{SEBS} and We_{LM} producing a desired core diameter. Thicker LM core requires higher We_{LM} for any specific Ca_{SEBS}. Experimental data points are also plotted: open circles correspond to an LM core within a range of 390 ~ 450 μm, open triangles are for 670 ~ 730 μm and open squares are for 980 ~ 1040 μm. The SEBS extrudate with LM droplets extruded with $u_{SEBS} = 2\ mm/s$ and $u_{LM} = 2.5\ mm/s$ which corresponds to $Ca_{SEBS} = 8.3$ and $We_{LM} = 9.8 \times 10^{-7}$ at (b) 180 ℃ and (c) 200 ℃. (d) By increasing the LM feed rate a thicker LM core was produced.

Figure 6.2(a) presents a state diagram showing different combinations of Ca_{SEBS} and We_{LM} favorable to LM jet formation with a desired core diameter. The lines represent different conditions favorable according to the Equation (6.5) to produce a LM wire with core diameters of 400 μm, 700 μm, and 1000 μm at 180 ℃. Since the internal diameter of the needle used in this experiment was ~ 400 μm, using this setup, a wire with a core diameter less than 400 μm could not be produced. Therefore, the area under the 400 μm curve (hatched rethe gion marked on the plot) corresponds to those conditions where rather than a continuous jet, a series of LM droplets were observed. On the other hand, in the grey region above the 400 μm curve, a continuous jet can be achieved with different core diameters.

In contrast to the lines which represent theoretical predictions, the data points show the experimental results when continuous jets with different core diameters were produced. Open circles represent when the desired core diameter was 400 μm, and it resulted in a slight variation of 390 μm to 450 μm of core diameter. Similarly, open triangles and squares represent when the achieved core diameter was between 670 μm to 730 μm, and 980 μm to 1040 μm, respectively. However, in all cases, the requirement of the We_{LM} was higher than the theoretical expectations. It is believed to be caused by a number of assumptions made in this experiment and limitations

of the experimental setup, as described in the supporting information. The flow speeds of both

SEBS (u_{SEBS}) and LM (u_{LM}) were varied to identify the combinations of Ca_{SEBS} and We_{LM} which

were favorable to a continuous LM jet formation. A system was assumed to be favorable to a

continuous jet if it produced extrudate over 1 metre long without any discrete droplets of LM. It

was further noticed that, at a very high We_{LM} and a relatively low Ca_{SEBS}, the higher feed rate of

LM causes the droplets to grow quickly which eventually results in bursting and the LM becomes

no longer contained in the SEBS shell.

Figure 6.2(b) shows an extrudate with LM droplets which was produced using $u_{SEBS} = 2$ mm/s

and $u_{LM} = 2.5$ mm/s at 180 °C which corresponds to $Ca_{SEBS} = 8.3$ and $We_{LM} = 9.8 \times 10^{-7}$. Their

microscopic images are shown in the inset to observe the shape of the droplets and the sections

between them. At 200 °C, when free extruding under gravity, the lower viscosity of the SEBS

dictates the thinner size of the extrudate as shown in Figure 6.2(c), which was produced with the

same feed rates as the extrudate in Figure 6.2(b). By increasing the feed rate of LM from $u_{LM} =$

3.5 mm/s to $u_{LM} = 4.5$ mm/s, while keeping the same SEBS feed rate ($u_{SEBS} = 2$ mm/s), a thicker

LM core was produced as shown in Figure 6.2(d). Due to Plateau-Rayleigh instabilities, at very

low LM feed rates, non-uniform pressure distribution along the length of the core cylindrical LM

causes material displacement and results in discontinuities. Optical microscope images of the LM

wires produced at different LM feed rates but identical SEBS feed rates are shown in Figures

6.3(a) – (d). The diameter of the LM core increases with increasing LM feed rate. A simple stretch

test was performed to show the elongation of the LM wire without any mechanical or electrical

loss as shown in Figure 6.3(e) and 6.3(f), where no voids or electrical issues were observed when stretched up to 400%.
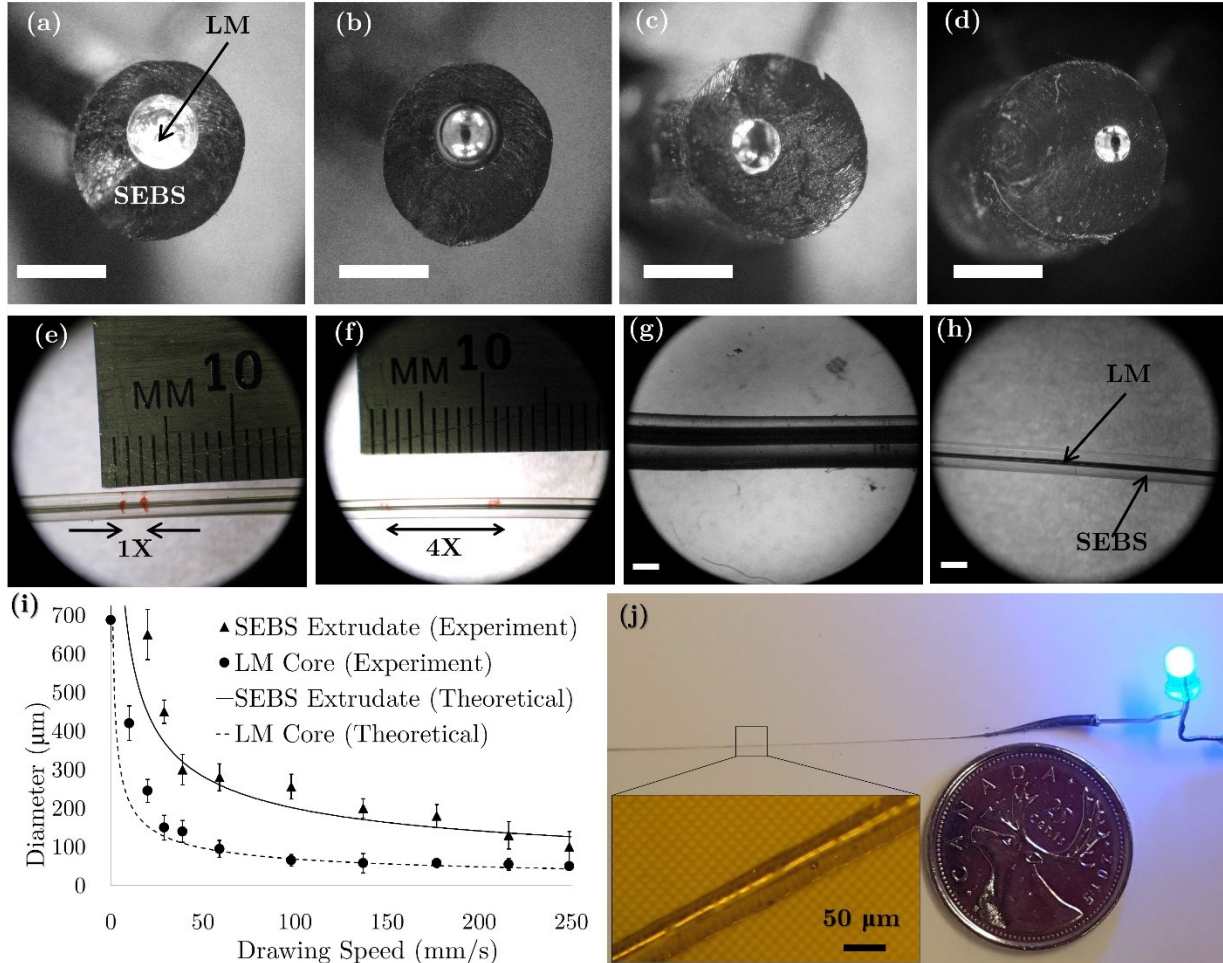
Figure 6. 3: Microscope images of representative cross-sections of LM wires produced at 180 ℃, having the same $Ca_{SEBS} = 4.8$ but different We_{LM}, producing LM wires with core diameter (a) 800 $\pm$ 70 μm from $We_{LM} = 5.2 \times 10^{-5}$, (b) 670 $\pm$ 55 μm from $We_{LM} = 4.0 \times 10^{-5}$, (c) 560 $\pm$ 60 μm from $We_{LM} = 3.3 \times 10^{-5}$ and (d) 390 $\pm$ 20 μm from $We_{LM} = 2.1 \times 10^{-5}$. (e) & (f) The LM wire is stretched up to 400% without any noticeable change in continuity of the LM core. (g) the side view of LM wire having a core of 670 $\pm$ 55 μm, which was drawn at 20 mm/s to produce ~ 190 μm of LM core shown in (h). (i) The changes in diameters of the drawn SEBS extrudate and LM core as a function of the drawing speed; the lines show the estimated dimensions from Equation (6.7), whereas data points with error bar represents experimental measurements. (j) A micro-wire drawn at ~250 mm/s was used to transmit power to a LED which ran for 72 hours without any aging effect. (Inset) The microscope image of the micro-wire with a background of an array of micro fibers with 20 μm pitch. Scale bars are 1 mm unless specified.

164

6.4 DRAWING OF THE LM WIRE

If an ultrafine LM micro-wire is desired, an additional drawing step immediately after the coaxial LM wire is extruded can be applied, if the temperature of the polymer melt is still above the glass transition temperature (T_g). We hypothesized that the ratio of the diameters of the LM core and SEBS shell would be a constant. If there are no voids in the LM core, by considering a circular and uniform cross-section one can deduce the following Equation (6.6) from the conservation of mass.

$$\pi \left(\frac{d_{Extrusion}}{2}\right)^2 S_{Extrusion} = \pi \left(\frac{d_{Drawing}}{2}\right)^2 S_{Drawing} \tag{6.6}$$

Which reduces to,

$$d_{Drawing} = d_{Extrusion}\sqrt{\frac{S_{Extrusion}}{S_{Drawing}}} \tag{6.7}$$

where $d_{Extrusion}$ is the diameter of either the as-extruded LM core or SEBS extrudate, $d_{Drawing}$ is their diameter after drawing, $S_{Extrusion}$ is the extrusion speed and $S_{Drawing}$ is the drawing speed. The final size of the ultrafine LM wire is directly proportional to the square root of the ratio of extrusion speed to drawing speed. This fact is supported by the drawing test where the as-extruded wires were drawn in a controlled fashion using different drawing speed. The test was performed using a motorized winder with a 7.5 cm wheel, placed on the print bed when the tri-extruder head was raised at a height of 20 cm above the bed. The motorized winder was carefully placed directly below the nozzle so that only a vertically downward drawing force is applied. Figure 6.3(g) shows a wire having 670 ± 55 µm of LM core produced, which was then drawn with a speed of 20 mm/s resulting in approximately 190 µm diameter of LM core shown in Figure 6.3(h). Using this simple

drawing technique, the LM micro-wire having a core diameter as narrow as ~ 25 μm was achieved without any mechanical and electrical loss, by drawing with the maximum attainable speed (250 mm/s) of the current setup. After the drawing step, the LM micro-wires were examined using an optical microscope to measure core and shell diameters. The plot in Figure 6.3(i) shows the effect of drawing speed on the size of the drawn wires. During this experiment, the average extrusion speed ($S_{Extrusion}$), core diameter and shell diameter were kept constant at 1 mm/s, ~ 390 μm, and ~ 2000 μm, respectively. This plot suggests that as the drawing speed increases, initially the size of both the LM core and SEBS shell drastically decrease, and theoretically they should approach a plateau which would be determined by Plateau–Rayleigh instabilities and mechanical failures of the SEBS shell resulting in LM leakage. The latter effect might be partially attributed to the eccentricity of the LM core with respect to the SEBS shell due to alignment imperfections. A more concentric coaxial extrusion would further push the limit of smallest size of drawn wires. The extremely rapid cooling of the extrudate prevents fully plastic behavior, and immediate drawing in a heated environment may potentially reduce achievable smallest diameters. To demonstrate the electrical performance, a micro-wire (~25 μm of LM core with ~ 50 μm of SEBS shell) was used as a connector for an LED with no aging effect on its conductivity over a period of 72 hours of continuous operation (Figure 6.3(j)). In the inset, a close-up microscopic image of the micro-wire is presented. This image was taken while the wire was placed on an array of microscale fibers with a 20 μm pitch to demonstrate the size of the wire.
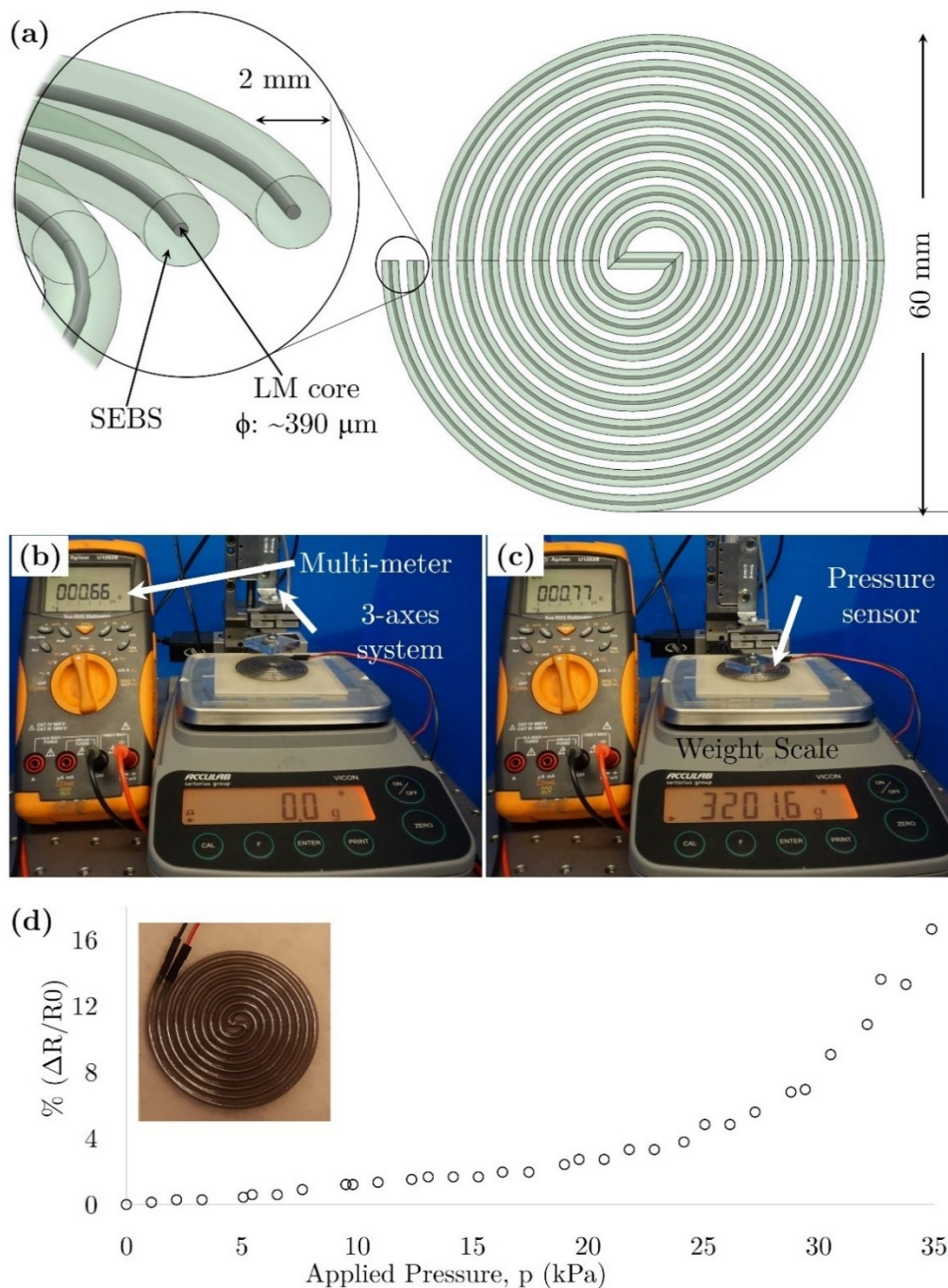
Figure 6. 4: (a) The 3D model of the spiral-shaped 2D pressure sensor composed of SEBS channels with an LM core directly printed on an SEBS substrate. (b) The experimental setup to measure the change in electrical resistance as a function of pressure applied with no load and (c) with a load of 3.2 kg. (d) Percent change of electrical resistance of the sensor as a function of the pressure applied, (inset) the spiral-shaped 2D pressure sensor composed of SEBS with an LM core directly printed on an SEBS substrate.

6.5   2D SPIRAL PRESSURE SENSOR

The ability to directly extrude LM wire embedded in hyper-elastic SEBS enables printing of 2D or 3D sensors which are mechanically durable as well as stretchable up to several times their original length and has immediate applications in wearable systems [139]. While LM filled micro-electronics as sensors have already been reported in the literature [89,127,139], the novelty of the current research comes from the unique fabrication technique to directly print these functional devices in a single step as opposed to the multiple casting, injecting and sealing processes used previously. We have directly printed a spiral-shaped 2D pressure sensor on to an SEBS sheet inspired by Park *et al.* [139]. The sensor was designed to have 2 mm thick extrudates with a 1 mm gap between adjacent deposits. The size of the overall sensor was approximately 60 mm in diameter.

The 3D model of the 2D pressure sensor is given in Figure 6.4(a). Figure 6.4(b) shows the experimental setup to measure the change in electrical resistance and corresponding pressure applied with no load and with a full load in Figure 6.4(c). A multimeter (Agilent, U1252B) was used to continuously measure the resistance of the pressure sensor while the load was applied on to the sensor by means of a 3-axis system. To evenly distribute the load, a 30 mm × 30 mm square acrylic piece of ~ 6 mm thickness was attached to the probe, which was pressed down against the pressure sensor held on top of a digital weight scale to measure the load applied. The test was repeated three times, and the plot was based on the average data points from different loading and unloading cycles. The test shows significant repeatability by having almost no hysteresis within the range of the experiment performed. As a pressure sensor, the force applied

on the sensor causes deformation of the circular cross-section of the LM core resulting in a change in the electrical resistance. The original electrical resistance of the un-stressed sensor was 0.66 Ω, which increased non-linearly to 0.77 Ω for a load of 3.2 kg, equivalent to 34.9 kPa. This non-linearity is supported by the model developed by Park *et al.* [139]. Figure 6.4(d) shows the change in electrical resistance as a function of the pressure applied. In the inset of Figure 6.4(d), the photograph of the pressure sensor is presented.
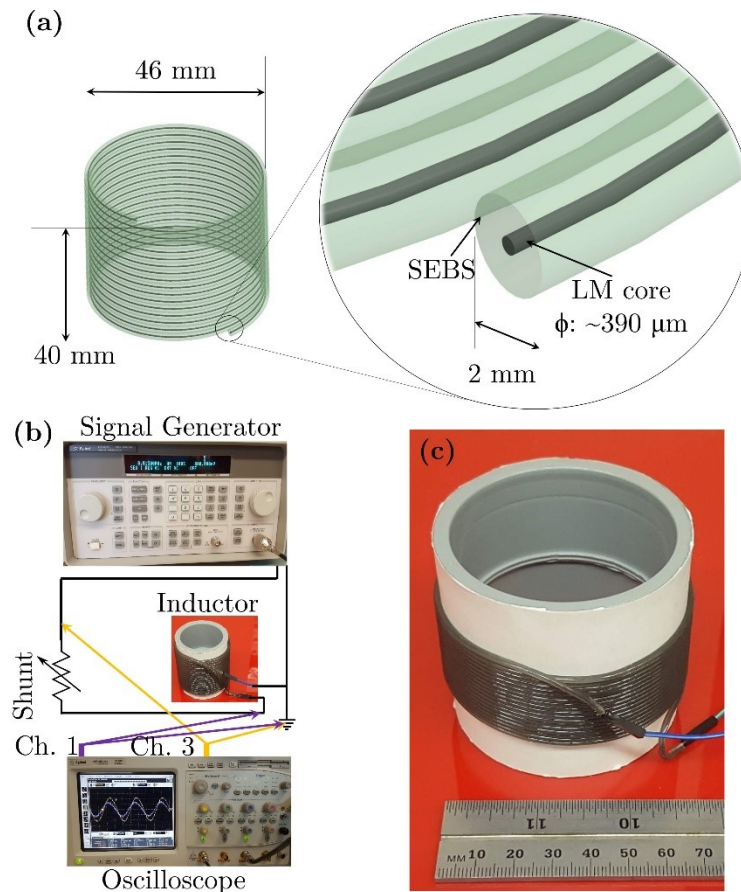
Figure 6. 5: (a) The 3D model of the 3D inductor as a circumferential strain sensor composed of SEBS channels with an LM core. (b) The experimental setup to measure the change in inductance of the inductor using a signal generator and oscilloscope, (c) the inductor (initial nominal diameter 44 mm) is strained by stretching it around a PVC pipe coupling with a 70 mm OD.

6.6   3D INDUCTOR AS CIRCUMFERENTIAL STRAIN SENSOR

We also have printed a three-dimensional multifunction inductor using LM wire. The inductor has an outer diameter of 46 mm, a height of 40 mm, and 2 mm thick SEBS coils having an LM core of ~ 390 μm. A radial axisymmetric circumferential strain was applied on the inductor which results in a change in both the cross-sections of the individual LM cores in SEBS channels as well as the overall circular area perpendicular to the inductor axis. The inductance of the inductor (L) can be computed using Equation (6.8):

$$\text{Inductance, L} = \frac{\mu_o N^2 A}{h} \tag{6.8}$$

where μ_o is the permeability of vacuum, N is the number of coils, A is the cross-sectional circular area of the inductor, and h is the height of the inductor.

Figure 6.5(a) shows the 3D model of the inductor. If the overall outside diameter of the inductor is D, then by assuming SEBS extrudates with ca ircular cross-section of diameter (d_S), the following Equation (6.9) can be used to simplify Equation (6.8) to form Equation (6.10):

$$h = d_S\, N \tag{6.9}$$

$$L = \frac{\pi \mu_o N D^2}{4\, d_S} \tag{6.10}$$

From Equation (6.10), the inductance of an inductor is directly proportional to the diameter squared of its cross-section, provided other parameters remain the same. Hence, changing the inductor area would have the most significant effect on the inductance of a given inductor. Moreover, having stretchable SEBS as the sealing material, it is also quite reasonable to use this type of inductor as a circumferential strain sensor to measure the radial expansion where desired.

Therefore, we have applied different degrees of radial uniform expansion on the same inductor and measured its inductance. To apply radial expansion, a number of PVC pipe couplings were used where the inductor was put on. Once the circumferential strain was applied, the inductance of the inductor was measured by the experimental setup shown in Figure 6.5(b). A signal generator (Agilent 8648C, 9kHz-3200MHz) and an oscilloscope (Agilent infiniium 1.5 GHz, 8 GSa/s) were used to measure the inductance. When strained, approximating the LM core as a continuous circular core with a diameter d_C, the conservation of mass would provide the following relationship between original geometries (denoted by subscript "1") and strained geometries (denoted by subscript "2"), which applies to diameters of both SEBS extrudate and LM core:

For SEBS extrudate: $\frac{\pi}{4}\left(d_{S_1}\right)^2 \times \pi D_1 \times N = \frac{\pi}{4}\left(d_{S_2}\right)^2 \times \pi D_2 \times N$ (6.11)

For LM core: $\frac{\pi}{4}\left(d_{C_1}\right)^2 \times \pi D_1 \times N = \frac{\pi}{4}\left(d_{C_2}\right)^2 \times \pi D_2 \times N$ (6.12)

Hence, by re-writing the Equation (6.10) for the original and strained inductor and using Equation (6.11) and (6.12), we can deduce to the following relationship:

$$\frac{L_1}{L_2} = \left(\frac{D_1}{D_2}\right)^{3/2}$$

As it is uniformly radially expanded the inductance increases as a function of its diameter (D) according to the following Equation (6.13).

$$L^2 \; \alpha \; D^3 \tag{6.13}$$

Hence, the inductance of the inductor increases as the diameter increases. To measure inductance, the inductor was connected with a specified shunt, as shown in Figure 6.5(b). The 3D inductor strained by putting on a PVC coupling having 70-mm of outside diameter is presented in Figure

6.5(c). When the voltage drop across the inductor and voltage generated by the signal generator were measured using an oscilloscope for a sinewave voltage. The electrical and mathematical models are presented in Figure 6.6(a) and 6.6(b), respectively.

Let,

f = Frequency

V_g = The RMS value of the voltage generated

V_I = The RMS value of the voltage across the inductor

V_R = The RMS value of the voltage across the ohmic component of the inductor

V_L = The RMS value of the voltage across the inductive component of the inductor

V_S = The RMS value of the voltage across the shunt

I_g = The RMS value of the current generated

α = The phase shift between V_g and V_I

ϕ = Loss angle, between V_L and V_I

The shunt used in this experiment was $R_S = 1.9\,\Omega$

Inductance of un-strained inductor can be calculated as follows. From Figure 6.6(c):

$\alpha = 17.438°$; $V_g = 0.0922$ V, $V_I = 0.0443$ V; $f = 14999.65$ Hz;

So, $V_S = \sqrt{\left(V_g - V_I \cos\alpha\right)^2 + (V_I \sin\alpha)^2} = 0.052\,V$;

$I_g = \frac{V_S}{R_S} = 0.027\,A$;

172

$$\phi = 90° - \left[\alpha + \sin^{-1}\left(\frac{V_I \sin\alpha}{V_S}\right)\right] = 57.77°$$

Inductance, $L = \frac{V_I \cos\phi}{2\pi f\, I_g} = 9.28\ \mu H$

Nagaoka coefficient (k) is a correction factor which is, by definition, a ratio of measured inductance (L_m) to theoretical inductance (L) of a solenoid. This correction factor decreases as the aspect ratio $\left(h/_D\right)$ increases. Here, the correction factor was used from the table proposed by Nagaoka in 1909 [343].

$$L_e = k \times L \tag{6.14}$$

Table 6.1 summarizes the aspect ratio of tested inductor at different degree of circumferential strain and corresponding Nagaoka coefficient suggested in [343].

Table 6. 1: The aspect ratio correction factor determined for all the strain conditions applied on the inductor.

	Aspect Ratio $\left(h/_D\right)$	Nagaoka coefficient (k)
Un-strained (44 mm diameter)	1.10	0.67
Strained to 50-mm of diameter	0.75	0.75
Strained to 55-mm of diameter	0.61	0.79
Strained to 65-mm of diameter	0.48	0.82
Strained to 70-mm of diameter	0.35	0.87
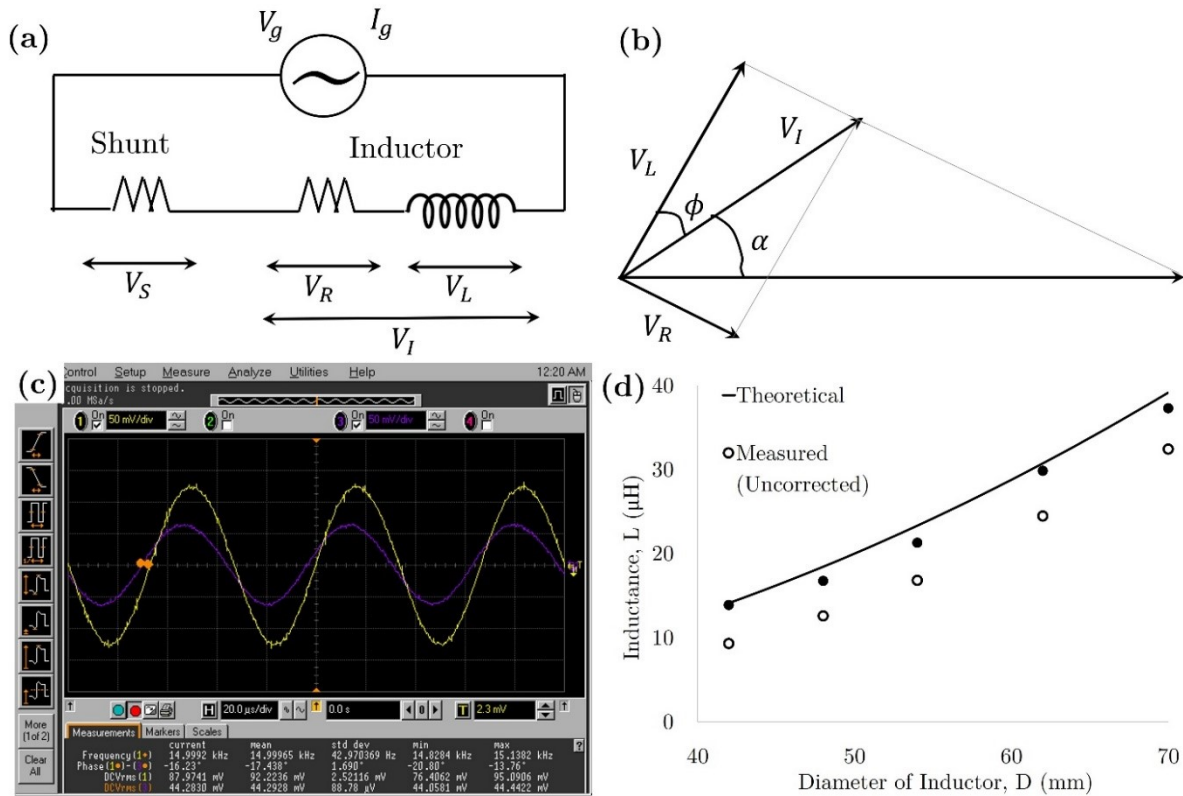
Figure 6. 6: (a) The electrical model circuitry of the setup to measure inductance, (b) the equivalent vector model of the circuitry. (c) The output of the oscilloscope when measuring the inductance of the un-strained inductor. (d) the relationship between inductance and the diameter of the inductor. The solid line represents the theoretical prediction of the inductance according to Equation (6.13). Open circles are uncorrected experimentally measured inductances whereas the closed circles are data points corrected using an aspect ratio correction factor.

In Figure 6.6(d), the relationship between the inductor's inductance and diameter is presented. Each measurement was repeated three times and their average data was used to plot the relationship. In the figure, the solid line represents the theoretical relation from Equation (6.13) and the open circles are experimental data points. It shows that inductance increases non-linearly with an increase in the inductor diameter. By introducing an aspect ratio correction factor, namely the Nagaoka coefficient (k) [343], the measured inductances were corrected, and it was found that the corrected data well coincide with the theoretical prediction. The minor discrepancy between

predicted and corrected data are believed to be caused by the possible contact resistance and the self-inductance of the connecting wires. A second 3D printed inductor (Diameter: 50 mm, Height: 40 mm) was used to demonstrate electromagnetic induction by moving a permanent magnet using a 3-axis stage through the center of the inductor. A maximum voltage of 50 mV was induced in the inductor. These micro-wires also have self-healing property, if the continuity of the core is raptured.

6.7   CONCLUSIONS

In summary, we describe a novel technique to directly print stretchable and flexible electronic devices by coaxially extruding an LM (namely, EGaIn) core with an elastomeric shell made of SEBS. We also discussed the mechanism of forming LM droplets vs. an LM jet, which is followed by the state diagram showing favorable conditions for a continuous LM core with the desired diameter. This novel technique is the first of its kind to directly fabricate LM based conductive patterns in a single step without any post-processing such as injecting or casting. Along with coaxial extrusion, an additional immediate drawing step resulted in a continuous high-quality LM micro-wire with a core size as small as ~ 25 µm. The technique could be improved by using a smaller nozzle and a smaller needle to achieve even smaller LM patterns. However, it would require a mechanism to hold the LM needle more precisely at the center of the nozzle, which is a promising goal for future work. The technique developed here is believed to be equally useful for low-melting point metals or alloys with a hard thermoplastic shell for the applications where stretchability and flexibility are not desired, rather mechanical strength and rigidity are of primary concern.

7. CHAPTER: CONCLUSIONS AND RECOMMENDATIONS

7.1 CONCLUSIONS

In this dissertation, a multi-material smart extruder system for FDM style 3D printing technology has been developed which allows printing with dissimilar materials. The following section lists all the key findings discussed in individual chapters.

7.1.1 Summary of Findings

In chapter 3, a bi-extruder system has been demonstrated by printing intermixed extrudate of two different thermoplastic materials. It also describes the components and detail design of the extruder system and its intermixing technology. The dynamic control of the extrudate composition while printing the parts is also presented. To the best of authors knowledge, this printing extruder is the first of its kind to print two different polymers with enhanced mechanical bonding.

In chapter 4, a unique feeding system has been developed which allows 3D printing users to input arbitrary any thermoplastic polymers regardless of their mechanical properties. Material choice is no more limited by the commercial availability of filaments of any thermoplastics. This heated hose-based feeding system uses a load of raw pellets and transports the polymer melt to the print head through a heated hose. This feeding system fills the gap between regular 3D printing

176

techniques and injection molding, by enabling users to use any thermoplastic materials. Before this development, the 3D printed filament-based elastomer with the lowest hardness reported in the literature was ~72 Shore A, whereas printing with SEBS having a hardness of only 47 Shore A has been successfully achieved. A number of functional devices such as pneumatic network based soft robotic actuators, tendon-driven soft robots and SMP auxetic structures have been successfully printed to demonstrate utility.

In chapter 5, a tri-extruder system has been presented where two chemically immiscible polymers (SEBS and HIPS) have been printed in the same job with their intermixed extrudate. By introducing mechanical bonding or keying it was possible to enhance the adhesion between SEBS and HIPS. Mechanical characterizations of the printed parts with and without intermixing have been performed and it was found that the 2D printed layers with intermixed extrudate have up to 12 times higher ultimate strength compared to that of the 2D layers printed without intermixed extrudate. A tendon driven soft robotic gripper made of parts printed with intermixed SEBS and HIPS was tested up to 10,000 cycles without any noticeable mechanical bonding issues due to a high number of repeated bending operations. This result justifies the necessity of intermixed co-extrusion for multi-material 3D printing.

In chapter 6, the tri-extruder has been further developed to print liquid metal-based 2D and 3D stretchable electronic devices. The extruder system allows users to extrude liquid metal alloy with a thermoplastic elastomer shell coaxially. An extremely stretchable micro-wire with superior electrical conductivity is realized. The chapter also discusses the mechanism of this coaxial

177

extrusion from the theory of the coflowing system. It also presents state diagrams showing the conditions favorable to achieve a continuous jet of the liquid metal while extruding inside SEBS. These analyses are important to predict the droplets vs. continuous jet of liquid metal when extruding under non-standard conditions. It was found that the viscous drag force applied by the elastomer melt on the liquid metal must dominate the surface tension force of the liquid metal to realize continuous jet of LM core. Lowering the extrusion temperature and adjusting the LM needle outside of the nozzle are ways to lower the shear rate and increase the melt viscosity which favors the condition of a continuous LM jet. By applying an immediate drawing step while the extrudate temperature is still above T_g, it was possible to produce LM based micro-wire (~25 μm LM core with ~50 μm SEBS extrudate) which is still highly electrically conductive without any mechanical failure.

7.1.2   The significance of the Research

When this research started, to the best of author's knowledge, no FDM style 3D printer existed to print mechanically tunable RF antenna, which requires hard plastic part along with soft, stretchable components containing conductive pathways sustainable up to the very high mechanical strain. Hence the capability of this extruder system to print both rigid and stretchable plastics along with liquid metal-based conductive pathways has the potential to revolutionize the field of tunable RF applications. It does not only overcome the necessity of complicated fabrication steps in expensive cleanroom environments, but it also significantly reduces the material cost, provides a wide range of material choice and requires less manual expertise. This research also opens new possibilities to novel applications described in the following section.

7.2   RECOMMENDATIONS FOR FUTURE WORK

Considering the progress and related results of the entire research work, there have been some major recommendations listed below which could further advance the technology optimizing the system for specific applications.

1. The design of the static intermixer needs to be optimized for fulfilling the requirement of the degree of intermixing for specific applications. Co-continuous structure of a binary polymer system depends on the viscosity ratio and the volume fraction. Hence, the effect of the design of intermixer on the co-continuous range should be identified. This analysis would provide the minimum length of the intermixer required to achieve the desired degree of intermixing. For instance, to have just enough co-continuity structure of HIPS and SEBS may not require the 20 mm long intermixer used in this work. Since a long intermixer significantly increases the pressure required to extrude the material, knowledge on the minimum required a length of intermixer will be useful to avoid unnecessary pressure requirements. Similarly, if a higher degree of intermixing or blending is desired, the size of the intermixer (both length and diameter) needs to be optimized which favors the condition of blending while keeping the pressure requirement within the system's capacity.

2. The heated hose used in this work to directly feed raw pellets was commercially purchased, which is not optimized for this specific application. Most of the commercially available heated hoses are intended for either large extrusion systems or low-temperature applications, and the available length is at least 2 ft (0.61 m). In addition, having a Teflon core tube may not be suitable for a longer life cycle of the heated hose for this particular application due to large dynamic bend

radius. Therefore, there is a compelling need to optimize the design of the heated hose for a small volume but a higher temperature extrusion system. Hence, it may require to develop a custom heated hose having the desired length, using a silicone-based core tube resulting in smaller bend radius and suitable for higher temperature (up to 300℃) small volume extrusion system. The internal volume of the heated hose needs to be optimized to have a shorter residence time of the polymer before it enters the print head.

3. For coaxial extrusion of liquid metal, the dispensing needle has to be concentric with the nozzle tip to make sure the elastomeric shell has a uniform thickness around the LM core. The commercially available stainless-steel needle used in this work was assumed to be perfectly straight, and the vertical channel of the extruder head was assumed to align the needle at the center of the nozzle. However, in a practical situation, the needle was not concentric to the nozzle. It may be because of the inherent curviness of this long (4 in or 101.6 mm) needle or the geometric tolerances of the vertical channel of the print head. Hence, in the future design, the central needle may accompany a small spacer around it to ensure its concentricity with the nozzle. This design may not be appropriate to a machine with traditional machining steps, rather this needle-nozzle assembly with an internal spacer may need to be metal 3D printed.

7.3 LIST OF REFEREED CONTRIBUTIONS

The work in this dissertation has been submitted, published and presented in the following patents applications, journal articles, and conference proceedings.

7.3.1 Patents Pending

1. Khondoker, M. A. H. and Sameoto, D. Additive Manufacturing Extruder. U.S. Serial No.: 62/580,299, Ref. 2017025 (BFL File No.: TECE-0114PRV)

2. Khondoker, M. A. H. and Sameoto, D. Fused Pellets Printing System and Method. U.S. Serial No.: 62/729,259, BJ-L.FID4507057 (ENNET JONES REF.: 55326.292)

7.3.2 Journal Articles

1. Khondoker, M. A. H., Ostashek, A. and Sameoto, D. Direct 3D Printing of Stretchable Circuits via Liquid Metal Co-Extrusion. *Advanced Engineering Materials.* (Under review) ID: adem.201900060

2. Khondoker, M. A. H. and Sameoto, D. Soft is No Longer Hard: Extruding Anything with a Filament-Free FDM Technique. *Progress in Additive Manufacturing.* (Accepted) ID: PIAM-D-18-00034R3

3. Khondoker, M. A. H., Baheri, N. and Sameoto, D. Tendon Driven Functionally Gradient Soft Robotic Gripper 3D Printed with Intermixed Extrudate of Hard and Soft Thermoplastics. *3D Printing and Additive Manufacturing.* (Provisionally Accepted) ID: 3DP-2018-0102R2

4. Khondoker, M. A. H., Asad, A. and Sameoto, D. (2018) Printing with Mechanically Interlocked Extrudates using a Custom Bi-Extruder for Fused Deposition Modelling. *Rapid Prototyping Journal.* 24(6): 921-934

5. Khondoker, M. A. H. and Sameoto, D. (2016) Fabrication Methods and Applications of Microstructured Gallium Based Liquid Metal Alloys. *Smart Materials and Structures*. 25: 093001

7.3.3 Conference Articles

1. Khondoker, M. A. H., and <u>Sameoto, D.</u> (2019) Direct Printed Multi-Material Soft Robots by Fused Deposition Modelling. Proc. Adhesion Society 42nd Annual Meeting. Hilton Head, CA, USA, March 1 – 3.

2. <u>Khondoker, M. A. H.,</u> and Sameoto, D. (2018) Enhanced Bonding of Immiscible Polymers via Intermixed Co-extrusion in Fused Deposition Modelling. Proc. Adhesion Society 41st Annual Meeting & 6th World Congress Meeting. San Diego, CA, USA, February 25 – March 1

3. <u>Khondoker, M. A. H.,</u> and Sameoto, D. (2016) Design and Characterization of a Bi-material Co-extruder for Fused Deposition Modeling. Proc. ASME IMECE 2016. Phoenix, AZ, USA, November 11 – 17

REFERENCES

[1] L. Huang and P. Russer 2008 Electrically Tunable Antenna Design Procedure for Mobile Applications *IEEE Transactions on Microwave Theory and Techniques* **56** 2789-97

[2] Hmouda A 2017 Frequency Reconfigurable Antennas for Airborne Applications. Quebec, Canada: National Institute of Scientific Research - University of Quebec

[3] J. T. Aberle, Sung-Hoon Oh, D. T. Auckland and S. D. Rogers 2003 Reconfigurable Antennas for Wireless Devices *IEEE Antennas and Propagation Magazine* **45** 148-54

[4] E. Erdil, K. Topalli, M. Unlu, O. A. Civi and T. Akin 2007 Frequency Tunable Microstrip Patch Antenna Using RF MEMS Technology *IEEE Transactions on Antennas and Propagation* **55** 1193-6

[5] Hai Jiang, M. Patterson, Chenhao Zhang and G. Subramanyam 2009 Frequency agile microstrip patch antenna using ferroelectric thin film varactor technology *IEEE Antennas and Propagation Society International Symposium (Charleston, SC, USA)* IEEE) p 1

[6] Zhang Jin and A. Mortazawi 2003 An L-band tunable microstrip antenna using multiple varactors *IEEE Antennas and Propagation Society International Symposium (Columbus, OH, USA)* vol 4 IEEE) p 524

[7] Zandvakili M, Honari M M, Mousavi P and Sameoto D 2017 Gecko-Gaskets for Multilayer, Complex, and Stretchable Liquid Metal Microwave Circuits and Antennas *Adv.Mater.Technol.* **2** 1700144

[8] Y. Orlic, B. Lacroix, N. Tiercelin, V. Preobrazhensky, P. Pernod, P. Coquet and J. Papapolymerou 2012 Frequency agile mechanical antenna for low-cost millimeter-wave applications *IEEE International Symposium on Antennas and Propagation (Chicago, IL, USA)* IEEE) p 1

[9] Tiercelin N, Coquet P, Sauleau R, Senez V and Fujita H 2006 Polydimethylsiloxane membranes for millimeter-wave planar ultra flexible antennas *J Micromech Microengineering* **16** 2389

[10] W. Su, B. Cook, M. Tentzeris, C. Mariotti and L. Roselli 2014 A novel inkjet-printed microfluidic tunable coplanar patch antenna *Antennas and Propagation Society International Symposium (Memphis, TN, USA)* IEEE) p 858

[11] C. Mariotti, W. Su, B. S. Cook, L. Roselli and M. M. Tentzeris 2015 Development of Low Cost, Wireless, Inkjet Printed Microfluidic RF Systems and Devices for Sensing or Tunable Electronics *IEEE Sensors Journal* **15** 3156-63

[12] Wang M, Trlica C, Khan M R, Dickey M D and Adams J J 2015 A reconfigurable liquid metal antenna driven by electrochemically controlled capillarity *J. Appl. Phys.* **117** 194901

[13] Diebold A V, Watson A M, Holcomb S, Tabor C, Mast D, Dickey M D and Heikenfeld J 2017 Electrowetting-actuated liquid metal for RF applications *J Micromech Microengineering* **27** 025010

[14] Holcomb S, Brothers M, Diebold A, Thatcher W, Mast D, Tabor C and Heikenfeld J 2016 Oxide-Free Actuation of Gallium Liquid Metal Alloys Enabled by Novel Acidified Siloxane Oils *Langmuir* **32** 12656-63

[15] Tabatabai A, Fassler A, Usiak C and Majidi C 2013 Liquid-phase gallium-indium alloy electronics with microcontact printing *Langmuir* **29** 6194-200

[16] Khan M R, Hayes G J, So J, Lazzi G and Dickey M D 2011 A frequency shifting liquid metal antenna with pressure responsiveness *Appl.Phys.Lett.* **99** 013501

[17] Jeong S H, Hagman A, Hjort K, Jobs M, Sundqvist J and Wu Z 2012 Liquid alloy printing of microfluidic stretchable electronics *Lab Chip* **12** 4657-64

[18] M A H Khondoker and,D.Sameoto 2016 Fabrication methods and applications of microstructured gallium based liquid metal alloys *Smart Mater.Struct.* **25** 093001

[19] J. Maas, B. Liu, S. Hajela, Y. Huang, X. Gong and W. J. Chappell 2017 Laser-Based Layer-by-Layer Polymer Stereolithography for High-Frequency Applications *Proceedings of the IEEE* **105** 645-54

[20] H. Xin and M. Liang 2017 3-D-Printed Microwave and THz Devices Using Polymer Jetting Techniques *Proceedings of the IEEE* **105** 737-55

[21] T. Chio, G. Huang and S. Zhou 2017 Application of Direct Metal Laser Sintering to Waveguide-Based Passive Microwave Components, Antennas, and Antenna Arrays *Proceedings of the IEEE* **105** 632-44

[22] Chivel Y 2016 New Approach to Multi-material Processing in Selective Laser Melting *Physics Procedia* **83** 891-8

[23] S. A. Nauroze, J. G. Hester, B. K. Tehrani, W. Su, J. Bito, R. Bahr, J. Kimionis and M. M. Tentzeris 2017 Additively Manufactured RF Components and Modules: Toward Empowering the

Birth of Cost-Efficient Dense and Ubiquitous IoT Implementations *Proceedings of the IEEE* **105** 702-22

[24] Dimitrov D, de Beer N, Hugo P, Schreve K. Three Dimensional Printing. In: Yilbas,Saleem HashmiGilmar Ferreira BatalhaChester J.Van TyneBekir, editor. Comprehensive Materials Processing Oxford: Elsevier; 2014. p. 217-250

[25] Gibson I, Rosen D W and Stucker B 2010 Additive Manufacturing Technologies: Rapid Prototyping to Direct Digital Manufacturing (New York, NY: Springer US) p 459

[26] Zhang S, Njoku C C, Whittow W G and Vardaxoglou J C 2015 Novel 3D printed synthetic dielectric substrates *Microw.Opt.Technol.Lett.* **57** 2344-6

[27] S. Zhang 2016 Design and Fabrication of 3D-printed Planar Fresnel Zone Plate Lens *Electronics Letters* **52** 833-5

[28] Bur A J 1985 Dielectric properties of polymers at microwave frequencies: a review *Polymer* **26** 963-77

[29] Apeldorn T, Keilholz C, Wolff-Fabris F and Altstädt V 2013 Dielectric properties of highly filled thermoplastics for printed circuit boards *J Appl Polym Sci* **128** 3758-70

[30] Premix Oy. Available at: https://www.preperm.com/. Accessed November/20, 2018

[31] Ultimaker. Available at: https://ultimaker.com/en/products/ultimaker-3. Accessed November/20, 2018

[32] Geeetech Prusa I3 M201. 2016; Available at: http://www.geeetech.com/wiki/index.php/Geeetech_Prusa_I3_M201. Accessed Dec/02, 2016

[33] Villacres J, Nobes D and Ayranci C 2018 Additive manufacturing of shape memory polymers: effects of print orientation and infill percentage on mechanical properties *Rapid Prototyping J.* **24** 744-51

[34] Boley J W, White E L, Chiu G T - and Kramer R K 2014 Direct writing of gallium-indium alloy for stretchable electronics *Adv. Funct. Mater.* **24** 3501-7

[35] Khang D Y, Jiang H, Huang Y and Rogers J A 2006 A stretchable form of single-crystal silicon for high-performance electronics on rubber substrates *Science* **311** 208-12

[36] Sun Y and Rogers J A 2007 Inorganic semiconductors for flexible electronics *Adv. Mater.* **19** 1897-916

[37] Unsworth J, Conn C, Jin Z, Kaynak A, Ediriweera R, Innis P and Booth N 1994 Conducting polymers: properties and applications *J. Intell. Mater. Syst. Struct.* **5** 595-604

[38] Yang S and Ruckenstein E 1993 Preparation and mechanical properties of electrically conductive polypyrrole-poly(ethylene-co-vinyl acetate) composites *Synth. Met.* **60** 249-54

[39] Jung H C, Moon J H, Baek D H, Lee J H, Choi Y Y, Hong J S and Lee S H 2012 CNT/PDMS composite flexible dry electrodes for long-term ECG monitoring *IEEE Trans. Biomed. Eng.* **59** 1472-9

[40] Liu C X and Choi J W 2010 Strain-dependent resistance of PDMS and carbon nanotubes composite microstructures *IEEE Trans. Nanotechnol.* **9** 590-5

[41] Khosla A and Gray B L 2009 Preparation, characterization and micromolding of multi-walled carbon nanotube polydimethylsiloxane conducting nanocomposite polymer *Mater. Lett.* **63** 1203-6

[42] Chen M, Tao T, Zhang L, Gao W and Li C 2013 Highly conductive and stretchable polymer composites based on graphene/MWCNT network *Chem.Commun.* **49** 1612-4

[43] Chen Z, Xu C, Ma C, Ren W and Cheng H M 2013 Lightweight and flexible graphene foam composites for high-performance electromagnetic interference shielding *Adv. Mater.* **25** 1296-300

[44] Hu W, Niu X, Li L, Yun S, Yu Z and Pei Q 2012 Intrinsically stretchable transparent electrodes based on silver-nanowire-crosslinked-polyacrylate composites *Nanotechnology* **23** 344002

[45] Cong H and Pan T 2008 Photopatternable conductive PDMS materials for microfabrication *Adv. Funct. Mater.* **18** 1912-21

[46] Niu X, Peng S, Liu L, Wen W and Sheng P 2007 Characterizing and patterning of PDMS-based conducting composites *Adv. Mater.* **19** 2682-6

[47] Khondoker M A H, Yang S Y, Mun S C and Kim J 2012 Flexible and conductive ITO electrode made on cellulose film by spin-coating *Synth.Met.* **162** 1972-6

[48] Seyedin M Z, Razal J M R, Innis P C and Wallace G G 2014 Strain-responsive polyurethane/PEDOT:PSS elastomeric composite fibers with high electrical conductivity *Adv. Funct. Mater.* **24** 2957-66

[49] Yin Z P, Huang Y A, Bu N B, Wang X M and Xiong Y L 2010 Inkjet printing for flexible electronics: materials, processes and equipments *Chin. Sci. Bull.* **55** 3383-407

[50] Ko S H, Pan H, Grigoropoulos C P, Luscombe C K, Frechet J M and Poulikakos D 2007 All-inkjet-printed flexible electronics fabrication on a polymer substrate by low-temperature high-resolution selective laser sintering of metal nanoparticles *Nanotechnology* **18** 345202

[51] Khondoker M A H, Mun S C and Kim J 2013 Particle based conductive silver ink customized for ink jet printing on cellulose electro-active paper *Proc. SPIE (San Diego, California, USA)* p 86910Q

[52] Stoyanov H, Kollosche M, Risse S, Wache R and Kofod G 2013 Soft conductive elastomer materials for stretchable electronics and voltage controlled artificial muscles *Adv. Mater.* **25** 578-83

[53] Hosoda K, Tada Y and Asada M 2006 Anthropomorphic robotic soft fingertip with randomly distributed receptors *Robot Auton. Syst.* **54** 104-9

[54] Cagatay E, Kohler P, Lugli P and Abdellah A 2015 Flexible capacitive tactile sensors based on carbon nanotube thin films *IEEE Sensors J.* **15** 3225-33

[55] Lee H K, Chang S I and Yoon E 2006 A flexible polymer tactile sensor: fabrication and modular expandability for large area deployment *J. Microelectromech. Syst.* **15** 1681-6

[56] Kuo C M, Lin C H and Huang Y C 2005 Plastic deformation mechanism of pure copper at low homologous temperatures *Mat. Sci. Eng. A - Struct.* **396** 360-8

[57] Rogers J A, Someya T and Huang Y 2010 Materials and mechanics for stretchable electronics *Science* **327** 1603-7

[58] Rojas J P, Hussain A M, Arevalo A, Foulds I G, Torres Sevilla G A, Nassar J M and Hussain M M 2015 Transformational electronics are now reconfiguring *Proc. SPIE* **9467** 946709

[59] Befahy S, Yunus S, Pardoen T, Bertrand P and Troosters M 2007 Stretchable helical gold conductor on silicone rubber microwire *Appl. Phys. Lett.* **91** 141911

[60] Brosteaux D, Axisa F, Gonzalez M and Vanfleteren J 2007 Design and fabrication of elastic interconnections for stretchable electronic circuits *IEEE Electron Device Lett.* **28** 552-4

[61] Gonzalez M, Axisa F, Bulcke M V, Brosteaux D, Vandevelde B and Vanfleteren J 2008 Design of metal interconnects for stretchable electronic circuits *Microelectron. Reliab.* **48** 825-32

[62] Huyghe B, Rogier H, Vanfleteren J and Axisa F 2008 Design and manufacturing of stretchable high-frequency interconnects *IEEE Trans. Adv. Packag.* **31** 802-8

[63] Gray D S, Tien J and Chen C S 2004 High-conductivity elastomeric electronics *Adv. Mater.* **16** 393-7

[64] Miller M S, Davidson G J E, Sahli B J, Mailloux C M and Carmichael T B 2008 Fabrication of elastomeric wires by selective electroless metallization of poly(dimethylsiloxane) *Adv. Mater.* **20** 59-64

[65] Morent R, Geyter N D, Axisa F., Smet N D, Gengembre L., Leersnyder E D, Leys C, Vanfleteren J, Rymarczyk-Machal M, Schacht E. and Payen E 2007 Adhesion enhancement by a dielectric barrier discharge of PDMS used for flexible and stretchable electronics *J. Phys. D: Appl. Phys.* **40** 7392-401

[66] Rosset S, Niklaus M, Dubois P and Shea H R 2009 Metal ion implantation for the fabrication of stretchable electrodes on elastomers *Adv. Funct. Mater.* **19** 470-8

[67] Kim J, Banks A, Cheng H, Xie Z, Xu S, Jang K, Lee J W, Liu Z, Gutruf P, Huang X, Wei P, Liu F, Li K, Dalal M, Ghaffari R, Feng X, Huang Y, Gupta S, Paik U and Rogers J A 2015 Epidermal electronics with advanced capabilities in near-field communication *Small* **11** 906-12

[68] Huang X, Liu Y, Chen K, Shin W, Lu C, Kong G, Patnaik D, Lee S, Cortes J F and Rogers J A 2014 Stretchable, wireless sensors and functional substrates for epidermal characterization of sweat *Small* **10** 3083-90

[69] Huang X, Liu Y, Cheng H, Shin W, Fan J A, Liu Z, Lu C, Kong G, Chen K, Patnaik D, Lee S, Hage-Ali S, Huang Y and Rogers J A 2014 Materials and designs for wireless epidermal sensors of hydration and strain *Adv. Funct. Mater.* **24** 3846-54

[70] Gao L, Zhang Y, Malyarchuk V, Jia L, Jang K, Chad Webb R, Fu H, Shi Y, Zhou G, Shi L, Shah D, Huang X, Xu B, Yu C, Huang Y and Rogers J A 2014 Epidermal photonic devices for quantitative imaging of temperature and thermal transport characteristics of the skin *Nat. Commun.* **5** 4938

[71] Kim D, Lu N, Ma R, Kim Y, Kim R, Wang S, Wu J, Won S M, Tao H, Islam A, Yu K J, Kim T, Chowdhury R, Ying M, Xu L, Li M, Chung, Hyun-Joong, Keum H, McCormick M, Liu P, Zhang Y, Omenetto F G, Huang Y, Coleman T and Rogers J A 2011 Epidermal electronics *Science* **333** 838-43

[72] Rahimi R, Ochoa M, Yu W and Ziaie B 2014 A sewing-enabled stitch-and-transfer method for robust, ultra-stretchable, conductive interconnects *J Micromech. Microengineering* **24** 095018

[73] Wang X, Hu H, Shen Y, Zhou X and Zheng Z 2011 Stretchable conductors with ultrahigh tensile strain and stable metallic conductance enabled by prestrained polyelectrolyte nanoplatforms *Adv. Mater.* **23** 3090-4

[74] Whitney R J 1953 The measurement of volume changes in human limbs *J.Physiol.(Lond.)* **121** 1-27

[75] Beni G, Hackwood S and Jackel J L 1982 Continuous electrowetting effect *Appl.Phys.Lett.* **40** 912-4

[76] Liu T, Sen P and Kim C J 2012 Characterization of nontoxic liquid-metal alloy galinstan for applications in microdevices *J. Microelectromech. Syst.* **21** 443-50

[77] Winter T G 2003 The evaporation of a drop of mercury *Am. J. Phys.* **71** 783-6

[78] Furr A K 2000 CRC Handbook of Laboratory Safety (Boca Raton, Florida, USA: CRC Press) p 808

[79] Cheng S and Wu Z 2012 Microfluidic electronics *Lab Chip* **12** 2782-91

[80] Lide D R 2007 CRC Handbook of Chemistry and Physics (United Kingdom: CRC Press)

[81] Chandler J E, Messer H H and Ellender G 1994 Cytotoxicity of gallium and indium ions compared with mercuric ion *J.Dent.Res.* **73** 1554-9

[82] Joshipura I D, Ayers H R, Majidi C and Dickey M D 2015 Methods to pattern liquid metals *J.Mater.Chem.C* **3** 3834-41

[83] Mott N F 1934 The Resistance of Liquid Metals *P. Roy. Soc. Lond. A Mat.* **146** 465-72

[84] Scharmann F, Cherkashinin G, Breternitz V, Knedlik C, Hartung G, Weber T and Schaefer J A 2004 Viscosity effect on GaInSn studied by XPS *Surf. Interface Anal.* **36** 981-5

[85] Sangeeth C S S, Wan A and Nijhuis C A 2014 Equivalent circuits of a self-assembled monolayer-based tunnel junction determined by impedance spectroscopy *J.Am.Chem.Soc.* **136** 11134-44

[86] Regan M J, Tostmann H, Pershan P S, Magnussen O M, DiMasi E, Ocko B M and Deutsch M 1997 X-ray study of the oxidation of liquid-gallium surfaces *Phys.Rev.B* **55** 10786-90

[87] Plech A, Klemradt U, Metzger H and Peisl J 1998 In situ x-ray reflectivity study of the oxidation kinetics of liquid gallium and the liquid alloy $Ga_{0.93}Hg_{0.07}$ *J. Phys. Condens. Matter* **10** 971

[88] Cademartiri L, Thuo M M, Nijhuis C A, Reus W F, Tricard S, Barber J R, Sodhi R N S, Brodersen P, Kim C, Chiechi R C and Whitesides G M 2012 Electrical resistance of Ag^{TS}-$S(CH_2)_{n-1}CH_3$//Ga2O3/EGaIn tunneling junctions *J. Phys. Chem. C* **116** 10848-60

[89] Dickey M D, Chiechi R C, Larsen R J, Weiss E A, Weitz D A and Whitesides G M 2008 Eutectic gallium-indium (EGaIn): a liquid metal alloy for the formation of stable structures in microchannels at room temperature *Adv. Funct. Mater.* **18** 1097-104

[90] Chabala J M 1992 Oxide-growth kinetics and fractal-like patterning across liquid gallium surfaces *Phys. Rev. B* **46** 11346-57

[91] Khan M R, Eaker C B, Bowden E F and Dickey M D 2014 Giant and switchable surface activity of liquid metal via surface oxidation *Proc. Natl. Acad. Sci. U.S.A.* **111** 14047-51

[92] Chiechi R C, Weiss E A, Dickey M D and Whitesides G M 2008 Eutectic gallium-indium (EGaIn): a moldable liquid metal for electrical characterization of self-assembled monolayers *Angew. Chem. Int. Ed.* **47** 142-4

[93] Doudrick K, Liu S, Mutunga E M, Klein K L, Damle V, Varanasi K K and Rykaczewski K 2014 Different shades of oxide: from nanoscale wetting mechanisms to contact printing of gallium-based liquid metals *Langmuir* **30** 6867-77

[94] Irshad W and Peroulis D 2009 A silicon-based galinstan magnetohydrodynamic pump *Proc. of the 9th Int. Workshops on Micro and Nanotechnology for Power Generation and Energy Conversion Applications (Washington DC, USA)* Power MEMS) p 127

[95] Eddings M A and Gale B K 2006 A PDMS-based gas permeation pump for on-chip fluid handling in microfluidic devices *J Micromech. Microengineering* **16** 2396

[96] Lazar I M and Karger B L 2002 Multiple open-channel electroosmotic pumping system for microfluidic sample handling *Anal. Chem.* **74** 6259-68

[97] Grover W H, Skelley A M, Liu C N, Lagally E T and Mathies R A 2003 Monolithic membrane valves and diaphragm pumps for practical large-scale integration into glass microfluidic devices *Sens. Actuators B-Chem.* **89** 315-23

[98] Hansson T and Sjolander S 1997 Valve, especially for fluid handling bodies with microflowchannels *US Patent* US5593130 A

[99] Tang S, Khoshmanesh K, Sivan V, Petersen P, O'Mullane A P, Abbott D, Mitchell A and Kalantar-zadeh K 2014 Liquid metal enabled pump *Proc. Natl. Acad. Sci. U.S.A.* **111** 3304-9

[100] Gao M and Gui L 2014 A handy liquid metal based electroosmotic flow pump *Lab Chip* **14** 1866-72

[101] Kim D, Yoo J H, Choi W, Yoo K and Lee J - 2014 Real-time dynamically reconfigurable liquid metal based photolithography *27th Int'l Conf. on Micro. Electro. Mechanical Systems (San Francisco, CA, USA)* IEEE) p 540

[102] Kim D - and Rogers J A 2008 Stretchable electronics: materials strategies and devices *Adv. Mater.* **20** 4887-92

[103] Li M, Yu B and Behdad N 2010 Liquid-tunable frequency selective surfaces *IEEE Microw. Compon. Lett.* **20** 423-5

[104] Gmati I E, Calmon P F, Ali B, Pons P, Fulcrand R, Pinon S, Boussetta H, Kallala M A and Besbes K 2011 Fabrication and evaluation of an on-chip liquid micro-variable inductor *J Micromech. Microengineering* **21** 025018

[105] Knoblauch M, Hibberd J M, Gray J C and van Bel A J E 1999 A galinstan expansion femtosyringe for microinjection of eukaryotic organelles and prokaryotes *Nat. Biotech.* **17** 906-9

[106] Ladd C, So J H, Muth J and Dickey M D 2013 3D printing of free standing liquid metal microstructures *Adv. Mater.* **25** 5081-5

[107] Vetrovec J, Litt A S, Copeland D A, Junghans J and Durkee R 2013 Liquid metal heat sink for high-power laser diodes *Proc.SPIE* **8605** 86050E,86050E-7

[108] Hodes M, Rui Zhang, Lam L S, Wilcoxon R and Lower N 2014 On the potential of galinstan-based minichannel and minigap cooling *IEEE Trans. Compon. Packag. Manuf. Technol.* **4** 46-56

[109] Ma K Q and Liu J 2007 Nano liquid-metal fluid as ultimate coolant *Phys. Lett. A* **361** 252-6

[110] Kim H -, Maleki T, Wei P and Ziaie B 2009 A biaxial stretchable interconnect with liquid-alloy-covered joints on elastomeric substrate *J. Microelectromech. Syst.* **18** 138-46

[111] Larsen R J, Dickey M D, Whitesides G M and Weitz D A 2009 Viscoelastic properties of oxide-coated liquid metals *J. Rheol.* **53** 1305-26

[112] Zrnic D and Swatik D S 1969 On the resistivity and surface tension of the eutectic alloy of gallium and indium *J. Less-Common Metals* **18** 67-8

[113] Surmann P and Zeyat H 2005 Voltammetric analysis using a self-renewable non-mercury electrode *Anal. Bioanal. Chem.* **383** 1009-13

[114] Aqra F and Ayyad A 2011 Theoretical calculations of the surface tension of liquid transition metals *Metall. Mater. Trans. B* **42** 5-8

[115] Takahashi K, Yoshikawa A and Sandhu A 2007 Wide Bandgap Semiconductors: Fundamental Properties and Modern Photonic and Electronic Devices Springer-Verlag Berlin Heidelberg)

[116] Miller P H 1941 The electrical conductivity of zinc oxide *Phys.Rev.* **60** 890-5

[117] Osagawara M, Funahashi K, Demura T, Hagiwara T and Iwata K 1986 Enhancement of electrical conductivity of polypyrrole by stretching *Synth. Met.* **14** 61-9

[118] Zhao W, Bischof J L, Hutasoit J, Liu X, Fitzgibbons T C, Hayes J R, Sazio P J A, Liu C, Jain J K, Badding J V and Chan M H W 2015 Single-fluxon controlled resistance switching in centimeter-long superconducting gallium-indium eutectic nanowires *Nano Lett.* **15** 153-8

[119] Roberts P, Damian D D, Shan W, Lu T and Majidi C 2013 Soft-matter capacitive sensor for measuring shear and pressure deformation *Int. Conf. on Robotics and Automation (Karlsruhe, Germany)* IEEE) p 3529

[120] Kramer R K, Majidi C and Wood R J 2013 Masked deposition of gallium-indium alloys for liquid-embedded elastomer conductors *Adv.Funct.Mater.* **23** 5292-6

[121] Gozen B A, Tabatabai A, Ozdoganlar O B and Majidi C 2014 High-density soft-matter electronics with micron-scale line width *Adv. Mater.* **26** 5211-6

[122] Truong T D 2000 Selective deposition of micro scale liquid gallium alloy droplets. Los Angeles, CA, USA: University of California

[123] Daeyoung Kim, Jun Hyeon Yoo, Yunho Lee, Wonjae Choi, Koangki Yoo and Jeong-Bong Lee 2014 Gallium-based liquid metal inkjet printing *IEEE 27th Int'l Conf. on Micro Electro Mechanical Systems* p 967

[124] Zheng Y, He Z, Yang J and Liu J 2014 Personal electronics printing via tapping mode composite liquid metal ink delivery and adhesion mechanism *Sci. Rep.* **4** 4588

[125] Tang S, Zhu J, Sivan V, Gol B, Soffe R, Zhang W, Mitchell A and Khoshmanesh K 2015 Creation of liquid metal 3D microstructures using dielectrophoresis *Adv. Funct. Mater.* **25** 4445-52

[126] Lu T, Finkenauer L, Wissman J and Majidi C 2014 Rapid prototyping for soft-matter electronics *Adv. Funct. Mater.* **24** 3351-6

[127] Kim H -, Son C and Ziaie B 2008 A multiaxial stretchable interconnect using liquid-alloy-filled elastomeric microchannels *Appl. Phys. Lett.* **92** 011904

[128] Fassler A and Majidi C 2013 3D structures of liquid-phase GaIn alloy embedded in PDMS with freeze casting *Lab Chip* **13** 4442-50

[129] So J -, Thelen J, Qusba A, Hayes G J, Lazzi G and Dickey M D 2009 Reversibly deformable and mechanically tunable fluidic antennas *Adv. Funct. Mater.* **19** 3632-7

[130] So J - and Dickey M D 2011 Inherently aligned microfluidic electrodes composed of liquid metal *Lab Chip* **11** 905-11

[131] Cheng S, Wu Z, Hallbjorner P, Hjort K and Rydberg A 2009 Foldable and stretchable liquid metal planar inverted cone antenna *IEEE Trans. Antennas Propag.* **57** 3765-71

[132] Fassler A and Majidi C 2013 Soft-matter capacitors and inductors for hyperelastic strain sensing and stretchable electronics *Smart Mater. Struct.* **22** 055023

[133] Liu S, Sun X, Hildreth O J and Rykaczewski K 2015 Design and characterization of a single channel two-liquid capacitor and its application to hyperelastic strain sensing *Lab Chip* **15** 1376-84

[134] Pekas N, Zhang Q and Juncker D 2012 Electrostatic actuator with liquid metal–elastomer compliant electrodes used for on-chip microvalving *J. Micromech. Microeng.* **22** 097001

[135] Kubo M, Li X, Kim C, Hashimoto M, Wiley B J, Ham D and Whitesides G M 2010 Stretchable microfluidic radiofrequency antennas *Adv. Mater.* **22** 2749-52

[136] Cheng S and Wu Z 2010 Microfluidic stretchable RF electronics *Lab Chip* **10** 3227-34

[137] So J -, Koo H, Dickey M D and Velev O D 2012 Ionic current rectification in soft-matter diodes with liquid-metal electrodes *Adv. Funct. Mater.* **22** 625-31

[138] Koo H -, So J, Dickey M D and Velev O D 2011 Towards all-soft matter circuits: prototypes of quasi-liquid devices with memristor characteristics *Adv. Mater.* **23** 3559-64

[139] Park Y -, Majidi C, Kramer R, Berard P and Wood R J 2010 Hyperelastic pressure sensing with a liquid-embedded elastomer *J. Micromech. Microeng.* **20** 125029

[140] Park Y L, Chen B R and Wood R J 2012 Design and fabrication of soft artificial skin using embedded microchannels and liquid conductors *IEEE Sensors J.* **12** 2711-8

[141] Park Y -, Chen B - and Wood R J 2011 Soft artificial skin with multi-modal sensing capability using embedded liquid conductors *Sensors, 2011 IEEE (Limerick, Ireland)* IEEE) p 81

[142] Ponce Wong R D, Posner J D and Santos V J 2012 Flexible microfluidic normal force sensor skin for tactile feedback *Sens. and Actuators A* **179** 62-9

[143] Kramer R K, Majidi C and Wood R J 2011 Wearable tactile keypad with stretchable artificial skin *IEEE Int. Conf. on Robotics and Automation (Shanghai, China)* IEEE) p 1103

[144] Cheng S and Wu Z 2011 A microfluidic, reversibly stretchable, large-area wireless strain sensor *Adv. Funct. Mater.* **21** 2282-90

[145] Majidi C, Kramer R and Wood R J 2011 A non-differential elastomer curvature sensor for softer-than-skin electronics *Smart Mater. Struct.* **20** 105017

[146] Kramer R K, Majidi C, Sahai R and Wood R J 2011 Soft curvature sensors for joint angle proprioception *IEEE/RSJ Int. Conf. on Intelligent Robots and Systems (San Francisco CA, USA)* IEEE) p 1919

[147] Zhu S, So J, Mays R, Desai S, Barnes W R, Pourdeyhimi B and Dickey M D 2013 Ultrastretchable fibers with metallic conductivity using a liquid metal alloy core *Adv. Funct. Mater.* **23** 2308-14

[148] Mineart K P, Lin Y, Desai S C, Krishnan A S, Spontak R J and Dickey M D 2013 Ultrastretchable, cyclable and recyclable 1- and 2-dimensional conductors based on physically cross-linked thermoplastic elastomer gels *Soft Matter* **9** 7695-700

[149] Cheng S, Rydberg A, Hjort K and Wu Z 2009 Liquid metal stretchable unbalanced loop antenna *Appl.Phys.Lett.* **94** 144103

[150] Cumby B L, Hayes G J, Dickey M D, Justice R S, Tabor C E and Heikenfeld J C 2012 Reconfigurable liquid metal circuits by Laplace pressure shaping *Appl. Phys. Lett.* **101** 174102

[151] Jeong S H, Hjort K and Wu Z 2015 Tape transfer atomization patterning of liquid alloys for microfluidic stretchable wireless power transfer *Sci. Rep.* **5** 8419

[152] Hrehorova E, Rebros M, Pekarovicova A, Bazuin B, Ranganathan A, Garner S, Merz G, Tosch J and Boudreau R 2011 Gravure printing of conductive inks on glass substrates for applications in printed electronics *J. Display Technol.* **7** 318-24

[153] Gravure Association of America and Gravure Education Foundation 1991 Gravure: process and Technology (Rochester, NY: Gravure Association of America) p 462

[154] Jeong S H, Hjort K and Wu Z 2014 Tape transfer printing of a liquid metal alloy for stretchable RF electronics *Sensors* **14** 16311

[155] Sen P and Chang-Jin Kim 2009 Microscale liquid-metal switches—A review *IEEE Trans. Ind. Electron.* **56** 1314-30

[156] Zheng Y, Zhang Q and Liu J 2013 Pervasive liquid metal based direct writing electronics with roller-ball pen *AIP Adv.* **3** 112117

[157] Gao Y, Li H and Liu J 2012 Direct Writing of Flexible Electronics through Room Temperature Liquid Metal Ink *PLoS ONE* **7** e45485

[158] Gao Y, Li H and Liu J 2013 Directly Writing Resistor, Inductor and Capacitor to Composite Functional Circuits: A Super-Simple Way for Alternative Electronics *PLoS ONE* **8** e69761

[159] Yang J and Liu J 2014 Direct printing and assembly of FM radio at the user end via liquid metal printernull *Circuit World* **40** 134-40

[160] Wang Q, Yu Y, Yang J and Liu J 2015 Fast Fabrication of Flexible Functional Circuits Based on Liquid Metal Dual-Trans Printing *Adv. Mater.* **27** 7109-16

[161] Zheng Y, He Z, Gao Y and Liu J 2013 Direct Desktop Printed-Circuits-on-Paper Flexible Electronics *Sci. Rep.* **3** 1786

[162] Li G, Wu X and Lee D 2016 A galinstan-based inkjet printing system for highly stretchable electronics with self-healing capability *Lab Chip*

[163] Boley J W, White E L and Kramer R K 2015 Mechanically Sintered Gallium-Indium Nanoparticles *Adv. Mater.* **27** 2355-60

[164] E. L. White, J. C. Case and R. K. Kramer 2016 Multi-Element Strain Gauge Modules for Soft Sensory Skins *IEEE Sensors Journal* **16** 2607-16

[165] Siegel A C, Bruzewicz D A, Weibel D B and Whitesides G M 2007 Microsolidics: fabrication of three-dimensional metallic microstructures in poly(dimethylsiloxane) *Adv. Mater.* **19** 727-33

[166] Pourbaix M 1974 Atlas of Electrochemical Equilibria in Aqueous Solutions 16.1 (Houston, TX: National Association of Corrosion Engineers)

[167] Dickey M D 2014 Emerging applications of liquid metals featuring surface oxides *ACS Appl. Mater. Interfaces* **6** 18369-79

[168] Zuckerman J J 2007 Inorganic Reactions and Methods (Wiley: Online Library)

[169] Kim D, Thissen P, Viner G, Lee D -, Choi W, Chabal Y J and Lee J - 2013 Recovery of nonwetting characteristics by surface modification of gallium-based liquid metal droplets using hydrochloric acid vapor *ACS Appl. Mater. Interfaces* **5** 179-85

[170] Kim D, Lee Y, Lee D, Choi W and Lee J 2013 Hydrochloric acid-impregnated paper for liquid metal microfluidics *The 17th Int'l Conf. on Solid-State Sensors, Actuators and Microsystems* Transducers & Eurosensors) p 2620

[171] Wang J, Liu S, Guruswamy S and Nahata A 2013 Reconfigurable liquid metal based terahertz metamaterials via selective erasure and refilling to the unit cell level *Appl.Phys.Lett.* **103** 221116

[172] Li G, Parmar M and Lee D 2015 An oxidized liquid metal-based microfluidic platform for tunable electronic device applications *Lab Chip* **15** 766-75

[173] Dezellus O and Eustathopoulos N 2010 Fundamental issues of reactive wetting by liquid metals *J.Mater.Sci.* **45** 4256-64

[174] Kramer R K, Boley J W, Stone H A, Weaver J C and Wood R J 2014 Effect of microtextured surface topography on the wetting behavior of eutectic gallium-indium alloys *Langmuir* **30** 533-9

[175] Bico J, Thiele U and Quere D 2002 Wetting of textured surfaces *Colloids Surf. Physicochem. Eng. Aspects* **206** 41-6

[176] Kim D, Lee D W, Choi W and Lee J B 2013 A super-lyophobic 3-D PDMS channel as a novel microfluidic platform to manipulate oxidized galinstan *J. Microelectromech. Syst.* **22** 1267-75

[177] Kim D, Jung D, Yoo J H, Lee Y, Choi W, Lee G S, Yoo K and Lee J B 2014 Stretchable and bendable carbon nanotube on PDMS super-lyophobic sheet for liquid metal manipulation *J. Micromech. Microeng.* **24** 055018

[178] Jung Y C and Bhushan B 2009 Mechanically durable carbon nanotube-composite hierarchical structures with superhydrophobicity, self-cleaning, and low-drag *ACS Nano* **3** 4155-63

[179] Lau K K S, Bico J, Teo K B K, Chhowalla M, Amaratunga G A J, Milne W I, McKinley G H and Gleason K K 2003 Superhydrophobic Carbon Nanotube Forests *Nano Lett.* **3** 1701-5

[180] Bayer I S, Steele A and Loth E 2013 Superhydrophobic and electroconductive carbon nanotube-fluorinated acrylic copolymer nanocomposites from emulsions *Chem. Eng. J.* **221** 522-30

[181] Li H, Wang X, Song Y, Liu Y, Li Q, Jiang L and Zhu D 2001 Super-"amphiphobic" aligned carbon nanotube films *Angew. Chem. Int. Ed.* **40** 1743-6

[182] Madou M J 2012 Fundamentals of Microfabrication and Nanotechnology (Boca Raton: CRC Press)

[183] Mack C 2007 Fundamental Principles of Optical Lithography: The Science of Microfabrication Wiley)

[184] Gao Y and Bando Y 2002 Nanotechnology: carbon nanothermometer containing gallium *Nature* **415** 599-600

[185] Liu Z, Bando Y, Mitome M and Zhan J 2004 Unusual freezing and melting of gallium encapsulated in carbon nanotubes *Phys. Rev. Lett.* **93** 095504

[186] Wang L and Liu J 2014 Liquid phase 3D printing for quickly manufacturing conductive metal objects with low melting point alloy ink *Sci. China Technol. Sc.* **57** 1721-8

[187] Wang L and Liu J 2014 Compatible hybrid 3D printing of metal and nonmetal inks for direct manufacture of end functional devices *Sci. China Technol. Sc.* **57** 2089-95

[188] Gross F B 2010 Frontiers in Antennas: Next Generation Design & Engineering (New York: McGraw-Hill) p 512

[189] Ohta A T, Guo S, Lei B J, Hu W and Shiroma W A 2012 A liquid-metal tunable electromagnetic-bandgap microstrip filter *Int'l Conf. on Wireless Information Technology and Systems (ICWITS) (Maui, Hawaii)* IEEE) p 1

[190] Khan M R, Hayes G J, Zhang S, Dickey M D and Lazzi G 2012 A pressure responsive fluidic microstrip open stub resonator using a liquid metal alloy *IEEE Microw. Compon. Lett* **22** 577-9

[191] Chen C and Peroulis D 2007 Liquid RF MEMS wideband reflective and absorptive switches *IEEE Trans. Microw. Theory Techn.* **55** 2919-29

[192] Li M and Nader B 2012 Fluidically tunable frequency selective/phase shifting surfaces for high-power microwave applications *IEEE Trans. Antennas Propag.* **60** 2748-59

[193] Morishita A M, Kitamura C K Y, Ohta A T and Shiroma W A 2013 A liquid-metal monopole array with tunable frequency, gain, and beam steering *IEEE Antennas Wireless Propag. Lett.* **12** 1388-91

[194] Dey A, Guldiken R and Mumcu G 2013 Wideband frequency tunable liquid metal monopole antenna *Int'l Symp. on Antennas and Propagation Society (APSURSI) (Orlando, Florida, USA)* IEEE) p 392

[195] Kim D, Pierce R G, Henderson R, Doo S J, Yoo K and Lee J 2014 Liquid metal actuation-based reversible frequency tunable monopole antenna *Appl.Phys.Lett.* **105** 234104

[196] Hayes G J, So J, Qusba A, Dickey M D and Lazzi G 2012 Flexible liquid metal alloy (EGaIn) microstrip patch antenna *IEEE Trans. Antennas Propag.* **60** 2151-6

204

[197] Wang J, Liu S and Nahata A 2012 Reconfigurable plasmonic devices using liquid metals *Opt.Express* **20** 12119-26

[198] Li G, Parmar M, Kim D, Lee J (B) and Lee D 2014 PDMS based coplanar microfluidic channels for the surface reduction of oxidized Galinstan *Lab Chip* **14** 200-9

[199] Kim D, Lee D -, Choi W and Lee J 2012 A super-lyophobic PDMS micro-tunnel as a novel microfluidic platform for oxidized Galinstan® *25th Int'l Conf. on Micro Electro Mechanical Systems (Paris, France)* IEEE) p 1005

[200] Hutter T, Bauer W C, Elliott S R and Huck W T S 2012 Formation of spherical and non-spherical eutectic gallium-indium liquid-metal microdroplets in microfluidic channels at room temperature *Adv. Funct. Mater.* **22** 2624-31

[201] Koo C, LeBlanc B E, Kelley M, Fitzgerald H E, Huff G H and Han A 2015 Manipulating liquid metal droplets in microfluidic channels with minimized skin residues toward tunable RF applications *J Microelectromech Syst* **24** 1069-76

[202] Khan M R, Trlica C, So J, Valeri M and Dickey M D 2014 Influence of water on the interfacial behavior of gallium liquid metal alloys *ACS Appl. Mater. Interfaces* **6** 22467-73

[203] Gough R C, Morishita A M, Dang J H, Hu W, Shiroma W A and Ohta A T 2014 Continuous electrowetting of non-toxic liquid metal for RF applications *IEEE Access* **2** 874-82

[204] Tang S, Lin Y, Joshipura I D, Khoshmanesh K and Dickey M D 2015 Steering liquid metal flow in microchannels using low voltages *Lab Chip* **15** 3905-11

[205] Khan M R, Trlica C and Dickey M D 2015 Recapillarity: electrochemically controlled capillary withdrawal of a liquid metal alloy from microchannels *Adv. Funct. Mater.* **25** 671-8

[206] Diedhiou D L, Sagazan O d, Sauleau R and Boriskin A V 2014 Contactless microstrip transition for flexible microfluidic circuits and antennas *IEEE Antennas Wireless Propag Lett* **14** 1502-5

[207] Chua C K, Leong K F and Lim C S 2010 Rapid Prototyping: Principles and Applications World Scientific)

[208] Subcommittee F42.91 on Terminology. Standard Terminology for Additive Manufacturing Technologies. 2012; Available at: https://www.astm.org/Standards/ISOASTM52900.htm. Accessed November/17, 2017

[209] Hashmi S 2014 Comprehensive Materials Processing 10 Elsevier Science)

[210] Yadroitsev I 2009 Selective Laser Melting: Direct Manufacturing of 3D-Objects by Selective Laser Melting of Metal Powders Lambert Academic Publishing)

[211] Surhone L M, Timpledon M T and Marseken S F 2010 Selective Laser Sintering VDM Publishing)

[212] Park J 1998 Characterization of the Laminated Object Manufacturing (LOM) Process and Applications University of California, Los Angeles)

[213] Bartolo P J 2011 Stereolithography: Materials, Processes and Applications Springer US) p 340

[214] Lipson H and Kurman M 2013 Fabricated: The New World of 3D Printing John Wiley & Sons) p 320

[215] Pandey P M, Venkata Reddy N and Dhande S G 2003 Improvement of surface finish by staircase machining in fused deposition modeling *J. Mater. Process. Technol.* **132** 323-31

[216] Taufik M and Jain P K 2016 A Study of Build Edge Profile for Prediction of Surface

Roughness in Fused Deposition Modeling *J. Manuf. Sci. Eng.* **138** 061002

[217] Turner B N and Scott A G 2015 A review of melt extrusion additive manufacturing processes:

II. Materials, dimensional accuracy, and surface roughness *Rapid Prototyping J.* **21** 250-61

[218] Faes M, Ferraris E and Moens D 2016 Influence of Inter-layer Cooling time on the Quasi-

static Properties of ABS Components Produced via Fused Deposition Modelling *Procedia CIRP*

42 748-53

[219] Sung-Hoon Ahn, Montero M, Odell D, Roundy S and Wright P K 2002 Anisotropic material

properties of fused deposition modeling ABS *Rapid Prototyping J.* **8** 248-57

[220] Espalin D, Medina F, Arcaute K, Zinniel B, Hoppe T and Wicker R 2009 Effects of Vapor

Smoothing on ABS Part Dimensions *In Technical Paper - Society of Manufacturing Engineers*

(Schaumburg, IL) vol TP09PUB14 University of Texas) p pp 1-17

[221] Ahn D K, Kim H C and Lee S H 2005 Determination of fabrication direction to minimize

post-machining in FDM by prediction of non-linear roughness characteristics *Journal of*

Mechanical Science and Technology **19** 144-55

[222] Elkins K, Nordby H, Janak C, Gray R W, Bohn J H and Baird D G 1997 Soft elastomers

for fused deposition modeling *Annual International Solid Freeform Fabrication Symposium (The*

University of Texas in Austin) Laboratory for Freeform Fabrication and University of Texas at

Austin) p 441

[223] Bschaden B S 2014 Developing design guidelines for improved gecko inspired dry adhesive.

Edmonton, AB, Canada: University of Alberta

[224] M. Zandvakili, M. M. Honari, D. Sameoto and P. Mousavi 2016 Microfluidic liquid metal based mechanically reconfigurable antenna using reversible gecko adhesive based bonding *2016 IEEE MTT-S International Microwave Symposium (IMS)* p 1

[225] Rabin B H and Shiota I 1995 Functionally Gradient Materials *MRS Bull.* **20** 14-8

[226] Koizumi M and Niino M 1995 Overview of FGM Research in Japan *MRS Bull.* **20** 19-21

[227] Kaysser W A and Ilschner B 1995 FGM Research Activities in Europe *MRS Bull.* **20** 22-6

[228] Bruyas A, Geiskopf F and Renaud P 2014 Towards Statically Balanced Complaint Joints Using Multimaterial 3D Printing *Proc. IDETC/CIE (Buffalo, New York, USA)* ASME)

[229] Flory P J 1942 Thermodynamics of High Polymer Solutions *J.Chem.Phys.* **10** 51-61

[230] Vadori R 2012 Studies on the Blending of Poly(Lactic Acid) and Acrylonitrile Butadiene Styrene. Guelph, ON, Canada: University of Guelph

[231] Tan Z Y, Xu X F, Sun S L, Zhou C, Ao Y H, Zhang H X and Han Y 2006 Influence of rubber content in ABS in wide range on the mechanical properties and morphology of PC/ABS blends with different composition *Polym. Eng. Sci.* **46** 1476-84

[232] Koning C, Van Duin M, Pagnoulle C and Jerome R 1998 Strategies for compatibilization of polymer blends *Prog. Polym. Sci.* **23** 707-57

[233] Kim Y F, Choi C N, Kim Y D, Lee K Y and Lee M S 2004 Compatibilization of immiscible poly(l-lactide) and low density polyethylene blends *Fibers Polym.* **5** 270-4

[234] Dong W, He M, Wang H, Ren F, Zhang J, Zhao X and Li Y 2015 PLLA/ABS Blends Compatibilized by Reactive Comb Polymers: Double Tg Depression and Significantly Improved Toughness *ACS Sustainable Chem. Eng.* **3** 2542-50

[235] Chen J, Shi Y, Yang J, Zhang N, Huang T and Wang Y 2013 Improving interfacial adhesion between immiscible polymers by carbon nanotubes *Polymer* **54** 464-71

[236] Zeng J, Li K and Du A 2015 Compatibilization strategies in poly(lactic acid)-based blends *RSC Adv.* **5** 32546-65

[237] Dong W, Wang H, He M, Ren F, Zheng Q and Li Y 2015 Synthesis of Reactive Comb Polymers and Their Applications as a Highly Efficient Compatibilizer in Immiscible Polymer Blends *Ind. Eng. Chem. Res.* **54** 2081-9

[238] Jin X, Heepe L, Strueben J, Adelung R, Gorb S N and Staubitz A 2014 Challenges and Solutions for Joining Polymer Materials *Macromolecular Rapid Communications* **35** 1551-70

[239] Potschke P and Paul D R 2003 Formation of Co-continuous Structures in Melt-Mixed Immiscible Polymer Blends *Journal of Macromolecular Science, Part C* **43** 87-141

[240] Avgeropoulos G N, Weissert F C, Biddison P H and Böhm G G A 1976 Heterogeneous Blends of Polymers. Rheology and Morphology *Rubber Chemistry and Technology* **49** 93-104

[241] Everaert V, Aerts L and Groeninckx G 1999 Phase morphology development in immiscible PP/(PS/PPE) blends influence of the melt-viscosity ratio and blend composition *Polymer* **40** 6627-44

[242] Steinmann S, Gronski W and Friedrich C 2002 Quantitative rheological evaluation of phase inversion in two-phase polymer blends with cocontinuous morphology *Rheologica Acta* **41** 77-86

[243] Utracki L A and Wilkie C A 2014 Polymer Blends Handbook Springer Netherlands) p 2378

[244] Luciani A and Jarrin J 1996 Morphology development in immiscible polymer blends *Polym.Eng.Sci.* **36** 1619-26

[245] Ho R M, Wu C H and Su A C 1990 Morphology of plastic/rubber blends *Polym.Eng.Sci.* **30** 511-8

[246] Kitayama N, Keskkula H and Paul D R 2000 Reactive compatibilization of nylon 6/styrene–acrylonitrile copolymer blends. Part 1. Phase inversion behavior *Polymer* **41** 8041-52

[247] Utracki L A 2013 Commercial Polymer Blends Springer US) p 658

[248] Paul D R and Newman S 1978 Polymer Blends (Volume 2) (New York: Academic Press) p 435

[249] Metelkin V I and Blekht V P 1984 Formation of a Continuous Phase in Heterogeneous Polymer Mixtures *Colloid Journal of the USSR* **46** 425-9

[250] Agarwala M K, Jamalabad V R, Langrana N A, Safari A, Whalen P J and Danforth S C 1996 Structural quality of parts processed by fused deposition *Rapid Prototyping J.* **2** 4-19

[251] Bellini A, Guceri S and Bertoldi M 2004 Liquefier Dynamics in Fused Deposition *J. Manuf. Sci. E -T. ASME* **126** 237-46

[252] Khondoker M A H and Sameoto D 2016 Design and Characterization of a Bi-Material Co-Extruder for Fused Deposition Modeling *Proc. International Mechanical Engineering Congress and Exposition (Phoenix, AZ, USA)* vol 2 The American Society of Mechanical Engineers) p IMECE2016-65330

[253] Turner B N, Strong R and Gold S A 2014 A review of melt extrusion additive manufacturing processes: I. Process design and modeling *Rapid Prototyping J.* **20** 192-204

[254] Osswald T A and Hernandez-Ortiz J P 2006 Polymer Processing: Modeling and Simulation (Munich: Hanser Publishers) p 649

[255] Dawson PC. Flow Properties of Molten Polymers. In: Swallowe GM, editor. Mechanical Properties and Testing of Polymers. 1st edition ed.: Springer Netherlands; 1999. p. 88-95

[256] Brydson J A 1981 Flow Properties of Polymer Melts (London, UK: Van Nostrand Reinhold Co.) p 226

[257] Wang T, Xi J and Jin Y 2007 A model research for prototype warp deformation in the FDM process *Int. J. Adv. Manuf. Technol.* **33** 1087-96

[258] Cverna F 2002 ASM Ready Reference: Thermal Properties of Metals (Materials Park, Ohio: ASM International) p 560

[259] Michaeli W 2003 Extrusion Dies for Plastics and Rubber Carl Hanser Verlag GmbH & Co. KG) p 362

[260] Ramanath H S, Chua C K, Leong K F and Shah K D 2008 Melt flow behaviour of poly-epsilon-caprolactone in fused deposition modelling *J.Mater.Sci.Mater.Med.* **19** 2541-50

[261] Altınkaynak A, Gupta M, Spalding M A and Crabtree S L 2011 Melting in a Single Screw Extruder: Experiments and 3D Finite Element Simulations *Intern. Polymer Processing* **26** 182-96

[262] McKelvey J M 1962 Polymer Processing (New York, USA: John Wiley and Sons, Inc.) p 409

[263] Cengel Y A 2007 Heat & Mass Transfer: A Practical Approach (India: McGraw-Hill) p 879

[264] Jo WH, Yang JS, Creton C, Kramer EJ, Brown HR, Hui C, et al. Molecular Simulation Fracture Gel Theory. Advances in Polymer Science: Springer-Berlin Heidelberg; 2002. p. 228

[265] Cole P J, Cook R F and Macosko C W 2003 Adhesion between immiscible polymers correlated with interfacial entanglements *Macromolecules* **36** 2808-15

[266] Hessel V, Löwe H and Schönfeld F 2005 Micromixers—a review on passive and active mixing principles *Chemical Engineering Science* **60** 2479-501

[267] Lee C, Wang W, Liu C and Fu L 2016 Passive mixers in microfluidic systems: A review *Chem.Eng.J.* **288** 146-60

[268] Rodríguez J F, Thomas J P and Renaud J E 2001 Mechanical behavior of acrylonitrile butadiene styrene (ABS) fused deposition materials. Experimental investigation *Rapid Prototyping J.* **7** 148-58

[269] Srivatsan T S and Sudarshan T S 2015 Additive Manufacturing: Innovations, Advances, and Applications CRC Press)

[270] Yardimci M A, Guceri S I and Danforth S C 1997 Thermal Analysis of Fused Deposition *Annual International Solid Freeform Fabrication Symposium (Austin, TX)* The University of Texas at Austin)

[271] Venkataraman N, Rangarajan S, M.J. Matthewson, Harper B, Safari A, S.C. Danforth, Wu G, Langrana N, Guceri S and Yardimci A 2000 Feedstock material property – process relationships in fused deposition of ceramics (FDC) *Rapid Prototyping J.* **6** 244-53

[272] Available at: https://ninjatek.com/products/filaments/ninjaflex/. Accessed Nov/29, 2017

[273] Available at: http://www.polymaker.com/shop/polyflex/. Accessed Nov/29, 2017

[274] Available at: http://www.madesolid.com/. Accessed Nov/29, 2017

[275] Saari M, Galla M, Cox B, Krueger P, Cohen A and Richer E 2015 Additive manufacturing of soft and composite parts from thermoplastic elastomers *Annual International Solid Freeform Fabrication Symposium (Austin, TX)* The University of Texas at Austin) p 949

[276] TITAN Robotics. Available at: http://www.titan3drobotics.com/atlas/. Accessed October/9, 2018

[277] Linthicum T, Simpson DS, Linthicum B, Peterson P, inventors. Sculptify LLC, assignee. Extrusion system for additive manufacturing and 3-d printing. US patent US20150321419A1. 2014 Pending

[278] Whyman S, Arif K M and Potgieter J 2018 Design and development of an extrusion system for 3D printing biopolymer pellets *The International Journal of Advanced Manufacturing Technology* **96** 3417-28

[279] Woern A L, Byard D J, Oakley R B, Fiedler M J, Snabes S L and Pearce J M 2018 Fused Particle Fabrication 3-D Printing: Recycled Materials' Optimization and Mechanical Properties *Materials* **11** 1413

[280] Moreno Nieto D, Casal López V and Molina S I 2018 Large-format polymeric pellet-based additive manufacturing for the naval industry *Additive Manufacturing* **23** 79-85

[281] Ajinjeru C, Kishore V, Liu P, Lindahl J, Hassen A A, Kunc V, Post B, Love L and Duty C 2018 Determination of melt processing conditions for high performance amorphous thermoplastics for large format additive manufacturing *Additive Manufacturing* **21** 125-32

[282] Singamneni S, Smith D, LeGuen M and Truong D 2018 Extrusion 3D Printing of Polybutyrate-Adipate-Terephthalate-Polymer Composites in the Pellet Form *Polymers* **10** 922

[283] Sameoto D. Manufacturing Approaches and Applications for Bioinspired Dry Adhesives. In: Heepe L, Xue L, Gord S, editors. Bio-inspired Structured Adhesives Cham, Germany: Springer; 2017. p. 221-244

[284] Available at: https://www.filastruder.com/products/filastruder-kit. Accessed March/20, 2018

[285] Khondoker M A H and Sameoto D 2017 Printing with mechanically interlocked extrudates using a custom bi-extruder for fused deposition modelling *Rapid Prototyping J.* **24** 921-34

[286] Morton-Jones D H 1989 Polymer Processing (New York: Chapman and Hall)

[287] Crawford R J 1981 Plastics Engineering (Oxford: Butterworth-Heinemann)

[288] Stevens M J and Covas J A 1995 Extruder Principles and Operation (UK: Springer Science+Business Media)

[289] Munson B R, Okiishi T H, Huebsch W W and Rothmayer A P 2013 Fundamentals of Fluid Mechanics Wiley)

[290] Hannan M W and Walker I D 2003 Kinematics and the Implementation of an Elephant's Trunk Manipulator and Other Continuum Style Robots *J.Robotic Syst.* **20** 45-63

[291] Laschi C, Cianchetti M, Mazzolai B, Margheri L, Follador M and Dario P 2012 Soft Robot Arm Inspired by the Octopus *Adv.Rob.* **26** 709-27

[292] Bobak M, Panagiotis P, Christoph K, Sophia W, Shepherd R F, Unmukt G, Jongmin S, Katia B, Walsh C J and Whitesides G M 2014 Pneumatic networks for soft robotics that actuate rapidly *Adv.Funct.Mater.* **24** 2163-70

[293] Wagner M, Chen T and Shea K 2017 Large Shape Transforming 4D Auxetic Structures *3D Printing and Additive Manufacturing* **4** 133-42

[294] Liu Y and Hu H 2010 A review on auxetic structures and polymeric materials *Scientific Research and Essays* **5** 1052-63

[295] Rossiter J, Takashima K, Scarpa F, Walters P and Mukai T 2014 Shape memory polymer hexachiral auxetic structures with tunable stiffness *Smart Mater.Struct.* **23** 045007

[296] Grima J N, Alderson A. and Evans K E 2005 Auxetic behaviour from rotating rigid units *phys.stat.sol.(b)* **242** 561-75

[297] Dolla W J, Fricke B A and Becker B R 2006 Structural and Drug Diffusion Models of Conventional and Auxetic Drug-Eluting Stents *Journal of Medical Devices* **1** 47-55

[298] Cebeci T 1974 Laminar-Free-Convective-Heat Transfer from the Outer Surface of a Vertical Slender Circular Cylinder *Proc. Int'l Conf. Fluid Mech. Heat Trans. (Tokyo, Japan)* vol 3 Society of Heat Transfer of Japan) p 15

[299] Available at: http://slic3r.org/download. Accessed November/17, 2017

[300] Raasch J, Ivey M, Aldrich D, Nobes D S and Ayranci C 2015 Characterization of polyurethane shape memory polymer processed by material extrusion additive manufacturing *Additive Manufacturing* **8** 132-41

[301] Trivedi D, Rahn C D, Kier W M and Walker I D 2008 Soft robotics: Biological inspiration, state of the art, and future research *Applied Bionics and Biomechanics* **5** 99-117

[302] Chirikjian G S and Burdick J W 1994 A hyper-redundant manipulator *IEEE Robotics & Automation Magazine* **1** 22-9

[303] Chirikjian G S and Burdick J W 1995 The kinematics of hyper-redundant robot locomotion *IEEE Transactions on Robotics and Automation* **11** 781-93

[304] Mutlu R, Yildiz S K, Alici G, in het Panhuis M and Spinks G M 2016 Mechanical stiffness augmentation of a 3D printed soft prosthetic finger *2016 IEEE International Conference on Advanced Intelligent Mechatronics (AIM) (Banff, Canada)* IEEE) p 7

[305] Hannan M W and Walker I D 2001 Analysis and experiments with an elephant's trunk robot *Adv.Rob.* **15** 847-58

[306] Huai-Ti Lin and Gary G Leisk and,Barry Trimmer 2011 GoQBot: a caterpillar-inspired soft-bodied rolling robot *Bioinspiration & Biomimetics* **6** 026007

[307] Martinez R V, Fish C R, Xin C and Whitesides G M 2012 Elastomeric Origami: Programmable Paper-Elastomer Composites as Pneumatic Actuators *Adv.Funct.Mater.* **22** 1376-84

[308] Bartlett N W, Tolley M T, Overvelde J T B, Weaver J C, Mosadegh B, Bertoldi K, Whitesides G M and Wood R J 2015 A 3D-printed, functionally graded soft robot powered by combustion *Science* **349** 161-5

[309] MacCurdy R, Katzschmann R, Kim Y and Rus D 2016 Printable hydraulics: A method for fabricating robots by 3D co-printing solids and liquids *IEEE Int'l Conf. on Robotics and Automation (Stockholm, Sweden)* IEEE) p 3878

[310] Drotman D, Jadhav S, Karimi M, deZonia P and Tolley M T 2017 3D printed soft actuators for a legged robot capable of navigating unstructured terrain *IEEE Int'l Conf. on Robotics and Automation (Singapore)* IEEE) p 5532

[311] Wang Z, Torigoe Y and Hirai S 2017 A Prestressed Soft Gripper: Design, Modeling, Fabrication, and Tests for Food Handling *IEEE Robotics and Automation Letters* **2** 1909-16

[312] Peele B N, Wallin T J, Zhao H and Shepherd R F 2015 3D printing antagonistic systems of artificial muscle using projection stereolithography *Bioinspiration & Biomimetics* **10** 055003

[313] Tolley M T, Shepherd R F, Mosadegh B, Galloway K C, Wehner M, Karpelson M, Wood R J and Whitesides G M 2014 A Resilient, Untethered Soft Robot *Soft Robotics* **1** 213-23

[314] Zhou C, Chen Y, Yang Z and Khoshnevis B 2011 Development of a Multi-material Mask-Image-Projection-based Stereolithography for the Fabrication of Digital Materials *SFF Symposium (Austin, TX, USA)* Laboratory for Freeform Fabrication and University of Texas at Austin) p 65

[315] M.A. Jafari, Han W, Mohammadi F, Safari A, S.C. Danforth and Langrana N 2000 A novel system for fused deposition of advanced multiple ceramics *Rapid Prototyping J.* **6** 161-75

[316] Pilleux M E, Safari A, Allahverdi M, Chen Y, Lu Y and Jafari M A 2002 3-D photonic bandgap structures in the microwave regime by fused deposition of multimaterials *Rapid Prototyping J.* **8** 46-52

[317] Garland A and Fadel G 2015 Design and Manufacturing Functionally Gradient Material Objects With an Off the Shelf Three-Dimensional Printer: Challenges and Solutions *J. Mech. Design* **137** 111407

[318] Kumar K, Liu J, Christianson C, Ali M, Tolley M, T., Aizenberg J, Ingber D E, Weaver J, C. and Bertoldi K 2017 A Biologically Inspired, Functionally Graded End Effector for Soft Robotics Applications *Soft Robotics* **4** 317-23

[319] Lee J, Kim W, Choi W and Cho K 2016 Soft Robotic Blocks: Introducing SoBL, a Fast-Build Modularized Design Block *IEEE Robotics & Automation Magazine* **23** 30-41

217

[320] Geeetech Prusa I3 M201 3D printer. 2014; Available at: http://www.geeetech.com/geeetech-prusa-i3-m201-3d-printer-diy-kit-p-965.html. Accessed Nov 17, 2017

[321] Big Builder 3D Printer Dual – Feed. 2016; Available at: http://builder3dprinters.com/product/builder-premium-large-red/. Accessed Nov 17, 2017

[322] Govers F X 2015 Diamond Hotend makes multi-color 3D printing possible from a single nozzle *New Atlas* **Electronics**

[323] Brochard F, Jouffroy J and Levinson P 1983 Polymer-polymer diffusion in melts *Macromolecules* **16** 1638-41

[324] Available at: https://www.astm.org/Standards/D1708.htm. Accessed November/17, 2017

[325] Torrado A R and Roberson D A 2016 Failure Analysis and Anisotropy Evaluation of 3D-Printed Tensile Test Specimens of Different Geometries and Print Raster Patterns *Journal of Failure Analysis and Prevention* **16** 154-64

[326] Dinwiddie R B, Vlastimil Kunc, Lindal J M, Brian Post, Smith R J, Lonnie Love and Duty C E 2014 Infrared imaging of the polymer 3D-printing process *Proc. SPIE Thermosense: Thermal Infrared Applications (Baltimore, MD, USA)* vol 9105 SPIE) p 910502

[327] Malloy R A 1994 Plastic Part Design for Injection Molding (Cincinnati, OH: Hanser Publications)

[328] Pan A Q, Huang Z F, Guo R J and Liu J 2016 Effect of FDM Process on Adhesive Strength of Polylactic Acid(PLA) Filament *Key Eng Mat* **667** 181-6

[329] Service R F 2003 Electronic Textiles Charge Ahead *Science* **301** 909-11

[330] Gibbs P T and Asada H H 2005 Wearable Conductive Fiber Sensors for Multi-Axis Human Joint Angle Measurements *Journal of NeuroEngineering and Rehabilitation* **2** 7

[331] Daalkhaijav U, Yirmibesoglu O D, Walker S and Mengüç Y 2018 Rheological Modification of Liquid Metal for Additive Manufacturing of Stretchable Electronics *Adv.Mater.Technol.* **3** 1700351

[332] Helseth L E 2018 Interdigitated electrodes based on liquid metal encapsulated in elastomer as capacitive sensors and triboelectric nanogenerators *Nano Energy* **50** 266

[333] Yan H, Chen Y, Deng Y, Zhang L, Hong X, Lau W, Mei J, Hui D, Yan H and Liu Y 2016 Coaxial printing method for directly writing stretchable cable as strain sensor *Appl.Phys.Lett.* **109** 083502

[334] Yu Y, Liu F and Liu J 2017 Direct 3D printing of low melting point alloy via adhesion mechanism *Rapid Prototyping Journal* **23** 642-50

[335] KRATON G1657 M Polymer. Available at: http://www.kraton.com/products/pdsDocs/polymer/G1657M.pdf?. Accessed September/30, 2018

[336] Khondoker M A H and Sameoto D 2018 Soft is no longer hard: extruding anything with a filament free FDM technique *Progress in Additive Manufacturing* (**Under review: PIAM-D-18-00034**)

[337] Khondoker M A H, Baheri N and Sameoto D 2018 Tendon Driven Functionally Gradient Soft Robotic Gripper 3D Printed with Intermixed Extrudate of Hard and Soft Thermoplastics *3D Printing and Additive Manufacturing* (**Under review: 3DP-2018-0102.R1**)

[338] Hallfors N, Khan A, Dickey M D and Taylor A M 2013 Integration of pre-aligned liquid metal electrodes for neural stimulation within a user-friendly microfluidic platform *Lab Chip* **13** 522-6

[339] Lin Y, Ladd C, Wang S, Martin A, Genzer J, Khan S A and Dickey M D 2016 Drawing liquid metal wires at room temperature *Extreme Mechanics Letters* **7** 55-63

[340] Utada A S, Fernandez-Nieves A, Stone H A and Weitz D A 2007 Dripping to Jetting Transitions in Coflowing Liquid Streams *Phys.Rev.Lett.* **99** 094502

[341] Eggers J 1997 Nonlinear dynamics and breakup of free-surface flows *Rev.Mod.Phys.* **69** 865-930

[342] Umbanhowar P B, Prasad V and Weitz D A 2000 Monodisperse Emulsion Generation via Drop Break Off in a Coflowing Stream *Langmuir* **16** 347-51

[343] Nagaoka H 1909 The Inductance Coefficients of Solenoids *Journal of the College of Science, Imperial University* **27** 6

APPENDIX

CAD DRAWINGS OF THE TRI-EXTRUDER SYSTEM
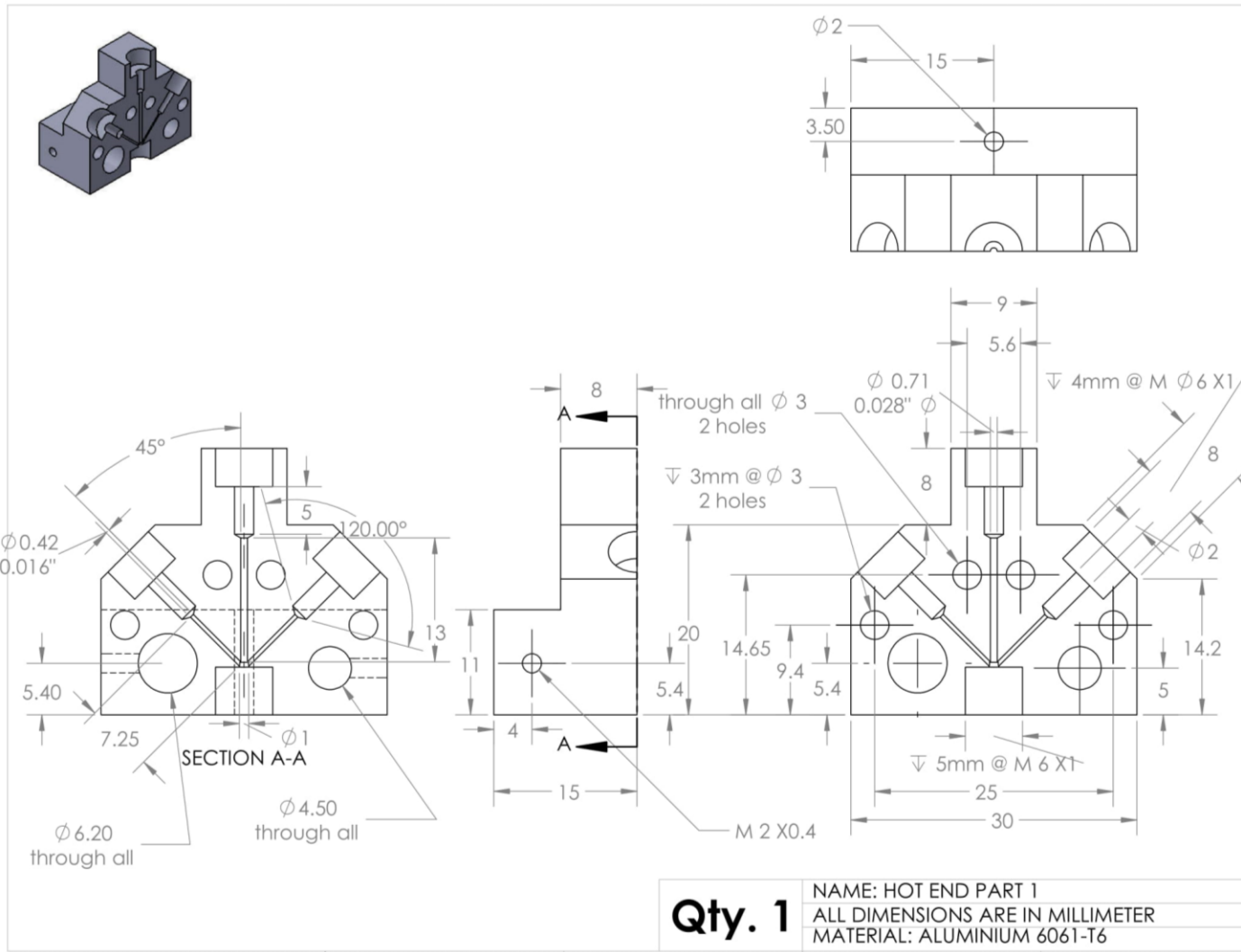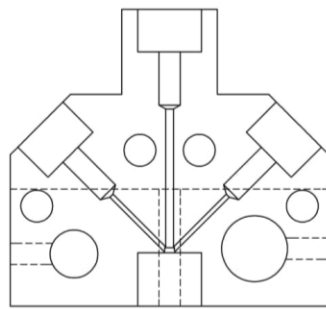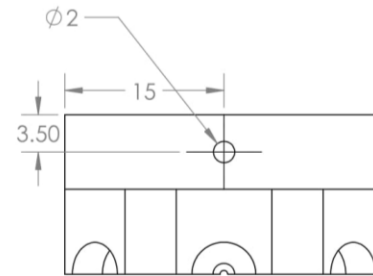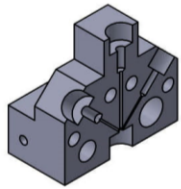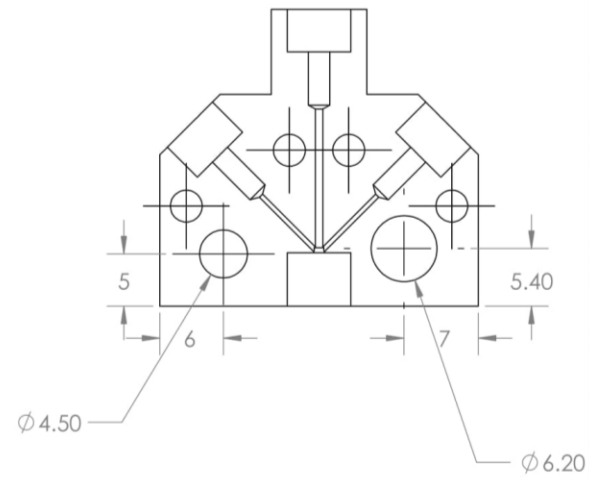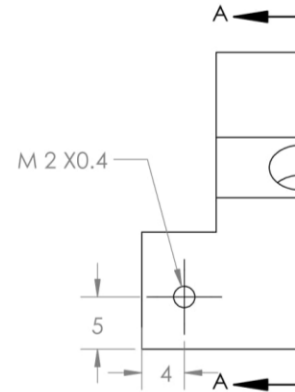
NAME: HOT END PART 1
Qty. 1
ALL DIMENSIONS ARE IN MILLIMETER
MATERIAL: ALUMINIUM 6061-T6

SECTION A-A

Ø2

15

3.50

M 2 X0.4

5

4

A

A

5

6

Ø4.50

5.40

7

Ø6.20

Ø 6
M6X1 mm Thread �álv 9.5 mm

Ø 3
Ø 2
Ø 2

30.5

20.50

6.50   Ø 6

M6X1 mm ⍱ 6 mm; Ø 6

SECTION A-A
SCALE 3 : 1

A

Each fin 0.5 mm
thick

Each gap 1 mm

Ø 18

A

Qty. 2

NAME: GUIDE WAYS_WITH TEFLON TUBE
ALL DIMENSIONS ARE IN MILLIMETER
MATERIAL: STAINLESS STEEL 18-8
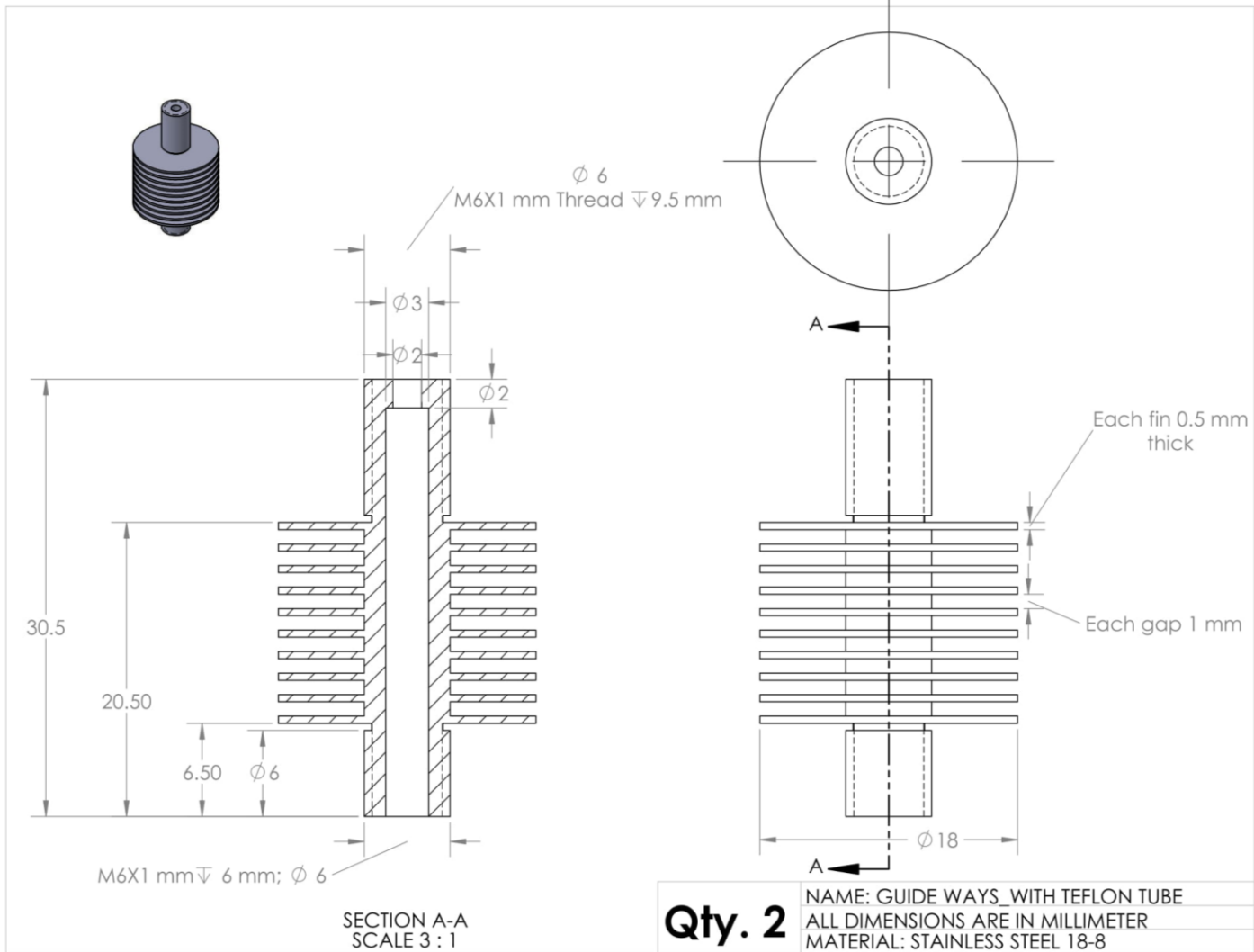
COPYRIGHTS AND PERMISSIONS

Permission to include the journal article as chapter 2:

Permission to include the journal article as chapter 3:

Permission to reproduce Figure 2.1:

227

Permission to reproduce Figure 2.2:

Permission to reproduce Figure 2.3:

Permission to reproduce Figure 2.4:

Permission to reproduce Figure 2.7:

Permission to reproduce Figure 2.8:

Permission to reproduce Figure 2.9:

Permission to reproduce Figure 2.10:

Permission to reproduce Figure 2.13:

Permission to reproduce Figure 2.14:

Permission to reproduce Figure 3.3:

Dear Mr. Khondoker,

It is our pleasure to grant you permission to use the ASME **Figure 1** from "Design and Characterization of a Bi-Material Co-Extruder for Fused Deposition Modeling," by Mohammad Abu Hasan Khondoker and Dan Sameoto, Paper No. IMECE2016-65330, cited in your letter for inclusion in a PhD thesis entitled Development of a Multi-material Extruder System to 3D Print Hard Thermoplastics, Soft Elastomers and Liquid Metals to be published by University of Alberta, Edmonton, AB, Canada.

Permission is granted for the specific use as stated herein and does not permit further use of the materials without proper authorization. Proper attribution must be made to the author(s) of the materials. **Please note**: if any or all of the figures and/or Tables are of another source, permission should be granted from that outside source or include the reference of the original source. ASME does not grant permission for outside source material that may be referenced in the ASME works.

As is customary, we request that you ensure full acknowledgment of this material, the author(s), source and ASME as original publisher. Acknowledgment must be retained on all pages where figure is printed and distributed.

Many thanks for your interest in ASME publications.

Sincerely,

Beth Darchi

Publishing Administrator

ASME

2 Park Avenue

New York, NY 10016-5990

Tel 1.212.591.7700

darchib@asme.org

237

Permission to reproduce Figure 3.7:

Dear Mr. Khondoker,

we herewith grant you the right to use the figure cited below in your publication. Please make sure to publish the correct copy right.

If there are any further questions please let me know.

Best regards

Antje Schmitt

_____

Antje Schmitt
Assistant to the Managing Director

Hello Antje,

I am contacting you regarding a permission request to use a figure from an article published in International Polymer Processing 26(2). Would you please advise me where to contact for such a request?
I intend to use figure 2 of this article (http://www.hanser-elibrary.com/doi/abs/10.3139/217.2419) in my PhD thesis to be submitted soon. I will make sure to cite properly as follows:

"from the journal IPP, Vol…., no…., pp … - …, year…, by … (authors name), ©Carl Hanser Verlag GmbH & Co.KG, Muenchen".

Thank you very much.

Best regards,
_____
Mohammad Abu Hasan Khondoker, E. I. T.
Graduate Research Assistant
PhD Candidate, Department of Mechanical Engineering
University of Alberta, Edmonton, Canada